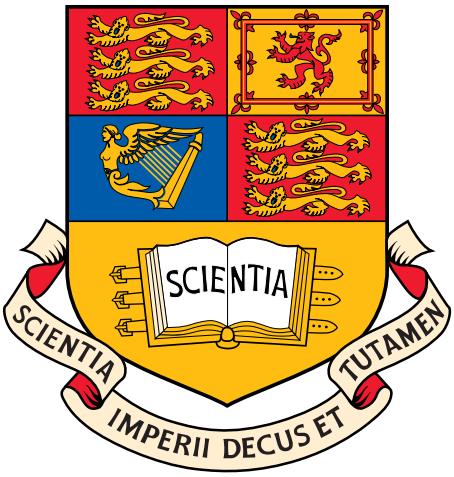
Consistent Aeroelastic Linearisation and Reduced-Order Modelling in the Dynamics of Manoeuvring Flexible Aircraft

Henrik Hesse



Imperial College London
Department of Aeronautics

This thesis is submitted for the degree of Doctor of Philosophy and the Diploma of Imperial College London.

August 2013

Declaration

I hereby declare that this thesis, and the research to which it refers, are the product of my own work, and has not been submitted for any other reward. Ideas and quotations from the work of other people, published or otherwise, are fully acknowledged.

The copyright of this thesis rests with the author and is made available under a Creative Commons Attribution Non-Commercial No Derivatives licence. Researchers are free to copy, distribute or transmit the thesis on the condition that they attribute it, that they do not use it for commercial purposes and that they do not alter, transform or build upon it. For any reuse or redistribution, researchers must make clear to others the licence terms of this work

Henrik Hesse

To my parents, Brigitte & Georg Egger,
for encouraging me to explore.

Acknowledgements

A very special thanks goes to my academic supervisor, Dr Rafael Palacios. I am truly grateful to have had such an inspirational guide and mentor over the last years. The endless support that I have received from him is reflected throughout this work and goes beyond anything I could have ever expected. Rafa truly deserves the Student Academic Choice Award 2013 for Best Supervision among all academics at Imperial College!

I would also like to thank the examiners of this thesis, Professor Jonathan Cooper from the University of Bristol and Dr Georgios Papadakis from Imperial College London, for their time and interest leading to an insightful discussion about this work. I do hope that they were also able to benefit from this experience.

The multidisciplinary nature of this work has made it a very collaborative effort. It would not have been so much fun and I would still not be able to present a manoeuvring aircraft without the contribution from Dr Joseba Murua. His implementation and the interfacing of the aircraft aerodynamics form one of the pillars of this work. I am glad that I could share the challenges, frustration and beauty of large rotations with him and that our (unstable) aircraft was finally trimmed! I would also like to thank the PhD students at the Department of Aeronautics, especially all the members of the Aeroelastics Group, for making the time at Imperial College such a great experience.

My PhD was sponsored by the UK Engineering and Physical Sciences Research Council (EPSRC) which is gratefully acknowledged. I would also like to acknowledge the important financial contributions from the Royal Aeronautical Society, the Imperial College Trust and the Old Centralians' Trust which enabled me to present my work at a number of conferences. I hope that the outcome of this contribution will trigger exciting new projects that enable us to venture beyond the limits of the currently possible, like the concept of perpetual flight as discussed in this work.

This curiosity is something that I have seen so often in my parents, which is why I want to dedicate this work to them. Even though I did not return to Berlin as much as I had initially promised, I am also very grateful to Carlotta and Emil who thought of me for a long time as the man behind all aircraft; thanks to Philipp and Sabine for encouraging this illusion. At last, I would like to acknowledge Carla for her general support throughout my time in London and making it four very special years. Thank you all!

Abstract

This work proposes a novel reduced-order modelling approach in time domain for the coupled flight dynamics and aeroelastic response of manoeuvring very flexible aircraft. The starting point is the coupling of a displacement-based, geometrically-nonlinear flexible-body dynamics formulation with a 3-D unsteady vortex-lattice method. This is followed by a linearisation of the structural degrees of freedom, which are assumed to be small in a body-fixed reference frame. The translations and rotations of that reference frame and their time derivatives, which describe the vehicle flight dynamics, can be arbitrarily large. As a result, all couplings between the rigid and elastic motions are introduced without the *a priori* assumptions of the mean axes approximation, traditionally used to decouple the equations in flexible-aircraft dynamics. The resulting system can be projected onto a few vibration modes of the unconstrained aircraft with geometrically-nonlinear static deflections at a trim condition. Equally, the unsteady aerodynamics are approximated on a fixed lattice defined by the deformed static geometry. The resulting high-order aerodynamic system, which defines the mapping between the small number of generalised coordinates and unsteady aerodynamic loads, is then reduced through balanced truncation. This unified description of the flexible aircraft dynamics provides a hierarchy of aeroelastic model fidelities, which will be illustrated on a representative high-altitude, long-endurance aircraft to identify the importance of geometrically-nonlinear wing deformations on the vehicle dynamics. Application of the reduced-order modelling approach further shows a very substantial reduction in model size that leads to model orders (and computational cost) similar to those in conventional frequency-based methods but with higher modelling fidelity to compute manoeuvre loads. Closed-loop results for the Goland wing finally demonstrate the application of this approach in the synthesis of a robust flutter suppression controller.

Contents

Acknowledgements **7**

Abstract **9**

List of Figures **13**

List of Tables **17**

Nomenclature **18**

1 Introduction **21**
- 1.1 Literature Review 25
  - 1.1.1 Flexible-Body Dynamics 25
  - 1.1.2 Flight Dynamics of Flexible Aircraft 30
  - 1.1.3 Reduced-Order Modelling in Aeroelasticity and Fluid-Structure Interaction 37
- 1.2 Research Questions of the Thesis 40
- 1.3 Present Approach 40
  - 1.3.1 Original Contributions of this Work 42
- 1.4 Dissertation Outline 43
- 1.5 Publications Based on this Work 44

2 Flexible-Body Dynamics Formulation **47**
- 2.1 Geometrically-Nonlinear Flexible-Body Dynamics Equations 47
  - 2.1.1 Kinematics of Finite Rotations 48
  - 2.1.2 Geometrically-Exact Beam Kinematics 50
  - 2.1.3 Dynamic Equations of Motion of Unconstrained Structures 52
  - 2.1.4 Discrete Form of the Equations of Motions 54
- 2.2 Consistent Structural Linearisation in Nonlinear Flexible-Body Dynamics . 56
  - 2.2.1 Perturbation of Structural Dynamic Equations 56
  - 2.2.2 Fully-Linearised Flexible-Body Dynamics 59
- 2.3 Modal Projection of the System Equations 60
- 2.4 Time integration of the System Equations 62

3 Integrated Aeroelastic and Flight Dynamics Framework **65**
- 3.1 Unsteady Vortex Lattice Method 65

3.1.1 Governing Equations of the Potential Flow . . . 66
3.1.2 Discretisation with Vortex Ring Elements . . . 67
3.1.3 Time-Stepping Solution of the Aerodynamic Lattice . . . 68
3.1.4 Wake Propagation . . . 70
3.1.5 Unsteady Aerodynamic Loads . . . 71
3.1.6 Linearised Formulation in State Space . . . 72
3.2 Coupled Aeroelastic and Flight Dynamics . . . 74
3.2.1 Mapping between Aerodynamic and Flexible-Body Degrees of Freedom 75
3.2.2 Nonlinear Equations of Motion of Very Flexible Aircraft . . . 77
3.2.3 Perturbation Equations for the Dynamics of Manoeuvring Flexible Aircraft . . . 79
3.2.4 Monolithic Framework for Linear Stability Analysis of Very Flexible Aircraft . . . 81

4 Reduced-Order Models for Coupled Aeroelasticity and Flight Dynamics 83
4.1 Numerical Issues in Reduced-Order Modelling of Aeroelastic Systems . . . 84
4.1.1 Transformation of the UVLM to Continuous Time . . . 85
4.1.2 Stability and Conditioning of Aeroelastic Systems . . . 87
4.2 Overview of Balancing Approximations . . . 90
4.2.1 Balanced Realisation and Truncation . . . 91
4.2.2 Balancing of Unstable Systems by Normalised Coprime Factorisation 93
4.3 Balanced Approximation for Flexible Aircraft Dynamics . . . 94
4.3.1 Balanced Truncation of the Linearised State-Space Aeroelastic System 94
4.3.2 Reduced-Order Modelling of Manoeuvring Flexible Aircraft . . . 95

5 Numerical Studies of Flexible Unconstrained Structures . . . 99
5.1 Verification of the Flexible-Body Dynamics Module . . . 100
5.1.1 Flying Flexible Beam (FFB) with Large Deformations . . . 100
5.1.2 Dynamic Response of a Flexible Multi-Beam (FMB) Configuration . 102
5.2 Structural Linearisation in the Flexible-Body Dynamics of the FMB Configuration . . . 105
5.2.1 Modal Reduction of the FMB Configuration . . . 107
5.2.2 Assessment of the Mean-Axes Approximation on the FMB Configuration . . . 110

6 Application of the Aeroelastic Simulation Framework to the Analysis of Flexible Aircraft . . . 119
6.1 The Clamped Goland Wing Problem . . . 120
6.1.1 Verification of the Aeroelastic Module . . . 121
6.1.2 Model Reduction of the Unstable Aeroelastic System . . . 123
6.1.3 Robust Control Synthesis for Flutter Suppression . . . 125
6.2 Flight Dynamics of a Flexible Aircraft Configuration . . . 127

6.2.1 Nonlinear Trim for Steady Flight . . . 129
6.2.2 Linear Stability Analysis . . . 131
6.2.3 Inertial Coupling Effects on the Aircraft Open-Loop Response . . . 136
6.2.4 Reduced-Order Modelling of the Manoeuvring Flexible Aircraft . . . 141

7 Conclusions . . . 149
7.1 Overall Conclusions . . . 149
7.1.1 Theoretical Development . . . 149
7.1.2 Numerical Simulations . . . 151
7.2 Key Contributions of this Thesis . . . 153
7.3 Recommendations for Future Work . . . 154
7.3.1 Application of the Simulation Framework . . . 154
7.3.2 Improvements to the Current Methodology . . . 155

Bibliography . . . 159

List of Figures

1.1 The Subsonic Ultra Green Aircraft Research (SUGAR) Volt design concept. Image credit: NASA & The Boeing Company. 22
1.2 Examples of high-altitude, long-endurance unmanned aerial vehicles. Image credit: NASA & The Boeing Company. 23

2.1 Multi-beam configuration with the definition of reference frames. 48

3.1 Flow chart of the unsteady vortex lattice method solution procedure. 66
3.2 Unsteady vortex lattice method with vortex ring discretisation of lifting surface and wake for free-stream flow in positive x direction. 68
3.3 Different wake models for a rigid plate subject to sinusoidal pitch excitation. 70
3.4 Fluid-structure interface between the UVLM and the beam formulation. . . 75
3.5 Flow diagram of the nonlinear time-marching routine. 78
3.6 Linearised time-marching solution for manoeuvring flexible aircraft. 80

4.1 Root locus of the aeroelastic system for the Goland wing at 180 m/s. . . . 86
4.2 Coupling effects on root locus of the Goland wing at free-stream velocity $V = 180$ m/s with structural (Eq. (2.42)), aerodynamic (Eq. (3.13)) and the coupled aeroelastic (Eq. (3.19)) modes. 88
4.3 Effect of numerical damping, α, on aeroelastic modes of the Goland wing at free-stream velocity $V = 180$ m/s. 88
4.4 Model reduction of the aeroelastic system with model orders shown as an indication for typical problem sizes. 95
4.5 Model reduction approach for the time-marching solution of manoeuvring flexible aircraft based on the vehicle free-free vibration modes. 96

5.1 FFB geometry, material properties and load histories [177, 179]. 101
5.2 Snapshots of deformed shapes for the 2-D FFB problem in increments of 0.5 for different time steps Δt. [10 2-noded elements] 101
5.3 Snapshots of deformed shapes for the 3-D FFB problem with different number of elements. [$\Delta t = 0.01$] 102
5.4 Snapshots of 3-D FFB problem in increments of 0.4 in x-z plane (solid lines) with positions of both tips (dashed lines) and centre of mass (stars). [$\Delta t = 0.01$ and 20 2-noded elements] 102
5.5 Definition of the FMB problem. 103

5.6 Snapshots of deformed shapes for the FMB, load case 1, obtained with SHARP at consecutive steps from $t = 0$ s (grey) to $t = 20$ s (black) in increments of 0.5 s. 104
5.7 Comparison of FMB, load case 1, in SHARP (curves) with SAMCEF *Mecano* (markers). 104
5.8 Rigid-body velocities of the FMB for load case 2. $[\sigma = 10]$. 105
5.9 Tip deformations of FMB, load case 2, for varying stiffness parameter σ. . 106
5.10 Linearisation of elastic DoF for FMB with load case 2. Maximum relative error norm of linearised formulation (solid) and simplified nonlinear solution with constant mass matrix $\mathcal{M} = \mathcal{M}(\eta_0)$ (dashed) for different σ. 106
5.11 First elastic mode shapes for the FMB problem. $[\sigma = 10]$ 108
5.12 Response of the first eight elastic modes for FMB, load case 2. $[\sigma = 10]$ . . 108
5.13 Modal projection of linearised EoM for the FMB, load case 2. Maximum relative error norm of rigid-body velocities and right tip displacement against number of elastic modes. $[\sigma = 10]$ 109
5.14 Maximum relative error norm of rigid-body angular velocities and right tip displacement of mean axes solution for the FMB, load case 2, compared to linearised for different values of σ. [$\Delta t = 0.01$ s and 120 2-noded elements] 112
5.15 Comparison of fully-nonlinear, linearised and mean-axes approaches in predicting the vertical tip displacement of point P in Figure 5.5 for the FMB problem with load case 2 and different σ values. 113
5.16 Load history of the FMB spiral problem. 114
5.17 Trajectory of the FMB spiral problem for the different formulations. 115
5.18 Comparison of fully-nonlinear, linearised and mean-axes approaches in predicting the vertical tip displacement of point P_{tip} for the FMB spiral problem and different σ values. 115
5.19 Relative error norms of maximum tip displacements of Point P_{tip} for FMB spiral problem comparing linearised and mean-axes approximations to the fully-nonlinear solution. 116
5.20 Trajectory of the A frame for the FMB spiral problem with $\sigma = 50$ and different p_R using the fully nonlinear model. Displacement in the z-direction is the same for all cases and markers are plotted every 20 time steps. . . . 117
5.21 Comparison of fully-nonlinear, linearised and mean-axes approaches in predicting the normalised vertical displacement of point P_{tip} for the FMB spiral problem with $\sigma = 50$. 117
5.22 Maximum error norm of displacements at point P_{tip} for the FMB problem, comparing mean-axes approximation to the nonlinear solution for different radii. 118

6.1 Undeformed Goland wing geometry with definition of system in- and outputs. Material properties have been defined in Table 4.1. 121

6.2 Open-loop response of the Goland wing subject to sinusoidal aileron input with 1 deg amplitude at different free-stream velocities, V. 122
6.3 ν-gap metric between full- and reduced-order models using balanced truncation and balanced coprime factorisation. Superimposed are the Hankel singular values of the balanced system. 123
6.4 Comparison of different reduced-order balanced system responses against the full-order model for a range of reduced frequencies, $k = \omega c/(2V)$, at free-stream velocity $V = 180$ m/s $(1.07V_f)$. 124
6.5 Block diagram of a closed-loop system. 126
6.6 Demonstration of flutter suppression for the Goland wing at free-stream velocity $V = 180$ m/s $(1.07V_f)$ for varying number of $\mathcal{H}_\infty$ controller states, n_K. The imaginary part has been normalised with $c/(2V)$. 127
6.7 Undeformed HALE aircraft geometry with front and top view (not to scale). 128
6.8 Trim angle of attack, elevator deflection, thrust per propeller, and vertical tip deflection of the main wing, $\Delta R_{Az}/B$, as a function of wing flexibility, σ, and dihedral member ratio, λ. 130
6.9 Trim deformation of HALE aircraft with $\lambda = 1/2$ and different stiffness parameters σ. (Figure shows actual deformations.) 130
6.10 Root loci of the eigenvalue analysis with the stiffness of the main wing, σ, as parameter: flight dynamic, aeroelastic, and aerodynamic modes highlighted with solid, dashed, and dotted curves. The imaginary part has been normalised with $c/(2V)$. 131
6.11 Zooms of the root loci of Figure 6.10(b) showing the flight dynamic modes close to the origin. The imaginary part has been normalised with $c/(2V)$. . 132
6.12 Root loci of the eigenvalue analysis for $\sigma = 1.1$ (in blue) and $\sigma = 1000$ (in black) with the dihedral ratio λ as parameter: (a) dominant roots, and (b) zoom near to the origin. The imaginary part has been normalised with $c/(2V)$. 133
6.13 Aerodynamic component of the mode shapes for a very flexible aircraft, $\sigma = 1$, showing the circulation strengths of the vortex rings for the six modes highlighted in Figure 6.10(b). 135
6.14 Control inputs for ailerons (δ_a^*) and elevator (δ_e^*). Transients are sine functions. 137
6.15 Rigid-body angular velocity components of the HALE aircraft in response to Figure 6.14: (a) time history of the rigid vehicle and (b) maximum norm of ω_A and its individual components for varying stiffness computed using the geometrically nonlinear model. 137
6.16 Trajectory of the HALE aircraft in response to Figure 6.14 for $\lambda = 1/4$ with stiffness of the main wing, σ, as parameter. 138

6.17 Maximum relative error norm of aircraft altitude using linearised and mean axes approximations compared to the nonlinear solution for $\lambda = 1/4$ and varying stiffness σ. 139
6.18 Vertical tip deflection of the right main wing normalised with the semi-span of $B = 16$ m for dihedral ratio of $\lambda = 1/4$. 139
6.19 Maximum relative error norm of vertical wing tip deflections for $\lambda = 1/4$ and varying σ. 140
6.20 Aerodynamic coefficients for the flexible HALE wing ($\sigma = 5$, no dihedral, and 5 deg AoA) subject to forced harmonic rigid-body motions of the A frame with $\omega = 2\pi$ rad/s: comparison between the geometrically-nonlinear time-marching and the linearised full-order state-space solutions. 141
6.21 Comparison of reduced-order models in terms of frequency response of flexible HALE wing ($\sigma = 5$) with aerodynamic loads due to the harmonic plunging, pitching and rolling motions for different reduced frequencies, $k = \omega c/(2V_\infty)$. 142
6.22 Open-loop response of HALE aircraft subject to antisymmetric aileron inputs for the full-order state-space system for varying stiffness, σ. Tip deflections are normalised with $B \cdot \sigma^{-1}$. 143
6.23 Effect of model order of aerodynamic system on open-loop response of HALE for $\sigma = 2$ and all flexible-body dynamics modes. 144
6.24 History of the wake for the manoeuvring flexible aircraft with $\sigma = 2$ subject to aileron inputs, showing circulation strengths of the wake vortex rings, Γ_w. 145
6.25 Effect of number of flexible-body dynamics modes (ascending order of frequency) on open-loop response of HALE for $\sigma = 2$ and full-order aerodynamic system. 145
6.26 First antisymmetric (a) bending and (b) torsion structural modes of the flexible HALE configuration ($\sigma = 2$) around trimmed flight condition (trim geometry superimposed in gray). 146
6.27 Relative L_∞ error of the HALE aircraft reduced-order open-loop response for varying number of aerodynamic states and free-free modes (including the six rigid-body modes) and three values of the stiffness parameter, σ. . 147

List of Tables

4.1 Goland wing properties. 85

5.1 Load cases for the FMB problem. 103
5.2 First elastic modes for the FMB problem. [$\sigma = 10$] 107
5.3 Perturbed modal damping matrix in tensor form, c_{ilr}, for the FMB problem using the first three elastic modes in addition to the six rigid-body modes. Entries have been rounded to full integers. [$\sigma = 10$]. 110

6.1 Flutter speed, V_f, and frequency, ω_f, of the Goland wing for M chordwise and N spanwise bound vortex panels. 121
6.2 HALE aircraft properties. 128

Nomenclature

Symbols

A	aerodynamic influence coefficient matrix
c	chord length
C	coordinate transformation matrix from frame A to B
C^{GA}	coordinate transformation matrix from frame A to G
$\mathcal{C}$	global tangent damping matrix
F	nodal external forces
$\mathbb{F}$	sectional internal forces
H	sectional angular momenta
I	unit matrix
J	cross-sectional inertia tensor
k	reduced frequency
K	sectional local curvature
$\mathcal{K}$	global tangent stiffness matrix
$\vec{n}$	normal vector
m	mass per unit length
M	nodal external moments
$\mathbb{M}$	sectional internal moments
$\mathcal{M}$	global tangent mass matrix
$\mathcal{M}_{cs}$	cross-sectional mass matrix
N	matrix of shape functions
p	pressure
P	sectional translational momenta
q	generalised displacements in modal basis;
	velocity induced by the Biot-Savart law (§3.1)
$Q_.$	global vector of gyroscopic, elastic or external forces distinguished by subscript
r	position vector of the origin of body-fixed frame, A
R	local position vector along the beam reference line
s	arc-length along beam reference line
$\mathcal{S}_{cs}$	cross-sectional stiffness matrix
t	physical time
T	tangential operator (§2);
	thrust per propeller (§6)
$\mathcal{T}$	kinetic energy density

u	input vector
$\mathcal{U}$	internal energy density
v	inertial translational velocity of the body-fixed frame
V	inertial translational velocity at a beam cross section
w	non-vortical normalwash at the collocation point
W_c	controllability Gramian
W_o	observability Gramian
$\delta\mathcal{W}$	virtual work per unit length
x	state vector of a linear system identified by subscripts
X	inertial position vector of a point on a local cross section
y	output vector

Greek Symbols

α	algorithmic damping parameter in Newmark time integration
β	vector of global translational and rotational velocities
γ	beam local force strain
Γ	circulation strength of a vortex ring
$\delta_{a,e}$	aileron/elevator deflection
Δ	increment
ε	$\mathcal{L}_\in$ relative error norm
ζ	quaternion for global orientation of the body-fixed frame, A
η	vector of nodal displacements and rotations
Θ	Euler angles
κ	beam local moment strain
λ	parameter of winglet ratio
ν	global displacements and rotations as time integral of β
ξ	beam cross-sectional coordinates
σ	stiffness parameter
$\delta\phi$	global virtual rotations
Φ	matrix of mode shapes (§2); velocity potential (§3.1)
$\delta\Phi$	local virtual rotations
χ	grid coordinates of the aerodynamic lattice
Ψ	local Cartesian rotation vector (CRV) along the beam reference line
ω	inertial angular velocity of the body-fixed frame, A
Ω	inertial angular velocity at a beam cross section

Subscripts

A	body-fixed reference frame
b	bound, corresponding to lifting surface
B	local reference frame on flexible members

f	flutter
F	aerodynamic
FS	aeroelastic, including rigid-body and structural states
gyr	gyroscopic
G	inertial reference frame
R	rigid-body
S	structural
w	wake

Superscripts

$(\dot{\bullet})$	derivatives with respect to time, t
$(\bullet)'$	derivatives with respect to arc-length, s
$(\bar{\bullet})$	small perturbations around an equilibrium
$(\tilde{\bullet})$	cross-product operator
$(\vec{\bullet})$	vector quantity
$(\bullet)^*$	conjugate transpose of a matrix
$\langle\bullet\rangle$	integral over the area contour at a cross section
$\delta(\bullet)$	variational operator

Abbreviations

AoA	Angle of Attack
CFD	Computational Fluid Dynamics
CM	Centre of Mass
CRV	Cartesian Rotation Vector
DLM	Doublet-Lattice Method
DoF	Degree of Freedom
EoM	Equations of Motion
FoR	Frame of Reference
HALE	High-Altitude Long-Endurance
LCO	Limit-Cycle Oscillation
MPC	Model Predictive Control
PID	Proportional-Integral-Derivative
POD	Proper Orthogonal Decomposition
ROM	Reduced-Order Model
SHARP	Simulation of High-Aspect-Ratio Planes
UAV	Unmanned Aerial Vehicle
UVLM	Unsteady Vortex-Lattice Method
VFA	Very Flexible Aircraft

Chapter 1

Introduction

To meet the demands of a growing and increasingly affluent world population, the face of aviation in the 21st century needs to adjust. Due to urbanisation, more and more people are expecting to fly but are equally affected by the resulting growth in air travel. The next generation of aircraft has to demonstrate significant improvements in noise reduction and fuel efficiency to tackle the detrimental impact of aviation on our everyday lives [184]. Apart from the important environmental impact, fuel economy of current and next-generation aircraft has naturally been a driving force for aircraft manufacturers to respond to uncertainties in the fuel price and the public debate about the impact of aviation on our climate.

These important social, economic and environmental issues have been addressed by the European Union with the establishment of an Advisory Council for Aeronautics Research in Europe (ACARE) and the definition of ambitious targets for 2020 [1] and 2050 [2] to reduce the detrimental impact of aviation and to promote efficiency improvements. To achieve these goals, recent efforts in the aviation industry have focused on:

- novel airframe configurations to improve structural performance,
- engine technology for optimised fuel burn and noise reduction,
- low-drag wings to improve aerodynamic efficiency and
- advanced materials for weight reduction.

The motivation to focus on these key technologies is best summarised by the Breguet range equation which provides a simple expression for the range, R, of typical long-haul flights, given as [157]

$$R = \eta_p \frac{L}{D} \ln\left(\frac{W_0}{W_e}\right), \tag{1.1}$$

with the overall propulsion system efficiency, η_p, the ratio of lift over drag, L/D, and the ratio of the aircraft initial over final weight, W_0/W_e. Naturally, one of the criteria for

an aeronautical engineer is to maximise the vehicle range, R, for a given flight condition by focusing on the key technologies above to maximise L/D (aerodynamic efficiency), minimise W_e (weight reduction) and increase η_p (engine technology).

An example of the recent development in these key technologies is the Boeing SUGAR Volt concept which was developed as part of the NASA Subsonic Fixed Wing Project to identify solutions for lower noise, lower emissions and higher performance of subsonic aircraft [25]. The resulting low-speed design, shown in Figure 1.1, features high-aspect-ratio wings without sweep to reduce drag and hence improve the vehicle aerodynamic performance. A fundamental barrier to achieving such performance improvements, however, is that such slender configurations are susceptible to flexibility resulting in possibly large wing deformations. Longer wings also have to withstand larger bending moments which threaten their structural integrity. The strut design of the SUGAR Volt concept, which is typical for high-wing aircraft to support the structure during flight (lift) and on the ground (gravity), introduces a drag penalty opposing the aerodynamic benefits of high-aspect-ratio wing designs. The relatively low stiffness of load-carrying surfaces to achieve further weight reduction also leads to low natural frequencies which can interact with the flight dynamic response of the vehicle during piloted manoeuvres or gust disturbances. The conventional approach to alleviate these effects by adding more material (and weight) opposes the performance gains of aerodynamically more efficient designs. Hence, the development of advanced aircraft requires the integration of key technologies in structures, aerodynamics, control systems, materials and power management which is likely to cause a higher level of aeroelastic interaction between these disciplines



Figure 1.1: The Subsonic Ultra Green Aircraft Research (SUGAR) Volt design concept. Image credit: NASA & The Boeing Company.

Such technological improvements, combined with current breakthroughs in power management and telecommunication technologies, would also facilitate the development of very

long endurance (even perpetual) unmanned flight, which promises great potential as a cost effective substitute for geostationary satellites with possible applications in telecommunication, navigation and atmospheric research. Apart from the obvious military applications for surveillance and reconnaissance, high-altitude long-endurance unmanned aerial vehicles (HALE UAVs) provide a platform for humanitarian applications in the detection of disasters such as forest fires and tsunamis. Commercial applications are currently limited by the available autonomy of these vehicles, which is crucial for crop control in agriculture or monitoring and maintenance of vast offshore wind turbine arrays.

The nature of these possible applications highlights the endurance requirement of autonomous HALE UAVs, which has been achieved using photovoltaic arrays or hydrogen fuel cells as demonstrated by the two HALE UAV concepts shown in Figure 1.2. Because of their extreme mission requirements – both examples have been designed to remain airborne for years – modern UAVs have to be highly efficient which results in very flexible designs that can exhibit large geometry changes during normal flight operation. The extent of large (geometrically nonlinear) wing deformations is exemplified by the NASA *Helios* concept, shown in Figure 1.2(a), which successfully demonstrated the concept of solar-powered flight at high altitudes. However, its mishap in 2004 following a gust disturbance also highlights the effect of large wing deformations on the vehicle dynamics and structural integrity. The investigation into the failure [132] concluded that multidisciplinary models, that incorporate structural, aerodynamic and control aspects to describe the vehicle geometrically-nonlinear behaviour, are needed to design the next generation of HALE UAVs. Such methods, among other technological advances, will provide the necessary tools for the realisation of increasingly complex concepts that are designed to operate at extreme atmospheric conditions. An example of this is the Boeing *Solar Eagle* in Figure 1.2(b) which consists of a very high-aspect-ratio wing that spans 120 m (150% the wing span of an Airbus A380).



(a) Wing dihedral of NASA *Helios* during test flight (b) Boeing *Solar Eagle* conceptual design

Figure 1.2: Examples of high-altitude, long-endurance unmanned aerial vehicles. Image credit: NASA & The Boeing Company.

Active control of structural vibrations and their possible interaction with the vehicle flight dynamics is key in the development of such highly-efficient UAVs and passenger aircraft to ensure dynamic stability even at large wing deformations and to reduce dynamic loads due to exogenous excitations or commanded manoeuvres. Hence, in addition to the conventional flight control and guidance systems, active load control is a necessary tool in the design of these vehicles to reduce critical loads and improve ride comfort for passengers by damping structural or flight-dynamic oscillations. On the other hand, flexibility can also be exploited taking advantage of the anisotropic behaviour of composites, which are emerging as advanced materials used for load-carrying subcomponents in weight-optimised aircraft. This so-called aeroelastic tailoring provides a promising passive control method to stabilise aeroelastic effects in aerodynamically-optimised, high-aspect-ratio, zero-sweep wing designs.

In summary, understanding the effect of flexibility on the aircraft dynamics is crucial in the design of advanced aircraft concepts for unmanned and passenger flight. Classic approaches which usually separate the aeroelastic response from the vehicle flight dynamic analysis are insufficient to understand the physics of the interaction between the flight dynamics and the structural response of modern aircraft. Instead, the problem needs to be tackled in a multidisciplinary manner whereby the vehicle aerodynamic, structural and flight dynamic behaviour is integrated in a coupled environment. The required model fidelity to accurately capture the dynamics of complex vehicle configurations with possibly large structural deformations also needs to be addressed to arrive at efficient solution methods. Numerical efficiency of the coupled simulation framework, in addition to the model fidelity, is crucial to incorporate flexibility effects in the early design stages of next-generation aircraft to expand the design envelope.

This research therefore aims to develop a framework for modelling the dynamics of flexible aircraft with a hierarchy of model fidelities to investigate the effect of large wing deformations on the vehicle response. The understanding of the complex interaction between the different disciplines (structural, rigid-body and aerodynamics) will provide the necessary knowledge to identify suitable reduced-order models (ROMs) that can accurately capture the underlying physics of the coupled problem. Despite the steady increase in computational power, low-order representations of the generally high-fidelity dynamics are needed for the design of robust control methods to actively control deformations that are inherent to highly-efficient aircraft designs. Finally, because of the critical importance of composites in aviation, this work considers anisotropic materials in the description of the dynamics of flexible vehicle. Note however that the numerical studies in this dissertation are limited to isotropic problems to primarily demonstrate the aeroelastic modelling approach.

1.1 Literature Review

Capturing the dynamic behaviour of manoeuvring aircraft with flexible subcomponents is indeed a multidisciplinary endeavour which relies heavily on the incorporation of established theory in the areas of aerodynamics, structural dynamics and multibody dynamics. This literature review will therefore provide a brief overview of each discipline and highlight the characteristics of the different models in terms of fidelity, numerical efficiency and ease of implementation. These aspects are crucial for the efficient modelling and design of next-generation aircraft.

In the context of aircraft design, the vehicle flight dynamics and aeroelastic response have traditionally been addressed separately. This was possible because of relatively stiff designs of conventional aircraft, as highlighted in several review papers and reference books on aeroelasticity [62, 106] and modern flight dynamics [162]. Depending on the starting point, either aeroelasticity or flight dynamics, the integration of flexibility effects on the vehicle flight dynamics has been addressed following two very different paths.

The following literature review will present this development according to the approach taken in this dissertation, whereby the next subsection will first summarise the extension of multibody dynamics problems to account for elastic deformations of flexible members. This provides a description of the coupled flexible-body dynamics of unconstrained configurations. Subsection 1.1.2 will then review the extension of flight dynamics formulations to include the vehicle structural dynamics in the description. This will be followed with a summary of the integration of geometrically-nonlinear structural models to capture possibly large deformations of very flexible HALE configurations. The necessary fidelity required to capture the interaction between the aircraft structural and flight dynamics may result in large models that require a large computational effort to be suitable for efficient aircraft design. Hence, Subsection 1.1.3 will conclude the review of previous work with a summary on model reduction techniques that have been developed to enable high-fidelity aeroelastic analyses.

1.1.1 Flexible-Body Dynamics

The effect of flexibility on the overall motion of spacecraft, as a result of extreme lightweight requirement, accelerated the research into flexible multibody dynamics (FMD) in the second half of the last century. Such systems are unconstrained structures subject to large translational and rotational motion. This is also relevant in the analysis of flexible aircraft, as discussed in Subsection 1.1.2, but the following review first summarises the work on flexible-body dynamic problems without aerodynamics.

The choice of reference frame in the integration of the body structural and rigid-body dynamics is crucial in the modelling of flexible bodies. Generally, the inertial frame is used in FMD to describe the overall (rigid-body) motion of the body, which differs from

the Lagrangian description commonly used in flight mechanics. Several approaches have been developed to include the effect of flexibility of subcomponents on the dynamics of flexible multibody systems. Following the review papers by Wasfy and Noor [198] and Shabana [167], they can be classified according to the type of reference frame used in the description as floating, co-rotational and inertial frame approaches.

The *floating frame approach* is a natural extension of existing rigid-body dynamics codes to account for the effect of flexibility by superposition of the body structural dynamics on its possibly large overall motion. To enable this superposition the floating frame needs to follow an averaged rigid-body motion of the structure and the approach is limited to small elastic deformations.

In the *co-rotational frame approach*, each finite element in the discretisation of the unconstrained flexible body has an associated frame which follows the average rigid-body motion of the element. The resulting Lagrangian description of the flexible-body dynamics eliminates the large rigid-body motion of each element from the total displacement vector which leads to a simple approach that can capture large deformations if the element size is sufficiently small.

Originating from continuum mechanics principles rather than a FMD point of view, the *inertial frame approach* directly measures the motion of an element without the necessity for an intermediate frame to express the local deformations which can have large translational and rotational components. Even though the governing equations of motion (EoM) are obtained with respect to a global inertial frame, it is convenient to introduce a body frame that is attached to (and moves with) a specific point on the flexible body to track the nodal orientations of each element. The resulting geometrically nonlinear formulations will be referred to as *body-fixed frame approaches* in this work.

Following the above classification of the reference frames, the following review of the development in flexible-body dynamics is divided into linear and geometrically nonlinear methods in FMD.

Unconstrained Flexible Bodies with Small Deformations

Linear approaches in flexible-body dynamics are a first approximation to include some flexibility effects in the modelling of weight-optimised spacecraft (and aircraft) with small elastic deformations. An efficient definition of the floating frame reference systems is required to enable the superposition of the elastic deformations on top of the rigid-body motion of the flexible body. Body-attached approaches have been considered in linear analyses [32, 166], but moving axes formulations were found to be beneficial as they tend to minimise the extent of (small) elastic deformations with respect to the floating frame [15, 28, 29]. Such a moving reference system is generally given by the Tisserand frame, as discussed in Refs. [28, 47, 133], which minimises the relative kinetic energy of the elastic motion noticed by an observer on the moving reference frame. This definition

of the floating frame balances the local linear and angular momenta due to the elastic deformations with respect to the moving frame, which fulfils the *mean axes approximation*. The latter was first formulated by Milne [122, 123] and assumes that there exists an instantaneous reference frame which decouples the structural and rigid-body dynamics degrees of freedom (DoF), thus providing a much simplified description that superimposes elastic deformations to the rigid-body dynamics, as demonstrated for the dynamics of relatively flexible spacecraft [4, 28, 33] and aircraft [63, 100, 122, 172, 199]. As a consequence of the mean axes approximation the resulting moving reference frame is positioned at the instantaneous centre of mass (CM) of the flexible body which further decouples the overall translational and rotational motion.

The mean axes approximation is naturally enforced by using the *free-free modes* of the unconstrained structure [34, 122], which preserve the position of the body CM following small amplitude vibrations. Modal projection of the flexible body-dynamics equations further allows the truncation of high-frequency modes that contribute little to the overall dynamics of the structure and enables experimental modal identification techniques to be used in FMD [3, 12]. For linear undamped systems, it is indeed possible to transform the system equations to a set of decoupled ordinary differential equations due to the orthogonality property of normal modes. However, if the structure is subject to arbitrary motion, especially large angular rotations, the classical modal analysis fails to decouple the system EoM due to the contribution of the Coriolis effect and centrifugal forces which introduce coupling terms between the rigid-body motion and elastic deformations. This implies that the mean axes approximation neglects some coupling terms even for small elastic deformations. This was demonstrated by Meirovitch [118] using a Lagrangian description of the coupled rigid-body and structural dynamics in terms of quasi-coordinates with respect to a body-fixed frame of reference attached to a specific point on the flexible body [115].

Higher-order strain measures are generally needed to capture the axial shortening and centrifugal stiffening effects due to bending and centrifugal forces, respectively. This has been extensively studied for rotating beams, e.g. Refs. [7, 41, 84, 96] which showed that neglecting the centrifugal stiffness terms can result in large errors. However, the incorporation of shear deformations, Coriolis effect and inertia force usually requires geometrically nonlinear models as demonstrated by Simo and Vu-Quoc [178] through a consistent linearisation of nonlinear EoM derived in a body-fixed frame of reference. The underlying geometrically-nonlinear beam formulation will be the focus of the next subsection.

Geometrically Nonlinear Beam Models

Geometrically nonlinear beam theories are key in understanding the global static or dynamic response in highly-optimised structures with slender subcomponents. An increase in flexibility of load carrying structures has been catalysed by the use of composite materials, which required a parallel effort in developing geometrically nonlinear composite beam

models. Those are typically based on a two step procedure: first, a process of dimensional reduction (*homogenisation*) in which the 3-D composite structure is reduced to averaged properties along the reference line [37, 50, 99, 135] and, second, the solution of the one-dimensional dynamic equations of motion on the homogenised structure (the composite beam) [15, 86, 87]. A comprehensive review of the literature on composite beam modelling can be found, for instance, in the monograph by Hodges [88].

Geometrically nonlinear beam theories are mostly based on the inertial frame approach, such that the beam kinematics are described with respect to an inertial reference frame which incorporates both the rigid-body motion of the beam and the structural deformations into one expression. The description of the kinematics is based on Cosserat's model [40] for the nonlinear analysis of space-curved beams, as written by Love [107] and Reissner [150]. The key aspect in the description of the geometrically exact theory is the representation of the cross-sectional orientation along the reference line of the beam which is achieved through parameterisation of rotations. Reissner [150] used classical Euler angles with their associated singularity to parameterise the orthogonal transformation and presented a definition for the variation of rotations in the solution of static problems using variational principles. Simo and Vu-Quoc [174, 176] were the first to generalise the approach to the fully 3-D dynamic case by introducing quaternions to describe the rotational degrees of freedom (DoF). The equations are solved using finite elements with displacement and finite rotation coordinates as the independent variables. Later, Simo and Vu-Quoc extended the theory to rods undergoing large unconstrained motions in space including rotations [177, 179]. They used a global body-fixed reference frame attached to the reference configuration to include the rigid-body motion of the beam. The geometrically exact description of the beam kinematics is based on nonlinear strain measures which accurately capture extension, shear, torsion and bending deformations.

A similar approach was used by Cardona and Géradin [30, 69] using the Cartesian Rotation Vector (CRV) to describe the sectional orientation. The three parameter representation of the rotation tensor using the CRV not only requires less storage compared to the quaternion parameterisation used in the original work by Simo and Vu-Quoc [179], it also provides expressions for the linearisation of the rotation tensor in terms of an exponential mapping of the rotational DoF. This is essential in a finite element implementation based on an *updated Lagrangian* formulation which removes the singularity of the CRV for rotations of 2π. More recent work has been concerned with further improving the parameterisation of the rotational DoF in the finite element discretisation to extend the formulation to initially curved beams [91].

Argyris [9] and Hodges [85] give detailed overviews on the matrix formulation of finite rotations. Following the representation by Hodges [85], Danielson and Hodges [46] obtained a simplified description of the beam strains by separating the rotation of the cross sections into their global and local components. The global contributions account for the

large rotations of a global body-fixed reference frame and the small local rotations describe the cross-sectional deformations.

Typically the nodal displacements and rotations have been chosen as primary variables [69, 179], but more recent work [35, 169] has focused on *strain-based* approaches to solve the geometrically exact beam equations using the decomposition of the beam strains as presented in Ref. [46]. The resulting nonlinear structural formulation can be cast into state-space form with a constant stiffness matrix which increases numerical efficiency but an additional post-processing is needed in coupled environments to extract displacements and rotations [137]. A hybrid solution procedure, the so-called *intrinsic* beam formulation, was developed by Hodges [86] which takes the beam strains and local translational and angular velocities as DoF in the problem. A comparison of structural (and aerodynamic) models for the modelling of flexible aircraft dynamics by Palacios *et al.* [137] confirmed the numerical benefits of the strain-based and intrinsic formulations, but also identified the advantage of the displacement-based approach for flexible aircraft applications in terms of ease of coupling with the aerodynamic model and implementation of boundary conditions and interconnectivity of the flexible subcomponents. Palacios [134] also derived a nonlinear modal form of the intrinsic beam equations to obtain the nonlinear normal modes in terms of the primary DoF, i.e. the nodal velocities and strains only. The resulting formulation retains the anisotropic material properties and geometrically exact description of the beam kinematics.

The intrinsic formulation [86] also guarantees objectivity which is the invariance of the strain measure with respect to arbitrary rigid-body motions. Crisfield and Jelenić [44] demonstrated that displacement-based beam formulations by nature violate the objectivity criterion in the interpolation of rotational DoF due to the inertial description of the beam kinematics. Instead they propose application of the co-rotational beam formulation [95] which, as defined above, separates the possibly large nodal rotations into rigid-body and pure elastic components. This is achieved by fixing a local reference frame to each element such that the local elastic deformations are small with respect to that frame. This allows the application of simplified strain measures to efficiently capture possibly large beam deflections [90]. Alternatively, Simpson *et al.* [181] have recently demonstrated that the error in the strain field of the interpolated rotations decreases with p- and/or h-refinement of the mesh ensuring the applicability of displacement-based formulations in the dynamics of very flexible structures.

Numerical Time Integration

The spatial discretisation of the EoM in FMD in general leads to nonlinear second-order ordinary differential equations that are numerically stiff due to the large frequency spectrum of the response and the presence of the rigid-body DoF. Hence, implicit numerical algorithms which offer unconditional stability properties are usually favoured for the time integration of the coupled EoM. Several such dissipative integration methods have been

developed from the original Newmark algorithm [130] and have been modified for nonlinear problems using implicit Newton-Raphson sub-iterations as proposed by Géradin and Rixen [70]. The implicit Newmark integration scheme has been demonstrated for geometrically nonlinear problems of unconstrained flexible bodies [90, 91] but it has also been shown to produce (unstable) high frequency oscillations especially in the presence of large rotations [69, 175]. This can be circumvented by introducing controlled positive algorithmic damping to the constant-acceleration Newmark integration scheme [70] which enables undesirable high frequency oscillations to be filtered easily, but it also degrades the order of accuracy. Shearer and Cesnik [168] modified the implicit Newmark scheme further tailored to the time integration of numerically stiff EoM of coupled flexible aircraft dynamics problems.

Other dissipative methods based on the Newmark scheme have been introduced that permit high-frequency dissipation without a significant effect on the accuracy of the lower-frequency response, such as the Hilber-Hughes-Taylor algorithm [83], the Generalised-α Method [168] and other energy-conserving methods [13, 16, 92, 180]. The latter can be specifically tailored to geometric problems taking advantage of differential geometry in the integration of the rotation tensor [92, 180]. The review by Fung [64] provides an in-depth summary on time marching algorithms using numerical dissipation.

1.1.2 Flight Dynamics of Flexible Aircraft

Following the review on the coupling between the aircraft rigid-body and structural dynamics, this section will now focus on the development of integrated models also including the vehicle aerodynamics for the analysis of manoeuvring flexible aircraft. As presented by Wright and Cooper [201], flexibility of aircraft subcomponents can have a significant impact on the vehicle aeroelastic response and dynamic loads due to gust excitations or pilot inputs. Modelling the flight mechanics of flexible aircraft is further complicated by the effect of wing deformations on the aircraft trim equilibrium and the resulting change in stability characteristics. A review by Friedmann [62] highlights the important role of aeroelasticity in the design of future aircraft concepts.

Linearised methods have traditionally dominated the integration of flexibility effects in the modelling of relatively stiff commercial aircraft, which was naturally done by extending existing flight dynamics tools. These methods initially relied on 2-D quasi-steady aerodynamics but higher-fidelity (linear) 3-D unsteady panel methods soon became the standard tool in the aerospace industry for aircraft design [201] and have provided great insight into the unsteady aerodynamic and aeroelastic effects in the exciting development of previous and current aircraft. The development of linear methods will be presented in the first part of this subsection, following the insightful overview by Meirovitch and Tuzcu [116].

By definition, linear methods are limited to small wing deformations and may fail to model the dynamics of unconventional aircraft configurations effectively putting a constraint on the possible design scope of next-generation aircraft, as presented in the outlook by Livne and Weisshaar [106]. Modern designs may feature aerodynamically more efficient high-aspect-ratio wings which tend to exhibit large wing deformations at trim and experience significant interaction between the vehicle flight dynamics and structural vibration modes. The incorporation of these complex features in the design of advanced aircraft concepts requires a higher-fidelity nonlinear modelling approach, which will be presented in the second part of this subsection.

Linear Methods in Flight Dynamics

A first approximation to account for the effect of small wing deformations on the aircraft flight dynamics is through *elastification* of the steady or quasi-steady aerodynamic coefficients commonly used in the flight dynamic analysis of rigid vehicles [165]. However, this approach neglects the inertia effects due to the structural deformations and requires a large separation between the vehicle structural and rigid-body frequencies.

The mean axes approximation based on a floating frame description, as introduced in Subsection 1.1.1 to decouple the structural response from the overall motion of flexible multibody system, has been developed by Milne [122, 123] for the analysis of the equilibrium and stability of deformable aircraft. The resulting linearised EoM around a steady-state condition, however, were limited to small elastic perturbations and small rigid-body motion of the aircraft. The latter is a necessary assumption to ensure that the mean axes coincide with the principal axes, as clarified in Ref. [123].

Application of the mean axes approximation was then demonstrated by Dusto *et al.* [33, 54] leading to the computer programme FLEXSTAB which superimposes the vehicle flight-dynamics with the aeroelastic response. The resulting flexible aircraft dynamics formulation was used to analyse the dynamic stability characteristics following gust perturbations about a reference motion. Correct implementation of the mean axes constraint however is critical as demonstrated by Rodden and Love [154] (with the later corrections in Ref. [55]), who found numerically that the inertial decoupling of the EoM without enforcing the additional constraint condition of the floating reference frame is incorrect.

To overcome this problem Buttrill *et al.* [27] used the aircraft undamped free vibration modes that automatically satisfy the first-order mean axes constraints to derive the EoM of flexible aircraft in manoeuvring flight using Lagrangian mechanics. A lumped mass model is used and the resulting equations include inertial coupling terms due to elastic deformations and the resulting local momenta coupled with the angular rigid-body momenta. Using a modal parameter the authors were able to identify inertial coupling terms in the resulting modal formulation and found that elastic deformations that change the vehicle mass distribution have a significant effect on the modal mass and frequencies.

Waszak and Schmidt [199] also derived the EoM for flexible aircraft in terms of the mean axes system using Lagrange's equations and the principle of virtual work. They also used free-free modes to enforce the location of the mean axes system but neglected all remaining inertial coupling terms assuming small deformations. The generalised aerodynamic forces are obtained using quasi-steady strip theory leading to closed-form expressions of the aircraft flight-dynamics and aeroelastic response. Numerical studies illustrate the effect of flexibility on the dynamic response of a relatively-stiff generic aircraft and the importance of mode residualisation in the truncation of the generalised coordinates. Schmidt and Raney [163] later used the same approach to demonstrate the real-time capability of the aeroelastic model in a flight simulator for a large flexible aircraft. The experiments showed that the effect of flexibility can significantly harm the handling qualities with decreasing frequency of the structural modes due to the frequency overlap of the flight dynamic modes and the lower elastic modes.

The aeroelastic/flight-dynamics approaches by Buttrill, Waszak and Schmidt [27, 163, 199], as summarised in the reference book by Schmidt [162], naturally evolved from the expansion of existing flight dynamics codes using the mean axes approximation to include flexibility effects. Following the standard approach in flight dynamics, this was done using quasi-steady 2-D aerodynamics to demonstrate the approach and to obtain analytical expressions of the coupled framework. For cases where the elastic response becomes dominant or even unstable, such as flutter, the quasi-steady assumption reaches the limit of applicability and the computation of aerodynamic loads needs to account for the variation with the frequency of the structural excitation. The formulation of the strip theory can be extended to account for the effect of sudden changes in incidence angle and harmonic motion of lifting surfaces using Wagner's [194] or Theodorsen's [190] functions, respectively, as derived in most textbooks on aeroelasticity, e.g. Refs. [20, 65]. For more complex geometries 3-D unsteady panel methods, such as the doublet lattice method (DLM) [5, 153, 154], are more suitable to capture the unsteady aerodynamics of full aircraft configurations including the interaction of multiple lifting surface.

The unsteady aerodynamic loads can then be computed using the DLM for a range of vibration modes of the unconstrained vehicle including rigid-body modes to obtain aerodynamic influence coefficients. These can be used directly in the mean axes approximation to describe the generalised aerodynamic forces in frequency domain. Alternatively, the unsteady aerodynamic loads can be approximated in time domain through rational function approximations, as given by Roger's classical approach [58] or the minimum-state method by Karpel [97]. The resulting modelling approach to the dynamics of flexible aircraft based on 3-D panel methods has become the predominant tool in industry for aircraft design and certification, as presented in detail in the reference book by Wright and Cooper [201], and has been used in a number of studies mostly for control synthesis of flexible aircraft, e.g. Refs. [43, 149, 171, 173].

Reschke [151] revisits the mean axes description using Lagrange's equations in terms of quasi-coordinates and the DLM to arrive at a set of nonlinear EoM to model the dynamics of large flexible aircraft in time domain. Unlike the approach by Waszak and Schmidt [199], the resulting formulation includes all inertial coupling terms due to Coriolis forces and centrifugal loading which allowed them to investigate the effect of inertial decoupling [152]. Numerical studies on a large transport aircraft subject to roll manoeuvres showed the significant influence of inertial coupling on the vehicle loads especially for flight manoeuvres leading to high angular velocities or accelerations. The resulting EoM are therefore only valid for perturbations about steady flight of relatively stiff vehicles.

A more general solution has been proposed using Lagrange's equations in terms of quasi-coordinates [115] which directly solve the fully-coupled EoM of the flexible aircraft in a body-attached reference frame. Using strip theory to obtain the aerodynamic forces, Meirovitch and Tuzcu [116] have developed a unified framework for the dynamic analysis of manoeuvring flexible aircraft subject to small elastic deformations of the vehicle fuselage, wings and empennage components. The resulting EoM have been obtained using a perturbation approach which separates the problem into the nonlinear description of the aircraft flight dynamics and an *extended aeroelasticity* problem [116]. Hence, the structural deformations are treated as perturbations in the flight dynamics description. The resulting flexible aircraft dynamics model was demonstrated for control design and stability analysis of a generic transport aircraft. The problem size of the extended aeroelasticity problem has been reduced with the extension of the formulation in Ref. [117] using modal projection of the aircraft structural DoF on the free-free modes of the unconstrained aircraft at a linear equilibrium. This modal description also served Meirovitch and Tuzcu [118] to numerically illustrate flaws of the mean axes approximation.

Finally, Haghighat *et al.* [76] have also developed a unified dynamics framework based on quasi-coordinates with respect to a body-fixed frame for the synthesis of a gust load alleviation controller for mildly flexible aircraft using model-predictive control (MPC). In a second study [77] they also implemented a co-rotational beam formulation coupled with a 3-D panel code to model large trim deformations. They demonstrated for a flexible wing that trim deformations can have an adverse effect on the stability and performance of the closed-loop system.

Modelling of Very Flexible Aircraft

The NASA Helios experiment [132] and other efforts to achieve long endurance [38] or human-powered [164, 202] flight have demonstrated the significant effect of wing deformations on the flight dynamic response of these vehicle designs. Modelling of such highly optimised vehicles with possibly large wing deformations requires the incorporation of geometrically nonlinear structural and flight dynamic models. Another important aspect is the interaction between the aircraft structural and flight dynamics. As flexibility increases, the frequencies of the structural modes are bound to decrease, which reduces

the frequency separation between structural and flight dynamic modes and deems floating frame approaches insufficient. Hence, the recent research into the dynamics of very flexible aircraft has focused on body-fixed Lagrangian descriptions of the possibly large vehicle deformations.

The work by Drela [53] was one of the first contributions to develop an integrated simulation tool, called ASWING, for the preliminary design of highly flexible aircraft. The possibly large structural deformations of the aircraft were modelled as isotropic nonlinear joined bending/torsion beams coupled with a compressible lifting-line method with wind-aligned trailing vorticity to capture the unsteady aerodynamic loads. Linearisation of the integral system equations enabled very efficient time-domain or frequency-based calculations and stability analyses for preliminary design studies. The simulation toolbox ASWING was later used by Love *et al.* [108] to investigate the open-loop and closed-loop stability characteristics of a swept flying wing SensorCraft concept. The bending mode of the flexible high-aspect-ratio wing was found to couple with the flight-dynamic short-period mode leading to body freedom flutter which is typical for flying wing configurations with low pitch inertia. By varying the wing stiffness, flight altitude and location of the centre of mass (CM), they identified passive measures to increase flutter speed which highlights the importance of a coupled approach to aircraft design. This is especially important for novel vehicle configurations with possible dynamic interactions.

Patil *et al.* [141, 142] also developed a multidisciplinary formulation for the modelling of high-aspect-ratio vehicles. The intrinsic beam formulation by Hodges [86] was implemented to capture large wing deformations and also account for material anisotropy. The unsteady aerodynamics were modelled using the 2-D finite-state strip theory of Peters [145] with the ONERA stall model [146] to include stall effects at high angles of attack due to wing twisting. The resulting framework was exercised on flying wing [140] and HALE aircraft [142] configurations to investigate the effect of geometric nonlinearity on the dynamic vehicle behaviour through eigenvalue analysis of the linearised equations and nonlinear time simulations. Among others, the numerical results indicated a significant reduction in flutter speed due to an increased wing dihedral at steady state. The stability tool further highlighted the effect of geometric nonlinearity on the flight dynamic modes of a very flexible HALE configuration, specifically the short-period and phugoid modes, by linearising the EoM around different rigid, linear and nonlinear trim equilibria [141]. Further studies also demonstrated the effect of aerodynamic nonlinearities such as stall leading to limit cycle oscillations [143] or changes in the unsteady aerodynamic loading due to nonplanar effects of highly-curved lifting surfaces at steady state [139]. The latter was investigated using a 3-D fixed-wake nonplanar vortex method at steady state and the DLM to obtain the unsteady perturbations around the geometrically-nonlinear steady equilibrium [139]. The aeroelastic framework with 2-D finite-state aerodynamics was later used by Raghavan and Patil [148, 149] for trajectory tracking and gust load alleviation of a high-aspect-ratio flying wing. To facilitate the control synthesis, they de-

veloped a reduced-order flight dynamics model of the flexible aircraft using the mean axes approximation to minimise the coupling between the rigid-body and structural response of the vehicle. However, by identifying the strong effect of large trim deformations on the dynamic response of the flying wing [148], the original mean axes approach was extended to account for large static aeroelastic deformations of the flying in the control design [149].

Cesnik and Brown [23, 35] developed an integrated framework for the analysis of very flexible aircraft using a strain-based formulation. Coupled with a 2-D finite-state aerodynamics model [145], the formulation was applied to investigate the use of anisotropic piezoelectric materials for active manoeuvring of a joined-wing aircraft through warping of the flexible composite wings [36]. Su and Cesnik [187] extended the work by also considering the effect of flexibility of the fuselage and vertical tails on the aeroelastic performance of the SensorCraft. In a different study they also studied the effect of stall and skin wrinkling on the gust response of a highly-flexible flying wing configuration [188]. Shearer and Cesnik [168] reformulated the time-marching solution methodology to include the flight dynamics EoM and incorporated a modified implicit Newmark integration method in the aeroelastic framework developed in Ref. [23] which was originally based on an explicit scheme. The numerical studies also confirmed the significant effect of geometric nonlinearity on the flight dynamic response of a very flexible aircraft configuration [169] and methods for trajectory control were developed [170].

The resulting Nonlinear Aeroelastic Simulation Toolbox (UM/NAST) was recently used by Dillsaver *et al.* [48] for the design of a gust load alleviation system for very flexible aircraft using linear quadratic Gaussian (LQG) control techniques. The controller was obtained from a linear reduced-order model, using balancing model reduction techniques, and exercised on a very flexible HALE configuration subject to continuous turbulence. In a second study [49] they also explored LQG pitch control of a flexible flying wing subject to temporally and spatially distributed (DARPA) gusts. In a parallel work, Cook *et al.* [39] used UM/NAST to demonstrate the application of linear robust control synthesis for gust load alleviation in highly-flexible HALE UAVs with geometrically-nonlinear transient deformations.

The experimental validation of UM/NAST for free-flying configurations subject to large wing deformations remains an ongoing research effort at the University of Michigan. The development of a small-scale very flexible UAV, denoted X-HALE, is aimed at addressing this issue [38]. Other studies have extensively focused on the SensorCraft concept which is a joined wing configuration aimed to provide enhanced capabilities for the next generation of intelligence, surveillance and reconnaissance (ISR) operations [105, 109]. These complex geometries are susceptible to buckling of the composite joined-wing structure which requires a nonlinear modelling approach that accounts for the displacement constraints of the closed kinematic chains [21, 138]. To experimentally validate a full-scale finite-element model of a SensorCraft design, Bond *et al.* [22] tested a joined wing structure subject to

large deformations due to applied follower loads. Comparison also to linear results highlighted the importance of geometrically nonlinear methodologies to capture the follower force effect inherent to aerodynamic loading.

To identify suitable geometrically-nonlinear structural and aerodynamic models, Palacios *et al.* [137] firstly re-derived different composite beam formulations (displacement-based, strain-based and intrinsic) in a common framework. They found that strain-based and intrinsic formulations demonstrate a small computational advantage in the solution of the nonlinear EoM but require a post-processing step in the context of full aircraft applications to consider non-follower gravity loads. Displacement-based methods were also found to be more suitable for the modelling of joined wing configurations, since the displacement constraints due to closed kinematic chains can be directly incorporated in the finite element description. Comparison also of aerodynamic methods, namely 2-D unsteady thin-strip methods [104, 145] and the 3-D unsteady vortex-lattice method (UVLM) [98], found that the 2-D approximations, as used in the studies presented in Refs. [142, 169], sufficiently model the unsteady aerodynamic loads of high-aspect-ratio wings subject to low-frequency oscillations. Note that steady 3-D results are used to obtain the accurate coefficients in the 2-D approximations. In general, higher fidelity 3-D models are required to capture the unsteady effects due to large amplitude and high frequency wing oscillations.

Unlike the linear doublet-lattice method, the UVLM can predict the aerodynamics of complex kinematics and interference effects which are both relevant in advanced aircraft design. The latter was shown by Elzebda *et al.* [56] for an aircraft configuration representative of the X-29 to demonstrate the effect of wake inteference from the canard on the forward-swept main wing. They modelled the unsteady aerodynamics using the UVLM developed by Mook and Nayfeh [124] and Konstadinopoulos *et al.* [101] which can account for wake roll-up instead of assuming a flat wake. The effect of wake-tail interference was also shown by Murua *et al.* [127] for a representative HALE T-tailed configuration using the integrated framework for the Simulation of High-Aspect-Ratio Planes (SHARP), which couples a displacement-based geometrically-exact beam model with the 3-D UVLM. Linearisation of the flight-dynamic and aeroelastic EoM around a geometrically nonlinear trim equilibrium leads to a monolithic state-space formulation of the coupled model suitable for linear stability analysis and control synthesis. Numerical studies demonstrated the dramatic effect of large trim deformations on the vehicle dynamic stability characteristics [128] and the coupled nature of the linearised formulation was exploited for the synthesis of PID controllers for gust load alleviation and trajectory control of a very flexible aircraft configuration [129].

Wang *et al.* [196, 197] also coupled a UVLM with the geometrically-nonlinear intrinsic formulation by Hodges [86] leading to the framework for nonlinear-aerodynamics/nonlinear-structure interactions (NANSI) [196]. The tightly-coupled model has been extended in Ref. [197] to include stall effects and gust disturbances which were

exercised on a flexible flying wing configuration with prescribed motions at high angles of attack. The instability onset at high gust levels with excessive wing displacements was found to be delayed if stall was considered. The 3-D UVLM coupled with geometrically-nonlinear beam models, as demonstrated in Refs. [127, 197], provides a medium-fidelity tool that can capture important nonlinear aeroelastic phenomena that are relevant in the design of highly-efficient aircraft. The review by Murua *et al.* [128] provides a detailed overview of the development of the UVLM and its application in an aeroelasticity and flight dynamics context.

To address some limitations of the UVLM, which is restricted to low-speed small-incidence problems due to the inviscid and incompressible nature of potential flow methods, higher fidelity computational fluid dynamics (CFD) models have been applied to nonlinear aeroelastic problems, mostly for static cases [67, 136, 183], but dynamic problems have also been explored [45, 59, 79]. The major barriers that need to be addressed for these solution methods to be applicable in aircraft design is the computational cost involved in unsteady time simulations and the distortion of the mesh to adapt the fluid domain discretisation to possibly large wing deformations. Computational power alone is not enough to tackle these issues and a vast number of powerful model reduction techniques have been developed to enable the use of high fidelity methods for the cost-effective design of high efficiency devices (not necessarily aircraft). The next subsection will provide a brief overview of the application of reduced-order modelling techniques to aeroelasticity.

1.1.3 Reduced-Order Modelling in Aeroelasticity and Fluid-Structure Interaction

Even with the latest advances in computing power, state-of-the-art high-fidelity aeroelastic tools can require significant time to obtain the solution for a specific aircraft concept. The resulting solution may be optimal for one problem, however, it may not necessarily contribute to finding the optimal design for a given problem which requires a large number of simulations to broaden the design space or iterate within an optimisation framework. Instead of relying on lower-fidelity methods to explore the design space (and verify it with high-fidelity analyses), model reduction provides a low-order representation of the high-fidelity system but retains the relevant physics of the problem. The insightful discussion in the paper by Spieck [184] highlights the role of reduced-order modelling techniques in the multidisciplinary design of next-generation greener aircraft. Such a top-down methodology can also enhance the performance of robust control systems, e.g. for gust load alleviation or stability augmentation, where the use of high-fidelity low-order models helps to reduce the level of uncertainty in the control synthesis.

The computation of the unsteady aerodynamics in an integrated aeroelasticity/flight-dynamics formulation is generally the driving factor that dominates the overall model order of the system. However, due to the coupled nature of the problem, modal reduction

also of the structural subsystem improves numerical efficiency and can enhance the stability of the solution process as it enables the control of high-frequency dynamics. This is usually done by projecting the structural EoM on a few dominant vibration modes. This is very much the standard approach in linear aeroelasticity and structural dynamics to model transient deformations of relatively stiff structures. Model reduction of geometrically nonlinear structural systems has also been addressed by Wang *et al.* [195] using the intrinsic beam formulation projected on a few linear normal modes. The same could not be achieved using the nonlinear strain-based beam equations, as demonstrated by Su and Cesnik [189], who attempted a modal approach to solve the dynamics of flexible aircraft. The reduced system matrices were still dependent on the modal amplitudes and the computational advantage of the modal truncation was small. In a separate effort, Harmin and Cooper [81, 82] combined a modal/finite element analysis technique [114] with a doublet-lattice method to include the effect of geometric nonlinearities in the dynamic response of flexible wings. The nonlinear mapping between the static prescribed elastic forces and resulting displacements in modal space (based on the modal transformation of the underlying linear system) was curve-fitted through a regression analysis to obtain the nonlinear modal stiffness coefficients. They demonstrated the reduced-order modelling approach using commercial tools for static aeroelastic problems, gust responses and the prediction of limit cycle oscillations for a clamped high-aspect-ratio wing. Additional work is required to extend the methodology to free-free problems with nonlinear inertia behaviour.

Inspired by the effective modal projection of large structural dynamics problems, Hall [78] demonstrated that the governing equations of a time-domain UVLM can also be formulated as a generalised eigenvalue problem to produce a very compact, reduced-order aerodynamic model. As in structural problems, the resulting modal form of the unsteady aerodynamic system needs to be computed only once and can subsequently be used for a large number of time simulations. This modal reduction approach was demonstrated in Ref. [78] for a relatively small aerodynamic system (100×100), but the approach can be extended for larger systems as demonstrated in the paper by Romanowski and Dowell [156] for the Euler equations.

Computing eigenvalues for even larger systems, e.g. to resolve transient flow features around complex geometries using 3-D CFD, becomes impractical. This problem has been addressed in the fluid dynamics community using the proper orthogonal decomposition (POD) to produce basis functions of the system based on sample data of the flow [19, 155]. The POD modes are obtained directly from so-called snapshots of the flow through perturbations of the full-order system, where a smart choice of response functions is critical to reduce the computational cost of the decomposition. Dowell *et al.* [51] and Lucia *et al.* [110] both provide in-depth reviews of the application of POD to high-order linear and nonlinear computational fluid dynamic problems.

The resulting basis functions, obtained through either eigenanalysis or POD, accurately capture the internal dynamics of the system, but a large number of modes (not only lightly-damped ones) may be required to effectively represent the particular input/output mapping in a typical aeroelastic problem. This has been demonstrated by Rule *et al.* [158] for the UVLM. They also proposed an alternative model reduction method, adopted from the controls community, to obtain a reduced-order aerodynamic model that is optimal in terms of the particular transmission path between the system inputs and outputs. Following the balanced truncation method first introduced by Moore [125] and further developed by Glover [72], the states of the full-order system are internally balanced according to the system controllability and observability Gramians, i.e. the contribution of the states to the system input/output mapping. Balanced states that have little contribution to a particular system mapping can be efficiently discarded [51]. Such balancing methods are especially useful in unsteady aerodynamics, where a large number of states is used to transmit information from a comparably small number of inputs (geometry of the structure) to a small number of outputs (unsteady aerodynamic forces). This has been demonstrated for aeroelastic systems on a 2D pitch-plunge problem [158] and on a full linear aircraft model to obtain the flight loads following wake vortex encounters [113].

The computational effort required to find a balanced realisation of the linear system is similar to a direct eigensolution ($\mathcal{O}\left(N^3\right)$) and can become badly conditioned and impractical for large systems. Safonov and Chiang [160] addressed the numerical stability of balancing methods using the stabilising Schur decomposition to directly obtain similarity transformations. To address the computational effort of finding such balancing transformations, Baker *et al.* [10] proposed an iterative method which directly calculates an approximation to the reduced-order balanced system without prior transformation. Numerical studies on the UVLM demonstrated the potential of the proposed methodology which in principle can also be applied to large CFD models. Willcox and Peraire [200] proposed a balanced POD approach which uses the POD modes to directly obtain a balanced realisation of very large systems. They demonstrated the approach on a 2D high-order plunging aerofoil problem reducing the number of states substantially by four orders of magnitude compared to the full CFD model.

The model reduction techniques presented in this summary are restricted to linear and stable responses. Although the linearisation can be obtained around a nonlinear equilibrium, the resulting ROM are limited to a specific aeroelastic reference flight condition with the dynamic pressure as a parameter. Hence, the ROMs usually lack sufficient robustness to accurately predict the system dynamics at different flight conditions, which is relevant in the computation of the unsteady aerodynamic loads of manoeuvring aircraft. Ghoreyshi and Cummings [71] proposed the development of a time-dependent surrogate model to fit the unsteady aerodynamic loads from indicial step response sample simulations to the instantaneous flight condition of a manoeuvring aircraft. Finally, Amsallem and Farhat [6] developed a ROM adaptation method to interpolate reduced-order models

between different parameter values, such as flight speed or altitude, to enlarge the vehicle flight envelope. They illustrated the adaptation method for CFD-based aeroelastic ROMs of complete aircraft configurations at different free-stream Mach numbers. However, application of these interpolation methods to very flexible manoeuvring HALE UAVs is still an open question in the literature.

1.2 Research Questions of the Thesis

The main shortcomings in the literature on the modelling of flexible aircraft can be best summarised by returning to the NASA *Helios* mishap and the following recommendation from the investigation into the accident [132]:

> [A need to] *develop more advanced,* ***multidisciplinary*** *(structures, aeroelastic, aerodynamics, atmospheric, materials, propulsion, controls, etc.)* ***time-domain*** *analysis methods appropriate to highly flexible, morphing vehicles.*

As evident from the literature review, substantial progress has been made to enable the development of next-generation aircraft with very high-aspect-ratio wings and this work will further contribute to the effort by seeking answers to the following research questions:

1. When do we need to consider the effects of geometrically-nonlinear wing deformations on the flight dynamics response of very flexible aircraft? What is the effect of nonplanar (deformed) lifting surfaces on the 3-D aerodynamic loads at trim and during transient manoeuvres? What is the effect of steady wing deformations and complex geometries on the stability characteristics of novel aircraft configurations?
2. What are the dominant coupling effects between the vehicle structural, rigid-body and aerodynamics? In particular, what is the effect of inertial decoupling, using the mean axes approximation, on the prediction of the vehicle flight-dynamics response and the calculation of dynamic loads?
3. In the context of robust control synthesis and real-time simulations, can we devise a numerical solution which has a similar cost to the mean axes approximation but provides a higher fidelity for flexible vehicles with large trim deformations?

1.3 Present Approach

This work aims to address these research questions with the development of an aeroelastic/flight-dynamics framework that can account for possibly large deformations of the aircraft structural subcomponents (lifting surfaces and fuselage). The starting point for this formulation will be the geometrically-exact composite beam formulation by Palacios *et al.* [137]. This displacement-based beam model will be extended in this work to also account for arbitrary rigid-body motions of very flexible vehicles modelled as

multi-beam configurations. An implicit Newmark time integration scheme, as proposed by Shearer and Cesnik [168], will be used to directly solve the second-order, numerically-stiff differential equations of the coupled dynamic system.

The unsteady aerodynamic loads in this formulation will be obtained directly in time domain from the implementation of the 3-D unsteady vortex-lattice method by Murua *et al.* [127], which is also geometrically nonlinear in its original form [98]. Coupled with the geometrically-exact flexible-body dynamics equations, this completes the unified aeroelastic/flight-dynamics approach to model the dynamics of manoeuvring very flexible aircraft with large wing deformations due to vehicle instabilities, atmospheric disturbances and/or pilot inputs. Unlike previous work based on 2-D aerodynamics [36, 142], the resulting formulation can capture the 3-D effects of the low-speed unsteady flow including wake interference. This provides the necessary tools to investigate the effect of large wing deformations on the dynamic response of flexible aircraft, as formulated in the first research question. To also identify the effect of geometric nonlinearity, however, a consistent linearisation of the EoM is required.

Under the assumption that the vehicle subcomponents exhibit only small transient deformations, the structural DoF will be first linearised using perturbation methods. Next, linearisation also in the aerodynamic states [128], tightly coupled with the perturbed form of the flexible-body dynamics equations, will complete the consistent aeroelastic linearisation in the dynamics of manoeuvring flexible aircraft subject to small transient wing deformations and large rigid-body motions. Comparison with the geometrically nonlinear solution allows to determine the effect of geometric nonlinearity in the aeroelastic DoF. As the linearisation is done around a geometrically-nonlinear static equilibrium condition, it also captures the impact of geometry changes due to large wing deformations on the vehicle stability characteristics. This will also be explored in this work using the monolithic state-space formulation of the aeroelastic/flight-dynamics system by Murua *et al.* [128].

Since the linearisation is consistent in this work, it preserves all couplings between the nonlinear rigid-body dynamics and the linearised structural dynamics. These coupling terms are neglected in the mean axes approximation typically used in flexible aircraft flight dynamics [162]. To address the second research question posed in this thesis, the proposed formulations will be used to study the effect of neglecting the inertial couplings. This is not only relevant in the flight-dynamic analysis of flexible aircraft but also crucial for the structural optimisation of highly-efficient manoeuvring vehicles. The linearised EoM will then be projected onto a small number of vibration modes of the unconstrained vehicle to obtain a compact description of the vehicle flexible-body dynamics. Although of similar size to the mean axes approximation, this modal approach provides a higher-fidelity description of the coupled flexible-aircraft dynamics.

The third research question is motivated by the relatively large system size due to the increased model fidelity of the 3-D unsteady aerodynamics which may hinder the

efficient application of the framework in the design of very flexible aircraft concepts (when compared to the performance of DLM-based aerodynamics). Hence, taking advantage of the time-domain description of the flexible-aircraft dynamics, this work will seek efficient model reduction techniques to tackle the system size of the aeroelastic/flight-dynamics formulation to enable robust control synthesis and real-time simulations. In particular, balancing methods will be demonstrated on the linearised aeroelastic subsystem in the transient analysis of manoeuvring flexible aircraft. The standard balanced truncation has been shown to provide optimal model reduction [158] which will be leveraged in this work with potential reductions of the aeroelastic system comparable in size to (rigid) flight dynamics models.

In summary, this work will introduce a low-order, medium-fidelity aeroelastic/flight-dynamics framework for the complete analysis of very flexible aircraft which accounts for the 3-D effects of the unsteady flow over the instantaneous geometry of highly flexible configurations. This higher fidelity, compared to current methods in literature, provides the numerical tools to investigate the physics of the interaction between vehicle structural and flight dynamics. The proposed model reduction approach preserves the fidelity of the solution methodology and further enables the incorporation of flexibility effects in real-time simulations, dynamic load calculations, multidisciplinary design optimisation, gust load alleviation, trajectory control and stability augmentation of highly-efficient configurations. All these applications should be very relevant in the design of advanced aircraft concepts tailored to the challenges of the 21st century.

1.3.1 Original Contributions of this Work

It is clear that the current work is the result of a collaborative effort and the extension of previous work to arrive at the multidisciplinary framework for the complete analysis of very flexible aircraft. The following overview therefore aims to isolate the original contributions of this thesis:

1. extension of the geometrically-nonlinear, displacement-based composite beam formulation by Palacios *et al.* [137] to account for the rigid-body motions of flexible aircraft,

2. consistent structural linearisation around the nonlinear static trim equilibrium of very flexible aircraft using a perturbation approach and subsequent modal projection of the unconstrained nonlinear vehicle dynamics subject to large rigid-body motions,

3. analytical and numerical evaluation of neglecting some gyroscopic coupling terms in the mean axes approximation for vehicles subject to lateral manoeuvres,

4. model reduction of the linearised unsteady aerodynamics by Murua *et al.* [128] using balancing methods for the efficient prediction of manoeuvre loads of flexible aircraft,

5. robust $\mathcal{H}_\infty$ control synthesis of unstable aeroelastic systems.

1.4 Dissertation Outline

The development and integration of the different building blocks leading to the aeroelastic/flight-dynamics framework is presented in the first three chapters of this dissertation. The theoretical development is followed by two chapters demonstrating the application of the framework on flexible multi-beam configurations with and without unsteady aerodynamics.

Chapter 2 introduces the geometrically-exact, displacement-based composite beam formulation and presents the extension of the differential beam equations to account for the rigid-body dynamics of the vehicle. This geometrically-nonlinear flexible-body dynamics formulation then provides the starting point for the consistent linearisation of the structural DoF only, which is derived in the second part of Chapter 2 using perturbation methods. At last, the Newmark integration scheme is presented.

Chapter 3 presents the integration of the aeroelastic/flight-dynamics framework for the Simulation of High-Aspect-Ratio Planes (SHARP). The chapter first introduces the geometrically-nonlinear and linearised implementations of the 3-D unsteady vortex-lattice methods which is used in this work to obtain the unsteady aerodynamic loads. Beginning with the mapping between the aerodynamic loads and the elastic deformations, Chapter 3 then presents the integration of the different aerodynamic and flexible-body dynamic modules which produces a variety of simulation capabilities in SHARP:

1. geometrically-nonlinear trim equilibrium and time-marching simulations of very flexible aircraft,
2. linearised approach for manoeuvring flexible aircraft with small transient wing deformations and
3. fully-linear monolithic state-space formulation for the coupled stability analysis of free-flying very flexible aircraft with large wing deformations at trim.

Chapter 4 presents the model reduction of the linearised aeroelastic/flight-dynamics modules in SHARP using balancing methods. The chapter first outlines the numerical aspects that need to be considered for the robust reduction of numerically-stiff, discrete-time systems. An efficient model reduction approach – a combination of the standard balanced truncation method and the coprime factorisation approach – is subsequently developed to cater for possibly unstable and/or ill-conditioned systems.

Chapter 5 presents numerical studies of unconstrained flexible multi-beam configurations without aerodynamics to first verify the flexible-body dynamics module and to contribute further results for benchmarking of geometrically-nonlinear solution methods. The results are also used to verify the consistent linearisation of the structural DoF

and to evaluate the effect of inertial decoupling due to the mean axes approximations on the flexible body structural and rigid-body dynamics response.

Chapter 6 presents numerical studies that demonstrate the different simulation capabilities of SHARP on a representative HALE configuration to identify the effect of flexibility on the aircraft trim solutions, stability characteristics and open-loop time-marching response due to commanded control surface inputs. The latter also serves to investigate the effect of geometric nonlinearity on the vehicle response and to demonstrate the model reduction approach. Further numerical studies on a simplified clamped problem also demonstrate the application of balancing methods for the efficient synthesis of a robust flutter suppression system using $\mathcal{H}_\infty$ control.

Chapter 7 finally summarises the theoretical development and numerical applications in this work and highlights the key contributions. The chapter concludes with recommendations for future work to improve the numerical efficiency of the developed approach and to suggest further application of the aeroelastic framework for the design of advanced high-aspect-ratio aircraft.

1.5 Publications Based on this Work

The work presented in this dissertation has resulted in the following conference and journal publications.

Journal Publications

1. B. F. Ng, H. Hesse, R. Palacios, J. M. R. Graham and E. C. Kerrigan. Aeroservoelastic Modelling and Robust Load Alleviation of Very Large Flexible Wind Turbine Blades. *Wind Energy*. [under review at the time of writing].
2. H. Hesse and R. Palacios. Model Reduction in Flexible-Aircraft Dynamics with Large Rigid-Body Motion. *AIAA Journal*. [under review at the time of writing].
3. H. Hesse, R. Palacios, and J. Murua. Consistent Structural Linearisation in Flexible Aircraft Dynamics with Large Rigid-Body Motion. *AIAA Journal*. [accepted for publication at the time of writing].
4. H. Hesse and R. Palacios. Consistent Structural Linearisation in Flexible-Body Dynamics with Large Rigid-Body Motion, *Computers & Structures*, 110-111:1–14, 2012.

Conference Papers

1. H. Hesse and R. Palacios. Reduced-Order Aeroelastic Models for the Dynamics of Manoeuvring Flexible Aircraft. *16th International Forum of Aeroelasticity and Structural Dynamics*, Bristol, UK, June 2013.

2. B. F. Ng, H. Hesse, R. Palacios, J. M. R. Graham and E. C. Kerrigan. Aeroservoelastic Modelling and Robust Load Alleviation of Very Large Flexible Wind Turbine Blades. *American Wind Energy Conference WINDPOWER*, Chicago, USA, May 2013.

3. H. Hesse and R. Palacios. Model Reduction in Flexible-Aircraft Dynamics with Large Rigid-Body Motion. *54^{th} AIAA Structures, Structural Dynamics, and Materials Conference*, AIAA 2013-1895, Boston, USA, April 2013.

4. H. Hesse, R. Palacios, and J. Murua. Consistent Structural Linearisation in Flexible Aircraft Dynamics with Large Rigid-Body Motion. *53^{rd} AIAA Structures, Structural Dynamics, and Materials Conference*, AIAA 2012-1402, Honolulu, USA, April 2012.

5. H. Hesse and R. Palacios. Consistent structural linearisation in flexible-body dynamics with large rigid-body motion. *15^{th} International Forum of Aeroelasticity and Structural Dynamics*, Paris, France, June 2011.

6. J. Murua, H. Hesse, R. Palacios, and J. M. R. Graham. Stability and Open-Loop Dynamics of Very Flexible Aircraft Including Free-Wake Effects. *52^{nd} AIAA Structures, Structural Dynamics, and Materials Conference*, AIAA 2011-1915, Denver, CO, USA, April 2011.

Chapter 2

Flexible-Body Dynamics Formulation

The starting point for this work will be a *geometrically-exact* beam formulation to model the deformations of aircraft subcomponents using a displacement-based approach [69, 176], where the finite rotations of the beam cross-sections are parameterised with respect to a body-attached reference frame. The kinematic description is finalised with the rigid-body EoM of the body-attached frame to capture the large motions of the flexible body. Under the assumption that such large manoeuvres result in small elastic deformations, the elastic DoF of the resulting set of nonlinear EoM are linearised using a perturbation approach. This allows the modal projection of the nonlinear perturbation equations on the vibration modes of the unconstrained structure to reduce the problem size while keeping the nonlinearity in the rigid-body dynamics equations. This consistent linearisation of the structural DoF presented in this chapter also preserves all coupling between the rigid-body and structural dynamics of the moving body. The significant effect of these coupling effects will be established in this work by comparison to the mean axes approximation.

The derivation of the nonlinear EoM of the flexible unconstrained structure results in second-order differential equations which are time-marched using an unconditionally-stable, implicit integration scheme, as presented in Section 2.4.

2.1 Geometrically-Nonlinear Flexible-Body Dynamics Equations

A geometrically-exact composite beam model [69, 86] is used to represent the dynamics of very flexible structures subject to large manoeuvres. To facilitate the subsequent linearisation of the structural DoF, a description based on displacements and rotations was implemented. Finite rotations due to large deformations are parameterised in this work using the Cartesian rotation vector (CRV), which can be easily linearised around

an initially-curved beam geometry. A detailed description of the solution approach for isotropic materials can be found in Ref. [69] and the derivation presented here expands the formulation to anisotropic composite beams which can be initially curved and twisted.

This section presents the kinematic assumptions, which are derived in a Lagrangian approach with respect to a body-fixed reference frame attached to a material point on the moving body. The parametrisation of finite rotation is crucial for the derivation of the beam equations and will also be reviewed in this section before presenting the local velocity and finite strain measures in variational form. Hamilton's principle finally leads to the dynamic equations of the unconstrained vehicle which are discretised using a finite element implementation with displacements and rotations as the primary DoF.

2.1.1 Kinematics of Finite Rotations

As shown in Figure 2.1, the deformation of the structure is described in terms of a moving, body-fixed reference coordinate system, A, which moves with respect to an inertial (ground) frame, G, by the inertial translational and angular velocities, $v_A(t)$ and $\omega_A(t)$, of its origin. Subscripts are used to indicate the coordinate system in which each vector magnitude is projected. The orientation of the global frame, A, with respect to the inertial frame, G, is given by the coordinate transformation matrix $C^{GA}(\zeta)$ which is parameterised using quaternions, $\zeta(t) = \left[\zeta_0^\top \;\; \zeta_v^\top\right]^\top$, where ζ_0 is the scalar and ζ_v the vector part, respectively [69]. The resulting 4-dimensional column matrix has purely algebraic quantities and will be used in this work for the efficient description of the large rigid-body motion of the flexible body.

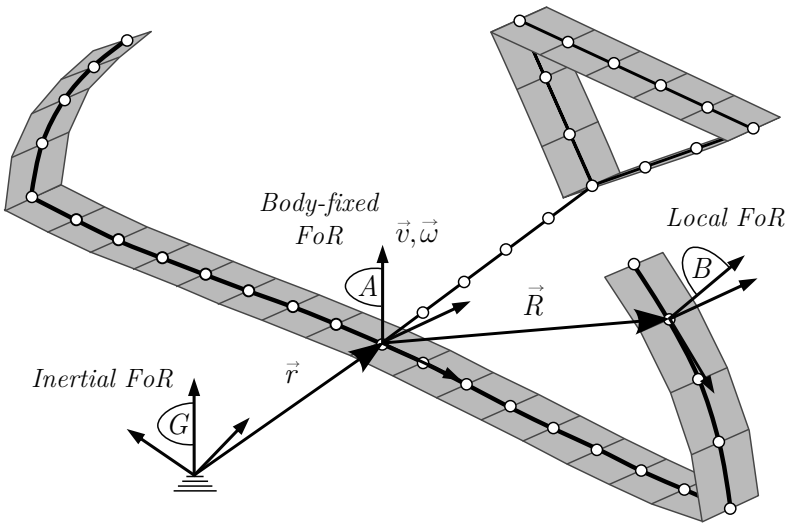


Figure 2.1: Multi-beam configuration with the definition of reference frames.

Assuming a flat Earth, the attitude propagation equations of the flexible vehicle are then given as [186]

$$\begin{Bmatrix} \dot{\zeta}_0 \\ \dot{\zeta}_v \end{Bmatrix} = -\frac{1}{2} \begin{bmatrix} 0 & \omega_A^\top \\ \omega_A & \widetilde{\omega}_A \end{bmatrix} \begin{Bmatrix} \zeta_0 \\ \zeta_v \end{Bmatrix}, \tag{2.1}$$

where $\widetilde{\omega}_A = C^{AG}\dot{C}^{GA}$ is the skew-symmetric matrix of ω_A at time t and corresponds to the matrix of angular velocities expressed in the body-fixed reference frame, A. Compared to other representation methods of finite rotations such as Euler angles, quaternions produce no singularities in the inversion procedure to obtain the transformation matrix, C^{GA}, which makes them ideal for tracking the orientation of the flexible structure given at time t as

$$C^{GA} = \left(2\zeta_0^2 - 1\right) I + 2\left(\zeta_v \zeta_v^\top + \zeta_0 \widetilde{\zeta}_v\right). \tag{2.2}$$

The above expression demonstrates the algebraic nature of the quaternion parametrisation, which is summarised in-depth in the work by Géradin and Cardona [69]. Finally, the position of the body-fixed reference frame, A, is defined in the inertial frame as $\dot{r}_G = C^{GA} v_A$.

The local rotation of each beam cross-section is defined by the local coordinate system, B, in the current configuration, as shown in Figure 2.1. The relative orientation between the global body-fixed reference frame, A, and the local deformed frame, B, is parameterised by the Cartesian rotation vector, $\Psi(s,t)$, where s is the arc length along the beam reference line. Note that the beam is continuous for the description of the geometrically-exact kinematics and that the finite element discretisation of the beam, as depicted in Figure 2.1, will only be applied at the end of this section to solve the set of partial differential equations.

Using the CRV to parameterise the finite rotations of the beam cross-sections caters for a Lagrangian formulation of the beam kinematics which allows for arbitrary curvatures of the reference line at the initial reference configuration. The definition of the rotation vector, Ψ, is based on Euler's rotation theorem, which implies that every sequence of rotations around a point on a rigid body can be compacted to a single rotation ϕ about a fixed axis around the unit vector n through that point. From this geometric interpretation, the CRV is defined as $\Psi = \phi n$ and the corresponding coordinate transformation matrix, $C^{BA}(s,t) = C(\Psi)$, from the global body-fixed frame, A, to the local frame, B, at each position along the reference beam reference line is given as [69]

$$C(\Psi) = I + \frac{\sin\phi}{\phi}\widetilde{\Psi} + \frac{1-\cos\phi}{\phi^2}\widetilde{\Psi}^2 = \sum_{k=0}^{\infty} \frac{1}{k!}\widetilde{\Psi}^k, \tag{2.3}$$

where I is the unit matrix. The latter series expansion of the exponential map representation of $\widetilde{\Psi}$ with $C(\Psi) = \exp(\widetilde{\Psi})$ allows the elimination of the singularity for $\phi = 0$. Note that, despite its name, the CRV is non-additive and hence does not form a vector

space. This has implications on the interpolation of rotational DoF, which is relevant in the discretisation of the EoM as discussed in Subsection 2.1.4.

The variational description of the rotation, $C(\Psi)$, is necessary in this work to obtain expressions for the local strain and velocity measures in terms of spatial and temporal derivatives of the rotation vector, Ψ. Similar to the matrix of angular velocities of the body-fixed frame, $\widetilde{\omega}_A$, the matrix of infinitesimal rotation of the local material frame, B, is obtained as

$$\delta\widetilde{\Phi}_B = C\delta C^\top = \widetilde{T\delta\Psi}, \tag{2.4}$$

with the definition of the *tangential rotation operator* $T(\Psi)$ as [179]

$$T(\Psi) = I + \frac{\cos\phi - 1}{\phi^2}\widetilde{\Psi} + \left(1 - \frac{\sin\phi}{\phi}\right)\frac{\widetilde{\Psi}^2}{\phi^2} = \sum_{k=0}^{\infty}\frac{(-1)^k}{(k+1)!}\widetilde{\Psi}^k. \tag{2.5}$$

The singularity for $\phi = 0$ is again removed using the series expansion of the tangent operator, which can also be truncated significantly for small values of Ψ. This description will form the backbone for the following geometrically-exact kinematic and dynamic formulation.

2.1.2 Geometrically-Exact Beam Kinematics

The following formulation of the beam kinematics is based on the geometrically-exact description of the deformed reference line by Hodges [86], but with the nodal positions, $R_A(s,t)$, expressed in the body-fixed frame, A, and the cross-sectional orientations, $\Psi(s,t)$, as the independent set of variables. Following the definitions given in Figure 2.1, the position vector of an arbitrary point on the local cross section can be expressed in the inertial frame as

$$X_G = r_G + C^{GA}R_A + C^{GA}C^\top\xi_B, \tag{2.6}$$

where ξ_B are the local cross-sectional coordinates in the local material frame B. The focus in this work is on flexible bodies with slender substructures and the small-scale motions of the cross sections will be ignored leading to constant ξ_B. Note however that the present formulation accounts for shear strain and can easily be extended to account for the warping of the cross sections through appropriate cross-sectional reduction methods [50, 135].

The deformation of the reference line going from the undeformed state at $t = 0$ to the current state at time t is given by the force and moment strains, which are written in terms of the CRV as [86]

$$\begin{aligned}\gamma(s,t) &= C\left(\Psi(s,t)\right)R'_A(s,t) - C\left(\Psi(s,0)\right)R'_A(s,0),\\ \kappa(s,t) &= T\left(\Psi(s,t)\right)\Psi'(s,t) - T\left(\Psi(s,0)\right)\Psi'(s,0).\end{aligned} \tag{2.7}$$

where $(\bullet)'$ is the derivative with respect to the arc-length s, and $T(\Psi)$ is the tangential operator defined in Eq. (2.5). The three components of the force strains are obtained from the spatial variation of the position vector in the local reference and current configurations, respectively, and account for the extensional and shear strains. Likewise, the three components of the moment strains, κ, describe the torsional and bending strains which are obtained from the difference of the local curvature K_B at each point along the reference line. Following Eq. (2.4), K_B is defined in terms of the spatial variation of the transformation matrix C as [69]

$$\widetilde{K}_B = C\left(C^\top\right)' = \widetilde{T(\Psi)\Psi'}. \tag{2.8}$$

Similarly, the temporal variation of the position and orientation of each point along the reference line leads to the description of the beam inertial properties and are given in terms of the translational and angular inertial velocities expressed in each local material frame at the arc-length s as

$$\begin{aligned} V_B(s,t) &= C(\Psi(s,t))\,\dot{R}_A(s,t) + C(\Psi(s,t))\left[v_A(t) + \widetilde{\omega}_A(t)R_A(s,t)\right], \\ \Omega_B(s,t) &= T(\Psi(s,t))\,\dot{\Psi}(s,t) + C(\Psi(s,t))\,\omega_A(t), \end{aligned} \tag{2.9}$$

where $(\dot{\bullet})$ is the derivative with respect to time t. The above expression can also be expressed in compact matrix form as

$$\begin{Bmatrix} V_B \\ \Omega_B \end{Bmatrix} = \Lambda \begin{Bmatrix} \dot{R}_A \\ \dot{\Psi} \end{Bmatrix} + A_{RC} \begin{Bmatrix} v_A \\ \omega_A \end{Bmatrix}. \tag{2.10}$$

Infinitesimal Beam Kinematics

At last, expressions for the infinitesimal changes on the beam force and moment strains are obtained by taking variations on the beam strains and curvatures given in Eq. (2.7). This results in the virtual strain-displacement relations, which are written as

$$\begin{aligned} \delta\gamma &= C\delta R'_A(s,t) + \widetilde{R}'_A\delta\Phi_B, \\ \delta\kappa &= \delta\Phi'_B + \widetilde{K}_B\delta\Phi_B, \end{aligned} \tag{2.11}$$

where the local virtual rotation vector, $\delta\Phi_B$, and the local curvature, K_B, are parameterised using the relations in Eqs. (2.4) and (2.8), respectively. In a similar fashion, variation of the inertial velocities leads to the expressions of infinitesimal beam velocities as

$$\begin{aligned} \delta V_B &= C\left(\delta\dot{R}_A + \widetilde{\omega}_A\delta R_A - \widetilde{R}_A\delta\omega_A + \delta v_A\right) + \widetilde{V}_B\delta\Phi_B, \\ \delta\Omega_B &= \delta\dot{\Phi}_B + \widetilde{\Omega}_B\delta\Phi_B + C\delta\omega_A. \end{aligned} \tag{2.12}$$

The above variation of the inertial rigid-body velocities, δv_A and $\delta\omega_A$, respectively, can be derived as

$$\begin{aligned}\delta v_A &= \delta\dot{r}_A + \widetilde{\omega}_A \delta r_A,\\ \delta\omega_A &= \delta\dot{\varphi}_A + \widetilde{\omega}_A \delta\varphi_A,\end{aligned} \tag{2.13}$$

with the virtual position vector δr_A of the body-fixed frame, A, and the global virtual rotation vector φ_A defined in a similar fashion to the local counterpart $\delta\Phi_B$ as $\delta\widetilde{\varphi}_A = C^{AG}\delta C^{GA}$.

This derivation of the beam kinematics highlights the benefits of using the CRV for the parametrisation of the cross-sectional orientations leading to compact definitions of the local strain and velocity measures, which will be applied next to develop expressions for the virtual work and energy densities of the flexible structure. The solution process of the resulting transient equations requires linearisation of the beam equations, which will repeatedly involve variations of the rotation operator, $C(\Psi)$, which has been defined already in Eq. (2.4), and the tangential rotation operator, $T(\Psi)$. The latter is given for an arbitrary 3×1 column matrix, h, as [69]

$$\begin{aligned}\delta T(\Psi)\,h = A_1(\Psi,h) =& \phi^{-2}(1-\cos\phi)\,\widetilde{h} + \phi^{-1}\left[\sin\phi - 2\phi^{-1}(1-\cos\phi)\right]\widetilde{h}nn^{\top} +\\ & \phi^{-1}\left(2+\cos\phi-3\phi^{-1}\sin\phi\right)\widetilde{n}\widetilde{h}nn^{\top} +\\ & \phi^{-1}\left(1-\phi^{-1}\sin\phi\right)\left(\widetilde{h}\widetilde{n}-2\widetilde{n}\widetilde{h}\right),\end{aligned} \tag{2.14}$$

with the Cartesian rotation vector written as before with $\Psi = \phi n$.

2.1.3 Dynamic Equations of Motion of Unconstrained Structures

With the established geometrically-exact description of the beam kinematics, it is now possible to analyse the dynamics of the beam in the (moving) body-attached reference frame A over a given time interval $[t_1, t_2]$. From Hamilton's principle, it is

$$\int_{t_1}^{t_2}\int_L \left[\delta\mathcal{T} - \delta\mathcal{U} + \delta\mathcal{W}\right] ds dt = 0, \tag{2.15}$$

where L refers to the total length of all reference lines of a possible multi-beam configuration. In this expression, $\mathcal{T}$ and $\mathcal{U}$ are the kinetic and internal energy densities per unit length, respectively, and $\delta\mathcal{W}$ is the virtual work per unit length of the applied loads.

Internal and Kinetic Energy Densities

The virtual strain and kinetic energies are written as [86]

$$\begin{aligned}\delta\mathcal{U} &= \begin{bmatrix}\delta\gamma^\top & \delta\kappa^\top\end{bmatrix}\mathcal{S}_{cs}\begin{bmatrix}\gamma^\top & \kappa^\top\end{bmatrix}^\top = \begin{bmatrix}\delta\gamma^\top & \delta\kappa^\top\end{bmatrix}\begin{bmatrix}\mathbb{F}_B^\top & \mathbb{M}_B^\top\end{bmatrix}^\top,\\ \delta\mathcal{T} &= \begin{bmatrix}\delta V_B^\top & \delta\Omega_B^\top\end{bmatrix}\mathcal{M}_{cs}\begin{bmatrix}V_B^\top & \Omega_B^\top\end{bmatrix}^\top = \begin{bmatrix}\delta V_B^\top & \delta\Omega_B^\top\end{bmatrix}\begin{bmatrix}P_B^\top & H_B^\top\end{bmatrix}^\top,\end{aligned} \tag{2.16}$$

where we have introduced the internal forces and moments, $\mathbb{F}_B$ and $\mathbb{M}_B$, and the local translational and angular momenta, P_B and H_B, respectively. In the above expression the internal energy in the deformation of the flexible vehicle was defined by the linearised strain energy, which is valid if the deformations of the flexible body remain in the linear elastic regime of the material properties. Note however that this does not prevent displacements and rotations from being large.

The 6×6 cross-sectional mass and stiffness matrices, $\mathcal{M}_{cs}$ and $\mathcal{S}_{cs}$, in Eq. (2.16) can be obtained through an appropriate cross-sectional analysis methodology [50, 135]. Both matrices can be fully populated to account for lightweight designs made of composite materials and an offset of the beam cross-sectional centroid. Note that the expressions of the kinetic energy density in Eq. (2.16) includes the rotational inertia of the beam cross-sections with the cross-sectional mass matrix, $\mathcal{M}_{cs}$, given as

$$\mathcal{M}_{cs} = \begin{bmatrix} mI & -m\widetilde{\xi}_B^{cg} \\ m\widetilde{\xi}_B^{cg} & J \end{bmatrix}, \tag{2.17}$$

with the mass per unit length, m, the cross-sectional inertia, J, and the distance between the beam reference line and its cross-sectional centroid, ξ_B^{cg}, expressed in the local material frame, B.

Virtual Work of External Forces

Consider next the applied volume (or surface) forces μ_G acting on the beam sections. The corresponding virtual work per unit length is $\delta\mathcal{W} = \langle \delta X_G^\top \mu_G \rangle$, where δX_G is the virtual position vector in the current configuration at the material points where forces μ_G are applied, and $\langle \bullet \rangle$ is the integral over the area (or area contour) of the local cross section. From the definition of the position vector X_G in Eq. (2.6), the virtual work per unit length is

$$\delta\mathcal{W} = \left[\delta r_G^\top C^{GA} + \delta R_A^\top + \delta\varphi_A^\top\left(\widetilde{R}_A + C^\top\widetilde{\xi}_B C\right)\right] C^\top F_B + \delta\Phi_B^\top M_B, \tag{2.18}$$

where the local virtual rotation $\delta\widetilde{\Phi}_B = C\delta C^\top$ was defined in Eq. (2.4) and $\delta\widetilde{\varphi}_A = C^{AG}\delta C^{GA}$ is the equivalent global virtual rotation of the body-fixed frame, A. The set of

resultant forces and moments per unit beam length has been defined as

$$\begin{aligned} F_B &= \langle \mu_B \rangle, \\ M_B &= \langle \widetilde{\xi}_B \mu_B \rangle. \end{aligned} \tag{2.19}$$

The distributed forces μ_B have been projected in the local material frame, B, which corresponds to follower loads such as the aerodynamic forces and thrust, but gravity forces can also be expressed using the rotations matrices C^{GA} and $C\left(\Psi(s,t)\right)$.

Equations of Motion at an Arbitrary Reference Line

Finally, all virtual magnitudes are expressed in terms of the independent set of variables, through the kinematic relations introduced in Eqs. (2.11) and (2.12). Substitution of the contributions of the virtual work and the energy densities in Eqs. (2.18) and (2.16), respectively, into the expressions of Hamilton's principle, Eq. (2.15), and integration by parts in time leads to the weak form of the beam EoM as [137]

$$\begin{aligned} &\int_{t_1}^{t_2} \Bigg\{ \int_L \Big\{ \delta R_A^\top C^\top \left(\dot{P}_B + \widetilde{\Omega}_B P_B - F_B \right) + \delta R'^\top_A C^\top \mathbb{F}_B \\ &\qquad + \delta \Phi_B^\top \left[\dot{H}_B + \widetilde{\Omega}_B H_B + \widetilde{V}_B P_B - \widetilde{K}_B \mathbb{M}_B - \widetilde{R'}_A F_B - M_B \right] + \delta \Phi'^\top_B \mathbb{M}_B \Big\} \, ds \\ &\quad + \delta r_G^\top C^{GA} \left[\dot{P}_A^R + \widetilde{\omega}_A P_A^R - F_A^R \right] + \delta \varphi_A^\top \left[\dot{H}_A^R + \widetilde{\omega}_A H_A^R - M_A^R \right] \Bigg\} \, dt = \\ &= \int_L \left[\delta R_A^\top C^\top P_B + \delta \Phi_B^\top H_B \right]_{t_1}^{t_2} ds + \left[\delta r_G^\top C^{GA} P_A^R + \delta \varphi_A^\top H_A^R \right]_{t_1}^{t_2} \end{aligned} \tag{2.20}$$

The local momenta, P_B and H_B, and the internal forces, $\mathbb{F}_B$ and $\mathbb{M}_B$, respectively, are expressed in the local material frame B and have been defined in Eq. (2.16). The total momenta and external forces can be obtained in the global body-fixed reference frame A through integration over all reference lines of the multi-beam configuration as

$$\begin{aligned} P_A^R &= \int_L C^\top P_B ds, \quad H_A^R = \int_L \left(\widetilde{R}_A C^\top P_B + C^\top H_B \right) ds, \\ F_A^R &= \int_L C^\top F_B ds, \quad M_A^R = \int_L \left(\widetilde{R}_A C^\top F_B + C^\top M_B \right) ds. \end{aligned} \tag{2.21}$$

2.1.4 Discrete Form of the Equations of Motions

To solve the governing beam EoM, Eq. (2.20), the position vector, R_A, and the Cartesian rotation vector, Ψ, are approximated using a finite-element discretisation in terms of the

shape functions $N_i(s)$ as [69]

$$\begin{aligned} R_A(s) &\cong \sum_{i=1}^{3} N_i(s) R_{Ai}, \\ \Psi(s) &\cong \sum_{i=1}^{3} N_i(s) \Psi_i, \end{aligned} \tag{2.22}$$

where R_{Ai} and Ψ_i are the nodal values of the position and rotation parameters. In this work, 2- and 3-noded elements, corresponding to linear and quadratic interpolation, have been implemented, but the coupled aeroelastic framework in Chapter 3 is implemented for linear elements only. There are known issues with *objectivity* of the interpolation operation of finite rotations [17, 44], however, good performance of the implementation is observed for quadratic elements or fine enough discretisation with linear elements [181].

If η is the column vector with all the nodal displacements and rotations and $\beta^\top = \{v_A^\top \;\; \omega_A^\top\}$, the discrete form of the dynamic equation, Eq. (2.20), is written in compact form as

$$\mathcal{M}(\eta) \begin{Bmatrix} \ddot{\eta} \\ \dot{\beta} \end{Bmatrix} + \begin{Bmatrix} Q^S_{gyr} \\ Q^R_{gyr} \end{Bmatrix} + \begin{Bmatrix} Q^S_{stif} \\ 0 \end{Bmatrix} = \begin{Bmatrix} Q^S_{ext} \\ Q^R_{ext} \end{Bmatrix}, \tag{2.23}$$

where structural and rigid-body components (denoted by superscripts S and R) have been identified in the gyroscopic, stiffness and external forces. The discrete generalised forces in the above equation are written as

$$\begin{aligned} Q^S_{stif}(\eta) &= \int_\Gamma \left(N^\top \Upsilon^\top A_K + N^\top \Upsilon'^\top + N'^\top \Lambda^\top \right) \hat{\mathbb{F}} ds, \\ Q_{gyr}(\eta, \dot{\eta}, \beta) &= \int_\Gamma \begin{bmatrix} \Lambda N & A_{RC} \end{bmatrix}^\top \left(\mathcal{M}_{cs} \hat{V}_{gyr} + A_{V\Omega} \mathcal{M}_{cs} \hat{V} \right) ds, \\ Q_{ext}(\eta, \dot{\eta}, \beta, \zeta) &= \int_\Gamma \begin{bmatrix} \Lambda N & A_{RC} \end{bmatrix}^\top \hat{F} ds, \end{aligned} \tag{2.24}$$

where ζ is the orientation of the body-fixed reference system, as defined in Eq. (2.1). Also, the following variables for resultant loads, local inertial velocities, and internal forces have been defined to simplify notation,

$$\hat{F} = \begin{Bmatrix} F_B \\ M_B \end{Bmatrix}, \;\; \hat{V} = \begin{Bmatrix} V_B \\ \Omega_B \end{Bmatrix}, \;\; \hat{\mathbb{F}} = \begin{Bmatrix} \mathbb{F}_B \\ \mathbb{M}_B \end{Bmatrix}. \tag{2.25}$$

The gyroscopic velocities $\hat{V}_{gyr}$ in the definition of the gyroscopic forces, Q_{gyr} in Eq. (2.24), are given as

$$\hat{V}_{gyr}(\eta, \dot{\eta}, \beta) = \begin{Bmatrix} V_{gyr} \\ \Omega_{gyr} \end{Bmatrix} = \begin{Bmatrix} C \widetilde{\omega}_A \dot{R}_A + \widetilde{V}_B T \dot{\Psi} \\ \dot{T} \dot{\Psi} + \widetilde{\Omega}_B T \dot{\Psi} \end{Bmatrix}, \tag{2.26}$$

and the following 6×6 matrix operators were used in the definition of the discrete generalised forces,

$$\Upsilon = \begin{bmatrix} I & 0 \\ 0 & T \end{bmatrix}, \quad A_K = \begin{bmatrix} 0 & 0 \\ -\widetilde{R}'_A & -\widetilde{K}_B \end{bmatrix}, \quad A_{V\Omega} = \begin{bmatrix} \widetilde{\Omega}_B & 0 \\ \widetilde{V}_B & \widetilde{\Omega}_B \end{bmatrix}. \tag{2.27}$$

The tangent mass matrices have been defined as a function of the deformed state, η, as

$$\mathcal{M}(\eta) = \begin{bmatrix} \mathcal{M}^{SS} & \mathcal{M}^{SR} \\ \mathcal{M}^{RS} & \mathcal{M}^{RR} \end{bmatrix} = \int_\Gamma \begin{bmatrix} \Lambda N & A_{RC} \end{bmatrix}^\top \mathcal{M}_{cs} \begin{bmatrix} \Lambda N & A_{RC} \end{bmatrix}, \tag{2.28}$$

where the operators Λ and A_{RC} have been defined in Eq. (2.10) to obtain the compact form of the inertial velocities. The resulting set of nonlinear second-order differential EoM, Eq. (2.23), couples the geometrically-nonlinear beam dynamics with the nonlinear rigid-body motion of the flexible body through the inertial and gyroscopic forcing terms. For aeroelastic problems, further coupling is introduced through the aerodynamic forces, which appear in the discrete external forces, Q_{ext}, and will be discussed in Chapter 3.

2.2 Consistent Structural Linearisation in Nonlinear Flexible-Body Dynamics

Under the assumption that the structural DoF remain small, while the rigid-body DoF are arbitrarily large, the discrete EoM of the unconstrained flexible body will be linearised in this section using perturbation methods. This linearised structural formulation coupled with the nonlinear rigid-body dynamics equations will form the basis for the subsequent modal projection of the flexible-body dynamics EoM in Section 2.3. The second part of this section will also present the full linearisation of the flexible-body dynamic equations, which is required to obtain the vibration modes for the modal projection. Linearisation also provides the incremental form of the EoM which is used for the implicit time integration method presented in Section 2.4.

2.2.1 Perturbation of Structural Dynamic Equations

Equation (2.23) can be linearised only in the elastic DoF by means of a perturbation approach. The (large) elastic deformations at the static equilibrium condition will be given by η, while $\bar{\eta}$ will be the small elastic deformations that occur together with the (not-necessarily small) rigid-body velocities β. Perturbation of the elastic DoF on the nonlinear EoM, Eq. (2.23), leads to linear inertial and elastic terms, which depend only on the static equilibrium geometry, η. Hence, the tangent mass matrix $\mathcal{M}(\eta)$, as defined in Eq. (2.28), is assumed to remain constant for small elastic deformations and the contribution of the elastic forces to the tangent stiffness matrix is obtained through direct linearisation as $\mathcal{K}^S_{stif} = \partial Q^S_{stif}/\partial\eta$.

However, perturbation of the gyroscopic forces, Q_{gyr}, will require particular attention because of the coupling between rigid-body and elastic states. The gyroscopic damping and stiffness matrices, due to the partial linearisation of Q_{gyr}, will be derived next starting from the definition of the structural and rigid-body components of the gyroscopic forces. However, it is convenient to firstly define the perturbed beam-kinematics which can be substituted into Eq. (2.24) to obtain an expression for the perturbed gyroscopic forces.

Elastic Perturbations of Beam Kinematics

Perturbations of the elastic DoF partially linearise the local translational and angular inertial velocities, introduced in Eq. (2.9), which can be expressed as

$$\hat{V}\left(\eta,\bar{\eta},\dot{\bar{\eta}},\beta\right)=\begin{Bmatrix}V_B^R\\ \Omega_B^R\end{Bmatrix}+\begin{Bmatrix}\bar{V}_B\\ \bar{\Omega}_B\end{Bmatrix}+H.O.T., \tag{2.29}$$

where the rigid-body and elastic contributions to the local velocities are, respectively,

$$\begin{Bmatrix}V_B^R\\ \Omega_B^R\end{Bmatrix}=A_{RC}\beta,\quad \begin{Bmatrix}\bar{V}_B\\ \bar{\Omega}_B\end{Bmatrix}=\Lambda\dot{\bar{\eta}}-\left(A_{V\Omega}^R\right)^\top\Lambda\bar{\eta}. \tag{2.30}$$

Additionally, the gyroscopic velocities defined in Eq. (2.26) are approximated as

$$\hat{V}_{gyr}\left(\eta,\bar{\eta},\beta\right)=\begin{Bmatrix}\bar{V}_{gyr}\\ \bar{\Omega}_{gyr}\end{Bmatrix}=-\left(A_{V\Omega}^R\right)^\top\Lambda\bar{\eta}+H.O.T., \tag{2.31}$$

with

$$A_{V\Omega}^R=\begin{bmatrix}\widetilde{\Omega}_B^R & 0\\ \widetilde{V}_B^R & \widetilde{\Omega}_B^R\end{bmatrix}. \tag{2.32}$$

Elastic Perturbations of Gyroscopic Forces

It is now possible to derive expressions for the contribution of the gyroscopic forces to damping and stiffness matrices, such that the perturbed gyroscopic forces can be expressed in the form of

$$Q_{gyr}(\eta,\bar{\eta},\dot{\bar{\eta}},\beta)=\begin{bmatrix}\bar{\mathcal{C}}^{SS} & \bar{\mathcal{C}}^{SR}\\ \bar{\mathcal{C}}^{RS} & \bar{\mathcal{C}}^{RR}\end{bmatrix}\begin{Bmatrix}\dot{\bar{\eta}}\\ \beta\end{Bmatrix}+\begin{bmatrix}\bar{\mathcal{K}}_{gyr}^S & 0\\ \bar{\mathcal{K}}_{gyr}^R & 0\end{bmatrix}\begin{Bmatrix}\bar{\eta}\\ 0\end{Bmatrix}+H.O.T., \tag{2.33}$$

with the components of the gyroscopic damping matrix given as

$$\begin{aligned}
\bar{\mathcal{C}}^{SS}(\eta,\beta) &= \int_\Gamma N^\top \Lambda^\top \left[A^R_{\partial\Omega}\mathcal{M}_{cs} - \mathcal{M}_{cs}\left(A^R_{V\Omega}\right)^\top\right]\Lambda N ds,\\
\bar{\mathcal{C}}^{SR}(\eta,\beta) &= \int_\Gamma A^\top_{RC}\left[A^R_{\partial\Omega}\mathcal{M}_{cs} - \mathcal{M}_{cs}\left(A^R_{V\Omega}\right)^\top\right]\Lambda N ds,\\
\bar{\mathcal{C}}^{RS}(\eta,\beta) &= \int_\Gamma N^\top \Lambda^\top A^R_{V\Omega}\mathcal{M}_{cs}A_{RC} ds,\\
\bar{\mathcal{C}}^{RR}(\eta,\beta) &= \int_\Gamma A^\top_{RC}A^R_{V\Omega}\mathcal{M}_{cs}A_{RC} ds,
\end{aligned} \tag{2.34}$$

and the gyroscopic contribution to the stiffness matrix as

$$\begin{aligned}
\bar{\mathcal{K}}^S_{gyr}(\eta,\beta) &= \int_\Gamma N^\top\left[\bar{\Lambda}\left(A^R_{V\Omega}\hat{P^R}\right) - \Lambda^\top A^R_{\partial\Omega}\mathcal{M}_{cs}\left(A^R_{V\Omega}\right)^\top\Lambda\right]N ds,\\
\bar{\mathcal{K}}^R_{gyr}(\eta,\beta) &= \int_\Gamma A^\top_{RC}A^R_{V\Omega}\mathcal{M}_{cs}B^R_{\partial\Omega}\Lambda N ds.
\end{aligned} \tag{2.35}$$

Writing the gyroscopic forces in this matrix form illustrates the coupling between the small elastic deformations and the arbitrarily-large rigid-body motions.

The following 6×6 matrix operators were used in the above expressions to obtain the compact form of the perturbed gyroscopic forces

$$\begin{aligned}
\bar{\Lambda}(\eta,\dot{\eta},\beta,\hat{p}) &= \begin{bmatrix} 0 & -C^\top\widetilde{p}T \\ 0 & -A_1(-\Psi,h)\end{bmatrix},\quad A^R_{PH}(\eta,\beta) = \begin{bmatrix} 0 & \widetilde{P}^R_B \\ \widetilde{P}^R_B & \widetilde{H}^R_B\end{bmatrix},\\
A^R_{\partial\Omega}(\eta,\beta) &= A^R_{V\Omega} - A^R_{PH}\mathcal{M}^{-1}_{cs},\\
B^R_{\partial\Omega}(\eta,\beta) &= -\left(\left(A^R_{V\Omega}\right)^\top + \mathcal{M}^{-1}_{cs}A^R_{PH}\right),
\end{aligned} \tag{2.36}$$

where the total translational and rotational momenta, P^R_B and H^R_B, respectively, have been defined in Eq. (2.21) and $\hat{p} = \left[p^\top\ h^\top\right]^\top$, with p and h being arbitrary 3×1 column matrices. The matrix operator $A_1(\Psi,h)$ is derived from linearisation of the tangential operator, $T(\Psi)$, and has been defined in Eq. (2.14). From Eq. (2.34), it is clear that the perturbed gyroscopic damping and stiffness matrices are functions of the initial deformation, η, but also of the instantaneous rigid-body velocity, β, with linear and quadratic dependencies in the rigid-body DoF.

Perturbation Equations of Motion

Finally, perturbation of the elastic DoF in Eq. (2.23) around the nonlinear static equilibrium, η, leads to an expression of the form

$$\mathcal{M}(\eta)\begin{Bmatrix}\ddot{\bar{\eta}}\\ \dot{\beta}\end{Bmatrix} + \bar{\mathcal{C}}(\eta,\beta)\begin{Bmatrix}\dot{\bar{\eta}}\\ \beta\end{Bmatrix} + \bar{\mathcal{K}}(\eta,\beta)\begin{Bmatrix}\bar{\eta}\\ 0\end{Bmatrix} = Q_{ext}(\bar{\eta},\dot{\bar{\eta}},\beta,\zeta) + H.O.T., \tag{2.37}$$

where the expressions of the gyroscopic damping and stiffness matrices in Eqs. (2.34)-(2.35) are substituted in the definition of the perturbed gyroscopic forces, Eq. (2.33), to obtain the gyroscopic contribution to $\bar{\mathcal{C}}$ and $\bar{\mathcal{K}}$, respectively. Note that the perturbed stiffness matrix, $\bar{\mathcal{K}}$, also includes $\mathcal{K}^S_{stif}$ due to the linearisation of the discrete elastic forces, Q^S_{stif}. As discussed above, matrices $\bar{\mathcal{C}}$ and $\bar{\mathcal{K}}$ are functions of the rigid-body velocities with linear and quadratic dependencies of β, respectively.

It is clear from this formulation that, even for small elastic deformations, the rigid-body and structural dynamics of free-flying flexible bodies are coupled through the gyroscopic terms. The six rigid-body EoM, which describe the translational and rotational dynamics of the structure, will still depend on the large number of elastic DoF. Hence, in Section 2.3, a reduction of the system size will be achieved by projecting the structural variables onto a few dominant vibration modes, which are obtained from the fully-linearised form of the flexible-body dynamic equations presented next.

2.2.2 Fully-Linearised Flexible-Body Dynamics

Linearisation of the dynamic equilibrium equation is necessary for the temporal discretisation of all nonlinear flexible-body systems presented in this work. To obtain the Jacobian of the system equations, linearisation of the full dynamic system will be done around an equilibrium condition, which in general is obtained by cancelling accelerations in Eq. (2.23) [69], that is,

$$Q_{gyr}(\eta, \dot{\eta}, \beta) + Q_{stif}(\eta) = Q_{ext}(\eta, \dot{\eta}, \beta, \zeta). \tag{2.38}$$

This arbitrary point with possibly large elastic deformations and rigid-body motions will be referred to as $(\eta, \dot{\eta}, \beta, \zeta)$, and small changes from this state will again be represented with over-bars, that is, $(\bar{\eta}, \dot{\bar{\eta}}, \ddot{\bar{\eta}}, \bar{\beta}, \dot{\bar{\beta}}, \bar{\zeta})$. For the general case, the linearised (incremental) form of Eq. (2.23) around a given point is

$$\mathcal{M}(\eta) \begin{Bmatrix} \ddot{\bar{\eta}} \\ \dot{\bar{\beta}} \end{Bmatrix} + \mathcal{C}(\eta, \dot{\eta}, \beta) \begin{Bmatrix} \dot{\bar{\eta}} \\ \bar{\beta} \end{Bmatrix} + \mathcal{K}(\eta, \dot{\eta}, \beta) \begin{Bmatrix} \bar{\eta} \\ 0 \end{Bmatrix} = \bar{Q}_{ext}\left(\bar{\eta}, \dot{\bar{\eta}}, \bar{\beta}, \bar{\zeta}\right), \tag{2.39}$$

where the tangent mass matrix, $\mathcal{M}$, was defined in Eq. (2.28). The constant tangent damping and stiffness matrices, $\mathcal{C}$ and $\mathcal{K}$, respectively, are obtained through direct linearisation of the discrete elastic and gyroscopic forces in Eq. (2.24), as

$$\begin{aligned} \mathcal{C}(\eta, \dot{\eta}, \beta) &= \begin{bmatrix} \mathcal{C}^{SS} & \mathcal{C}^{SR} \\ \mathcal{C}^{RS} & \mathcal{C}^{RR} \end{bmatrix} = \begin{bmatrix} (\partial Q^S_{gyr}/\partial \dot{\eta}) & (\partial Q^S_{gyr}/\partial \beta) \\ (\partial Q^R_{gyr}/\partial \dot{\eta}) & (\partial Q^R_{gyr}/\partial \beta) \end{bmatrix}, \\ \mathcal{K}(\eta, \dot{\eta}) &= \begin{bmatrix} \mathcal{K}^S_{gyr} + \mathcal{K}^S_{stif} & 0 \\ \mathcal{K}^R_{gyr} & 0 \end{bmatrix} = \begin{bmatrix} (\partial Q^S_{gyr}/\partial \eta) + \left(\partial Q^S_{stif}/\partial \eta\right) & 0 \\ (\partial Q^S_{gyr}/\partial \eta) & 0 \end{bmatrix} \end{aligned} \tag{2.40}$$

The resulting incremental form of the EoM now forms the basis for the numerical solution of the nonlinear Eq. (2.23), where the contribution of the derivative with the acceleration to the tangent stiffness matrix has been neglected to improve numerical efficiency of the iterative solution processes [69]. The coupled linearised equations, however, are less suited to compute the dynamic response of manoeuvring flexible aircraft which need to include the nonlinear effects of the vehicle flight dynamics, as presented in the previous sections.

To obtain the incremental form of the equations for stability analysis and to extract the vibration modes of the trimmed aircraft configuration, one can also linearise the full dynamic system around the static equilibrium condition, $Q_{stif}(\eta) = Q_{ext}(\eta, \zeta)$, with possibly large elastic trim deformations, η, at the reference condition. The unforced form of Eq. (2.39) around a given point can then be obtained as

$$\mathcal{M}(\eta) \begin{Bmatrix} \ddot{\bar{\eta}} \\ \dot{\bar{\beta}} \end{Bmatrix} + \mathcal{K}(\eta, \beta) \begin{Bmatrix} \bar{\eta} \\ 0 \end{Bmatrix} = 0, \tag{2.41}$$

which provides the elastic inputs to the aeroelastic stability analysis presented in Section 3.2.4 and will be used in the next section to obtain the vibration modes of the unconstrained vehicle.

2.3 Modal Projection of the System Equations

To reduce the size of the system, it is now possible to write the system of perturbation equations, Eq. (2.37), in terms of global shape functions by projecting the dynamics equations on the natural modes of the unconstrained structure at a reference condition. These vibration modes are obtained in the body-fixed frame A from the unforced linearised equation, Eq. (2.41), as

$$\begin{Bmatrix} \bar{\eta} \\ \bar{\nu} \end{Bmatrix} = \Phi^o \begin{Bmatrix} q \\ \bar{\nu}^o \end{Bmatrix} = \begin{bmatrix} \Phi^o_{SS} & \Phi^o_{SR} \\ \Phi^o_{RS} & \Phi^o_{RR} \end{bmatrix} \begin{Bmatrix} q \\ \bar{\nu}^o \end{Bmatrix}, \tag{2.42}$$

where we have introduced the new variable $\bar{\nu}$ with $\dot{\bar{\nu}} = \bar{\beta}$, such that the vector of modal rigid-body displacements and rotations, $\bar{\nu}^o$, describes the motion of the body-fixed frame, A, and the displacements of this frame due to the elastic mode shapes ($\Phi^o_{RS} \neq 0$). The vector of the projected modal coordinates is q and Φ^o is the matrix of the corresponding mode shapes, which include the six zero-frequency rigid-body modes $[{\Phi^o_{SR}}^\top \quad {\Phi^o_{RR}}^\top]^\top$.

Without loss of generality, the origin of the body frame A can be defined to initially coincide with the CM and its axes to be aligned to the principal axes of the structure. This simplifies the rigid-body modes, since Φ^o_{SR} and Φ^o_{RR} are then a null and a unit matrix, respectively. Note that this is the same initial condition as for a mean-axes description, but A is still a body-fixed frame. The remaining elastic mode shapes, $[{\Phi^o_{SS}}^\top \quad {\Phi^o_{RS}}^\top]^\top$, characterise the vibration modes of the unconstrained structure such that Φ^o_{SS} are the

deformations with respect to frame A and $\Phi^o_{RS} \neq 0$ accounts for the corresponding rigid-body motion of the body-fixed frame A.

However, using this modal basis for the projection of the perturbation EoM, Eq. (2.37), requires a linear transformation at each sub-iteration to obtain the instantaneous rigid-body velocities needed in the perturbation damping and stiffness matrices. A more convenient basis for projection is

$$\Phi = \begin{bmatrix} \Phi^o_{SS} & \Phi^o_{SR} \\ \Phi^o_{RS} & \Phi^o_{RR} \end{bmatrix} \begin{bmatrix} I_m & 0 \\ -\Phi^o_{RS} & I_6 \end{bmatrix}, \tag{2.43}$$

where m is the number of elastic modes used for the projection, which relieves the inertial coupling between the rigid-body motion of the vehicle and the elastic deformations. This approach is very similar to that followed by Rodden and Love [154] to obtain the rigid-body accelerations on the structure in a mean axes framework and it enables the separation of elastic from rigid-body modes in the following projection of the perturbation flexible-body EoM. Note however that in the present approach the modal basis is computed for the deformed configuration at trimmed flight, which is the same reference condition used for linearisation of the elastic DoF.

The structural and rigid-body velocities/accelerations are now expressed in terms of the modal basis, Φ, such that

$$\begin{Bmatrix} \dot{\bar{\eta}} \\ \beta \end{Bmatrix} = \Phi \begin{Bmatrix} \dot{q} \\ \beta \end{Bmatrix} \quad \text{and} \quad \begin{Bmatrix} \ddot{\bar{\eta}} \\ \dot{\beta} \end{Bmatrix} = \Phi \begin{Bmatrix} \ddot{q} \\ \dot{\beta} \end{Bmatrix}, \tag{2.44}$$

which is substituted in Eq. (2.37) to obtain the modal form of the coupled EoM for this system, as

$$\Phi^\top \mathcal{M}(\eta)\Phi \begin{Bmatrix} \ddot{q} \\ \dot{\beta} \end{Bmatrix} + \Phi^\top \bar{\mathcal{C}}(\eta,\beta)\Phi \begin{Bmatrix} \dot{q} \\ \beta \end{Bmatrix} + \Phi^\top \bar{\mathcal{K}}(\eta,\beta)\Phi \begin{Bmatrix} q \\ 0 \end{Bmatrix} = \Phi^\top \bar{Q}_{ext}(\bar{\eta}, \dot{\bar{\eta}}, \beta, \zeta). \tag{2.45}$$

The resulting modal EoM describes the arbitrarily-large rigid-body motion of the flexible body subject to small elastic deformations which are captured using the modified vibration modes of the unconstrained structure. Because of the linear mapping of the rigid-body velocities, Eq. (2.43), the orthogonality property of the resulting vibration modes with respect to the system mass and stiffness matrices is lost. However, the system is already coupled due to the contribution of the gyroscopic forces to the modal damping and stiffness matrices.

The modal damping and stiffness matrices remain functions of the rigid-body DoF, β. However, it is easy to see that they have, respectively, linear and quadratic dependencies

with β, and that it is possible to write them in terms of third- and fourth-order tensors,

$$\begin{aligned} \Phi_{ij}\bar{\mathcal{C}}_{jk}\Phi_{kl} &= c_{ilr}\beta_r\left(t\right), \\ \Phi_{ij}\bar{\mathcal{K}}_{jk}\Phi_{kl} &= k_{il}^{stif} + k_{ilrs}^{gyr}\beta_r\left(t\right)\beta_s\left(t\right), \end{aligned} \tag{2.46}$$

where we sum over repeated indices and have identified the contributions to the modal stiffness matrix from elastic and gyroscopic forces. The tensors c and k are constant in time and their dimensions are $i,l = \{1,...,m\}$ and $r,s = \{1,...,6\}$ for m number of modes used in the expansion. These tensors are typically very sparse, and this approach generates efficient numerical solutions that keep the nonlinearities in the rigid-body DoF and all couplings with the linear structure at a low computational cost.

2.4 Time integration of the System Equations

The spatial discretisation of the system EoM leads to nonlinear second-order ordinary differential equations, which are given in Eq. (2.23) for the geometrically-nonlinear problem and in Eq. (2.45) for linearised modal form of the perturbation equations. The resulting coupled EoM are generally numerically stiff which is characterised by a large condition number of the system due to the large spread between the singular values of the high-frequency structural modes and the comparatively small singular values of the zero-frequency rigid-body modes [31, 168]. The time integration of such stiff systems can lead to high-frequency errors which makes the application of explicit time marching methods less suitable, as they require an unnecessarily small time step to achieve numerical stability [14]. Instead, the implicit Newmark integration scheme, modified as proposed by Géradin and Rixen [70] to include controlled positive algorithmic damping for increased numerical stability independent of the time step, will be used in this work to integrate the coupled EoM of the flexible-body dynamics problem.

The following description provides an overview of the algorithm as derived in Ref. [70]. Without loss of generality, the approach is demonstrated next for the geometrically-nonlinear EoM, Eq. (2.23), which can be recast into the residual form

$$R\left(x,\dot{x},\ddot{x}\right) = \mathcal{M}\left(x\right)\ddot{x} + Q_{gyr}\left(x,\dot{x}\right) + Q_{stif}^{S}\left(x\right) - Q_{ext}\left(x,\dot{x}\right) = 0, \tag{2.47}$$

where the new states, x, have been defined such that $\dot{x} = \left[\dot{\eta}^\top\ \beta^\top\ \zeta^\top\right]^\top$ with the initial conditions $x(t=0)$ and $\dot{x}(t=0)$. Note that the time integration algorithm simultaneously solves the second-order structural and first-order rigid-body propagation equations and provides integral values of β and ζ as part of solution process, but these carry no relevant physical meaning and are discarded.

The solution to Eq. (2.47) is predicted at the next time step $n+1$ based on the information at the current time step n as

$$\begin{aligned} x_{n+1} &= x_n + \Delta t\, \dot{x}_n + \left(\frac{1}{2} - \vartheta_2\right) \Delta t^2\, \ddot{x}_n + \vartheta_2 \Delta t^2\, \ddot{x}_{n+1}, \\ \dot{x}_{n+1} &= \dot{x}_n + (1 - \vartheta_1)\, \Delta t\, \ddot{x}_n + \vartheta_1 \Delta t\, \ddot{x}_{n+1}, \end{aligned} \tag{2.48}$$

where Δt is the constant time step size while ϑ_1 and ϑ_2 are the constant Newmark parameters which define the accuracy and stability properties of the integration scheme. Following Géradin and Rixen [70], the scheme is unconditionally stable if the parameters are chosen as

$$\vartheta_1 = \frac{1}{2} + \alpha \quad \text{and} \quad \vartheta_2 = \frac{1}{4}\left(\vartheta_1 + \frac{1}{2}\right)^2, \tag{2.49}$$

where $\alpha > 0$ modifies the average constant-acceleration scheme to introduce small positive algorithmic damping.

The predictions for the displacements and velocities, x_{n+1} and $\dot{x}_{n+1}$, respectively, can be substituted into Eq. (2.47) to obtain the residual equation in terms of the future accelerations only, such that $R\left(\ddot{x}_{n+1}\right) = 0$. If the displacements are small enough, the (linear) state predictions in Eq. (2.48) may provide a reasonable solution to the dynamic equations, but for the general nonlinear case the predictions will be corrected using a sub-iteration Newton-Raphson method. For a small correction, $\Delta\ddot{x}_{n+1}^{k+1} = \ddot{x}_{n+1}^{k+1} - \ddot{x}_{n+1}^{k}$, the residual equation can be updated through a Taylor expansion at sub-iteration $k+1$, such that

$$R\left(\ddot{x}_{n+1}^{k+1}\right) = R\left(\ddot{x}_{n+1}^{k}\right) + S\left(\ddot{x}_{n+1}^{k}\right) \Delta\ddot{x}_{n+1}^{k+1} + H.O.T. \stackrel{!}{=} 0, \tag{2.50}$$

where $S\left(\ddot{x}_{n+1}^{k}\right)$ is the *Jacobian matrix* computed at the previous sub-iteration k. If the higher-order terms in Eq. (2.50) are neglected, the updated states are finally obtained based on the linearisation of the EoM in Eq. (2.39), as

$$\Delta\ddot{x}_{n+1}^{k+1} = -\left[S\left(\ddot{x}_{n+1}^{k}\right)\right]^{-1} R\left(\ddot{x}_{n+1}^{k}\right) = -\left[\mathcal{M} + \vartheta_1 \Delta t\, \mathcal{C} + \vartheta_2 \Delta t^2\, \mathcal{K}\right]^{-1} R\left(\ddot{x}_{n+1}^{k}\right) \tag{2.51}$$

where the tangent mass, damping and stiffness matrices, $\mathcal{M}$, $\mathcal{C}$ and $\mathcal{K}$, respectively, are evaluated at the current sub-iteration k and the updated displacements and velocities have been defined as [168]

$$\begin{aligned} x_{n+1}^{k+1} &= x_{n+1}^{k} + \vartheta_2 \Delta t^2\, \Delta\ddot{x}_{n+1}^{k+1}, \\ \dot{x}_{n+1}^{k+1} &= \dot{x}_{n+1}^{k} + \vartheta_1 \Delta t\, \Delta\ddot{x}_{n+1}^{k+1}. \end{aligned} \tag{2.52}$$

The Newton-Raphson sub-iteration is repeated until the residual of the equilibrium equation, Eq. (2.47), converges below a defined threshold relative to the discretised forces within the system [70].

Chapter 3

Integrated Aeroelastic and Flight Dynamics Framework

The modelling of flexible aircraft with significant wing excursions requires incorporation of the vehicle flexible-body dynamics and aerodynamics in a unified framework. The unsteady aerodynamic loads of the manoeuvring aircraft are given in this work by the unsteady vortex lattice method (UVLM) in time domain, which accounts for wing surfaces subject to large deformations and is introduced in Section 3.1. Unlike quasi-steady approximations to the unsteady flow, which are often used in aircraft flight dynamics [162], the UVLM models the wake as part of the solution process and hence accurately captures the aerodynamic lags over a large range of reduced frequencies at low flight velocities.

The flexible-body and aerodynamic formulations have been implemented independently, as presented in Chapter 2 and Section 3.1, respectively. Subsequent integration of the modules in the framework for Simulation of High-Aspect-Ratio Planes (SHARP) enables the complete study of very flexible aircraft with composite wings, including geometrically nonlinear static aeroelastic analyses, trim, open-/closed-loop time-marching simulations and linear stability analyses. Section 3.2 finally presents the different capabilities of the simulation framework.

3.1 Unsteady Vortex Lattice Method

This section summarises the main characteristics of the unsteady vortex lattice method, as implemented by Murua [126], to obtain the unsteady aerodynamic loads of the manoeuvring flexible aircraft. The formulation is based on potential flow theory, as outlined in Section 3.1.1, and can accurately resolve the unsteadiness effects of the 3-D low-speed flow around flexible lifting surfaces. For the purpose of completeness, this section will provide a brief overview of the UVLM following the description by Murua [126] and the reference book by Katz and Plotkin [98].

The solution of the potential flow problem is based on a vortex ring discretisation of the boundaries of the aerodynamic domain, presented in Section 3.1.2, and is discretised in time following a time-stepping procedure, summarised in Section 3.1.3. The wake of the aircraft is also obtained as part of the solution procedure, given in Section 3.1.4, which finally completes the discretisation of the flow field leading to the computation of the aerodynamic loads in Section 3.1.5. This solution procedure is repeated for every time step resulting in the discrete-time formulation of the UVLM, as illustrated in Figure 3.1.

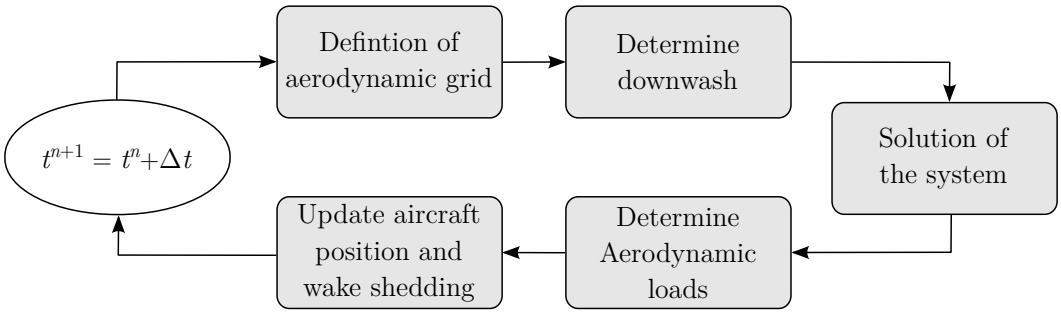


Figure 3.1: Flow chart of the unsteady vortex lattice method solution procedure.

The formulation of the UVLM is also geometrically nonlinear, as the boundary conditions are enforced on the deformed aerodynamic lattice which can capture the large deformations of very flexible aircraft configurations in a time-marching solution. The size of the resulting aerodynamic system however can become too large for the practical application of the UVLM in aircraft design, including control synthesis, optimisation and dynamic load calculations. Hence, the linearised version of the UVLM, as derived in Murua *et al.* [128], is also introduced in Section 3.1.6 in a state-space manner which is suitable for the dynamic analysis of flexible aircraft with small (linear) wing deformation but with possibly large trim deflections.

3.1.1 Governing Equations of the Potential Flow

The unsteady vortex lattice method is a solution to Laplace's equation,

$$\nabla^2 \Phi = 0, \tag{3.1}$$

for the disturbance velocity potential, Φ, due to the presence of a moving body in a 3-D flow field. Under the assumptions that the flow is incompressible, inviscid and irrotational, Laplace's equation provides a suitable starting point to solve the continuity equation of the flow around a flexible aerofoil at low Mach numbers. The resulting partial differential equation is solved by distributing singularity solutions on the problem boundaries where the velocity potential is determined through a pair of boundary conditions. The first boundary condition of zero flow normal to the impermeable boundaries of the wing surfaces

must be satisfied, such that

$$(\nabla\Phi + \vec{v}) \cdot \vec{n} = 0, \tag{3.2}$$

where $\vec{v}$ is the velocity of the surface which can include the contribution of the rigid-body motion and elastic deformations of the body as well as local atmospheric disturbances. The normal vector of the surface is given by $\vec{n}$. The second boundary condition requires that the velocity disturbance due to the moving body has to vanish in the far distance. This infinity boundary condition can be stated as

$$\lim_{|\vec{r}|\to\infty} \nabla\Phi = 0, \tag{3.3}$$

where $\vec{r}$ is the position vector from a point on the moving body to an arbitrary point in the fluid domain.

3.1.2 Discretisation with Vortex Ring Elements

The unsteady version of the vortex lattice method is implemented using vortex ring quadrilateral elements to discretise the lifting surfaces, as shown in Figure 3.2, such that the wing is divided into N spanwise and M chordwise panels. Each surface (bound) vortex ring has an associated circulation strength, Γ_k, and a collocation point, at which the impermeability boundary condition, Eq. (3.2), is satisfied. Note that the leading segment of the vortex ring is placed on the panel's quarter-chord line such that the collocation point is located at the panel's centre line, where the normal vector of each panel, $\vec{n}_k$, is also defined as shown in Figure 3.2. The discretisation of the problem is discussed in detail in Katz and Plotkin [98].

The positioning of the vortex ring elements automatically fulfils the 2-D Kutta-Joukowski condition, which requires the flow to leave the trailing edge of the lifting surface smoothly [98]. Hence, for the time-dependent problem, a wake in the form of an infinitely thin shear layer is generated behind the lifting surfaces following the Kelvin condition,

$$\frac{d\Gamma}{dt} = 0, \tag{3.4}$$

where Γ represents the total circulation in the domain. This implies that any change of the circulation strength of the bound vortex rings, Γ_b, affects the circulation in the wake, Γ_w, which forms the basis for the time-stepping procedure of the UVLM [113]. Note that Γ_b and Γ_w are column matrices of the circulation strengths of all bound and wake panels.

As the aircraft follows a trajectory, a row of wake panels is shed at each time step with equal circulation strength to the trailing edge segment at the previous time step, which automatically satisfies the Kelvin condition. The new row of wake vertices is placed at the trailing vortex segment of the trailing edge vortex ring, as shown in Figure 3.2, and advances in time according to the free stream conditions while its original circulation

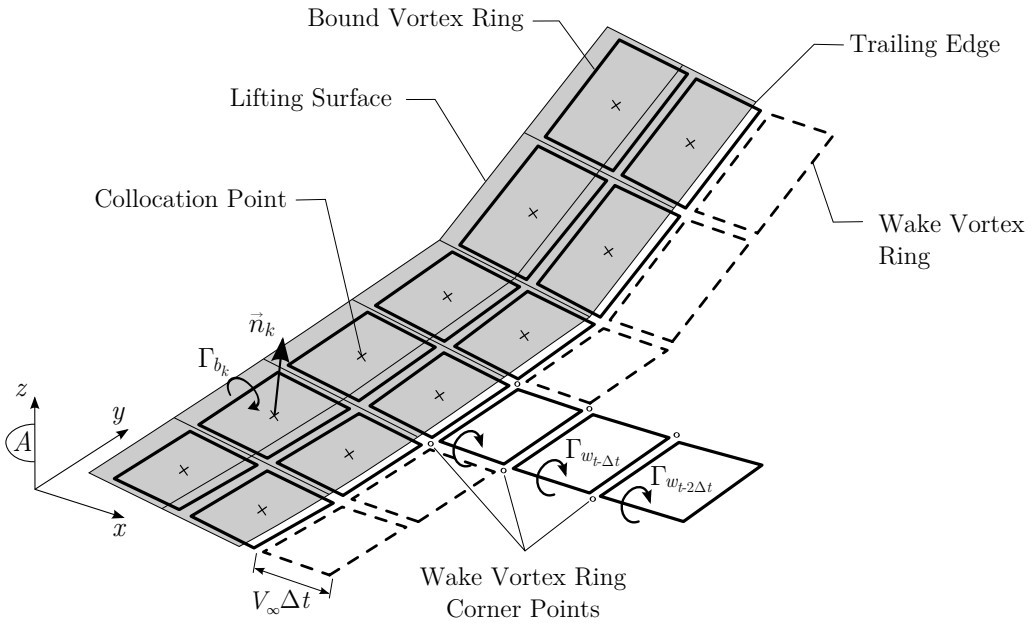


Figure 3.2: Unsteady vortex lattice method with vortex ring discretisation of lifting surface and wake for free-stream flow in positive x direction.

strength remains unchanged. This wake shedding procedure is repeated for each time step and produces the aerodynamic vortex lattice.

3.1.3 Time-Stepping Solution of the Aerodynamic Lattice

The solution to the potential flow problem, Eq. (3.1), is obtained in terms of the vorticity distribution of all vortex ring elements by applying the non-penetration boundary condition, Eq. (3.2), at each collocation point of the lifting surfaces. This yields the following equation at time step $n+1$

$$A_b \Gamma_b^{n+1} + A_w \Gamma_w^{n+1} - w^{n+1} = 0, \tag{3.5}$$

where Γ_b and Γ_w are column matrices of the circulation strengths of all bound (surface) and wake panels. The aerodynamic influence coefficient matrices, $A_b\left(\chi_b^{n+1}\right)$ and $A_w\left(\chi_b^{n+1}, \chi_w^{n+1}\right)$, are computed in terms of the column matrices of the bound and wake grid coordinates, χ_b and χ_w, respectively. The column vector of normal components of the non-vortical velocities at the collocation points, w, can include deployment of control surfaces, gust-induced velocities, wing deformations and rigid-body motions.

Elements of the aerodynamic influence coefficient matrices are obtained in terms of the cross-induced normalwash of all vortex rings, where the Biot-Savart law is used to describe the velocity induced by a vortex ring l at an arbitrary (collocation) point k. It is given

for unit circulation strength as

$$\vec{q}_{kl} = \oint \frac{d\vec{s}_l \times \vec{r}_{kl}}{4\pi \left|\vec{r}_{kl}\right|^3}, \tag{3.6}$$

where $d\vec{s}_l$ represents the contribution of one vortex segment of the complete ring and $\vec{r}_{kl}$ is the vector from the relevant vortex ring segment to point k. Hence, for the quadrilateral vortex rings used to discretise the problem, four evaluations of the Biot-Savart law are necessary to complete a whole ring. The singularity arising at the centre of the vortex ring is rectified by introducing a cut-off method for $|\vec{r}_{kl}| \to 0$. For points far away from the vortex ring l the Biot-Savart law automatically satisfies the far-field boundary condition, Eq. (3.3), of the potential flow problem such that the induced velocity, $\vec{q}_{kl}$, vanishes for $|\vec{r}_{kl}| \to \infty$. This implies that wake vortices that have propagated far downstream have a negligible effect on points close to the lifting surfaces and will be neglected in this work to improve numerical efficiency, whereby the truncation distance is determined for each problem through convergence studies.

Finally, the influence coefficient, $(A_b)_{kl}$, is given in terms of the velocity induced by a bound vortex ring l at the collocation point k as

$$(A_b)_{kl} = \vec{q}_{kl} \cdot \vec{n}_k \quad \text{with} \quad k, l = 1, \ldots, M \cdot N, \tag{3.7}$$

where $\vec{n}_k$ is the normal vector of the quadrilateral panel at the collocation point k and $M \cdot N$ is the total number of bound panels. The influence coefficients for the wake vortices, A_w, can be obtained in the same manner to account for the normal velocity component over the lifting surface induced by the wake.

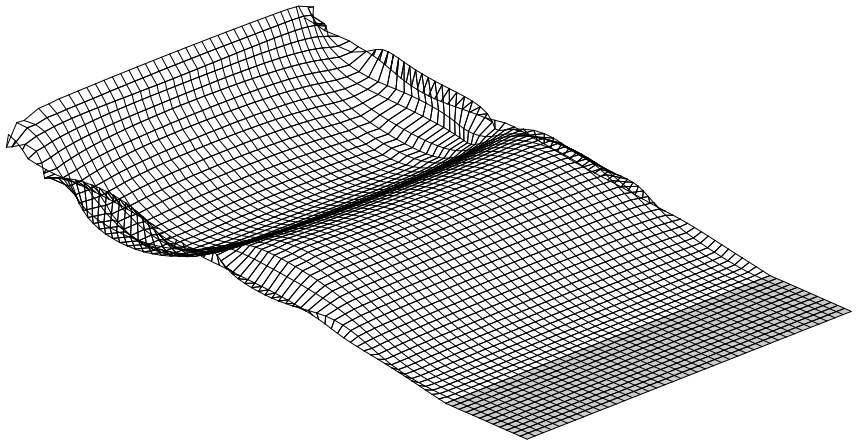
The non-penetration boundary condition, Eq. (3.5), is completed with the definition of the non-vortical normalwash at the collocation point k, given as

$$w^{n+1} = W_b \cdot \left(\dot{\chi}_b^{n+1} + v_d^{n+1}\right), \tag{3.8}$$

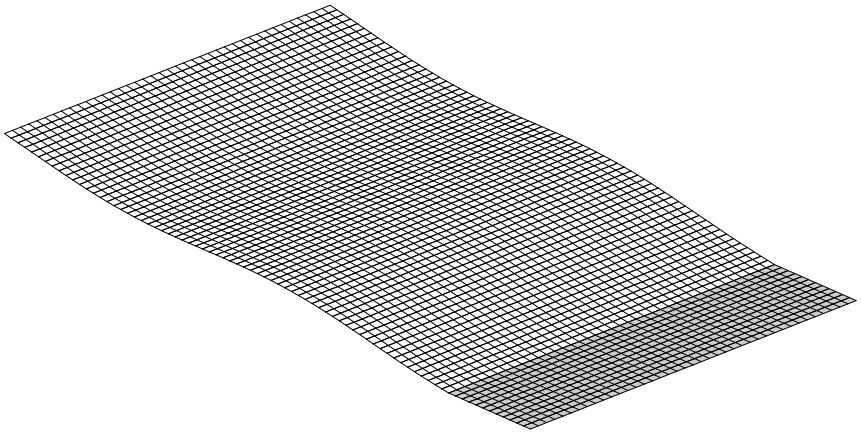
due to atmospheric disturbances, v_d, and the velocity of the aerodynamic grid of the lifting surfaces, $\dot{\chi}_b$, to account for elastic deformations and the overall rigid-body motion of the aircraft at time step $n+1$. The non-circulatory velocities are projected along the normal direction of the panels through matrix W_b which is a function of the instantaneous geometry, χ_b^{n+1}. As the circulation strengths of the wake panels, Γ_w, is know from the previous time step n, this provides all the information needed to solve Eq. (3.5) for the circulation strengths of the bound vortices, Γ_b, at each time step. Note that the non-penetration boundary condition is applied on the aerodynamic lattice of the current configuration, which implies that the method is also geometrically nonlinear and can account for large wing deformations.

3.1.4 Wake Propagation

The wake carries no aerodynamic loads and the propagation of the wake panels depends on the free stream condition, the atmospheric disturbances, v_d, and the cross-induced velocities from all bound and wake vortices obtained through the Biot-Savart law. A brief description of the two wake models implemented by Murua [126] is provided next but a detailed derivation of the wake propagation can be found in Katz and Plotkin [98].



(a) Force free wake



(b) Prescribed wake

Figure 3.3: Different wake models for a rigid plate subject to sinusoidal pitch excitation.

For a fully force-free wake, time integration over the induced local velocities at each wake vortex ring corner point results in a free wake with roll-up, as demonstrated in Figure 3.3(a) for a moving plate subject to sinusoidal pitch excitation. The resulting wake follows the motion of the surface, but each wake ring also moves according to the local velocity vector which includes the induction from all other vortex rings and the contribution from exogenous disturbances. The computational effort at each time step involves (a) updating the aerodynamic influence coefficients, A_b and A_w, in Eq. (3.5), (b)

computing the induced velocities among all wake elements using the Biot-Savart law and (c) updating the coordinates of the wake vortex ring corner points according to the local velocities.

The computational effort can be reduced significantly if the wake is prescribed. In this case the wake follows the motion of the trailing edge of the lifting surface but each wake panel remains fixed in space over time, which produces a prescribed wake as demonstrated in Figure 3.3(b). Hence, the influence of the induced velocities on the wake vortices is ignored and only the aerodynamic influence coefficients, A_b and A_w, need to be re-computed at each time step as the wake propagates.

Free wake effects may be important for flapping flight [185] and very flexible aircraft with excessive wing dihedral [128] where the cross-influence of the wake circulations can have a significant effect on the wake shape close to the lifting surfaces. For the reduced frequencies of interest in this work, however, the wake can be prescribed [137], which will be assumed for all studies presented in this thesis. Note that for small deformations the wake model can be simplified further leading to the flat-wake assumption, as done in DLM solutions. However, this assumption is not suitable for the complex aircraft geometries with possibly large trim deformations which will be the focus of this work.

3.1.5 Unsteady Aerodynamic Loads

Once the unknown circulation of the bound vortices, Γ_b, has been computed at each time step using Eq. (3.5), the pressure distribution over the lifting surface can be obtained in the absence of gravitational forces through the unsteady Bernoulli equation,

$$\frac{p_\infty - p}{\rho_\infty} = \frac{(\nabla\Phi)^2}{2} + \frac{\partial\Phi}{\partial t}, \tag{3.9}$$

where p is the pressure at a point in the fluid domain and subscript $(\bullet)_\infty$ represents free-stream conditions [126]. By applying the unsteady Bernoulli equation to the upper and lower surface of the camberline, one obtains the pressure difference across the aerofoil which acts along the normal vector, $\vec{n}_k$, of each panel, k. The contribution of each vortex ring to the resulting unsteady aerodynamic loads of the incompressible potential flow is given as

$$\Delta\vec{F}_k^{\,n} = -\left(\Delta p \Delta S\right)_k^n \vec{n}_k^{\,n}, \tag{3.10}$$

where ΔS_k is the area of each panel which can change in time according to the elastic deformations of the lifting surface.

The aerodynamic forces are subsequently projected onto the plane defined by the normal vector of the vortex ring and the instantaneous non-circulatory velocity at the collocation point to obtain the induced drag and lifting forces, which act parallel and perpendicular, respectively, to the flight direction of each panel. Note that the non-circulatory velocity

includes the contributions of rigid-body motions, elastic deformations and incident flow, but not the influence of the bound and wake circulation.

The unsteady Bernoulli equation yields adequate predictions for the lifting forces but it tends to overestimate the contribution to induced drag, since the UVLM is based on the thin-wing approximation and does not account for the leading-edge suction force [126]. Instead, the approximation by Katz and Plotkin [98] is used in this work to compute the induced drag aligned with the instantaneous non-circulatory velocity, which leads to the discrete form of the expressions for lift and drag forces, given as [98, 185]

$$\begin{aligned} L^n &= \rho_\infty G_L \left(U_L \Gamma_b^n + \dot{\Gamma}_b^n \right), \\ D^n &= \rho_\infty \left(U_D \Gamma_b^n + G_D \dot{\Gamma}_b^n \right), \end{aligned} \tag{3.11}$$

where L and D are column matrices of lift and drag forces at all bound panels of the lifting surfaces. The diagonal matrices $G_{L,D} = G_{L,D}\left(\chi_b^n, \dot{\chi}_b^n\right)$ account for the current geometry of the bound panels and the local angle of incidence and the matrices $U_L = U_L\left(\Gamma_w^n, \chi_b^n, \chi_w^n, \dot{\chi}_b^n\right)$ and $U_D = U_D\left(\Gamma_b^n, \Gamma_w^n, \chi_b^n, \chi_w^n\right)$ are obtained from the induced velocities of the bound and wake panels using the Biot-Savart law.

3.1.6 Linearised Formulation in State Space

In this section the linearised formulation of the UVLM is introduced which provides an efficient state-space representation of the vehicle aerodynamics for small transient deformations. Note however that the linearisation is done around a geometrically nonlinear equilibrium condition which corresponds to the trimmed aircraft configuration at forward flight with possibly large wing deformations.

The following description provides a brief overview of the linearisation of the unsteady aerodynamics [128]. The linearised formulation is obtained in time domain based on the following assumptions:

Assumption 1. The elastic displacements and rotations of the lifting surfaces in the transient response are assumed to be small around the overall possibly large deformations. This linearises the non-penetration boundary condition, Eq. (3.5), such that the governing equations become independent of the instantaneous geometry of the aerodynamic grid, χ_b. The non-vortical normalwash, w, in Eq. (3.8) depends however on the local angle of incidence, which changes with the deformation of the bound panels.

Assumption 2. For small wing deflections, the computation of the aerodynamic forces in Eq. (3.11) becomes independent of the geometry of the aerodynamic grid, χ_b and χ_w, respectively, but the derivative of the aerodynamic loads with the grid velocities, $\dot{\chi}_b$, is included in the linearisation to account for the change of local angle of attack.

Assumption 3. The wake is frozen around the deformed aerodynamic lattice and the possibly force-free wake at the geometrically nonlinear equilibrium condition. This important assumption freezes the coordinates of the wake vortex ring corner points, χ_w, which results in a constant wake aerodynamic influence coefficient, A_w, in Eq. (3.5). The wake however does not need to be flat and the linearised UVLM can capture the aerodynamics of unconventional aircraft configurations with flexible members.

Following these assumptions the independent variables of the linearised aerodynamic problem reduce to the distribution of the circulation strengths and the time derivative of the bound circulation strength leading to the state vector, Γ, given as

$$\Gamma = \begin{bmatrix} \Gamma_b^\top & \Gamma_w^\top & \dot{\Gamma}_b^\top \end{bmatrix}^\top. \tag{3.12}$$

The change in circulation strengths of the vortex rings around this steady-state solution is then given in discrete time as

$$\Delta\Gamma^{n+1} = A_F \Delta\Gamma^n + B_F \Delta u_F^n, \tag{3.13}$$

where superscripts n and $n+1$ refer to the current and next time steps and the subscript F refers to the linear time-invariant (LTI) aerodynamics. The inputs to the problem, given as

$$u_F = \begin{bmatrix} \chi_b^\top & \dot{\chi}_b^\top \end{bmatrix}^\top, \tag{3.14}$$

arise from the linearisation of the non-vortical normalwash, w, in Eq. (3.8) and can account for small elastic deformations of the lifting surfaces as well as the rigid-body velocities and orientation of the vehicle. The time derivative of the aerodynamic grid, $\dot{\chi}_b$, is also included in Eq. (3.12) to account for deployment of control surfaces and gust-induced velocities, as discussed in Assumption 1.

Finally, linearisation of the unsteady aerodynamic loads which result from the vorticity distribution at each time step and are written in general as Δy_F, leads to the linearised output equations written in symbolic form as

$$\Delta y_F^n = C_F \Delta\Gamma^n + D_F \Delta u_F^n. \tag{3.15}$$

where the system feedthrough, following Assumption 2, accounts for small changes of local angle of attack. All matrices of the non-strictly proper linear aerodynamic system $\{A_F, B_F, C_F, D_F\}$ have been derived in detail in Ref. [126].

The resulting aerodynamic state-space system can be tightly coupled with the flexible-body dynamics model, which leads to a very compact form of the aeroelastic and flight-dynamic EoM and provides an ideal environment for further model reduction, as described in Chapter 4.

3.2 Coupled Aeroelastic and Flight Dynamics

This section presents the coupled framework for the Simulation of High-Aspect-Ratio Planes (SHARP) to study flexible aircraft, including static aeroelastic analyses, trim, linear stability analyses, and fully nonlinear time-marching simulations. This coupled methodology is based on the description of the vehicle flexible-body dynamics in Chapter 2 and the formulation of the unsteady vortex lattice method in Section 3.1.

The crucial aspect of interfacing the structural and fluid problems is addressed first in Subsection 3.2.1, which provides the foundation for the subsequent assembly of the two models. Starting with the geometrically nonlinear description of the flexible-aircraft dynamics presented in Subsection 3.2.2, it is possible to capture the effect of flexibility and especially large wing deformations which can significantly alter the dynamic behaviour of manoeuvring flexible aircraft configurations.

However, there are cases in which linearised approaches can sufficiently predict the vehicle response providing a suitable tool for the preliminary design of very efficient aircraft including control synthesis and/or optimisation. Hence, Subsection 3.2.3 presents the EoM of manoeuvring flexible aircraft subject to small wing deformations. The resulting linearised approach allows the projection of the flexible-body dynamics equations on the vehicle free-free modes but, unlike the mean-axes approximation, it captures the inertial coupling between the possibly large vehicle flight dynamics and the small aeroelastic response. The aerodynamic loads are obtained in time domain from the state-space UVLM, presented in Subsection 3.1.6, which is tailored to the model reduction techniques described in Chapter 4, leading to a very compact but accurate description of the flexible-aircraft dynamics.

At last, linearisation also in the rigid-body DoF leads to the monolithic framework presented in Subsection 3.2.4, which can capture the integrate dynamics of flexible aircraft including flight dynamics and provides a powerful tool for fast open-/closed-loop transient simulations (with small angular velocities), linear stability analysis, the synthesis of robust load alleviation controllers and optimisation of vehicle configurations. In this work, the stability tool will be relevant to explore the coupling effects between the aerodynamic, aeroelastic and flight-dynamic modes of flexible aircraft.

The integration of the framework in MATLAB® is based on the implementation by Murua [126], especially the mapping procedure between the aerodynamic and flexible-body dynamics models (Subsection 3.2.1) and the monolithic framework for linear stability analysis (Subsection 3.2.4). This work will expand the framework with the linearised formulation for the simulation of manoeuvring flexible aircraft subject to small wing deformations in Subsection 3.2.3.

3.2.1 Mapping between Aerodynamic and Flexible-Body Degrees of Freedom

The integration of the flexible-body and aerodynamic equations of motion, described independently in the following sections, relies on the interfacing between the displacements of the flexible aircraft and the resulting aerodynamic loads. This is done through a linear mapping procedure between the 1-D beam representation as deformable curves in the 3-D space and the aerodynamic lattice distributed over the lifting surfaces. The mapping of the fluid-structure interaction (FSI) is shown in Figure 3.4 for the dynamic case, but the time-dependent variables can be neglected to also account for the static aeroelastic problems.

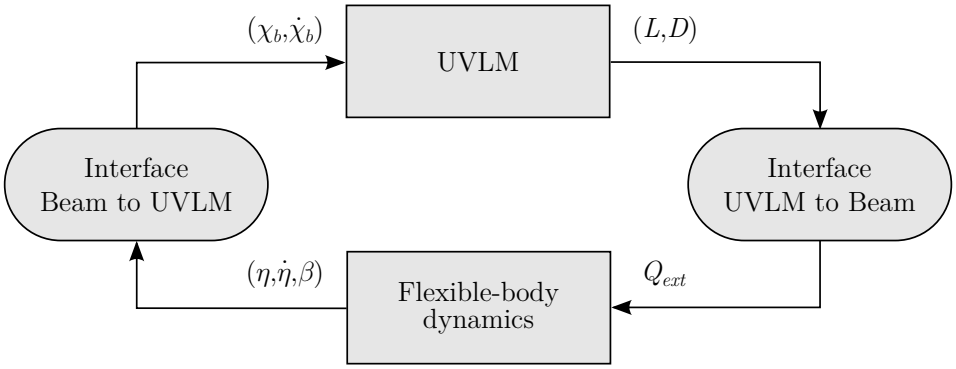


Figure 3.4: Fluid-structure interface between the UVLM and the beam formulation.

The implementation of the mapping procedure for the geometrically nonlinear formulation is based on the following assumptions [126]:

Assumption 1. The wing cross-sections remain rigid under elastic deformations. This assumption is used to simplify the mapping of the beam rotations to the aerodynamic lattice and likewise to compute the moments at the beam nodes generated by the aerodynamic forces. As aircraft wings are inherently slender structures, large-scale motion of the wing dominate over the small-scale motions of the cross sections, but the warping of the cross sections could be incorporated through appropriate cross-sectional reduction methods [50, 135].

Assumption 2. The spanwise discretisation of the aerodynamic lattice coincides with the beam mesh and beam elements are assumed to be linear. This assumption firstly simplifies the projection of the cross-sectional coordinates onto the aerodynamic lattice; and secondly, the contribution of the aerodynamic forces to each beam node is defined explicitly. As the discretisation of the aerodynamic and structural problems is prioritised differently – more aerodynamic panels are required at the wing tips and a finer beam mesh at the root – a coincident mesh results in an unnecessarily fine discretisation, but that did not pose a major problem. Alternatively, non-coincident

meshes with higher-order beam elements can be implemented based on the shape functions of the finite-element discretisation of the beam problem [60, 181], which is suggested for future work.

Assumption 3. The distributed aerodynamic loads are approximated as point forces applied at the leading edge of each vortex ring. This assumptions simplifies the lumping of the aerodynamic forces to the forces and moments at the beam nodes, but requires an adequate discretisation of the aerodynamic lattice in the chordwise direction to accurately capture the resultant moments.

Interface from Flexible-Body Model to Aerodynamic Inputs

Starting from the flexible-body dynamics module, the structural and rigid-body DoF, η and β, respectively, are used to update the aerodynamic grid of the bound vortex rings, χ_b, and the time derivative of the lattice, $\dot{\chi}_b$. Under the assumption of rigid beam cross-sections, the mapping from the beam reference line coordinates to the grid points of the aerodynamic lattice is introduced following the description of the beam kinematics in Section 2.1.2. The transformation for each grid point can be obtained with respect to the body-fixed frame, A, as

$$\begin{aligned}(\chi_b)_A &= R_A + C^\top \xi_B, \\ (\dot{\chi}_b)_A &= v_A + \dot{R}_A + \widetilde{\omega}_A R_A + C^\top \widetilde{\Omega}_B \xi_B,\end{aligned} \tag{3.16}$$

where ξ_B is the distance of a vortex-ring corner-point to the corresponding node on the beam reference line, which remains constant in the local frame of reference, B. Furthermore, even though the cross sections are assumed to be rigid, the lifting surfaces are allowed to twist and bend, which is captured through the change of orientation of each local frame in terms of the transformation matrix $C(\Psi)$ and the column matrix of local velocities Ω_B, as defined in Eqs. (2.3) and (2.9), respectively. The location of the collocation point of each vortex ring, where the non-penetration boundary condition, Eq. (3.5), is applied, is obtained through interpolation of the corner point coordinates of the corresponding panel. This completes the mapping of the displacements and rotations of the beam nodes to the aerodynamic lattice for the geometrically-nonlinear formulation of the UVLM.

For small changes in the flexible-body DoF, $(\Delta\eta, \Delta\dot{\eta}, \Delta\beta)$, around a static equilibrium condition at trimmed flight, Eq. (3.16) can also be written in the incremental form as

$$\begin{aligned}(\Delta\chi_b)_A &= \Delta R_A - C^\top \widetilde{\xi}_B T \Delta\Psi, \\ (\Delta\dot{\chi}_b)_A &= \Delta\dot{R}_A - C^\top \widetilde{\xi}_B T \Delta\dot{\Psi} + \Delta v_A - \left(\widetilde{R}_A + \widetilde{C^\top \xi_B}\right) \Delta\omega_A,\end{aligned} \tag{3.17}$$

with the incremental elastic displacements $\Delta\eta = (\Delta R_A, \Delta\Psi)$ and rigid-body velocities $\Delta\beta = (\Delta v_A, \Delta\omega_A)$. The resulting linear transformation maps the flexible-body DoF to the aerodynamic lattice which populates the matrices, B_F and D_F, of the linear aerodynamic system defined in Eq. (3.13). Note that linearisation of the aerodynamics can also be done around around a dynamic equilibrium, in which case Eq. 3.17 includes Coriolis terms due to the angular velocities at the reference condition.

Interface from Aerodynamic to Flexible-Body Forces

The unsteady aerodynamic loads are obtained from the pressure distribution at each panel using the unsteady Bernoulli equation, as discussed in Section 3.1.5. The resulting lift and induced drag are obtained as point forces applied at the centre of the leading segment of each vortex ring expressed in the reference frame of each lifting surface. The location of the applied aerodynamic forces has been determined by Murua [126] by a convergence study with respect to analytical solutions of 2-D flow.

Following the description in Section 3.1.5, the aerodynamic forces are computed in a local reference frame defined by the instantaneous non-circulatory velocity at each collocation point to obtain the induced drag and lifting forces, which act parallel and perpendicular, respectively, to the flight direction of each panel. The description of the flexible-body dynamics is however implemented in the global body-fixed frame, A, and the mapping procedure first projects the aerodynamic loads at each panel into the A frame.

Based on the assumptions that the wing cross-sections remain rigid and that the beam mesh coincides with the spanwise discretisation of the aerodynamic lattice, the aerodynamic point forces that act at the centre of the leading edge of each panel are lumped to the neighbouring beam nodes by splitting the contribution to each side. The resulting projection of the three aerodynamic load components to the six components of the external forces and moments, Q^S_{ext}, in the flexible-body dynamics formulation, Eq. (2.23), depends on the instantaneous geometry of the aerodynamic grid (following the displacements and rotation of the beam reference line) and is geometrically nonlinear.

In the linear case, the matrix that lumps the aerodynamic point forces to the beam nodes is assumed to remain constant, but the projection from the local aerodynamic frames to the body-fixed frame, A, depends on the aerodynamic grid velocities which needs to be accounted for in the linear mapping of the aerodynamic loads to the flexible-body dynamics formulation. These operations can be written in compact matrix form leading to the output equation of the linear aerodynamic system, as defined in Eq. (3.15).

3.2.2 Nonlinear Equations of Motion of Very Flexible Aircraft

Following the derivation of the flexible-body and unsteady aerodynamics formulations in Sections 2.1 and 3.1, respectively, it is now possible to model the dynamics of very flexible aircraft in an integrated fashion based on the mapping procedure outlined in

Subsection 3.2.1. The geometrically nonlinear time-marching solution, as illustrated in Figure 3.5, can account for the large elastic deformations of the manoeuvring aircraft coupled with the 3-D unsteady aerodynamics.

The dynamic simulation has been implemented following a partitioned time-marching scheme [59] to separate the solution of the nonlinear flexible-body dynamics from the computation of the aerodynamic loads at each time step. The resulting loosely-coupled approach is computationally more efficient, as the aerodynamic loads are frozen during the Newmark time-integration step of the structural response, but it requires a very small time step for the solution to converge. The solution method can be adjusted to follow a tightly-coupled approach [181], but this was not explored in this thesis.

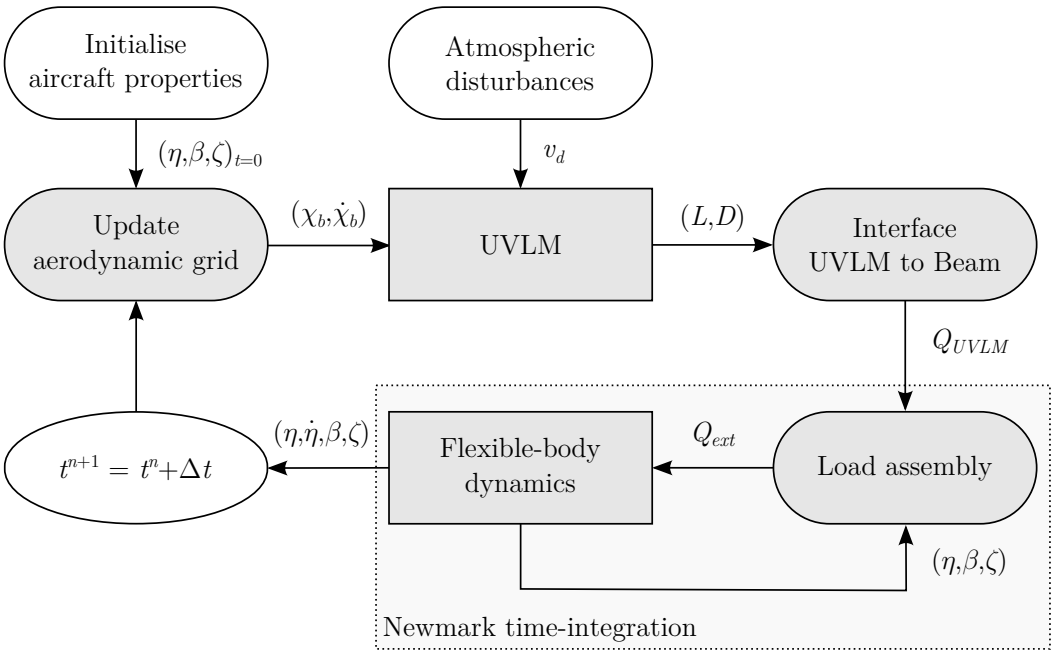


Figure 3.5: Flow diagram of the nonlinear time-marching routine.

Following the flow diagram in Figure 3.5, starting point for the nonlinear time-marching solution is the initialisation of the aircraft properties which will be given in this work by the vehicle steady (trim) condition with a developed wake. The unsteady aerodynamic loads are computed for the deformed wing geometry and instantaneous velocities following the solution procedure of the UVLM, as outlined in Section 3.1. Note that the inputs to the aerodynamic module, $(\chi, \dot{\chi})$, also account for the instantaneous deployment of control surfaces, but the induced velocities due to atmospheric disturbances are included in the input v_d, as given in the definition of the non-vortical normalwash in Eq. (3.8).

Once the aerodynamic loads have been updated, they are mapped to the flexible-body dynamics problem to compute the resulting elastic and rigid-body displacements of the aircraft. The geometrically nonlinear EoM of the flexible aircraft have been defined in

Eq. (2.23) as

$$\mathcal{M}(\eta)\begin{Bmatrix}\ddot{\eta}\\ \dot{\beta}\end{Bmatrix}+\begin{Bmatrix}Q^{S}_{gyr}\\ Q^{R}_{gyr}\end{Bmatrix}+\begin{Bmatrix}Q^{S}_{stif}\\ 0\end{Bmatrix}=\begin{Bmatrix}Q^{S}_{ext}\\ Q^{R}_{ext}\end{Bmatrix}.$$

The resulting attitude and position propagation equations of the manoeuvring vehicle have been defined previously in terms of the body-fixed reference frame as

$$\dot{\zeta}=-\frac{1}{2}\begin{bmatrix}0 & \omega_A^{\top}\\ \omega_A & \widetilde{\omega}_A\end{bmatrix}\zeta,$$

$$\dot{r}_G=C^{GA}v_A.$$

The output of the aerodynamic model, Q_{UVLM}, is accounted for in the external forcing term, $Q^{S,R}_{ext}$, computed for each time step in the load assembly routine depicted in Figure 3.5 which also includes thrust and gravity loads. The nonlinear EoM are solved in an iterative manner following the Newmark time-integration scheme, as presented in Section 2.4. Note that the aerodynamic forces, Q_{UVLM}, are based on the structural information of the previous time step, but gravity and thrust are updated according to the instantaneous vehicle geometry, η, and orientation, ζ, during the Newmark sub-iterations until convergence is reached.

The dynamic simulations studied in this work are obtained around the static aeroelastic equilibrium condition which is computed from the static subset of the coupled dynamic system with prescribed (constant) rigid-body velocities. The trim solution of flexible configurations at steady-level flight with given free-stream velocity is computed using three trim inputs: the vehicle angle of attack, thrust per propeller and the elevator deflection at the tail. A standard Newton-Raphson method is used to minimise the vehicle net lift, thrust and pitch moment resulting from the contribution of the (steady) aerodynamic, thrust and gravity loads. More details on the computation of the aeroelastic trim equilibrium is given in Ref. [126].

3.2.3 Perturbation Equations for the Dynamics of Manoeuvring Flexible Aircraft

Under the assumption of small elastic deformations of the lifting surfaces during the transient dynamics, the coupled aerodynamics can be assumed to be linear, as presented in Subsection 3.1.6, while the corresponding elastic and rigid-body displacements are given by the perturbation EoM of the flexible body derived in Section 2.2.

Unlike aeroelastic approaches based on frequency-domain aerodynamics, the flexible-aircraft dynamics model in this work is developed directly in time domain by tightly coupling the modal form of the flexible-body equations, Eq. (2.45), with the linear unsteady vortex lattice model, Eq. (3.13). This leads to a time-domain formulation that can accurately predict the nonlinear dynamics of moderately flexible aircraft subject to large

manoeuvres, e.g. due to gusts or control surface inputs. Projection of the flexible-body dynamics DoF onto the vibration modes of the unconstrained flexible body, Φ, allows to reduce (a) the size of the flexible-body dynamics problem and (b) the number of inputs and outputs of the aerodynamic system, Eq. (3.13).

To enable the projection of the linear aerodynamic system onto these modes, the system inputs have been divided to account firstly for the contribution of the elastic deformations, given in terms of the generalised coordinates, q, and velocities, $\dot{q}$, of the flexible-body equations, i.e. $u_\Phi = \left[q^\top \ \dot{q}^\top \ \beta^\top\right]^\top$. Secondly, the aerodynamic inputs, u_F, still account for gust induced velocities and the deployment of control surfaces. The resulting generalised unsteady aerodynamics can then be obtained as

$$\begin{aligned} \Delta\Gamma^{n+1} &= A\Delta\Gamma^n + B_S\Phi\Delta u_\Phi^n + B_F\Delta u_F^n \\ \Delta y_F^n &= \Phi^\top C\Delta\Gamma^n + \Phi^\top D_S\Phi\Delta u_\Phi^n + \Phi^\top D_F\Delta u_F^n, \end{aligned} \tag{3.18}$$

where the structural contribution to the system input and feedthrough matrices, B_S and D_S, respectively, are obtained from a subset of the original linear aerodynamic system matrices as defined in Subsection 3.1.6. The output vector y_F contains the discrete-time unsteady aerodynamic loads due to the excitation of a certain vibration mode. Together with the instantaneous thrust and gravity loads, the resulting generalised aerodynamic forces are included in the assembly of the external generalised forces, $\Phi^\top\bar{Q}_{ext}$, which are the inputs to the perturbation equations of the linearised flexible-body dynamics problem defined in Eq. (2.45).

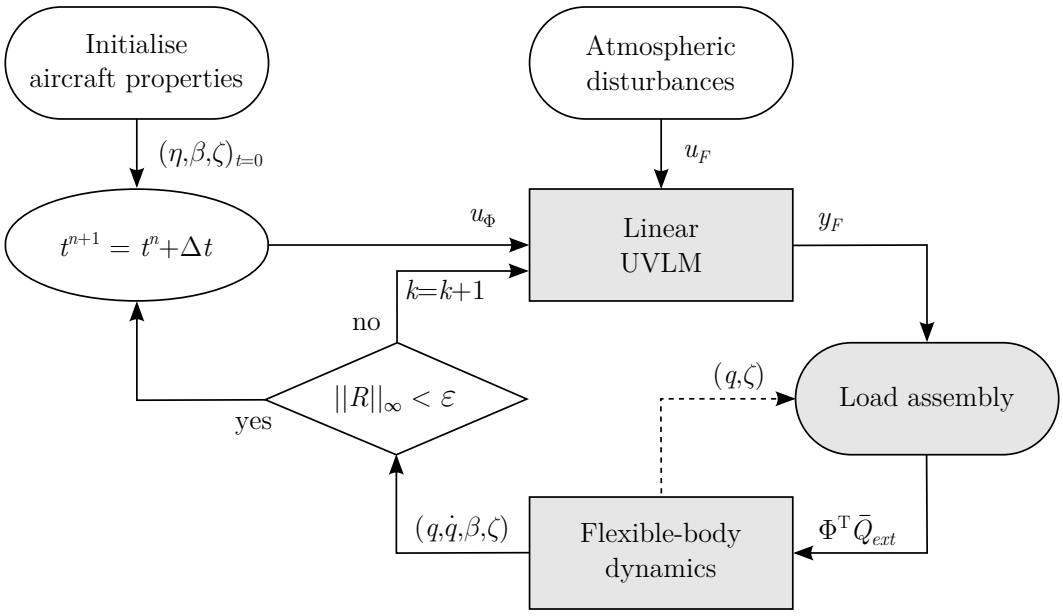


Figure 3.6: Linearised time-marching solution for manoeuvring flexible aircraft.

The integration of the linearised flexible-body and aerodynamic response is done in a tightly-coupled manner, as illustrated in Figure 3.6. Even though the elastic deformations are assumed to be small, the modal equations remain nonlinear in the rigid-body DoF to account for aircraft manoeuvres and the coupled problem is solved iteratively using the Newmark time-integration scheme. Convergence of the nonlinear system is reached at each time step, n, if the generalised external forces balance the generalised inertial, gyroscopic and elastic forces, i.e. when the residual R of the modal EoM, Eq. (2.45), reaches the tolerance ε. Note that the linear interfaces between the aerodynamic and flexible-body dynamic modules have been included in the system matrices of the linear aerodynamic system.

Note that this approach does not require transformation to frequency domain to obtain the generalised forces, but the linearisation of the unsteady aerodynamics is limited to a specific aeroelastic reference condition with the dynamic pressure as a parameter. This requires interpolation of the aerodynamic model between different parameter values, such as flight speed or altitude, to enlarge the flight envelope of very flexible aircraft configurations [6]. However, if the linearisation is done around the undeformed reference, as in DLM solutions, it is possible to show by dimensional analysis that the aerodynamic loads in the resulting linear system, Eq. (3.18), are proportional to the forward-flight dynamic pressure. This would generate aerodynamic models which are independent of the vehicle flight conditions, but this also constraints the admissible wing kinematics and will not be further investigated in this work.

3.2.4 Monolithic Framework for Linear Stability Analysis of Very Flexible Aircraft

Murua [126] demonstrated that the linearised formulation of the unsteady vortex lattice method, Eq. (3.13), enables rigid-body motions and elastic deformations (both small) to be incorporated in a unified monolithic framework. This provides a powerful formulation to determine the aircraft dynamic stability and it can be very useful for efficient control design provided the vehicle manoeuvres remain small.

Linearisation of the aerodynamic and flexible-body dynamic states, as presented in Subsections 3.1.6 and 2.2.2, respectively, is obtained around the geometrically nonlinear static equilibrium, which can account for possibly large wing deformations of the trimmed aircraft configuration. However, as the linear UVLM is written in discrete time, temporal discretisation of the flexible-body system, Eq. (2.41), is also required before the fluid/structure coupling. A standard Newmark-β discretisation, as discussed in Subsection 2.4, is used to discretise the linear system, which can also include algorithmic damping in the structural dynamics response.

Based on the linear interface between the aerodynamic and flexible-body models in Subsection 3.2.1 and after introducing the modal transformation of Eq. (2.42) for the

elastic DoF, the aeroelastic state-space system is given in discrete time as

$$\begin{aligned} \Delta x^{n+1} &= A_{FS}\Delta x^n + B_{FS}\Delta u_{FS}^n \\ \Delta y_{FS}^n &= C_{FS}\Delta x^n, \end{aligned} \tag{3.19}$$

where superscripts n and $n+1$ refer to the current and next time and the subscript FS is introduced here to separate the aeroelastic system variables from the linear equations of the UVLM in Eqs. (3.13) or (3.18). The state vector that completely determines the linear system is

$$x = \left[x_F^T \mid x_S^T\right]^T = \left[\Gamma_b^T \ \Gamma_w^T \ \dot{\Gamma}_b^T \mid q^T \ \dot{q}^T \ \ \beta^T \ \Theta^T\right]^T, \tag{3.20}$$

where the orientation of the aircraft is now given in terms of Euler angles, Θ, which have been traditionally used in linear flight dynamics. Although quaternions, as introduced in Subsection 2.1.1, provide a computationally more efficient parameterisation of the aircraft orientation for vehicles subject to large rigid-body motion [69], the resulting (nonlinear) attitude EoM, Eq. (2.1), are less suitable for linearisation due to the algebraic nonlinear constraints of quaternions [39].

The (aerodynamic) inputs, u_{FS}, to the monolithic system in Eq. (3.19) account for gusts and control inputs in a (closed-loop) time-marching solution. Depending on the nature of the problem, the system output vector y_{FS} can include aerodynamic loads, elastic deformations, aircraft position, attitude, etc. If the rigid-body states are neglected, Eq. (3.19) can also be used to describe the (linear) aeroelastic response of the clamped aircraft.

From the homogeneous form of Eq. (3.19) one finally obtains a discrete-time generalised eigenvalue problem to determine the dynamic stability of the vehicle which includes aeroelastic and flight dynamic modes. This provides a very efficient tool to predict the dynamic characteristics of flexible aircraft and to demonstrate the coupling effects between the vehicle aerodynamic, aeroelastic and flight-dynamic modes. Because the linearisation is done around a geometrically nonlinear equilibrium condition, the stability tool can predict flutter speed of very flexible aircraft with large trim deformations of the lifting surfaces, as demonstrated in detail by Murua [128].

Chapter 4

Reduced-Order Models for Coupled Aeroelasticity and Flight Dynamics

The geometrically-nonlinear aeroelastic framework presented in Chapter 3 provides a powerful simulation environment for direct time simulations of the integrated dynamics of flexible manoeuvring aircraft. However, the capability of capturing the nonlinear features of the aircraft geometry and flow comes with an increased numerical burden: (1) the computational cost to solve the unsteady aerodynamic loads for the instantaneous geometry and flight condition of the flexible aircraft and (2) the size of the 3-D aerodynamic system. Even though large trim deformations can be dominant, in many cases the dynamics of flexible aircraft remains small and can be efficiently modelled using linearised methods.

This has been tackled through linearisation of the aeroelastic degrees of freedom leading to a compact description of the flexible aircraft dynamics, as presented in Subsection 3.2.3, which captures the interaction between (small) structural deformations and the large flight dynamics of the manoeuvring vehicle with possibly large trim deformations. Even though the governing EoM of the manoeuvring flexible aircraft remain algebraically nonlinear, it is possible to isolate a linear subsystem to describe the unsteady aerodynamics of the flexible vehicle. The size of this linear system, however, is dominated by the number of vortex panels used in the aerodynamic discretisation of the lifting surfaces and wake of the aircraft and can become too large to be effective in the design of highly-efficient configurations.

To explore a sufficiently large design envelope, a large number of closed- and open-loop time simulations is required for dynamic load calculations of aircraft manoeuvres and gust responses. As outlined in the Chapter 3, the aeroelastic framework for manoeuvring aircraft presented in Subsection 3.2.3 provides a suitable platform for this task, but the size

of the high-order linear aerodynamic system can make this linearised approach ineffective. Hence, in this chapter model reduction techniques will be applied to the high-order linear aerodynamic system to develop a reduced-order representation that can capture the dominant dynamics of the original system. Likewise, the large size of the monolithic aeroelastic system will also be tackled in this work to facilitate the application of this integrated framework for effective aeroservoelasticity and optimisation.

A direct approach to reduce the size of the linear systems in time domain is modal projection (and truncation) of the system states on a few generalised coordinates [78]. However, as discussed in Chapter 1, this approach may require many states in the reduced-order model to capture the internal dynamics of the flow [158, 200]. Instead, this work will focus on balancing methods to obtain a more efficient basis function which can be found by balancing the system such that the input-output mapping drives the reduction process [72, 125, 158]. Such balancing-based model reduction techniques, originally developed in the control theory community, achieve optimal reductions for stable systems in continuous time which has been demonstrated for fluid-dynamics problems [200]. The full-order linear systems in this work however are obtained in discrete time, due to the nature of the state-space description of the UVLM, and transformation of the discrete-time systems as presented in Subsection 4.1.1 is required.

The linear aerodynamic subsystem in the simulation of manoeuvring flexible aircraft is naturally stable, but application of balanced truncation to the integrated aeroelastic system, Eq. (3.19), requires a different approach to handle unstable poles. Such instabilities are not only due to the physics of the problem (e.g. flutter), but also due to the numerical inaccuracy at very high frequencies which are stabilised using the methods proposed in Subsection 4.1.2. This leads to a more robust approach, which will be discussed in Section 4.3, to reduce the possibly unstable aeroelastic system and it also produces a very compact reduced-order representation of the dynamics of manoeuvring flexible aircraft.

4.1 Numerical Issues in Reduced-Order Modelling of Aeroelastic Systems

A number of numerical issues need to be addressed before balancing methods can be applied efficiently to the large-scale aeroelastic systems that have been introduced in the previous chapter. The first problem arises from the definition of the unsteady aerodynamics in discrete time. This section will first introduce the transformation of the discrete-time UVLM into a continuous-time system. This not only simplifies the use of standard balancing methods, as outlined in Section 4.2, but also facilitates a better interpretation of the system stability characteristics.

The second issue addressed in this section will focus on the numerical stability of the aeroelastic systems. Whereas the unsteady aerodynamics are highly damped due to their

physical nature, coupling of the linearised UVLM with the system structural dynamics can lead to an ill-conditioned representation of the aircraft aeroelastic response. The second subsection will explore numerical techniques to overcome this problem prior to any model reduction.

Both issues will be illustrated on the Goland wing problem, which serves as a simple starting point for the discussion. The Goland wing is a numerical benchmark problem that has been studied extensively in literature [73, 127, 141, 197] to compare predictions of flutter speed and frequency. It is a stiff cantilever for which Table 4.1 summarises the relevant properties [127]. The problem is solved using the monolithic aeroelastic approach, Eq. (3.19), to obtain the eigenvalue solution at a free-stream velocity of $V = 180$ m/s. This flight condition corresponds to 7 percent above flutter speed of the Goland wing, as will be demonstrated in further verification studies in Chapter 6.

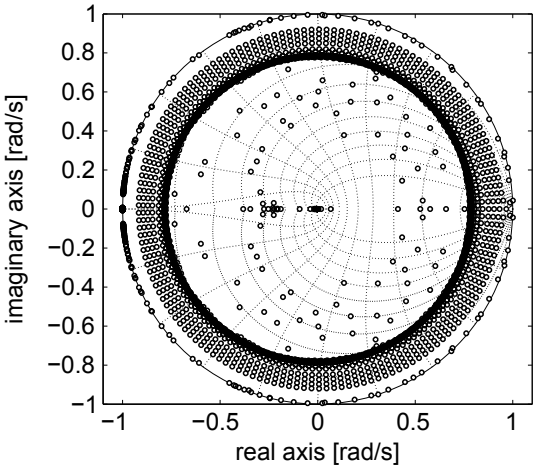
Table 4.1: Goland wing properties.

Chord, c	1.8288 m	Mass per unit length	35.71 kg/m
Semi-span	6.096 m	Moment of inertia	8.64 kg·m
Elastic axis (from l.e.)	$0.33 \cdot c$	Torsional stiffness	0.99×10^6 N·m^2
Centre of gravity (from l.e.)	$0.43 \cdot c$	Bending stiffness	9.77×10^6 N·m^2

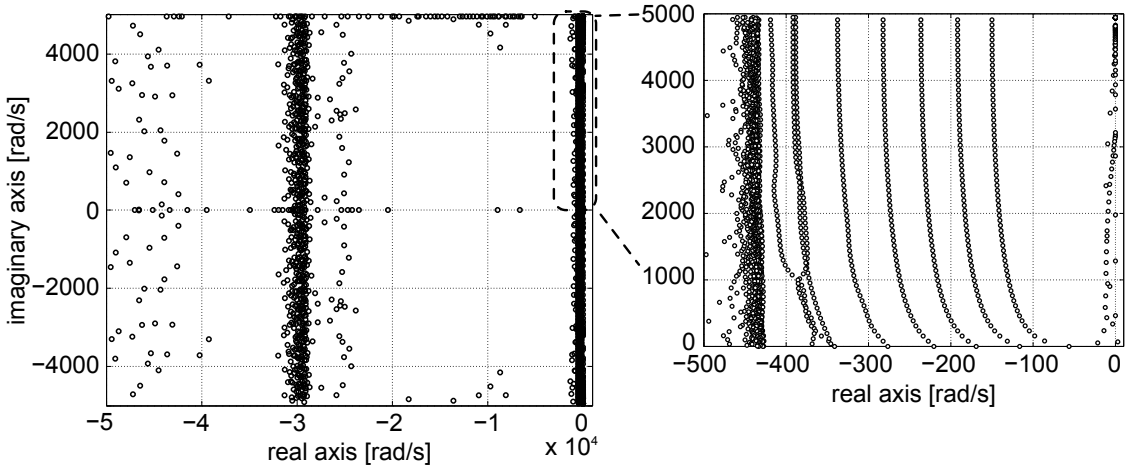
4.1.1 Transformation of the UVLM to Continuous Time

Even though most model reduction techniques have been formulated also for discrete-time linear systems [68], this work will take advantage of the vast amount of development in reduced-order modelling techniques for continuous-time systems. Hence, this subsection will briefly introduce the *bilinear transformation* which is applied to the discrete-time aerodynamic and aeroelastic systems to obtain an equivalent continuous-time representation.

The benefits of continuous-time systems are illustrated in Figure 4.1, which presents the root locus of the (clamped) Goland wing problem at $V = 180$ m/s. Figure 4.1(a) shows the eigenvalues of the discrete-time aeroelastic system given by Eq. (3.19) which tightly couples the aerodynamic and structural response. For the converged solution the aerodynamic domain was discretised using 16 chordwise and 24 spanwise bound panels which results in 4550 aeroelastic states. The resulting system matrix in discrete-time, $A(z)$, produces as many eigenvalues $\lambda_i\left(A(z)\right)$ as there are aeroelastic states in the problem. The dynamic system is stable if all its eigenvalues lie within the unit disc of the complex z-plane, i.e. $|\lambda_i\left(A(z)\right)| < 1, \forall i$. The meridian and latitudinal lines plotted in Figure 4.1(a) represent constant natural frequencies and system damping, respectively.



(a) Discrete-time aeroelastic system



(b) Continuous-time representation with zoom close to origin

Figure 4.1: Root locus of the aeroelastic system for the Goland wing at 180 m/s.

Alternatively, the discrete-time eigenvalues can be transformed to continuous time through the transformation [68],

$$\lambda_i\left(A(s)\right) = \log(\lambda_i\left(A(z)\right))/\Delta t, \tag{4.1}$$

where Δt is the time step size of the discrete-time problem and s denotes the familiar Laplace domain. The continuous-time eigenvalues for the same Goland wing problem are plotted in Figure 4.1(b), whereby the real axis denotes the system damping and the imaginary axis the natural frequencies. This presentation of the system stability is the familiar way in the flight dynamics community and it clearly identifies stable poles on the left half of the complex plane, i.e. $\Re\left(\lambda_i\left(A(s)\right)\right) < 0, \forall i$. All stability analyses in this dissertation will present the continuous-time eigenvalues of the top complex plane only, as indicated by the zoom in Figure 4.1(b).

The continuous-time representation of the discrete-time linear system $\{A, B, C, D\}$ will be obtained in this work using the bilinear transformation, given in terms of the system transfer function as [8]

$$H_c(s) = H_d\left(\frac{s+1}{s-1}\right), \tag{4.2}$$

where $H_d(z) = D + C\left(zI - A\right)^{-1} B$ is the z-plane transfer function of the discrete-time system. Hence, the system matrices of the resulting continuous-time representation $H_c(s) = \tilde{D} + \tilde{C}\left(sI - \tilde{A}\right)^{-1}\tilde{B}$ can be directly computed as [72]

$$\begin{aligned}
\tilde{A} &= (A+I)^{-1}(A-I), \\
\tilde{B} &= \sqrt{2}\,(A+I)^{-1} B, \\
\tilde{C} &= \sqrt{2} C\,(A+I)^{-1}, \\
\tilde{D} &= D - (A+I)^{-1} B.
\end{aligned} \tag{4.3}$$

The bilinear transformation preserves the stability properties of the original system and the frequency response is captured well for frequencies below the Nyquist frequency [8]. Matching the frequency response of the continuous-time filter at even higher frequencies is not a concern in this work, since for converged solutions the Nyquist frequency is usually above the frequency range for which the potential-flow UVLM provides a good approximation. As it neglects viscous effects, potential-flow theory is limited to problems with a reduced frequency around $k = \omega c/(2V) < 0.6$ [128], where c is the chord length of the aerofoil and V the free-stream velocity.

4.1.2 Stability and Conditioning of Aeroelastic Systems

Due to the large range of eigenvalues, aeroelastic systems such as the monolithic system in Eq. (3.19) are typically numerically ill-conditioned [52, 159], which can produce very inefficient reduced-order representations. Hence, this section will introduce two different approaches to improve the numerical stability of the system which will be illustrated again on the Goland wing problem.

To identify the problems that cause possible stability issues, Figure 4.2 firstly demonstrates the effect of coupling the highly-damped aerodynamic modes with the undamped structural response. The effect of aerodynamic damping decreases with increasing vibration frequency which can lead to lightly-damped poles at the high frequency range of the coupled aeroelastic system. The assembly of the integrated model can even produce unstable high-frequency modes which can hamper the model reduction of the high-order system and will be tackled next.

The first approach exploits the algorithmic damping introduced in the discretisation of the structural dynamics problem using the implicit Newmark-β integration scheme, as

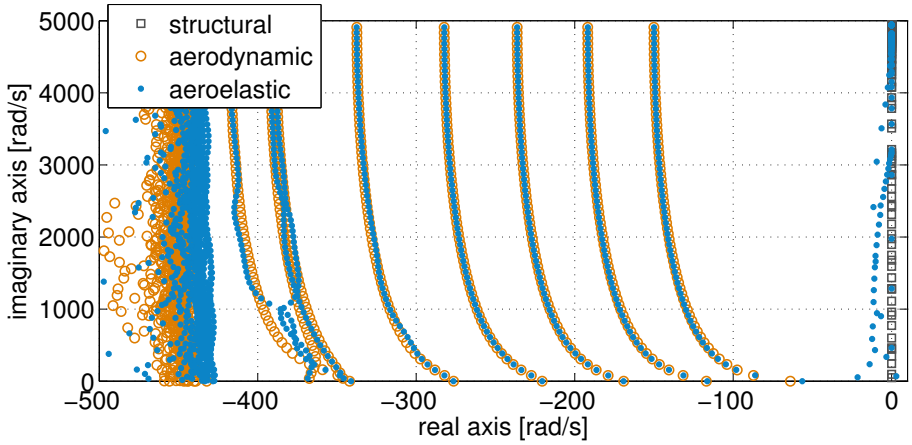


Figure 4.2: Coupling effects on root locus of the Goland wing at free-stream velocity $V = 180$ m/s with structural (Eq. (2.42)), aerodynamic (Eq. (3.13)) and the coupled aeroelastic (Eq. (3.19)) modes.

presented in Section 2.4. Even though the aeroelastic system is transformed to continuous time, discretisation of the structural model is a necessary step in the tight coupling procedure. The algorithmic damping parameter, α, as introduced in Eq. (2.49), shifts the undesired high-frequency modes away from the stability boundary, as shown in Figure 4.3. For the case of $\alpha = 0.005$, which will be applied throughout this work unless otherwise stated, the applied damping preserves the dominant modes to relatively large reduced frequencies of $k = 5$, which again is above the limit of validity of the UVLM ($k \sim 0.6$). Note that for the remainder of this dissertation the imaginary part of all root loci will be normalised with $\omega c/(2V)$ to present the aircraft stability characteristics in terms of reduced frequencies.

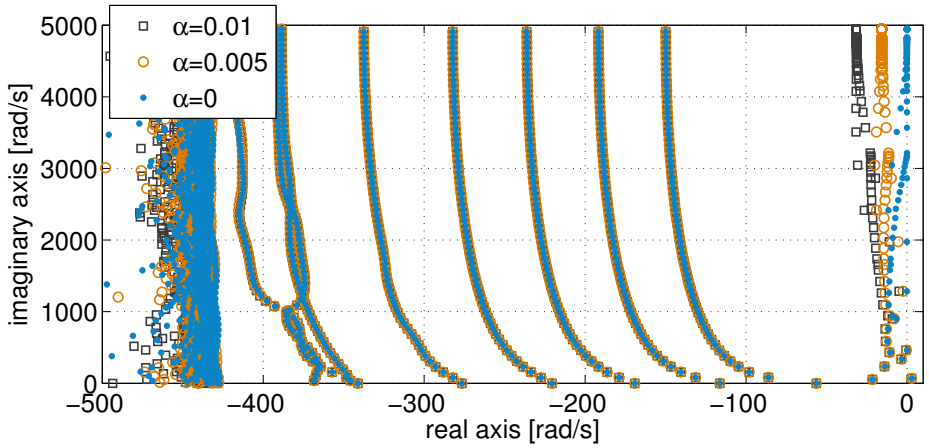


Figure 4.3: Effect of numerical damping, α, on aeroelastic modes of the Goland wing at free-stream velocity $V = 180$ m/s.

As a second approach, modal decomposition was explored to directly remove high-frequency or highly-damped modes. However, a conventional modal truncation ap-

proach [42] was found to perform poorly, as the modal basis for projection of the large aeroelastic system often becomes rank deficient at working precision. Transforming the system matrix to its Schur form, on the contrary, has stabilizing numerical properties [160]. Hence, Schur decomposition can be applied to the full-order system to remove certain undesirable modes, whereby the Nyquist frequency provides a suitable threshold frequency for truncation of high-frequency zero or unstable poles.

Modal Truncation via Schur Decomposition

Schur decomposition of the (discrete-time) system transforms the system matrix A to an upper-triangular Schur matrix, S, such that the system eigenvalues, $\lambda_i(z)$, are distributed along the diagonal of the Schur matrix. Schur decomposition is based on a unitary matrix U with $U^*U = I$, such that [74]

$$U^*AU = S = \begin{bmatrix} \lambda_1 & S_{12} & \cdots & S_{1n} \\ 0 & \lambda_2 & \cdots & S_{2n} \\ \vdots & \vdots & \ddots & \vdots \\ 0 & 0 & \cdots & \lambda_n \end{bmatrix}, \tag{4.4}$$

where the operator $(\cdot)^*$ denotes the conjugate transpose of a matrix. The unitary matrix U can be found efficiently through a number of *QR iterations* as demonstrated in Algorithm 1.

Algorithm 1: Schur decomposition of the system matrix A.

Input: $k = 1, S_k = U_0^* A U_0$,
Output: S_k in Schur form
while (S_k *not upper triangular* & $U_k^* U_k \neq I$) **do**
  $k = k + 1$;
  $U_k R_k = S_{k-1}$; % QR factorisation of S_{k-1}
  $S_k = R_k U_k$;
end

The core of this algorithm is the QR factorisation at each iteration k using the *Givens QR method*, which substitutes S_k with the matrix product $U_k R_k$ where U_k is orthogonal and R_k upper triangular. See the work by Golub and Van Loan [74] for details on suitable initial similarity transformations, U_0, and the Givens QR method. The converged Schur matrix is obtained as,

$$S = (U_0 U_1 \cdots U_k)^* A (U_0 U_1 \cdots U_k) = U^* A U, \tag{4.5}$$

which leads to the transformation of the linear aeroelastic system, Eq. (3.19), such that

$$\begin{aligned} \Delta x_s^{n+1} &= S\Delta x_s^n + U^* B_{FS} \Delta u_{FS}^n \\ \Delta y_{FS}^n &= C_{FS} U \Delta x_s^n, \end{aligned} \tag{4.6}$$

with $x = Ux_s$. As the eigenvalues of matrix A_{FS} are preserved on the diagonal entries of the resulting Schur matrix S, the Schur decomposition provides a computationally-efficient way to truncate high-frequency (or highly damped) modes. This numerically-stable modal truncation is implemented in the MATLAB® built-in function `modsep` [112], which has been explored in this work to filter undesired modes.

4.2 Overview of Balancing Approximations

Next, we introduce the model reduction techniques that will be used in the next section to tackle the large order of the linearised aerodynamic and aeroelastic systems. Because of the different numerical issues linked to each system, as outlined in Section 4.1, two different balancing approximations have been explored in this work to address these issues appropriately. Model reduction by *balanced truncation* will be introduced first, which is the standard approach in control theory and provides optimal reductions for stable systems. The aeroelastic system presented in Subsection 3.2.4, however, may have dominant unstable modes which will be addressed with another balancing method based on the system *normalised coprime factors*.

Balancing methods are based on the concept of *controllability* and *observability*, which provides a measure on how easily (or whether) a state is reached or observed, i.e. for given inputs and outputs how much effort is required to reach/observe a specific state of the linear system. Based on these measures a system can be reduced by truncating states that contribute little to the input-output mapping. Most states of the system, however, are observed differently than they can be reached. Hence, the underlying concept of balancing methods focuses on the projection of the linear system to balance the system states, such that they are equally controllable and observable.

Before the derivation of such balancing transformations in the next subsection, it is necessary to define a metric which indicates how close the reduced model represents the mapping of the original system. A common metric used to define the similarity between two systems is the error norm, which provides a measure of the "distance"between two systems. It will be shown in the next subsection that a balanced realisation provides *a priori* error bounds for the truncation. A more general quantity is the ν-gap metric [193], which provides a scalar measure of similarity between two systems based on the dot products of the corresponding coprime factors of both systems. The systems are identical for a zero ν-gap metric and completely dissimilar for unity.

4.2.1 Balanced Realisation and Truncation

Model reduction by balanced truncation was first discussed by Moore [125] and a detailed description is provided by Glover [72]. The concept of balancing is based on information about the past input and future output energy, which is expressed in terms of the system controllability and observability Gramians, W_c and W_o, respectively. These Gramians are used to identify a linear *balancing transformation* T that balances the stable system $\{A, B, C, D\}$, such that each balanced state is equally controllable and observable. The balanced system can then be written in terms of the transformed state coordinates $\hat{x} = T^{-1}x$ as

$$\begin{aligned} \Delta\hat{x}^{n+1} &= T^{-1}AT\Delta\hat{x}^n + T^{-1}B\Delta u^n \\ \Delta y^n &= CT\Delta\hat{x}^n + D\Delta u^n. \end{aligned} \tag{4.7}$$

To obtain an expression for the balancing transformation, T, this work will follow the standard implementation of balanced truncation in continuous time [11], even though expressions for the discrete-time counter-part exist [68]. Hence, the system will be transformed to continuous time through a bilinear transformation, as outlined in Subsection 4.1.1, prior to any model reduction. Note that this bilinear transformation preserves the system controllability and observability Gramians, which are given for stable LTI systems in continuous time by the algebraic Lyapunov equations [8],

$$\begin{aligned} AW_c - W_cA^\top + BB^\top &= 0, \\ A^\top W_o - W_oA + C^\top C &= 0. \end{aligned} \tag{4.8}$$

where the controllability Gramian, W_c, is correlated inversely to the input energy required by an actuator to reach a certain state and the observability Gramian, W_o, on the contrary, is related directly to the energy required by a sensor to observe an initial state [18].

The square root of the eigenvalues of the Gramian product, $\sqrt{\lambda_i(W_cW_o)}$, are the *Hankel singular values* (HSV) of the system denoted as [182]

$$\sigma_1 \geq \sigma_2 \geq \cdots \geq \sigma_n > 0. \tag{4.9}$$

Because the balancing transformation preserves the eigenvalues of the original system, it is a similarity transformation such that the HSV remain invariant to the transformation T. This can be seen from the definition of the balanced Gramians and their product, given as

$$\hat{W}_c = T^{-1}W_cT^{-\top}, \hat{W}_o = T^\top W_oT \quad \text{and} \quad \hat{W}_c\hat{W}_o = T^{-1}W_cW_oT. \tag{4.10}$$

The aim of balancing methods is to find a transformation T that diagonalises the Gramians such that they are equal and their diagonal entries are the HSV of the system, i.e.

$$\hat{W}_c = \hat{W}_o = \Sigma = diag\left(\sigma_1, ..., \sigma_n\right). \tag{4.11}$$

Hence, the states with the largest HSV are the ones most involved in the mapping between the system inputs and outputs and the least controllable/observable states can be truncated.

Algorithm 2 introduces the procedure to obtain such balancing transformation, T, which follows closely the *Square Root Method* presented by Laub *et al.* [103]. The Choleski factors P and Q of the Gramians in the first step are computed directly from the state-space representation of the stable system, $\{A, B, C, D\}$, using the method of Hammarling [80], without the need to evaluate W_c and W_o which is costly and ill-conditioned for large-scale systems.

Algorithm 2: Computation of the balancing transformation T.

Input: Linear system $\{A, B, C, D\}$

Output: Balancing transformation T

1. Compute Choleski factors P and Q of Gramians $W_c = PP^\top$ and $W_o = Q^\top Q$.
2. Compute singular value decomposition of matrix product $QP = U\Sigma V^\top$, where Σ are the system HSV.
3. Determine balancing transformation $T = PV\Sigma^{-1/2}$ and its inverse $T^{-1} = \Sigma^{-1/2}U^\top Q$.

The Square Root Method however can be numerically ill-conditioned for large-scale system with rapidly decaying HSV [8]. The problem of robustness can be tackled using the *Schur Method* [160], which is based on the Schur decomposition of the Gramian product W_cW_o to obtain orthonormal bases for the left and right eigenspaces of W_cW_o. Singular value decomposition of these orthonormal basis vectors provides the system HSV which can be used to obtain the balancing transformation T, as defined in step 3 of Algorithm 2.

Reduction of the balanced system, obtained from Eq. (4.7), can be achieved finally by truncating the corresponding rows and columns of the matrix T. The elimination of balanced states can be based on the HSV of each state, σ_i, which also provides an upper bound of the error between the reduced- and full-order models. The (additive) $\mathcal{H}_\infty$-norm of the difference between the two systems is defined in terms of the HSV of the truncated states as [8]

$$\|G(s) - G_r(s)\|_\infty \leq 2\left(\sigma_{k+1} + \cdots + \sigma_n\right), \tag{4.12}$$

where $G(s)$ and $G_r(s)$ are the transfer function of the full- and reduced-order systems of order n and k, respectively.

The built-in MATLAB® functions `balreal` and `modred` were used in this work to obtain the balanced realisation of the full-order system and to truncate the balanced states, respectively.

4.2.2 Balancing of Unstable Systems by Normalised Coprime Factorisation

The balanced truncation method is limited to stable systems. This is because stability is a necessary assumption in the definition of the controllability and observability Gramians using the Lyapunov equations, Eq. (4.8). To tackle this issue, Enns [57] has proposed a solution whereby the unstable system $\{A, B, C, D\}$ is divided into a stable and an unstable part and only the stable part is reduced through balanced truncation. Since this approach retains all unstable poles without reduction, it can yield unnecessarily-large reduced-order systems.

Alternatively, Meyer [120] has presented a balancing method for unstable strictly proper systems based on coprime factorisation. The idea is to represent the minimal realisation of the full system $G(s) = C(sI - A)^{-1}B$ in terms of its stable *normalised right coprime factors* (NRCF), $N_r(s)$ and $M_r(s)$, such that [191]

$$G(s) = N_r(s)M_r^{-1}(s). \tag{4.13}$$

To ensure uniqueness of the solution, the coprime factors are normalised as

$$N_r^\top(-s)N_r(s) + M_r^\top(-s)M_r(s) = I, \tag{4.14}$$

over the whole range of frequencies, s. Note that the approach is again presented in continuous time to obtain the system NRCF, which requires a bilinear transformation of the discrete-time systems, as introduced in Subsection 4.1.1. Alternative approaches in discrete time have been addressed in the literature [121], but this work will follow the standard implementation of the method, as done in the MATLAB® function `ncfmr`.

Following the approach by Meyer and Franklin [119], state feedback can be introduced to stabilise the system. This results in a modified system, $\bar{A} = A + BK$, from which we can now obtain the state-space realisations of the (stable) NRCF as

$$\begin{aligned} \bar{N}_r(s) &= C\left(sI - \bar{A}\right)^{-1} B, \\ \bar{M}_r(s) &= I + K\left(sI - \bar{A}\right)^{-1} B, \end{aligned} \tag{4.15}$$

where the state feedback gain, K, can be computed using a linear-quadratic regulator, such that $K = -B^\top P$ with P being the solution of the algebraic continuous-time Riccati equation [121]

$$PA + A^\top P - PBB^\top P + C^\top C = 0. \tag{4.16}$$

The state-space realisation of the resulting pair of *stable* transfer functions $\left(\bar{N}_r^\top(s), \bar{M}_r^\top(s)\right)^\top$ is given as

$$\left\{\bar{A}, B, \begin{pmatrix} C \\ K \end{pmatrix}, \begin{pmatrix} 0 \\ I \end{pmatrix}\right\}, \tag{4.17}$$

which can be balanced and truncated following the procedure outlined in Section 4.2.1 to obtain the stable reduced-order model $\left\{\bar{A}_{11}, B_1, \left(\begin{smallmatrix} C_1 \\ K_1 \end{smallmatrix}\right), \left(\begin{smallmatrix} 0 \\ I \end{smallmatrix}\right)\right\}$. Reversal of the state feedback and output augmentation finally leads to the reduced-order unstable model $\{A_{11}, B_1, C_1\}$ of the plant $G(s)$ [120]. Following Vidyasagar [192], the normalised coprime factorisation method can also be extended to balance *non-strictly proper* systems. This is relevant for the application of the introduced model reduction techniques to the non-strictly proper aerodynamics system, which will be addressed in the next section.

4.3 Balanced Approximation for Flexible Aircraft Dynamics

The introduced balancing-based model reduction techniques enable higher-order multidisciplinary tools to be effective in the design and optimisation of highly-efficient aircraft. This section will demonstrate the application of these reduction techniques to the aeroelastic models, where it is important to address the different numerical requirements of (a) the nonlinear flexible-aircraft dynamics model for manoeuvring vehicles and (b) the monolithic aeroelastic system in state-space form.

4.3.1 Balanced Truncation of the Linearised State-Space Aeroelastic System

The model order of the aeroelastic state-space system given by Eq. (3.19) will be tackled next to facilitate the application of this framework for effective aeroservoelasticity and optimisation. Since the aeroelastic system is ill-conditioned, as shown in 4.1.2, model reduction of the tightly-coupled framework requires a more robust approach that stabilises the system prior to any balanced truncation. This ensures that high-frequency disturbances are ignored without affecting the lower frequency spectrum which may be important to capture possibly unstable dynamics of the coupled aeroelastic system, such as flutter. The proposed reduction method is outlined in Figure 4.4 and will be described next.

In a first step, the ill-conditioned aeroelastic system is filtered to either stabilise or remove high-frequency or highly-damped modes which have negligible contribution to the system dynamics. This step enables a more efficient balanced truncation of the system without detrimental effects on accuracy. As described in Subsection 4.1.2, two methods have been explored in this work. The modification of the Newmark integration scheme in

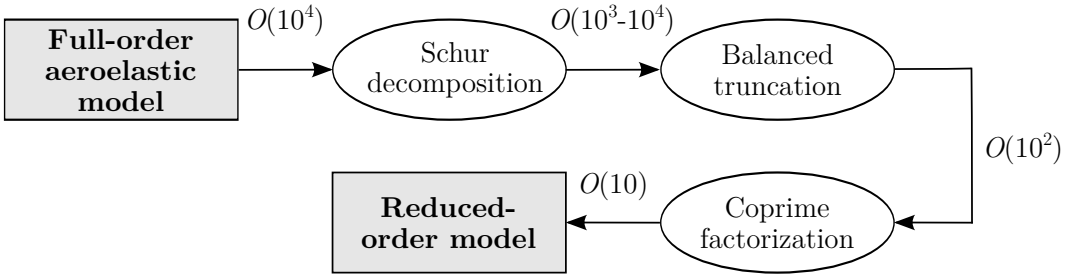


Figure 4.4: Model reduction of the aeroelastic system with model orders shown as an indication for typical problem sizes.

the discretisation of the flexible-body dynamics EoM to include positive algorithmic damping provides a very effective way to stabilise high-frequency aeroelastic modes without any significant effect on the dominant flight dynamic modes. As a second approach, Schur decomposition can also be applied to the full-order system to remove high-frequency or highly-damped modes, but it requires an additional operation which increases the computational effort of the solution process. Hence, algorithmic damping will be used throughout this work to stabilise the high-frequency modes of the aeroelastic system.

Subsequent balanced truncation significantly reduces the system size using the *a priori* error bound, Eq. (4.12), as an indication for the truncation order. Even further reduction with comparable system mismatch is achieved through subsequent truncation of the system normalised coprime factors. As introduced in Section 4.2, this approach was originally developed for unstable plants but it was found to be more effective in the reduction of the aeroelastic system with poles close to the stability boundary than the standard balanced truncation technique. The coprime factorisation approach, however, is much more computationally expensive and a combination of initial balanced truncation to the order $\mathcal{O}\left(10^2\right)$ followed by coprime factorisation of the truncated system, as indicated in Figure 4.4, was found to be a better compromise for aeroelastic applications.

4.3.2 Reduced-Order Modelling of Manoeuvring Flexible Aircraft

The dynamics of manoeuvring flexible aircraft will be modelled in this work using a top-down approach which enables higher-fidelity features, such as large deformations at trim and possible interference effects between the vehicle lifting surfaces, to be incorporated. The solution method of the coupled framework is formulated directly in time domain, as outlined in Figure 4.5, where the aerodynamic loads in the transient response are obtained from the linearised state-space description of the UVLM. Even though the possibly large manoeuvres of the flexible vehicle are captured with the nonlinear perturbation EoM of the aircraft flexible-body dynamics, (2.45), it is possible to separate the linear aerodynamic subsystem. The size of this linear system is dominated by the number of vortex panels used in the discretisation of lifting surfaces and the wake of the aircraft. Wake panels are

needed to capture the unsteady effects, but they are also an excellent target for model reduction which provides the justification for the top-down approach.

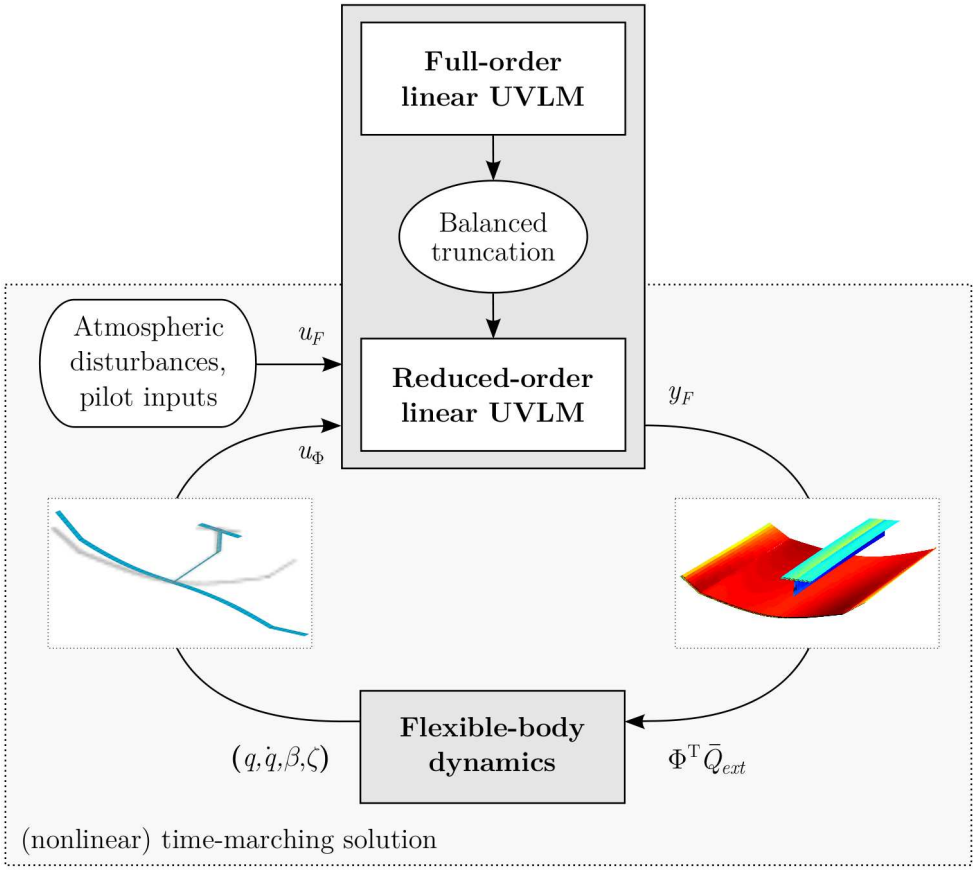


Figure 4.5: Model reduction approach for the time-marching solution of manoeuvring flexible aircraft based on the vehicle free-free vibration modes.

Unlike the aeroelastic system tackled in the previous subsection, the aerodynamic subsystem, given by Eq. (3.18), excludes the structural states and is therefore numerically well-conditioned and naturally highly-damped. Hence, the standard balanced truncation method can be applied directly to the full-order linear system of the UVLM to achieve significant model reductions without the initial stabilisation of the system.

As described in the previous chapter and shown in Figure 4.5, the inputs to the aerodynamic system account for atmospheric disturbances and pilot inputs, u_F, whereas the structural and rigid-body vehicle response given in terms of the generalised coordinates are included through u_Φ, i.e. the projection of the flexible-body DoF on the modes of the unconstrained structure. Hence, the truncation of (higher-frequency) structural modes provides additional model reduction, which (a) reduces the order of the flexible-body dynamics EoM, Eq. (2.45), and (b) significantly reduces the number of inputs and outputs of the aerodynamic system. Since balancing approximations provide optimal reductions for

a specific transmission map between the system inputs and outputs, the latter has a direct impact on the reduction potential of balanced truncation of the aerodynamic subsystem.

The resulting reduced-order aerodynamic system can capture unsteadiness effects from the (small) variations of circulation strength in the wake due to the system inputs, e.g. gusts, control surface deployment and structural deformations. Hence, the reduced-order modelling approaches presented in this section result in low-order representations of the dynamics of flexible aircraft which provide a very powerful tool for the design of highly-efficient configurations. This will be explored in the numerical studies in Chapter 6.

Chapter 5

Numerical Studies of Flexible Unconstrained Structures

The numerical studies presented in this chapter will focus on the flexible-body dynamics module in SHARP, as derived in Chapter 2. As high-aspect-ratio aircraft are likely to exhibit large deformations during normal flight operation, it is necessary to verify the coupled structural and rigid-body formulation before progressing to aeroelastic analyses of flexible-aircraft dynamics problems in the next chapter. The underlying geometrically nonlinear beam model has been validated extensively in Ref. [137] for clamped beam configurations subject to (a) static loading leading to large out-of-plane deformations and (b) dynamic excitations of the base. To verify the coupling of the structural EoM with the rigid-body dynamics equations, Section 5.1 will present studies of unconstrained multi-beam configurations subject to simultaneous geometrically nonlinear elastic deformations and large rigid-body motions comparing them to SAMCEF *Mecano*.

The geometrically nonlinear implementation of the flexible-body dynamics formulation will subsequently serve as a reference solution to explore the performance of the linearised flexible-body dynamics formulation in Section 5.2 on similar unconstrained multi-beam configurations with varying flexibility. The comparison also provides valuable insight into the effect of geometric nonlinearity on the overall motion of flexible bodies. Finally, modes are included into the problem to explore how the size of the linearised system can be reduced. Those results will also serve to evaluate the validity of the mean axes approximation, a common assumption in aeroelasticity to decouple the vehicle flight dynamics from the structural deformations. Note that there are no gravitational or aerodynamic forces acting on the structures in this chapter.

The $\mathcal{L}_2$ relative error norm defined at time t as

$$\varepsilon(t) = ||X_{com}(t) - X_{ref}(t)||/||X_{ref}(t)||, \tag{5.1}$$

will be used throughout this chapter to compare the different solution approaches, where X_{com} and X_{ref} are the computed approximate and reference solutions respectively.

5.1 Verification of the Flexible-Body Dynamics Module

As there are few results available in the literature for very flexible free-free beams, this work will first collate the existing results and will then contribute with additional relevant reference test cases. The motivation for these verification studies is to gain confidence in the geometrically nonlinear flexible-body dynamics formulation which will provide the starting point for the linearisation of the structural (and aerodynamic) DoF. Hence, the beam configuration are subjected to excessive loading leading to extreme out-of-plane elastic deformations which couple with the rigid-body motion of the bodies.

5.1.1 Flying Flexible Beam (FFB) with Large Deformations

In this section the dynamics of a flexible free-free beam undergoing large overall motion is analysed. The problem at hand was first introduced by Simo and Vu-Quoc for the planar case [177], later expanded to 3-D in Ref. [179], and has been used subsequently to validate various geometrically nonlinear flexible-body dynamics formulations [66, 89, 90, 94]. The unconstrained, inclined beam, shown in Figure 5.1, is subjected to a set of dead forces and moments acting at the origin of the body-fixed reference frame with the load history also indicated in Figure 5.1 for the planar and 3-D case. Following Refs. [177, 179], the beam is discretised using 10 2-noded elements and the simulation properties of the FFB problem are kept unitless.

The motion of the FFB for the planar case is shown in Figure 5.2 for two different time steps, where $\Delta t = 0.1$ corresponds to the original simulation properties used in Ref. [177]. However, a smaller time step of $\Delta t = 0.01$ is necessary to obtain a converged solution. Results show very good comparison with Simo and Vu-Quoc [177] for matching time steps of $\Delta t = 0.1$, but differences can be observed for the converged solution, shown as solid lines in Figure 5.2. Frequency domain analysis of the response suggests that the smaller time step of $\Delta t = 0.01$ is indeed needed to capture frequencies up to the fourth bending mode which are excited by the impulsive excitation.

In the 3-D case, the FFB is subjected to an additional dead moment $M_2(t)$ acting along the z axis, indicated in Figure 5.1, to cause out-of-plane motion. Figure 5.3 shows the resulting motion for 20 2-noded elements and a time step of $\Delta t = 0.01$ for the converged solution. Comparison with the original results published by Simo and Vu-Quoc [179] shows large discrepancies (not shown here), and the FFB in Ref. [179] appears to be much stiffer than in the results presented in Figure 5.3. (A good match with Ref. [179] was achieved for an increased stiffness of $EI_\alpha = GJ = 10^3$). Instead, for the given material properties

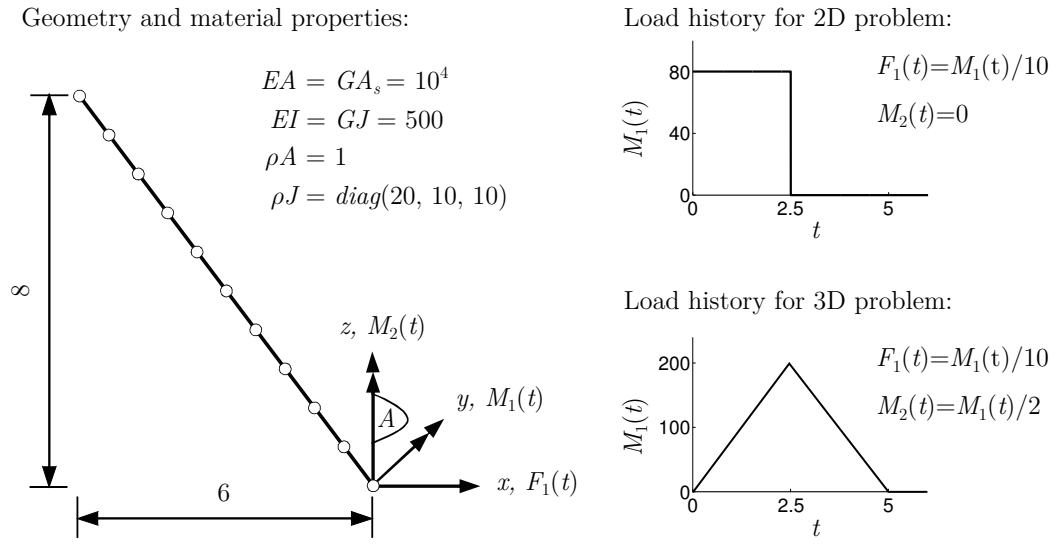


Figure 5.1: FFB geometry, material properties and load histories [177, 179].

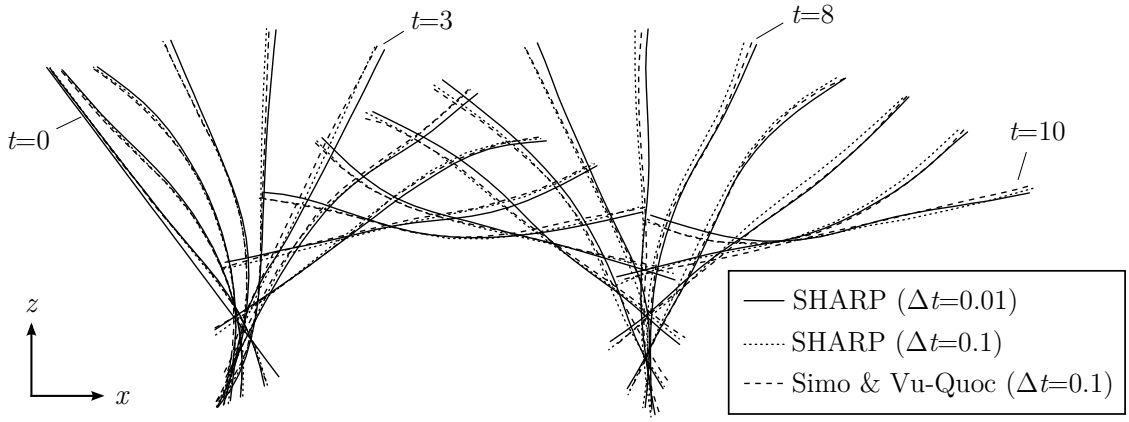
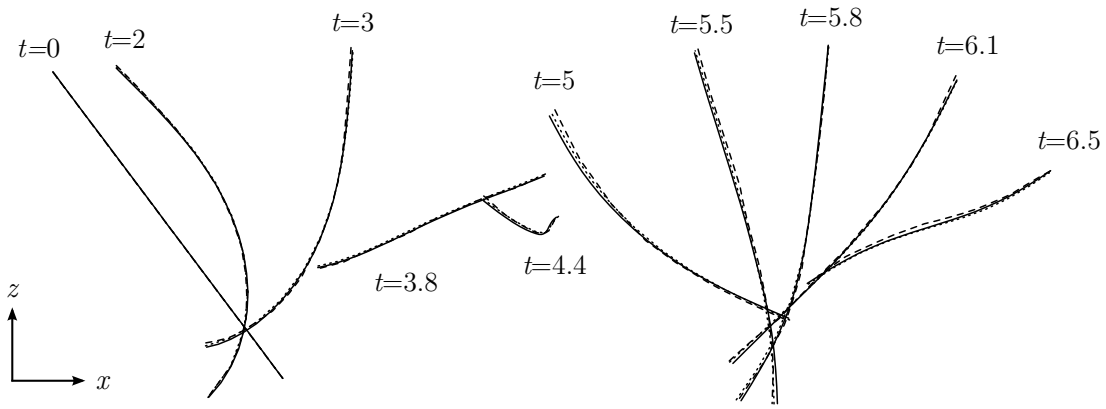


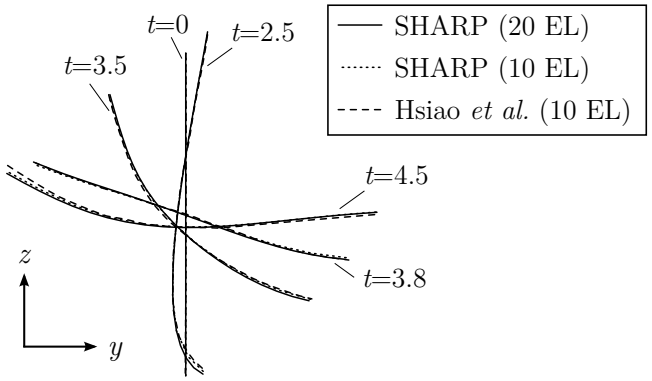
Figure 5.2: Snapshots of deformed shapes for the 2-D FFB problem in increments of 0.5 for different time steps Δt. [10 2-noded elements]

in Figure 5.1 very good comparison was found with the solution by Hsiao *et al.* [90] who also reported differences to Ref. [179]. Reference [90] used a co-rotational finite-element formulation with 10 beam elements. The comparison is shown in Figure 5.3.

Finally, since the FFB is subject to spatially-fixed forces and moments, the motion of the beam centre of mass (CM) becomes a rigid-body dynamics problem which can be solved analytically. A convergence study on the $\mathcal{L}_2$ relative error norm of CM positions, demonstrated that a time step of $\Delta t = 0.01$ gives an error below 1% up to $t = 50$. The motion of the FFB for that time step is shown in Figure 5.4 which indicates a CM moving along the x direction only.



(a) x-z plane



(b) y-z plane

Figure 5.3: Snapshots of deformed shapes for the 3-D FFB problem with different number of elements. [$\Delta t = 0.01$]

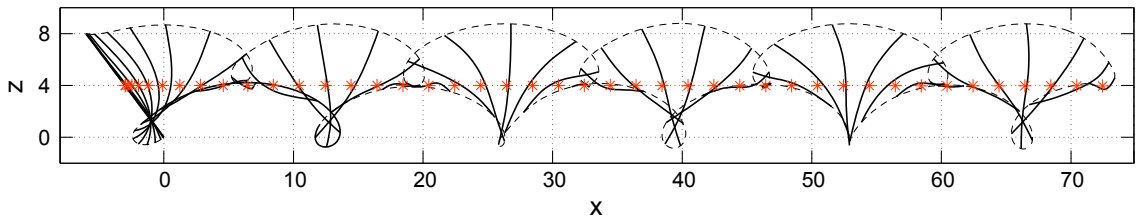


Figure 5.4: Snapshots of 3-D FFB problem in increments of 0.4 in x-z plane (solid lines) with positions of both tips (dashed lines) and centre of mass (stars). [$\Delta t = 0.01$ and 20 2-noded elements]

5.1.2 Dynamic Response of a Flexible Multi-Beam (FMB) Configuration

The dynamic response of an unsupported frame is analysed next to verify the geometrically nonlinear flexible-body dynamics formulation on a multi-beam configuration. This problem will also be used in Section 5.2 to exemplify the consistent structural linearisation and to study the application of the mean axes approximation. The geometry and material properties of the FMB are presented in Figure 5.5 with different load cases defined in Ta-

ble 5.1. The chosen configuration results in a multi-beam problem with shared nodes and large initial rotations. To obtain an acceptable interpolation of the rotation vector, 120 2-noded elements were used. Alternatively, quadratic elements can be used for improved convergence, as shown in Ref. [181]. All simulations in this section are for a time step of $\Delta t = 0.01$ s. The Newmark integration scheme was modified as described in Section 2.4 to include a numerical damping of 0.01 that filters high-frequency oscillations.

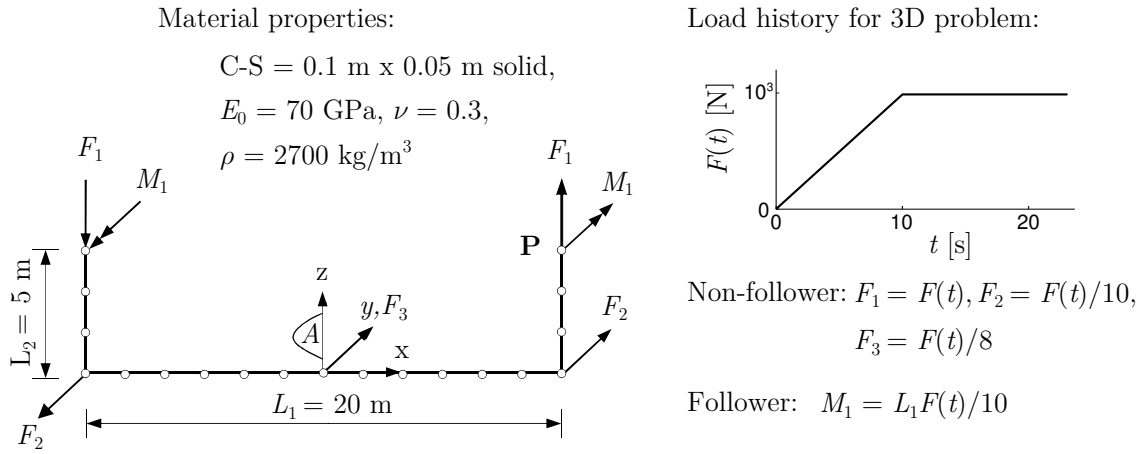


Figure 5.5: Definition of the FMB problem.

Table 5.1: Load cases for the FMB problem.

Load case	F_1	F_2	F_3	M_1
1	x	x	x	x
2	x	x		

SAMCEF *Mecano* is also used for comparison of results in this numerical study. It is a finite-element solver for nonlinear flexible multi-body dynamics problems based on the formulation by Géradin and Cardona [69]. A variety of forces and moments, load case 1 in Table 5.1, is applied here to verify the results in terms of 3-D geometrically nonlinear deformations with nonlinear rigid-body motions subject to Coriolis and centrifugal effects which augment the coupling between structural and rigid-body dynamics.

The response of the FMB is shown in Figures 5.6 and 5.7 for a time step of $\Delta t = 0.01$ s. First, the sequence of motion in Figure 5.6 clearly shows that the structure is subject to large deformations. The simultaneous rigid-body translations and rotations increase the effect of gyroscopic forces on structural and rigid-body dynamics. Comparison of tip

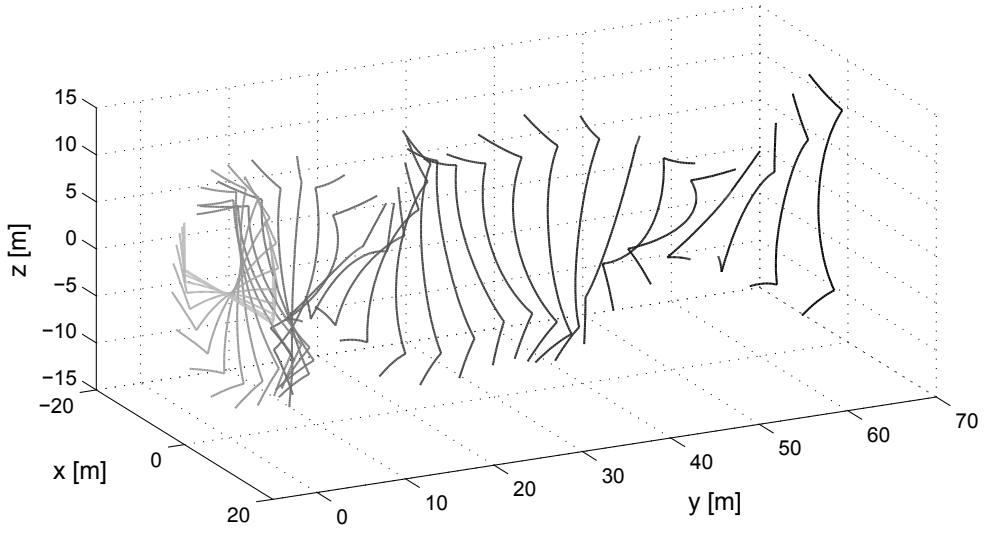
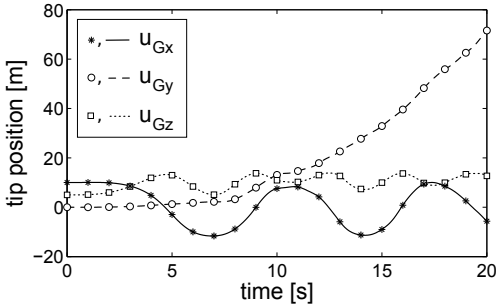
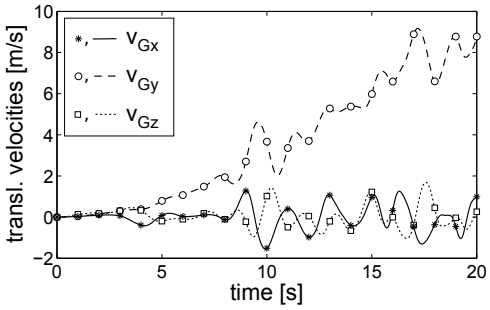


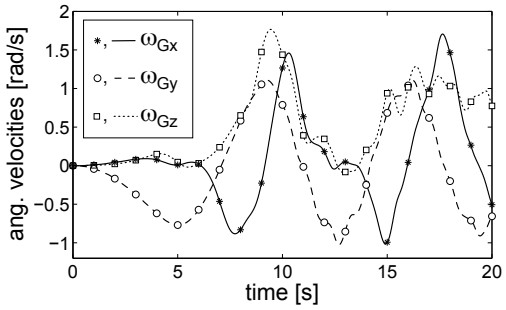
Figure 5.6: Snapshots of deformed shapes for the FMB, load case 1, obtained with SHARP at consecutive steps from $t = 0$ s (grey) to $t = 20$ s (black) in increments of 0.5 s.



(a) Inertial positions of point P, u_G.



(b) Translational rigid-body velocity, v_G.



(c) Angular rigid-body velocity, ω_G.

Figure 5.7: Comparison of FMB, load case 1, in SHARP (curves) with SAMCEF *Mecano* (markers).

positions and rigid-body velocities in Figure 5.7 show very good agreement with results obtained in SAMCEF. All properties in Figure 5.7 are expressed in terms of an inertial frame, G, which is initially aligned with frame A in Figure 5.5.

The verification studies presented in this section assure the correct implementation of the flexible-body dynamics module to capture the coupling between the possibly large structural and rigid-body response. This geometrically nonlinear formulation will now be the starting point to further explore the consistent linearisation of the elastic DoF for the FMB problem.

5.2 Structural Linearisation in the Flexible-Body Dynamics of the FMB Configuration

Test case FMB is now subjected to load case 2 in Table 5.1, which results in predominantly rotational 3-D rigid-body motion to exercise the linearised formulation derived in Section 2.2. A stiffness parameter, σ, is introduced to vary the elastic modulus of the material, such that $E = \sigma E_0$ with E_0 as defined in Figure 5.5. The translational and angular velocities of the body fixed frame, A, is presented in Figure 5.8 for $\sigma = 10$. Figure 5.9(a) shows the time history of the vertical tip deformation of point P, normalised with the arm length L_2, both defined in Figure 5.5, for varying stiffness. The maximum value of the strain measure, $\Delta R_{Az}/L_2$, is used to quantify the degree of flexibility and Figure 5.9(b) shows the maximum values for the range of $3 \leq \sigma \leq 10^3$.

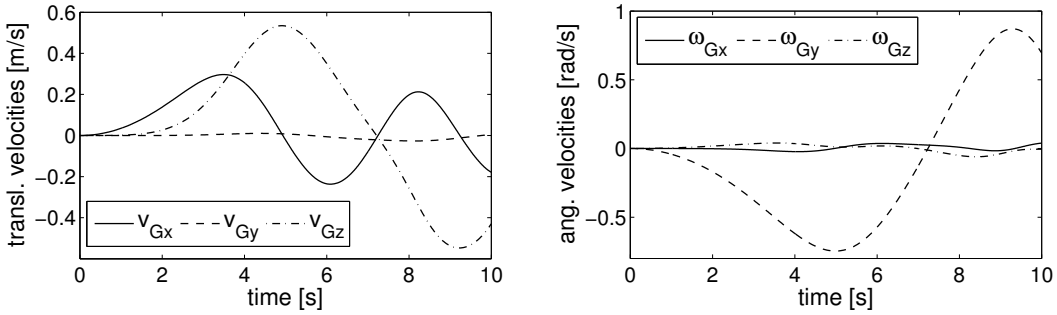
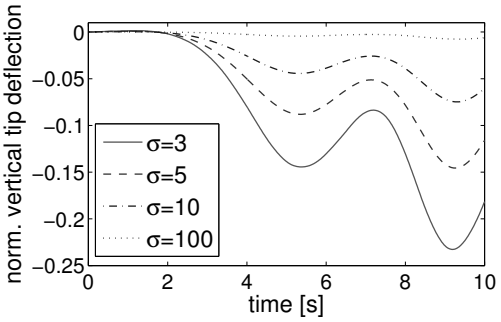
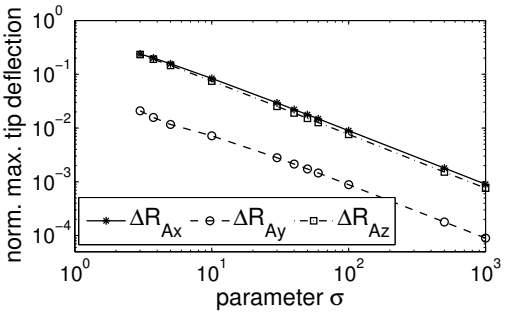


Figure 5.8: Rigid-body velocities of the FMB for load case 2. [$\sigma = 10$].

Figure 5.10 presents the maximum relative error norm of rigid-body velocities and tip deflection comparing the linearised and fully-nonlinear solutions for a range of σ values. The solid curves show that for very flexible cases with $\sigma < 10$ and relative maximum tip displacements of $10 - 25\%$ the dynamic response is nonlinear and cannot be captured by the linearised formulation with relative errors above 10%. However, the error decreases exponentially with increasing values of $\sigma \geq 10$. The effect of nonlinearity on the elastic deformations for this problem will be presented in detail in Section 5.2.2. The relative



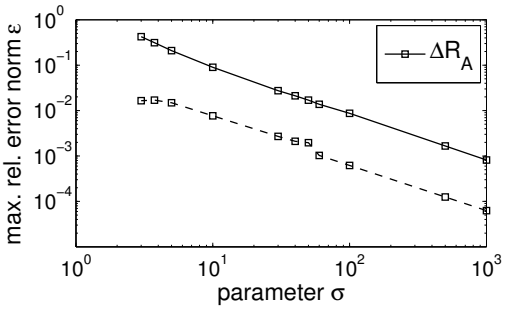
(a) Vertical displacement of point P, $\Delta R_{Az}/L_2$.



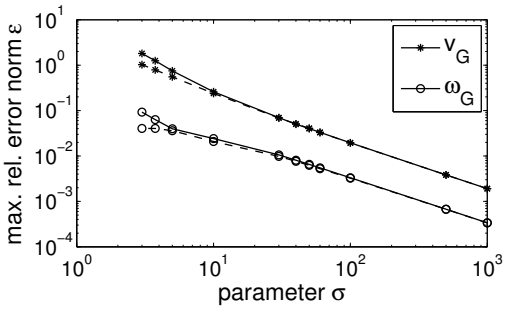
(b) Maximum tip deflection, $\max(\Delta R_A/L_2)$.

Figure 5.9: Tip deformations of FMB, load case 2, for varying stiffness parameter σ.

error of the rigid-body velocities, presented in Figure 5.10(b), shows that the relative error norm of the translational rigid-body velocities remains an order of magnitude higher than for the angular velocities. As the linearised solution assumes constant CM position with respect to frame A, the error in the angular velocities is compounded.



(a) Right tip displacement, $\Delta R_A/L_2$.



(b) Rigid-body velocities, v_G and ω_G.

Figure 5.10: Linearisation of elastic DoF for FMB with load case 2. Maximum relative error norm of linearised formulation (solid) and simplified nonlinear solution with constant mass matrix $\mathcal{M} = \mathcal{M}(\eta_0)$ (dashed) for different σ.

It is often assumed in dynamics that the mass matrix of the governing EoM is constant for small deformations [199]. Based on the fully-nonlinear formulation it is possible to analyse the different effects of geometric nonlinearities by "freezing" the mass matrix $\mathcal{M}(\eta_0)$ in Eq. (2.23) but keeping all other terms in the equation time-dependent. Figure 5.10 shows, superimposed with dashed curves, the relative error norm of this simplified-nonlinear formulation with respect to the fully-nonlinear solution. It suggests that for the analysed FMB problem within the linear-flexible regime ($\sigma \geq 10$), the error in the rigid-body response is predominantly affected by assuming constant mass matrix $\mathcal{M}$. Only for very large deformations ($\sigma < 10$), it is possible to distinguish between the linearised and simplified-nonlinear error norms in Figure 5.10(b). This is clearly not the case when predicting the

tip deflection, ΔR_A, shown in Figure 5.10(a), where linearisation of the elastic forces in addition to inertial forces has a detrimental effect.

In summary, this section demonstrated the applicability of the implemented linearised formulation to stiff multi-beam configurations subject to small deformations and large rigid-body motions. Different sources of nonlinearity were identified to have an effect on the dynamics of flexible bodies, where it was shown that changes in the global inertia tensor can have a strong effect on the rigid-body response of the structure.

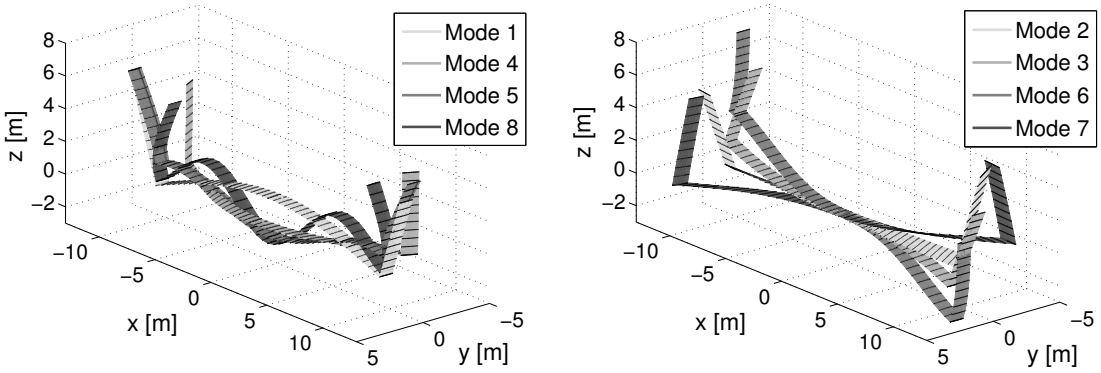
5.2.1 Modal Reduction of the FMB Configuration

Next, projection of the flexible-body dynamics equations with linearised elastic DoF on modes is explored. This is the application of the theory presented in Section 2.3, which forms the basis for the subsequent evaluation of the mean axes approximation. The problem at hand is the FMB with load case 2 and stiffness parameter $\sigma = 10$ resulting in maximum relative tip deflections of 8%, as shown in Figure 5.9. For this case the linearised solution proved to adequately predict angular rigid-body velocities and tip displacements with maximum relative errors of 2.4% and 9.0%, respectively, as shown in Figure 5.10.

Table 5.2: First elastic modes for the FMB problem. [$\sigma = 10$]

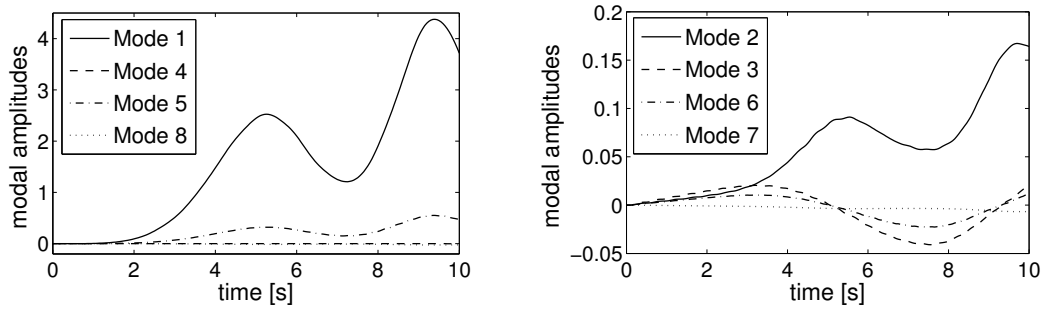
Mode	ω [rad/s]	Description
1	6.92	1st symmetric in-plane bending
2	15.32	1st torsion
3	16.37	1st antisymmetric in-plane bending
4	21.58	1st symmetric out-of-plane bending
5	23.13	2nd symmetric in-plane bending
6	40.23	2nd antisymmetric in-plane bending
7	61.46	2nd torsion
8	67.91	3rd symmetric in-plane bending

Vibration modes are obtained for the unconstrained structure at the initial configuration by solving the eigenvalue problem posed by the unforced fully-linearised EoM, Eq. (2.41). This results in n elastic free-free modes and 6 rigid-body modes, where n is the number of elastic DoF of the problem (here: $n = 6 \cdot 120$). Table 5.2 presents the first eight elastic modes characterised by their symmetry properties and the mode shapes shown in Figure 5.11. It is important to note that the CM position of these vibration modes remains constant.



(a) Symmetric modes (b) Antisymmetric modes

Figure 5.11: First elastic mode shapes for the FMB problem. [$\sigma = 10$]



(a) Symmetric modes (b) Antisymmetric modes

Figure 5.12: Response of the first eight elastic modes for FMB, load case 2. [$\sigma = 10$]

The dynamic problem is subsequently solved by projecting the linearised dynamics, Eq. (2.37), to modal coordinates. From the modal response of the FMB problem subject to load case 2 shown in Figure 5.12, it is clear that the dominant modes in the response are the first symmetric in-plane bending mode (Mode 1) and the first out-of-plane modes in torsion (Mode 2) and bending (Mode 4). This can also be seen in Figure 5.13, which compares the rigid-body response and elastic deformations of the projected solution with linearised results for varying number of elastic modes. The results demonstrate that we can reduce the system size from 366 DoF to 16 modes (10 elastic modes and the six rigid-body modes) with a relative error below 1%. The system size can be further reduced by only including modes in the projection that are dominant in the prediction of the response. However, since the loading is not know in general, it is better to truncate the system on the basis of frequency. Figure 5.13 also shows the effect of flexibility on the rigid-body response of the structure for zero elastic modes resulting in maximum relative errors above 10%.

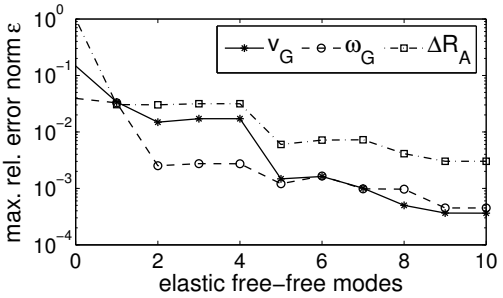


Figure 5.13: Modal projection of linearised EoM for the FMB, load case 2. Maximum relative error norm of rigid-body velocities and right tip displacement against number of elastic modes. [$\sigma = 10$]

Because of the linear and quadratic dependencies of the modal damping and stiffness matrices, $\Phi_{ij}\bar{\mathcal{C}}_{jk}\Phi_{kl}$ and $\Phi_{ij}\bar{\mathcal{K}}_{jk}\Phi_{kl}$ in Eq. (2.45), with the rigid-body velocities, β, the system matrices are written in terms of the constant third and fourth-order tensors, c_{ilr} and k_{ilrs}, defined in Eq. (2.46). Computing these tensors only once increases computational efficiency because of their sparse structure. This is illustrated in Table 5.3 for the third-order damping tensor, c_{ilr}, which explores the coupling terms of c_{ilr} for the FMB problem, isolating the effect of elastic and rigid-body velocities on the elastic state, c_r^{SS} and c_r^{SR}, respectively, and the effect on the rigid-body gyroscopic forces due to elastic excitations, c_r^{RS}. The remaining terms, c_r^{RR}, originate from the gyroscopic terms of the standard nonlinear rigid-body dynamics part of the structure and are not of interest here. Table 5.3 shows the coupling terms of c_{ilr} for the first 9 modes (3 elastic and 6 rigid-body) with

$$
\begin{aligned}
c_r^{SS} &= \{c_{ilr} | (i = 7..9) \wedge (l = 7..9)\},\\
c_r^{SR} &= \{c_{ilr} | (i = 7..9) \wedge (l = 1..6)\},\\
c_r^{RS} &= \{c_{ilr} | (i = 1..6) \wedge (l = 7..9)\},
\end{aligned}
$$

where modes 1-6 are rigid-body modes and 7-9 the remaining elastic modes, which are ordered such that the lower frequencies occur first (e.g. first bending mode for $i, l = 7$). Non-zero entries are shaded in Table 5.3 to (a) highlight the sparse structure of the tensor and (b) demonstrate the contribution of the coupling terms between elastic modes and rigid-body motion on the gyroscopic forces. The latter is mostly affected by rigid-body rotary motion ($r = \{4, 5, 6\}$) as expected from the physical origin of the gyroscopic terms.

Table 5.3: Perturbed modal damping matrix in tensor form, c_{ilr}, for the FMB problem using the first three elastic modes in addition to the six rigid-body modes. Entries have been rounded to full integers. [$\sigma = 10$].

r	c_r^{SS}			c_r^{SR}						$\left(c_r^{RS}\right)^\top$					
	0.	0.	1.	0.	0.	0.	-1.	0.	0.	0.	0.	0.	0.	0.	0.
1	0.	0.	0.	0.	0.	0.	0.	0.	0.	0.	0.	0.	0.	0.	0.
	0.	0.	0.	0.	0.	0.	0.	0.	0.	0.	0.	0.	0.	0.	0.
	0.	0.	0.	0.	0.	0.	0.	0.	0.	-1.	0.	0.	0.	0.	0.
2	0.	0.	3.	0.	0.	0.	-1.	0.	0.	0.	0.	0.	0.	0.	0.
	0.	0.	0.	0.	0.	0.	0.	0.	0.	0.	0.	0.	0.	0.	0.
	0.	0.	0.	0.	0.	0.	0.	0.	0.	0.	0.	0.	0.	0.	0.
3	0.	-1.	0.	1	-1.	-1.	0.	0.	1.	0.	0.	0.	0.	0.	0.
	0.	0.	0.	0.	0.	0.	0.	0.	0.	0.	0.	0.	0.	0.	0.
	0.	0.	0.	0.	0.	0.	0.	0.	0.	2.	0.	0.	0.	0.	0.
4	0.	0.	-5.	0.	0.	0.	2.	0.	0.	0.	0.	0.	2.	0.	0.
	0.	1.	0.	0.	0.	0.	0.	0.	0.	-3.	2.	2.	0.	0.	-3.
	0.	0.	-2.	0	0.	0.	1.	4.	0.	0.	0.	0.	-1.	2.	0.
5	0.	0.	0.	-5	-1.	3.	0.	0.	1.	5.	-1.	4.	0.	0.	-1.
	3.	0.	0.	0.	-1.	0.	0.	0.	0.	0.	-1.	0.	0.	0.	0.
	0.	-3.	0.	-1.	1.	1.	0.	0.	0.	1.	-1.	-1.	0.	0.	2.
6	-8.	0.	0.	0.	5.	3.	0.	0.	0.	0.	0	0.	0.	0.	0.
	0.	0.	0.	0.	1.	1.	0.	0.	-1.	7.	-2.	6.	0.	0.	-1.

5.2.2 Assessment of the Mean-Axes Approximation on the FMB Configuration

The previous sections demonstrated a procedure for the consistent linearisation of the elastic DoF and subsequent projection onto modes from a reference condition. This was done under the assumption of small deformations but with large (nonlinear) rigid-body motion. However, due to the contribution of the gyroscopic forces to tangent damping and stiffness matrices in Eq. (2.34), the projected EoM still have coupling terms between the rigid-body and structural dynamics of the body. These coupling terms are often neglected for small elastic deformations by writing the EoM at the CM in terms of the mean axes system, which is defined such that translational and angular momenta due to elastic deformations have zero contribution to the kinetic energy [122].

The mean axes approximation is naturally enforced by projecting the linear EoM onto *free-free* modes [162]. Here, we obtain the free-free modes in the inertial frame by solving the eigenvalue problem given by the unconstrained, undamped elastic EoM as, $\mathcal{M}^{SS}\ddot{\eta}^f +$

$\mathcal{K}^S_{stif}\eta^f = 0$, where η^f is the vector of elastic DoF without enforcing a constrained node at the origin of frame A. The corresponding stiffness matrix, $\mathcal{K}^S_{stif}$, is obtained through linearisation of the elastic forces, Q^S_{stif}. The relative displacements of the flexible body can then be described in terms of mode shapes, Φ^f, and generalised displacements, p^f, such that $\eta^f = \sum_i \Phi^f_i p^f_i$. Due to orthogonality of the free-free modes and if we neglect the contribution of elastic deformations to the gyroscopic forces in Eq. (2.23), it is possible to solve the mean-axes EoM,

$$\ddot{p}^f_i + \omega_i^2 p^f_i = \left(\Phi^f_i\right)^\top Q^f_{ext}\left(\bar{\eta}, \beta, \zeta\right), \tag{5.2}$$

separately from the nonlinear rigid-body dynamics EoM, extracted from Eq. (2.23), as

$$\mathcal{M}^{RR}\left(\eta\right)\dot{\beta} + Q^R_{gyr}\left(\eta, \beta\right) = Q^R_{ext}\left(\bar{\eta}, \beta, \zeta\right), \tag{5.3}$$

where ω_i is the vibration frequency of the i^{th} mode and $\mathcal{M}^{RR}$ the mass matrix of the rigid body at the CM and principal axes. Neglecting some gyroscopic terms in the damping matrix is a necessary assumption to diagonalise all modal system matrices. Note that the resulting set of EoM can still be coupled if the external forces, Q_{ext}, such as aerodynamic loads, not only depend on rigid-body velocities, β, and orientation, ζ, of the aircraft, but also on the instantaneous geometry due to deformation of the lifting surfaces, $\bar{\eta}$.

The effect of inertial decoupling between the elastic and rigid-body motion is analysed in this section first for the FMB problem with load case 2 for the range of stiffness parameters $10 \leq \sigma \leq 10^3$, as defined in Figure 5.5 and Table 5.1. For this range of parameters the linearised solution provides adequate solutions, as shown in Figure 5.10. In the second study the mean axes approximation is investigated on a more complex problem, where the FMB enters a spiral motion to investigate the effect of simultaneous translational and angular rigid-body motion. For both problems, the decoupled mean axes solution is compared to the linearised and fully-nonlinear solutions, to isolate the effect of neglecting the gyroscopic coupling terms on the vehicle elastic and rigid-body response. Note that sufficient modes were included in the mean axes solutions to reach convergence.

FMB in Rotation (load case 2)

For the FMB with load case 2, Figure 5.14 shows the relative error norm of the mean axes approximation in predicting the rigid-body response and tip deflection at point P for a range of σ values. To be able to compare to the mean axes solution, the rigid-body motion is computed in this problem at the CM of the initially undeformed geometry. Hence, only angular velocities are included in Figure 5.14. The results indicate that for small deformations ($\sigma > 30$ and relative tip deflections below 2%), the mean axes model predicts the rigid-body response of this problem with relative errors below 5%. However, it is obvious from the figure that neglecting the coupling terms results in a constant error

of about 17% for the elastic displacements over the same range of stiffness parameters. Note that root bending moments are proportional to these.

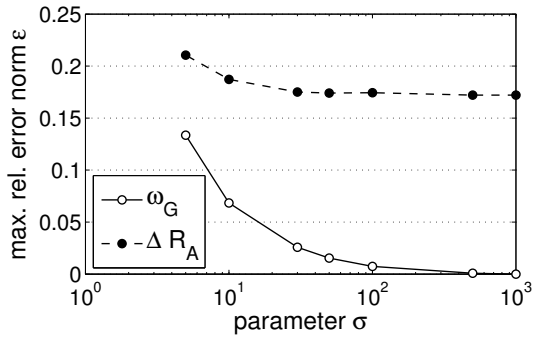
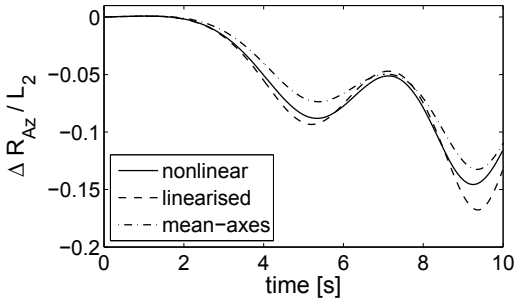


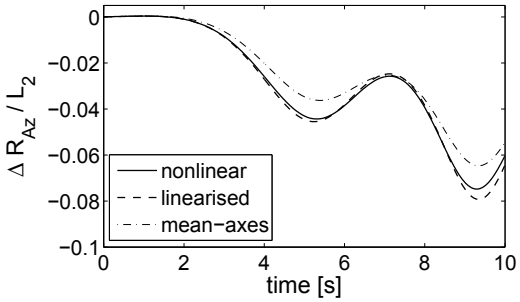
Figure 5.14: Maximum relative error norm of rigid-body angular velocities and right tip displacement of mean axes solution for the FMB, load case 2, compared to linearised for different values of σ. [$\Delta t = 0.01$ s and 120 2-noded elements]

To understand this effect, Figure 5.15 shows the normalised right tip deflections for a range of stiffness values to compare the fully-nonlinear (Eq. (2.23)), linearised (Eq. (2.37)) and mean axes solutions (Eq. (5.2)). Note that the elastic deformations are normalised as before with the arm length of the frame, L_2, to obtain a relative measure. The linearised formulation cannot capture the hardening effect due to large deformations which results in over-predicting the elastic response for the flexible configurations ($\sigma \leq 10$). However, it is clear that application of the mean axes approximation results in smaller deflections independent of the material stiffness, which happens to match the nonlinear solution closer for the very flexible case ($\sigma = 5$).

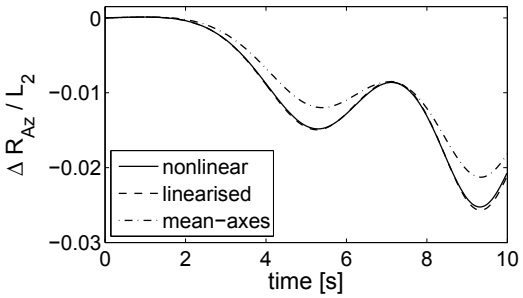
Under the mean axes approximation, the gyroscopic terms in the structural dynamics EoM, defined in Eqs. (2.33)-(2.34), are neglected. For large values of σ, the rigid-body dynamics of the structure do not change with increasing stiffness, which implies that the gyroscopic damping and stiffness matrices, $\bar{\mathcal{C}}^{SS}$, $\bar{\mathcal{C}}^{SR}$ and $\bar{\mathcal{K}}^{S}_{gyr}$, are independent of σ as $\sigma \to \infty$. Whereas the phase difference in the elastic response between the mean-axes and nonlinear solutions is evident for small values of σ, for stiff problems ($\sigma \geq 30$) the maximum relative error norm occurs at the $t = 9.35$ s, which explains why the relative contribution of the gyroscopic forces to the structural dynamics remains constant with σ, as previously identified in Figure 5.14.



(a) $\sigma = 5$



(b) $\sigma = 10$

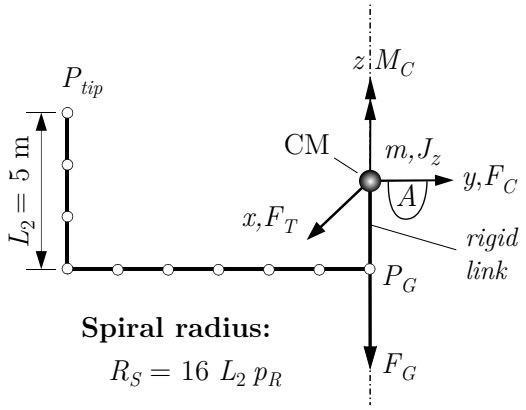


(c) $\sigma = 30$

Figure 5.15: Comparison of fully-nonlinear, linearised and mean-axes approaches in predicting the vertical tip displacement of point P in Figure 5.5 for the FMB problem with load case 2 and different σ values.

FMB in Spiral Motion

In the final study of this section, the FMB is loaded to enter a spiral motion to investigate the effect of geometric nonlinearity and inertial decoupling in the presence of large gyroscopic forces. The geometry and material properties of the FMB remain as defined in Figure 5.5, and a set of follower forces and moments is now acting at the CM of the initially undeformed geometry, which is rigidly-linked to the frame at point P_G as shown in Figure 5.16. Note that x-z is a plane of symmetry for the model. This implies that, under deformations of the structure, the point of application of the load may not remain at the CM. The follower loading is applied as a ramp with time t such that the FMB follows a circular trajectory with radius R_S. The parameter p_R is introduced in this study to vary the radius of the trajectory which is prescribed by the tangential and centripetal forces, F_T and F_C, respectively, and the moment M_C. The total mass of the frame is m and J_z is the (constant) moment of inertia around the z axis at the reference configuration. An additional dead load is applied at an offset at point P_G, shown in Figure 5.16, to stabilise the structure, as the FMB tends to diverge from the spiral path under deformation. The stiffness parameter σ is used again in this problem to vary the stiffness of the structure. A mesh size of 60 2-noded elements and a time step of $\Delta t = 0.1$ s was found to be sufficient to capture the main dynamics of the problem, which was simulated for 80 s.



Follower loads:

$$F_T(t) = 5\ \text{N/s} \cdot t$$
$$M_C(t) = J_z F_T(t)/(16\ mL_2 p_R)$$
$$F_C(t) = mv_{Ay}(t)^2/(16\ L_2 p_R)$$

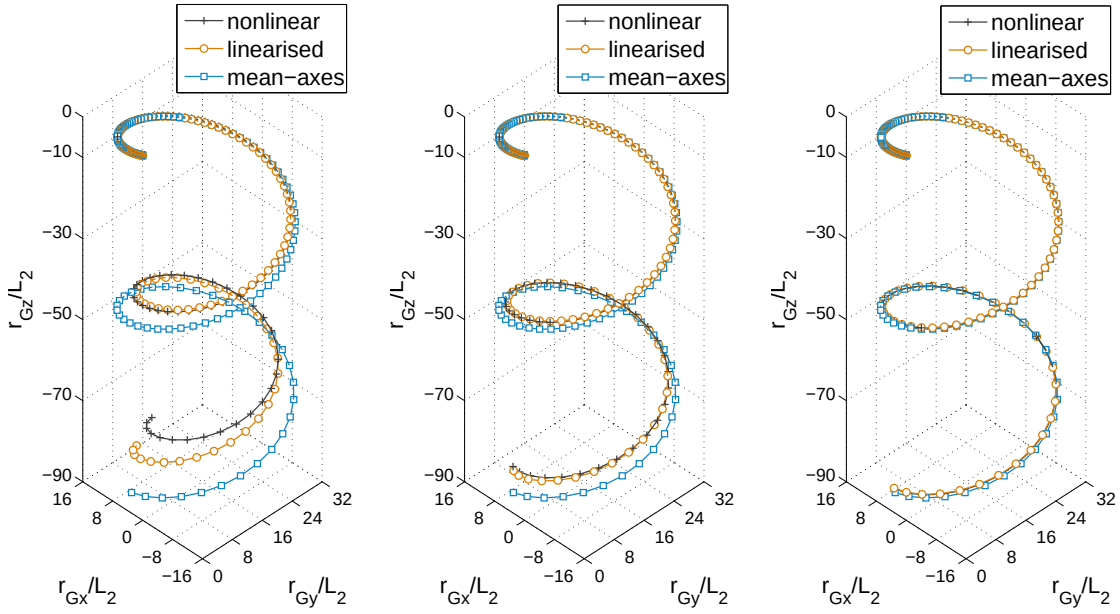
Dead loads:

$$F_G(t) = 2\ \text{N/s} \cdot t$$

Figure 5.16: Load history of the FMB spiral problem.

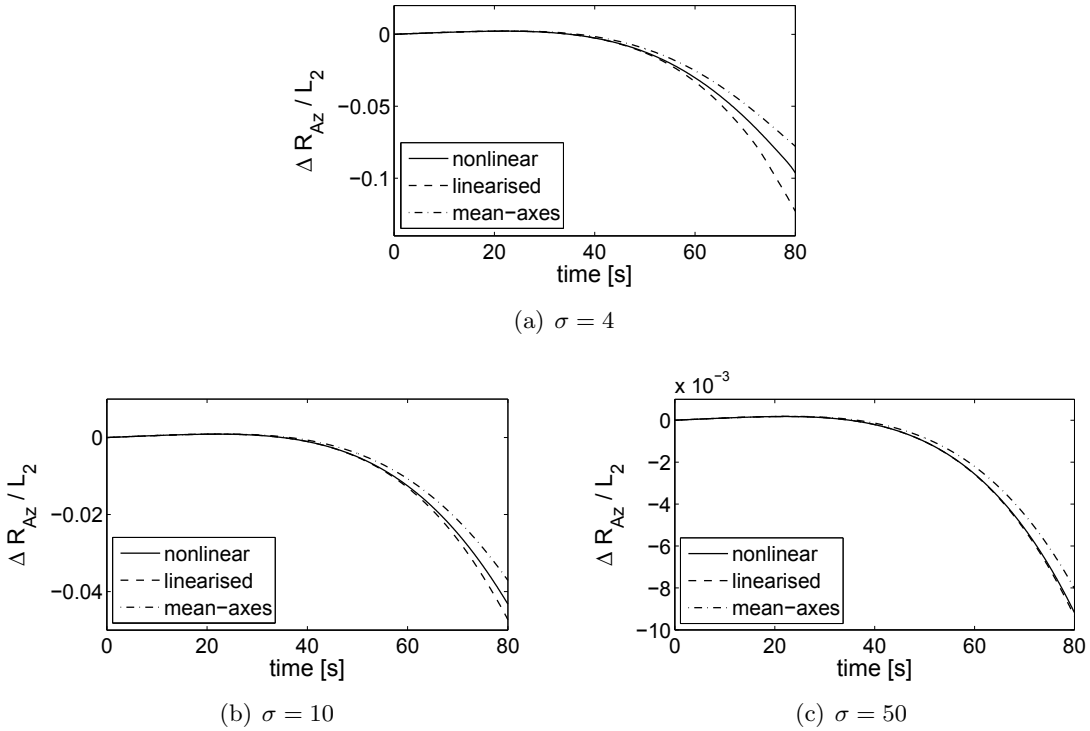
The first part of the study will analyse the effect of inertial decoupling for a fixed radius of $R_S = 80$ m, i.e. $p_R = 1$, and varying stiffness. In the second part the radius will be varied for a single stiff configuration to isolate the effect of varying gyroscopic forces on the mean axes approximation. Starting with $p_R = 1$, the overall motion of the CM is shown in Figure 5.17 for a range of stiffness parameters σ with the corresponding vertical tip deflections presented in Figure 5.18. The effect of large deformations on the rigid-body motion is captured in Figure 5.17(a), which shows large discrepancies between the linearised and fully-nonlinear solution for the very flexible case ($\sigma = 4$). With increasing values of σ both solutions converge, such that for $\sigma \geq 10$ the linearised formulation can accurately capture the very large and nonlinear rigid-body motion of the structure accurately with relative errors below 3.2%. However, the overall motion is still affected by the (small) elastic deformations. This is shown by including the trajectory of the rigid structure in Figure 5.17 to identify possible values of σ where the mean axes approximation can be applied. It can be seen that the spiral motion of the FMB converges to the rigid case for $\sigma \geq 50$ with relative errors below 1%.

Figure 5.18 shows the elastic deformations of the FMB comparing the fully-nonlinear solution with the linearised formulation and the mean-axes approximation. As expected, the linearised formulation tends to over-predict the structural deformations in the very flexible case with $\sigma = 4$, where geometric nonlinearity effects are dominant. However, the elastic response is becoming linear with increasing stiffness of the structure. Neglecting the nonlinear gyroscopic forcing terms in the mean-axes approximation counteracts this over-prediction and again happens to match the nonlinear solution more accurately for the flexible range ($\sigma < 10$), even though the rigid-body response is still largely affected by the elastic deformations in this range, as shown in Figure 5.17(a).



(a) $\sigma = 4$ (b) $\sigma = 10$ (c) $\sigma = 50$

Figure 5.17: Trajectory of the FMB spiral problem for the different formulations.



(a) $\sigma = 4$

(b) $\sigma = 10$ (c) $\sigma = 50$

Figure 5.18: Comparison of fully-nonlinear, linearised and mean-axes approaches in predicting the vertical tip displacement of point P_{tip} for the FMB spiral problem and different σ values.

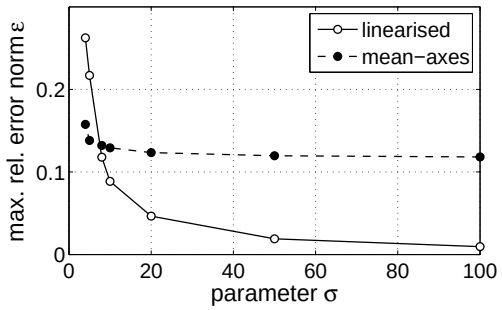


Figure 5.19: Relative error norms of maximum tip displacements of Point P_{tip} for FMB spiral problem comparing linearised and mean-axes approximations to the fully-nonlinear solution.

The same can be observed in Figure 5.19, which shows the relative error norm of linearised and mean-axes approximations compared to the fully-nonlinear solution in predicting the maximum tip displacement, $\max(\Delta R_A)$, at point P_{tip} for a range of σ values. The mean-axes approximation neglects the couplings and under-predicts elastic deformations, which results in smaller errors compared to the linearised solution for very flexible cases ($\sigma < 8$). However, this result is problem-specific and for stiff cases ($\sigma > 20$), the relative error norm of the mean-axes assumption converges to a constant value of about 12%. As before, when $\sigma \to \infty$, the relative contribution of the elastic gyroscopic forces to the structural dynamics is independent of σ resulting in constant relative errors in the displacements.

To complete the analysis, the last part of this section will investigate the effect of the vehicle kinematics (characterised by radius parameter p_R) on the error given by the mean-axes approximation. This will be done for the very stiff configuration with $\sigma = 50$ which exhibited maximum tip displacements below 1% for $p_R = 1$ but resulted in 12% error using the mean-axes approximations (compare Figure 5.18). The trajectory of the CM is shown in Figure 5.20 for four different load cases. For this very stiff problem the prescribed forces result in zero angular velocity components around x and y axes and the maximum ω_{Gz} component at $t = 80$ s is inversely proportional to p_R.

The centrifugal forces result in predominantly antisymmetric in-plane bending of the frame, where the comparison between the different solution methods in Figure 5.18(c) demonstrated that the elastic response remains linear for this very stiff problem and that application of the mean-axes approximation results in smaller deflections for $p_r = 1$. As expected, for larger radii the mean-axes solution converges to the nonlinear response and hence smaller angular velocities, as shown in Figure 5.21 for $p_R = 5$. This behaviour is demonstrated in detail in Figure 5.22 which shows the correlation between the maximum relative error norm of the right tip deflection and its components with the radius parameter p_R. The error in in-plane bending (R_{Ay} and R_{Az}) contributes the most to the overall

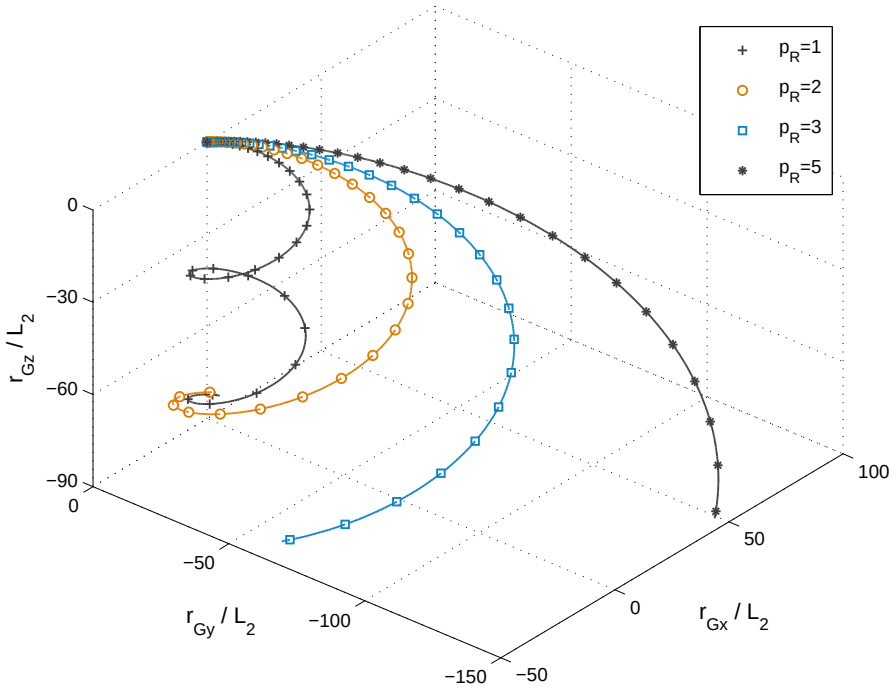


Figure 5.20: Trajectory of the A frame for the FMB spiral problem with $\sigma = 50$ and different p_R using the fully nonlinear model. Displacement in the z-direction is the same for all cases and markers are plotted every 20 time steps.

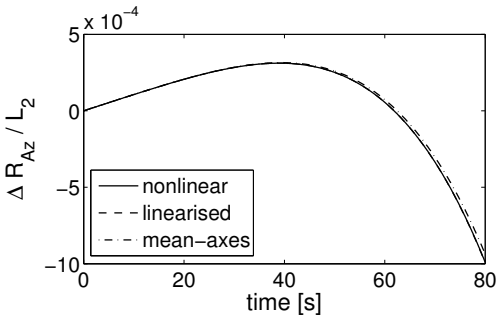


Figure 5.21: Comparison of fully-nonlinear, linearised and mean-axes approaches in predicting the normalised vertical displacement of point P_{tip} for the FMB spiral problem with $\sigma = 50$.

relative error norm. It is evident that there is a direct correlation between the angular velocity ω_{Gz}, which is inversely proportional to the radius parameter p_R, and the relative error of the mean-axes approximation in predicting the elastic response. The contribution of the gyroscopic forces to damping and stiffness matrices are neglected under the mean-axes approximation in order to decouple the modal system equations. The error of this approximation is dominated by the angular velocity ω_{Gz}, as the norm of the translational velocity, v_G, is constant for all radii.

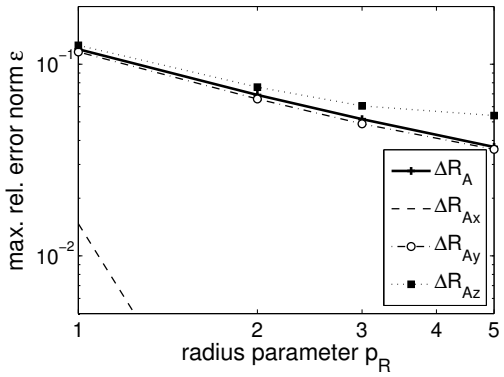


Figure 5.22: Maximum error norm of displacements at point P_{tip} for the FMB problem, comparing mean-axes approximation to the nonlinear solution for different radii.

The studies in this section have demonstrated that the gyroscopic forces can have a noticeable impact on the vehicle structural dynamics. This is particularly relevant for flexible aircraft subject to large manoeuvres, where the mean-axes approximation can lead large errors in dynamic load calculations. This will be explored in the next chapter, which will also exercise the proposed consistent linearisation on a full aircraft configuration.

Chapter 6

Application of the Aeroelastic Simulation Framework to the Analysis of Flexible Aircraft

This chapter will present different numerical studies that demonstrate the multidisciplinary environment for the Simulation of High-Aspect-Ratio Planes (SHARP) introduced in this work. The integrated aeroelastic and flight dynamics framework enables the complete analysis of flexible aircraft configurations including static aeroelastic analyses, trim, linear stability analyses and dynamic open- and closed-loop time simulations. The emphasis lies heavily on the coupling between the possibly large static and/or dynamic wing deformations and the vehicle flight dynamics.

SHARP is a complex simulation environment which couples three modules – structural, rigid-body and aerodynamics – in a unified framework. To gain a significant level of confidence in the numerical implementation, the individual modules and coupled solvers have been verified in previous work. These included verification studies of (a) the structural solver in Ref. [137] for static and dynamics problems with large elastic displacements, (b) the geometrically-nonlinear aeroelastic simulation environment in Ref. [127] for static problems with large wing displacements and dynamic time-domain solutions and (c) the state-space aeroelastic framework for flutter predictions in Ref. [128]. This work has contributed to the verification of the flexible-body dynamics module for flexible-body configurations without aerodynamics, as presented in the previous chapter. In this chapter further studies will verify the linearisation of the UVLM for prescribed rigid-body motions of flexible aerofoils.

The chapter will also demonstrate the reduced-order modelling capability in SHARP on two aeroelastic problems of increasing complexity, following the model reduction approaches presented in Chapter 4. The Goland wing problem will first serve to highlight the

reduced-order modelling approach on an unstable linear aeroelastic system, given by the monolithic framework presented in Subsection 3.2.4 (neglecting the rigid-body DoF), with the aim to synthesise a robust flutter suppression controller. Robust control methods, such as the proposed $\mathcal{H}_\infty$ controller, can provide sufficient control performance when applied to the full-order response, even in the presence of significant model mismatch between the reduced- and full-order systems. The use of higher-fidelity (reduced-order) aeroelastic tools in the control synthesis, however, can also guarantee a significant level of robustness if the controller is applied to real-world problems. This simple clamped aeroelastic problem will also contribute further verification studies to test the full-order state-space aeroelastic formulation.

The second section in this chapter will also include rigid-body DoF with the aim to exercise the linearised frameworks on a representative flexible HALE aircraft subject to large manoeuvres. This extensive study will firstly illustrate the effect of large wing deformation at trimmed flight on the dynamic stability behaviour of the aircraft which will also be explored in open-loop time-marching simulations. The latter will contribute significant insight into the effect of consistent linearisation of the structural DoF on the prediction of the flexible-aircraft dynamics response with emphasis on the interaction between the vehicle structural and rigid-body dynamics. This information will be used to evaluate the limits of applicability of the mean axes approximation for dynamic load calculations of a full aircraft configuration.

The last part of this chapter will then focus on model reduction of the manoeuvring HALE configuration subject to control surface inputs, as outlined in Subsection 4.3.2. Starting point for the reduced-order modelling approach is the consistent linearisation of the structural and aerodynamic DoF, but the vehicle rigid-body dynamics are allowed to remain large to capture the arbitrary manoeuvres of the flexible aircraft. Numerical studies in Subsection 6.2.4 will demonstrate the application of balancing methods to the resulting linearised aeroelastic framework. This will be seen to provide a very low-order alternative to standard aeroelastic tools.

6.1 The Clamped Goland Wing Problem

The Goland wing problem has been introduced in Section 4.1 to illustrate the numerical issues associated with reduced-order modelling of the aeroelastic response. In this section we will return to this simple benchmark problem to firstly verify the implementation of the aeroelastic framework, Eq. (3.19), and secondly to explore the proposed balanced truncation method for the linear system. The Goland wing is a stiff cantilever for which the relevant properties have been summarised previously in Table 4.1. Figure 6.1 illustrates the low-aspect-ratio wing geometry showing the different representations of the aerodynamic lattice and the beam discretisation. The aileron input also highlighted in the figure will be used next to verify the full-order aeroelastic system which will provide

a suitable starting point for reduced-order modelling of the problem in Subsection 6.1.3. These model reduction techniques will then be illustrated on a full HALE configuration in the subsequent Section 6.2.

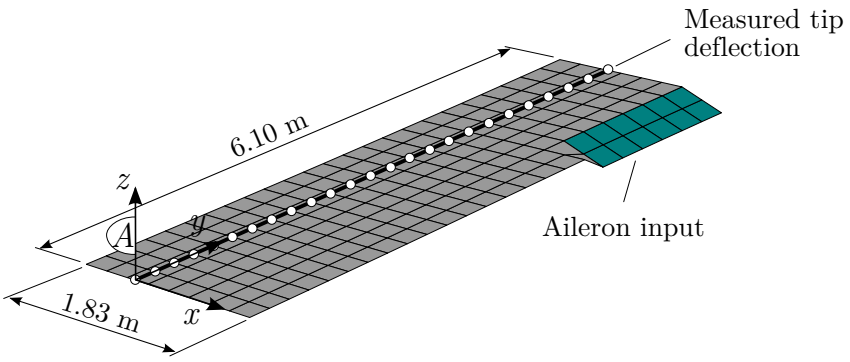


Figure 6.1: Undeformed Goland wing geometry with definition of system in- and outputs. Material properties have been defined in Table 4.1.

6.1.1 Verification of the Aeroelastic Module

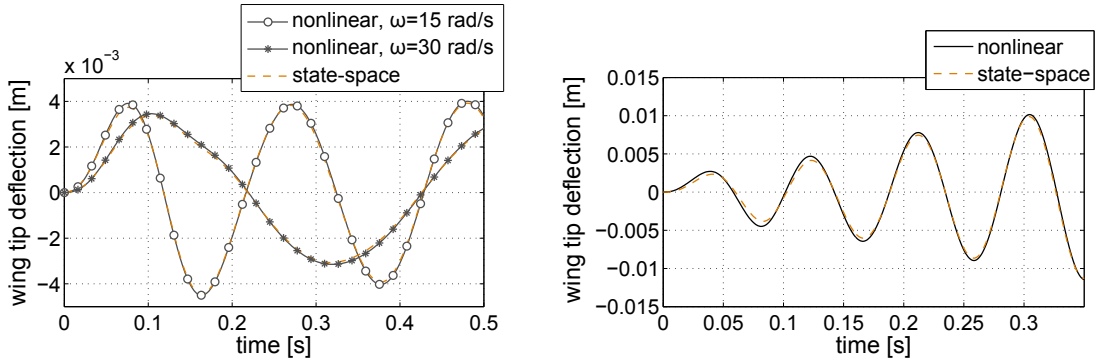
The homogeneous form of Eq. (3.19) defines the discrete-time generalised eigenvalue problem for each free-stream velocity. Comparison of the system eigenvalues over a range of velocities provides the aeroelastic flutter boundary of the Goland wing which will be benchmarked against published results [73, 128, 141, 197]. Note that Murua *et al.* [128] have presented a detailed flutter analysis of the Goland wing also using the framework SHARP but with a relatively coarse discretisation.

Table 6.1: Flutter speed, V_f, and frequency, ω_f, of the Goland wing for M chordwise and N spanwise bound vortex panels.

Source	Discretisation ($M \times N$)	States	V_f, m/s	ω_f, rad/s
Present	8×26	2444	165	73
Present	12×26	3484	168	71
Present	16×26	4550	169	70
Goland [73]	-	-	137.2	70.7
Wang *et al.* [197]	-	-	174.3	-
Murua *et al.* [128]	4×10	-	166	72

In this work, a convergence study is conducted first to determine an appropriate spatial discretisation in the coupled full-order model, which is dominated by the UVLM discretisation. To ensure mesh consistency, varying the number of chordwise bound panels also affects the time step of the discrete-time problem and, hence, the number of panels used to

discretise the wake. A wake length of 15 chord lengths was kept in this study as determine by another convergence study. Table 6.1 shows that $M = 16$ chordwise and $N = 26$ spanwise bound panels, resulting in over 4500 aeroelastic states, are required to solve the flutter problem accurately with a tolerance of ± 0.5 m/s. With this discretisation, the flutter speed is $V_f = 169$ m/s, and frequency, $\omega_f = 70$ rad/s, which is in excellent agreement with the values reported in the literature based on 3-D potential-flow aerodynamics [127, 197]. The flutter boundary for this wing, however, is sensitive to small variations in speed and a smaller number of panels may be needed at lower, stable free-stream velocities.



(a) Forced vibration for $V = 140$ m/s

(b) Free vibration for $V = 180$ m/s

Figure 6.2: Open-loop response of the Goland wing subject to sinusoidal aileron input with 1 deg amplitude at different free-stream velocities, V.

The converged state-space aeroelastic system with 16×26 bound panels (4550 aeroelastic states) is then verified against the nonlinear time-marching solution at two different free-stream velocities of $V = 140$ m/s ($0.83V_f$) and $V = 180$ m/s ($1.07V_f$), respectively. The reference solution is obtained using the geometrically nonlinear aeroelastic solver in SHARP with the nonlinear implementation of the UVLM, as defined in Subsection 3.2.2. As defined in Figure 6.1, the single input to the linear system operates an aileron of 25% chord length fixed to the last quarter of the wing and the system output is the vertical tip deflection. The open-loop response to a sinusoidal input of 1 deg amplitude in Figure 6.2(a) shows good comparison between the two solution methods below flutter speed over a range of excitation frequencies, ω. The (unforced) flutter response, as shown in Figure 6.2(b) for $V = 180$ m/s ($1.07V_f$), is obtained following an initial sinusoidal excitation of the aileron for one period with $\omega = 70$ rad/s and again 1 deg amplitude. Both solutions predict the exponential growth of the wing tip deflection at small amplitudes. Hence, if the size of the state-space aeroelastic model is reduced significantly, such a system can be used for robust flutter suppression using $\mathcal{H}_\infty$ control [203] and will provide the motivation here for model reduction of the aeroelastic system as outlined in the next subsection.

6.1.2 Model Reduction of the Unstable Aeroelastic System

Model reduction of the state-space aeroelastic system, as outlined in Subsection 4.3.1, will be explored next to reduce the unstable aeroelastic system of the Goland wing above flutter speed ($1.07V_f$). This simple single-input/single-output (SISO) system, which maps the aileron input to the resulting wing tip deflection output, will be used first to demonstrate the reduction process before applying the techniques to the full HALE configuration with multiple inputs and outputs. However, before balancing methods can be applied, the numerical issues introduced in Section 4.1 for the Goland wing problem need to be addressed. In this work, the ill-conditioned aeroelastic system will be stabilised using small algorithmic damping of $\alpha = 5 \times 10^{-3}$ in the modified Newmark integration scheme to shift undesired high-frequency modes away from the stability boundary.

Following the reduction approach outlined in Figure 4.4, the full-order aeroelastic system is firstly reduced through balanced truncation of the unstable plant whereby an initial truncation to 500 states, chosen based on the system Hankel singular values, was found to dramatically improves numerical efficiency of the subsequent reduction using the normalised coprime factorisation method. The potential of the resulting model reduction is shown in Figure 6.3 in terms of the scalar ν-gap metric which is zero if the reduced-order system captures the input-output mapping exactly and one if model reduction leads to a completely dissimilar representation [193]. For completeness, the ν-gap metric of a simple balanced realisation without coprime factorisation is also included, which shows that the proposed balanced coprime method can achieve marginally better reduced-order model fidelities of the unstable system.

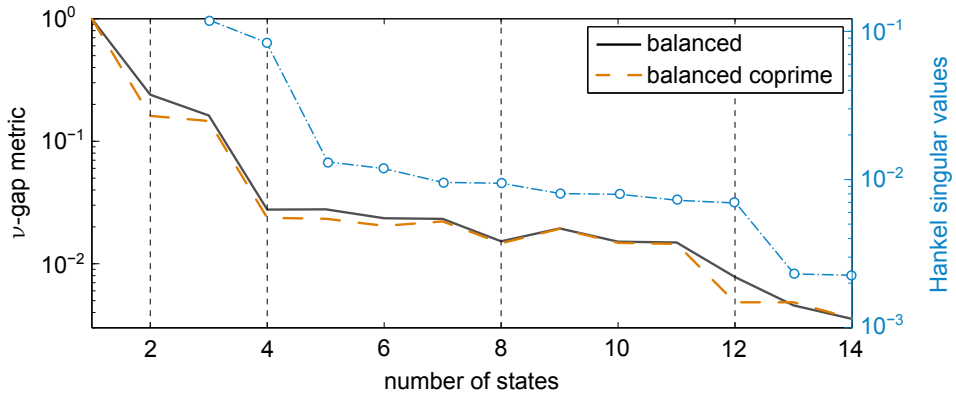


Figure 6.3: ν-gap metric between full- and reduced-order models using balanced truncation and balanced coprime factorisation. Superimposed are the Hankel singular values of the balanced system.

At last, the Hankel singular values of the balanced system are also superimposed in Figure 6.3. Note that the first two states have infinite HSV corresponding to the unstable complex conjugate pair of the flutter mode. Following the description of the balanced

truncation method in Subsection 4.2.1, the HSV indicate the contribution of each balanced state to the system input-output mapping and provide an error bound of the model reduction before the truncation. This is also evident from correlation of the HSV with the ν-gap metric of the reduced-order models, as demonstrated in Figure 6.3.

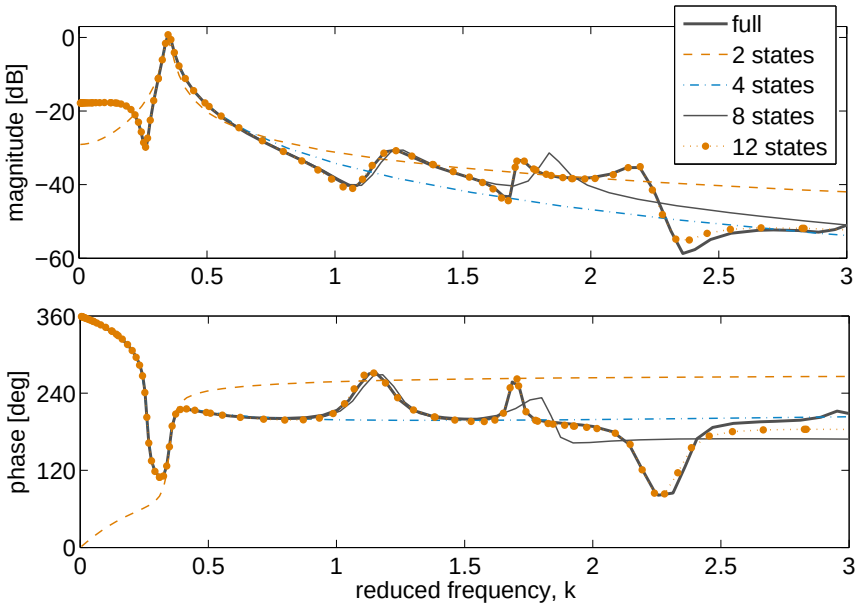


Figure 6.4: Comparison of different reduced-order balanced system responses against the full-order model for a range of reduced frequencies, $k = \omega c/(2V)$, at free-stream velocity $V = 180$ m/s $(1.07V_f)$.

Based on the HSV of the balanced system, four different reduced-order models with model orders of 2, 4, 8, and 12 states, as highlighted in Figure 6.3, are investigated in this study. The first two states correspond to the unstable flutter mode. Figure 6.4 compares the Bode response of the selected reduced-order systems with the full-order model in the mapping of the aileron input to the wing tip displacements over a range of reduced frequencies, $k = \omega c/(2V)$. It is clear from the results that only two balanced states are needed to capture the coupling of the complex 3D unsteady flow characteristics and the structural response of the Goland wing around the flutter point. More states are required to also capture the higher-frequency response, but as little as 12 states are sufficient to predict the response of the full-order system with 4550 states even at high reduced frequencies of $k = 3$. These results show the potential of reduced-order modelling using balancing methods, even for relatively large, unstable aeroelastic systems, leading to substantial reductions of three to four orders of magnitude. This top-down approach enables the use of higher-fidelity models for robust control synthesis, as illustrated in the next subsection.

6.1.3 Robust Control Synthesis for Flutter Suppression

Robust control techniques such as $\mathcal{H}_\infty$ control methods have been demonstrated to provide substantial alleviation of gust loads [39, 131] and, if included in aeroelastic design, can provide significant vehicle weight reductions. The robustness property of $\mathcal{H}_\infty$ methods provides consistent controller performance even in the presence of uncertainties, e.g. due to disturbances or model mismatch if controller is applied to the real plant [203]. The latter can be tackled using high-fidelity aeroelastic models in the control synthesis, but the large size and complexity of such models can make the design of robust controllers a very difficult endeavour.

Hence, in this section the reduced-order aeroelastic system will be used to compute a $\mathcal{H}_\infty$ controller for alleviation of vibrations, as demonstrated in Cook *et al.* [39] for gust alleviation of very flexible aircraft. In this work, however, the controller will be demonstrated for flutter suppression of the Goland wing at a free-stream velocity of $V = 180$ m/s $(1.07V_f)$. Even though pole placement could be a natural choice to directly stabilise the flutter mode on a SISO system, the flutter suppression problem provides a simple environment to demonstrate the $\mathcal{H}_\infty$ control synthesis based on a reduced-order model, which can be applied to gust alleviation in future work. Due to its robustness characteristics, $\mathcal{H}_\infty$ control synthesis of very low-order reduced systems is expected to maintain sufficient controller performance even if the controller is applied to the full-order (nonlinear) aeroelastic system.

Following Ng *et al.* [131], the aeroelastic system in Eq. (3.19) is expanded to account for a disturbance of the aileron, w. The resulting linear system can be written as [182]

$$\begin{aligned} \Delta x^{n+1} &= A\Delta x^n + B\Delta u^n + G\Delta w^n \\ \Delta z^n &= C_1 \Delta x^n \\ \Delta y^n &= C_2 \Delta x^n, \end{aligned} \tag{6.1}$$

where u is the control variable given by a second control surface and y is the measured variable. The objective of the $\mathcal{H}_\infty$ controller is to minimise the vertical wing tip deflection, z, which is also the observed state of the controller, y, i.e. $C_1 = C_2$. Both ailerons used to respectively disturb and control the system are assumed to be coincident which, even though it is non-physical, simplifies the system input to $B = G$. The block diagram shown in Figure 6.5 illustrates the feedback system, where the transfer function of the dynamic controller, $K(s)$, is given as

$$\Delta u^n = K(s)\Delta y^n. \tag{6.2}$$

The transfer function of the aeroelastic system, $G(s)$, in Eq. (6.1) can also be written as

$$\begin{bmatrix} \Delta z \\ \Delta y \end{bmatrix} = G(s) \begin{bmatrix} \Delta w \\ \Delta u \end{bmatrix} = \begin{bmatrix} G_{11}(s) & G_{12}(s) \\ G_{21}(s) & G_{22}(s) \end{bmatrix} \begin{bmatrix} \Delta w \\ \Delta u \end{bmatrix}, \tag{6.3}$$

By coupling Eqs. (6.2) and (6.3), the closed-loop transfer function $S(G, K)$ from w to z is finally given by linear fractional transformation as [182]

$$S(G, K) = G_{11} + G_{12}K(I - G_{22}K)^{-1}G_{21}. \tag{6.4}$$

The MATLAB® Robust Control Toolbox [11] is used in this exercise to compute the $\mathcal{H}_\infty$ controller, which is obtained through minimisation of the $\mathcal{H}_\infty$ norm of $S(G, K)$. The controller was tuned with the weights $W_1 = 2$ and $W_2 = 3$ applied to the system outputs, y, and inputs, u, respectively, to achieve maximum output performance for maximum aileron deflections of 10 deg, whereby no measurement noise was assumed in this exercise.

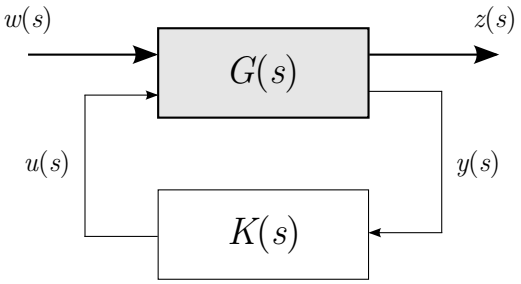
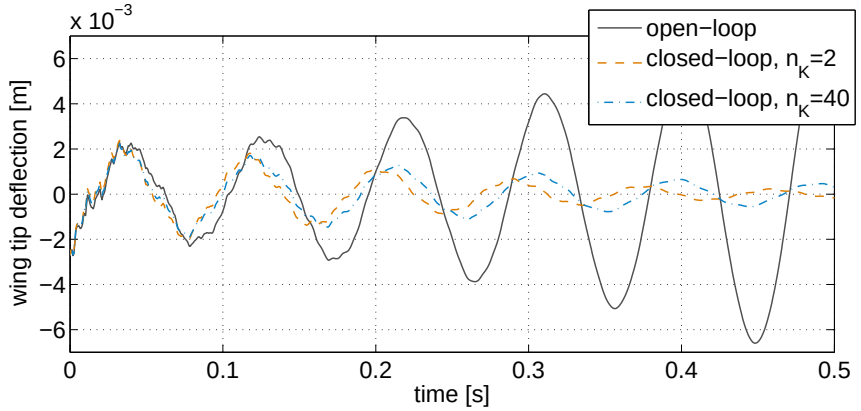


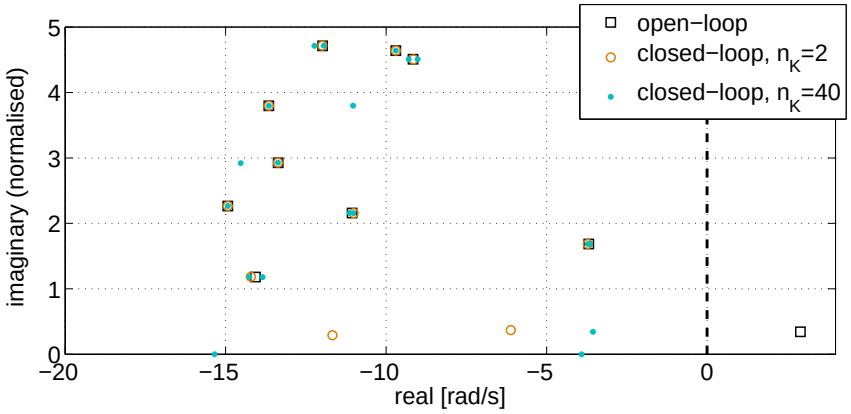
Figure 6.5: Block diagram of a closed-loop system.

To demonstrate the application of the proposed model reduction, the controller is synthesised based on the reduced-order system with n_K states and is then applied to the full-order system to stabilise the response. Figure 6.6(a) compares the state-space open-loop and closed-loop responses, which suggests that two controller states are sufficient to suppress flutter and that using more states in the control synthesis can deteriorate the controller performance. This is also reflected in the root locus of the closed-loop system shown in Figure 6.6(b) for the controller states $n_K = 2$ and 40, which correspond to the extreme cases considered in this study. The controller effectiveness varies with increasing number of controller states, n_K, but it can be seen from Figure 6.6(b) that the poles of the closed-loop systems are always moved away from the flutter boundary.

Hence, this simple example based on the Goland wing problem demonstrates that a very low-order, reduced system is sufficient to capture most features of the unsteady flow and the resulting structural vibrations. It has been shown that this top-down approach can be used for very efficient synthesis of a robust flutter suppression controller. This



(a) State-space open- and closed-loop impulse response



(b) Root locus of open- and closed-loop systems

Figure 6.6: Demonstration of flutter suppression for the Goland wing at free-stream velocity $V = 180$ m/s ($1.07V_f$) for varying number of $\mathcal{H}_\infty$ controller states, n_K. The imaginary part has been normalised with $c/(2V)$.

useful insight into the aeroelastic modelling of flexible aerofoils will be applied in the next section on a full HALE configuration.

6.2 Flight Dynamics of a Flexible Aircraft Configuration

This section will at last demonstrate the consistent aeroelastic linearisation and reduced-order modelling on a manoeuvring HALE configuration. The representative aircraft, shown in Figure 6.7, consists of large-aspect-ratio flexible wings, a rigid fuselage and a rigid empennage. It is similar to those of Patil *et al.* [142] and Murua *et al.* [128], but it includes winglets in the main wing for lateral stability and the point mass of 50 kg was moved to the centre of the main wing to guarantee static pitch stability [128]. The dihedral members are rigidly-linked to the main wing at both ends at an angle of 20 deg. The length fraction of each dihedral member over the semi-span of the main wing is defined as λ, which will be used in this work as a parameter to study the impact of wing dihedral on

the vehicle dynamics. The horizontal stabiliser and the vertical fin are modelled as lifting surfaces without camber or pretwist, and the former includes an elevator modelled as a quarter-chord-length control surface. The empennage is raised by 1.25 m with respect to the main wing to avoid wake-tail collisions and it is rigidly linked to the main wing by a non-lifting fuselage.

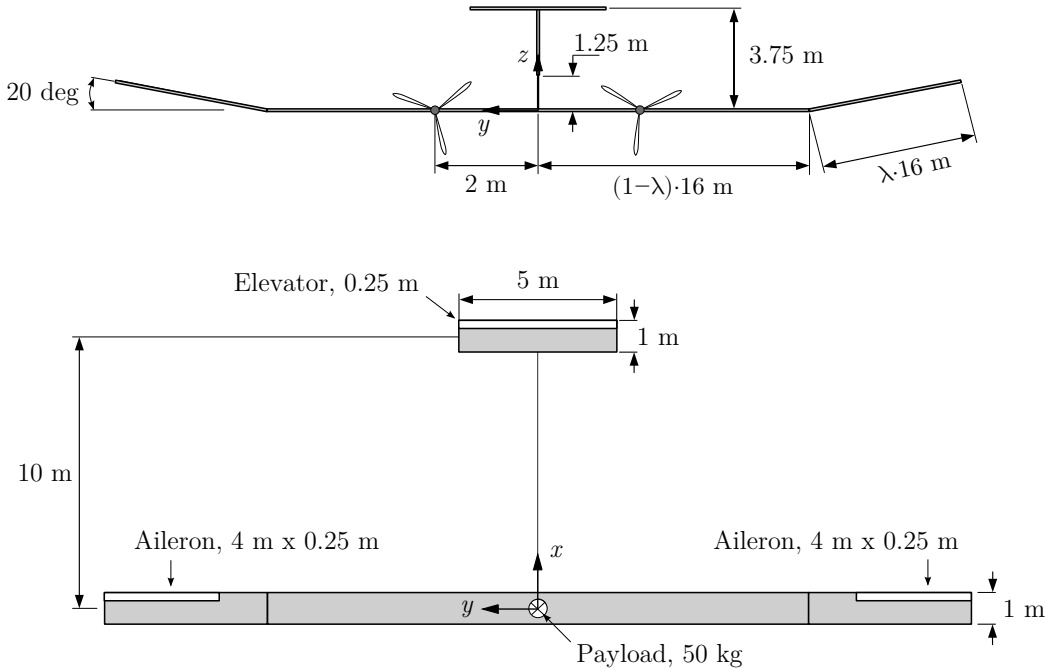


Figure 6.7: Undeformed HALE aircraft geometry with front and top view (not to scale).

Table 6.2: HALE aircraft properties.

	Main wing	Tail plane	Fuselage
Chord, c	1 m	0.5 m	N/A
Semi-span for $\lambda = 0$, B	16 m	2.5 m	N/A
Elastic axis (from l.e.)	0.5 m	0.25 m	N/A
Centre of gravity (from l.e.)	0.5 m	0.25 m	N/A
Mass per unit length	0.75 kg/m	0.08 kg/m	0.08 kg/m
Moment of inertia	0.1 kg·m	0.01 kg·m	0.01 kg·m
Torsional stiffness	$1\sigma\times10^4$ N·m^2	∞	∞
Bending stiffness	$2\sigma\times10^4$ N·m^2	∞	∞
In-plane bending stiffness	$4\sigma\times10^6$ N·m^2	∞	∞

This basic aircraft configuration also includes two massless propellers, which are modelled as point forces rigidly linked to the main wing. The mass per unit length of the fuselage is the same as that of the horizontal and vertical tail planes, and thus the total mass of this aircraft, including payload and structural mass, is 75.4 kg. The flight conditions are $V_\infty = 30$ m/s at an altitude of 20 km (air density 0.0889 kg/m^3). The relevant properties of the members are listed in Table 6.2. The stiffness parameter σ will be used in the following studies to vary the stiffness properties of the main wing (decreasing σ results in a more flexible main wing), whereas fuselage and T-tail are assumed to be rigid.

The following subsections will demonstrate the capabilities of the framework for Simulation of High-Aspect-Ratio Planes (SHARP) on the HALE configuration, starting with the geometrically-nonlinear trim solutions for the different geometry and material parameters, λ and σ. The effect of possibly large trim deformations on the aircraft dynamic behaviour and the coupling between the vehicle flight-dynamic and aeroelastic characteristics will then be explored through linear stability analyses and open-loop time marching solutions. The latter will also demonstrate the modal approach for manoeuvring flexible aircraft which will be used to evaluate the mean axes approximation for a full aircraft configuration including aerodynamics. At last, this section will demonstrate a low-order higher-fidelity alternative applying the reduced-order modelling approach to the manoeuvring flexible HALE configuration.

6.2.1 Nonlinear Trim for Steady Flight

As a first step, the vehicle is trimmed for steady level flight through three inputs, namely angle of attack, elevator deflection, δ_e^{trim}, and thrust per propeller. The trim characteristics of the HALE aircraft are presented in Figure 6.8 for dihedral member ratio, $0 \leq \lambda \leq 1/2$, and stiffness parameter of the main wing, $1.1 \leq \sigma \leq 1000$. The tip deflection of the main wing, non-dimensionalised with the overall semi-span of the main wing, B, is also included in Figure 6.8. Parameter $\sigma = 1$ corresponds to the original stiffness properties from Patil *et al.* [142], but it gives tip deflections over 40% at current flight conditions of 30 m/s (compared to original 25 m/s) which were deemed unrealistic.

It can be seen that the angle of attack initially drops with increasing flexibility due to favourable twisting of the wing. However, this is opposed by wing bending for very flexible configurations ($\sigma \geq 2$) resulting in loss of vertical forces because of the additional wing dihedral and illustrates the importance of geometrically nonlinear effects on the aircraft trim characteristics. Similarly, the increasing span ratio of the dihedral members, λ, is also compensated by a larger angle of attack and elevator deflection. The wing tip deflection decreases for increasing values of λ due to the decrease in bending moment from the dihedral members, as the lift vector is pointing inwards. The nonlinear variation of the tip deflection with σ also demonstrates the effect of geometric nonlinearity on the

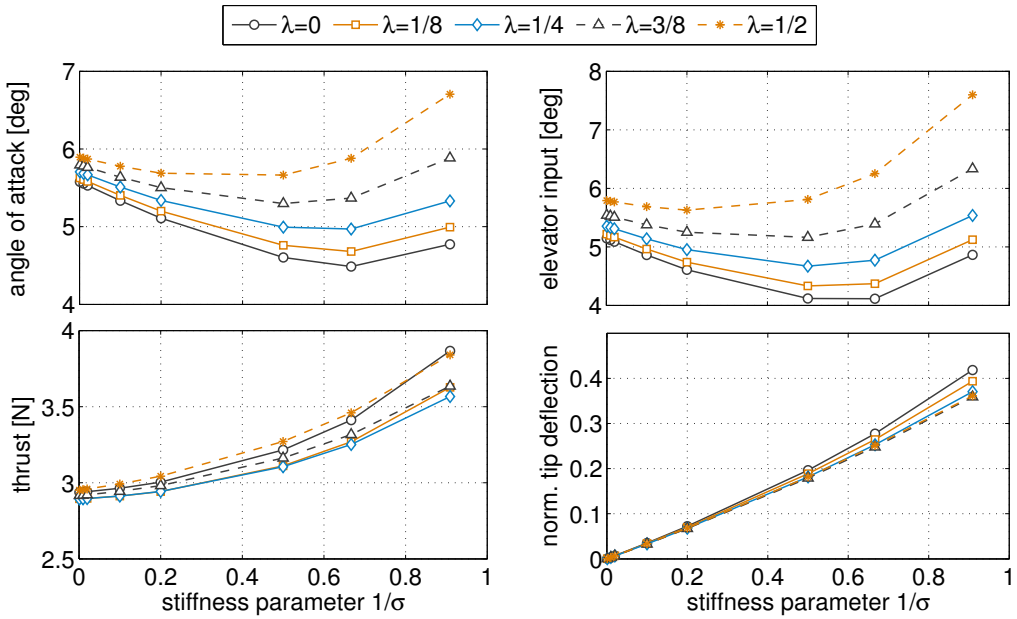


Figure 6.8: Trim angle of attack, elevator deflection, thrust per propeller, and vertical tip deflection of the main wing, $\Delta R_{Az}/B$, as a function of wing flexibility, σ, and dihedral member ratio, λ.

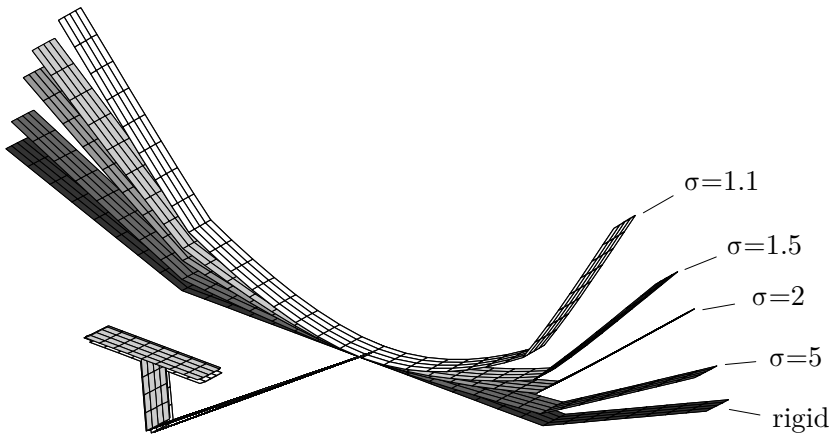


Figure 6.9: Trim deformation of HALE aircraft with $\lambda = 1/2$ and different stiffness parameters σ. (Figure shows actual deformations.)

wing deformations for very flexible configurations ($\sigma \leq 5$). This is also highlighted in Figure 6.9 which shows the large effective wing dihedral for very flexible trimmed HALE configurations with $\lambda = 1/2$ and different stiffness values σ.

6.2.2 Linear Stability Analysis

The dynamic stability of this HALE configuration is studied next to investigate the effect of dihedral member ratio, λ, and flexibility, σ, on the vehicle flight dynamics. For each trim solution, the dynamic stability characteristics of the deformed HALE configuration are directly obtained from the eigensolution of the homogeneous form of Eq. (3.19) which integrates the aircraft aeroelastic and flight dynamic response in a monolithic framework, as presented in Subsection 3.2.4. Mesh convergence in the discretisation of the aerodynamic domain was achieved for 8 bound panels per chordwise meter and 2 panels per spanwise meter of lifting surfaces which results in a finer aerodynamic lattice than the one shown in Figure 6.9. A convergence study indicated that a wake length of 15 m and a time step of 0.02 s are sufficient to accurately capture the flexible aircraft dynamics. The beam elements coincide with the aerodynamic panels in the spanwise direction. The resulting total system size is 6171 states, which includes 5094 aerodynamic states, 1068 structural states, and 9 rigid-body states.

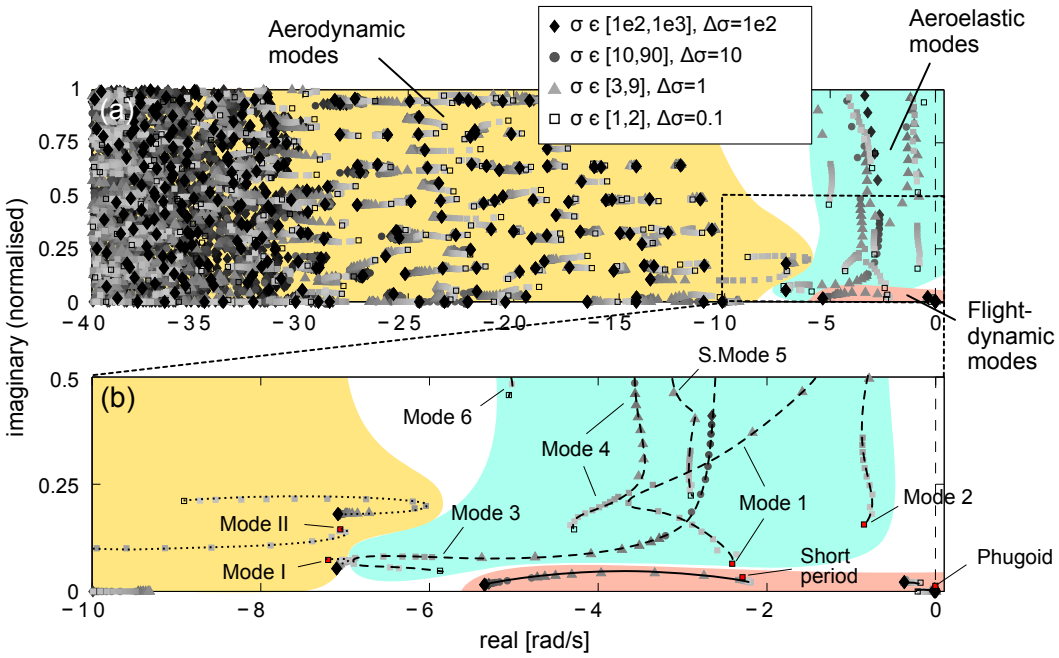


Figure 6.10: Root loci of the eigenvalue analysis with the stiffness of the main wing, σ, as parameter: flight dynamic, aeroelastic, and aerodynamic modes highlighted with solid, dashed, and dotted curves. The imaginary part has been normalised with $c/(2V)$.

Figure 6.10 presents the root locus of the linear flexible-aircraft dynamics system as a function of the wing stiffness, σ, for a dihedral ratio of $\lambda = 1/4$. As the aeroelastic system is derived in discrete time, we have converted the discrete-time eigenvalues to continuous time for an easier interpretation and the imaginary part of the eigenvalues has been normalised again with $c/(2V)$ to present the modes in terms of reduced frequency. Figure 6.10(a) only shows the roots near the origin and the highly-damped aerodynamic modes as well as the lightly-damped aeroelastic and flight dynamic modes have been identified by their mode shapes. The stiffness values have been unevenly spaced, as defined in Figure 6.10(a), where the two extreme cases are representative of a very flexible ($\sigma = 1$) and a stiff ($\sigma = 1000$) wing.

The zoom in Figure 6.10(b) shows the frequency and damping overlap between the aerodynamic, aeroelastic and flight dynamic modes, where the variation with σ has been traced with dotted, dashed and solid curves, respectively. The first few coupled modes of the flexible vehicle have been identified and are designated by the names of their rigid-aircraft counterparts, e.g., phugoid, short period, etc., although they also include vehicle deformations. The aeroelastic modes are labelled with Arabic numerals where Modes 1, 3, and 5 have been identified as symmetric bending/torsion modes and Modes 2, 4, and 6 correspond to the anti-symmetric modes. The two aerodynamic modes labelled with Roman numerals will also be investigated in this stability analysis.

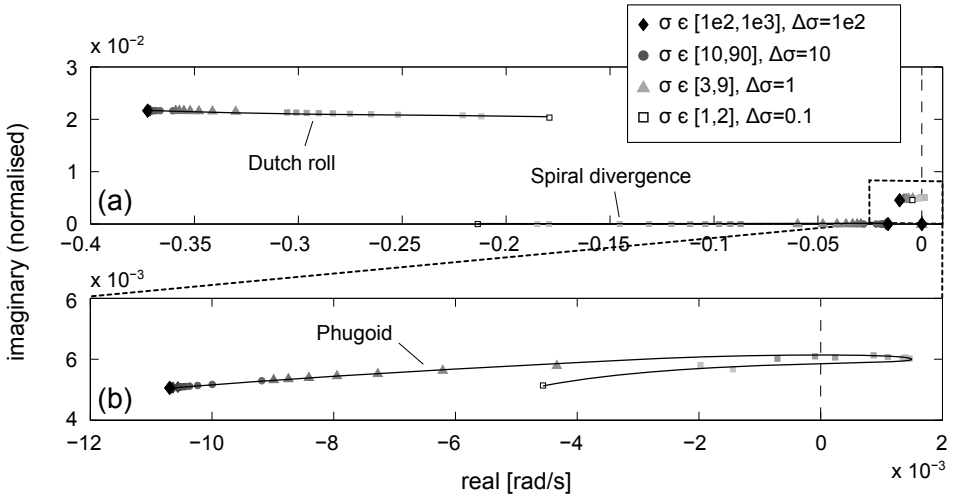


Figure 6.11: Zooms of the root loci of Figure 6.10(b) showing the flight dynamic modes close to the origin. The imaginary part has been normalised with $c/(2V)$.

From Figure 6.10(b) it is clear that, as the stiffness of the main wing is increased, the higher-frequency aeroelastic modes become less stable while the low-frequency flight dynamic modes show the opposite trend. The non-oscillatory spiral divergence on the other hand, becomes less stable with increasing stiffness. This can be observed in detail in Figure 6.11(a) which highlights two flight-dynamic lateral modes: Dutch roll and spiral

divergence. As flexibility increases, the less stable Dutch roll illustrates the detrimental impact flexibility might have on the handling qualities of the vehicle. In contrast, the spiral mode stability margin substantially increases with flexibility due to the larger static deformations of the main wing at trim conditions.

Figure 6.11(b) zooms further in the root loci in order to visualise the phugoid mode. For a rigid aircraft it is a lightly damped mode. As flexibility is increased, this mode demonstrates the complex interaction between the elastic and rigid-body DoF: as the aircraft pitches up and climbs first, the wings undergo a downward flapping-like motion. As the vehicle pitches down and descends, the wing bends upwards, reaching the maximum tip deflections before the cycle is finished. Whereas rigid and stiff aircraft present stable phugoid modes, damping drops with increasing wing flexibility resulting in an instability for $1.2 \leq \sigma \leq 1.7$. However, for highly flexible cases ($\sigma < 1.2$) this trend is reversed which results in stable configurations. To investigate this reversal in stability behaviour, we have included the extremely flexible case of $\sigma = 1$ in Figure 6.11 and will examine the effect of the outboard dihedral in the following.

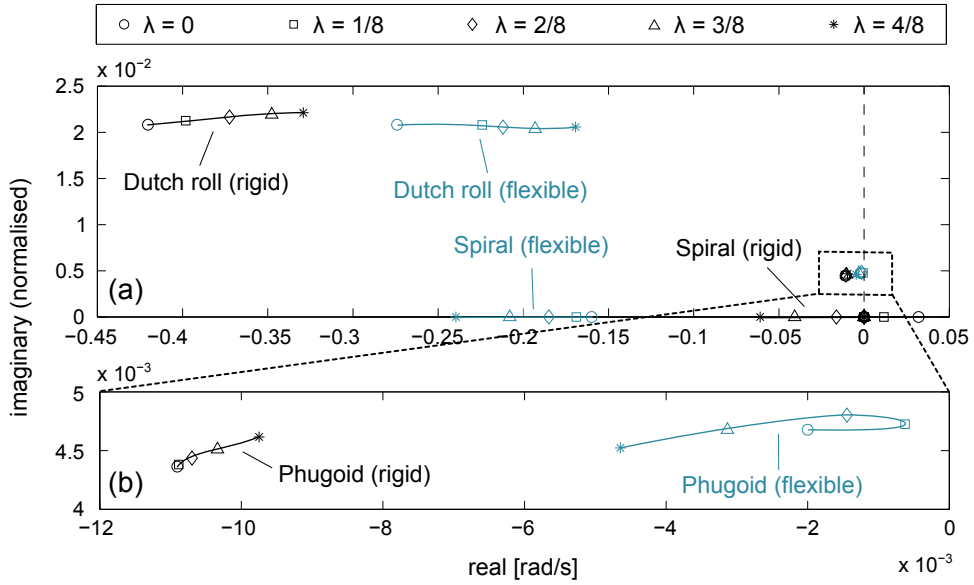


Figure 6.12: Root loci of the eigenvalue analysis for $\sigma = 1.1$ (in blue) and $\sigma = 1000$ (in black) with the dihedral ratio λ as parameter: (a) dominant roots, and (b) zoom near to the origin. The imaginary part has been normalised with $c/(2V)$.

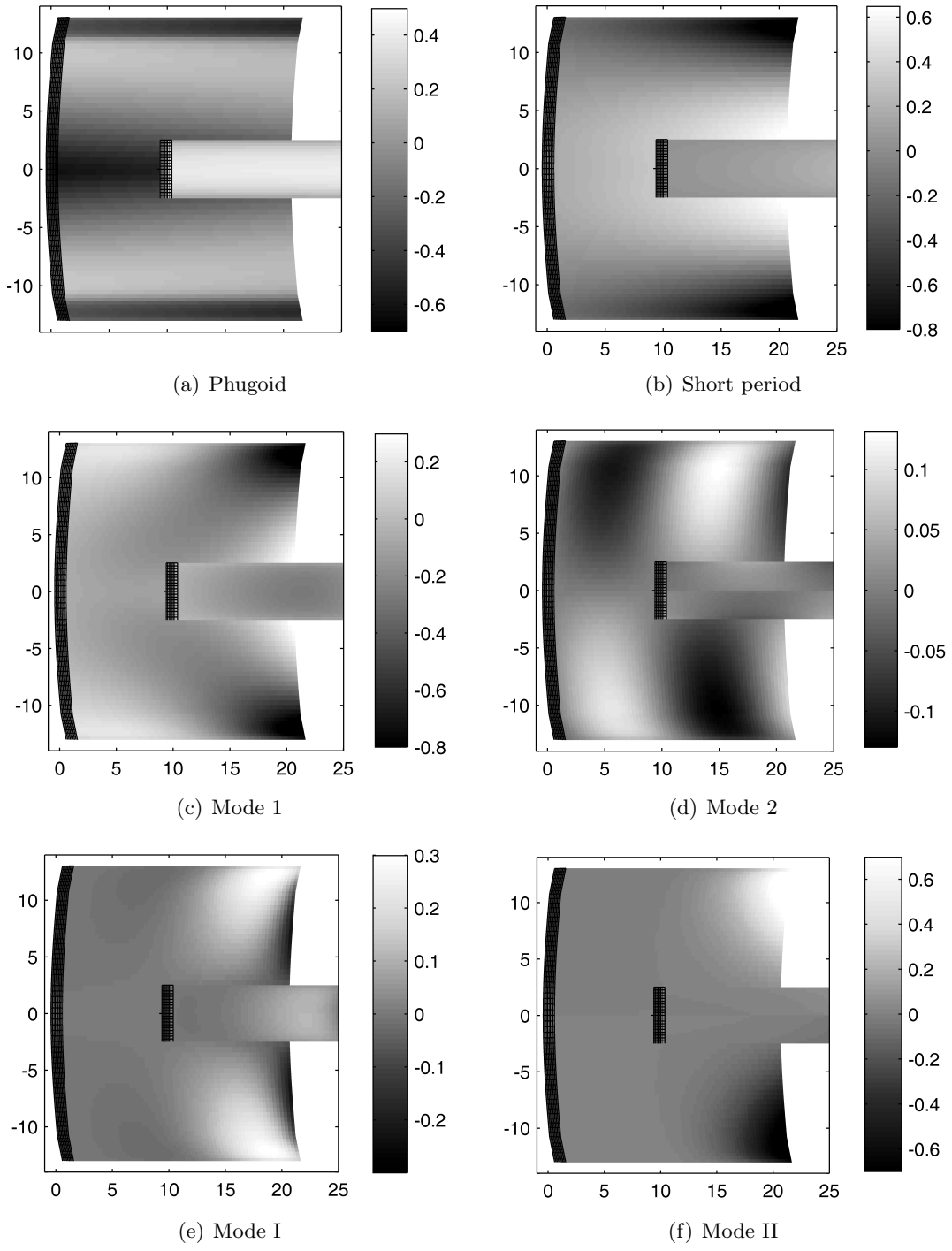
To complete this discussion, Figure 6.12 shows the root loci for a very stiff ($\sigma = 1000$) and a very flexible ($\sigma = 1.1$) aircraft for varying dihedral ratio, λ. Here, we only focus on the dominant flight dynamic modes: Dutch roll, spiral divergence, and phugoid. Figure 6.12(a) shows that an increase of the dihedral member ratio leads to a less stable Dutch roll, while it increases the resistance against spiral divergence, as already seen in Figure 6.10(a) for increasing flexibility. That is, static deformations and dihedral ratio

have the same effect on the lateral modes. As the dihedral ratio is varied, these trends are consistent for both the rigid and flexible vehicles. As expected, wings with very small or no dihedral lead to unstable spiral modes.

Figure 6.12(b) focuses on the region closer to the origin in order to expose the characteristics of the phugoid mode. Interestingly, the trends are opposite for the rigid and flexible vehicles: the increase of dihedral ratio leads to a more stable phugoid in the flexible aircraft (except for $\lambda = 0$), but the damping of the rigid phugoid decreases with λ. From the trends of the phugoid mode in Figures 6.11 and 6.12, it is clear that static and dynamic aeroelastic effects have opposing contributions, such that an increase of effective wing dihedral due to wing bending (static effect) decreases phugoid stability, as deduced from Figure 6.12, which explains the trend for $1.2 \leq \sigma \leq 1.7$ in Figure 6.11. For more flexible configurations the dynamic properties result in increased damping which dominate over the static effects and tend to stabilise the aircraft.

The eigenvalue analysis of the monolithic system also captures the aerodynamic part of the eigenvectors which will be investigated in the last part of this stability analysis for the six modes highlighted with red squares in Figure 6.10(b). These modes correspond to the most flexible configuration with $\lambda = 1/4$ and $\sigma = 1$ (42% tip deflection). The symmetric phugoid and short period modes have been selected to observe the effect of unsteadiness on two classical flight-dynamic modes of this very flexible aircraft configuration. Two aeroelastic modes have also been highlighted, which exhibit symmetric (Mode 1) and antisymmetric (Mode 2) bending/torsion couplings, and finally the symmetric (Mode I) and antisymmetric (Mode II) unsteady aerodynamic modes.

Figure 6.13 shows the amplitude of the bound and wake circulation strengths, Γ_b and Γ_w, of these mode shapes for the trimmed vehicle with $\sigma = 1$. As one would expect, unsteady effects are negligible for the phugoid mode and no variation of circulation in the chordwise direction of the wake is observed. With increasing frequency, however, quasi-steady models may fail to predict the flight-dynamic response accurately, as shown for the short-period mode in Figure 6.13(b). The higher-frequency aeroelastic modes (Modes 1 and 2) show distinct variations in the wake, which demonstrates the effect of elastic deformations on the unsteady aerodynamic loads. On the other hand, Modes I and II represent unsteady aerodynamic modes which couple with the structural and rigid-body dynamics of the aircraft and are excited in the similar frequency range as their aeroelastic and flight-dynamic counterparts (albeit highly damped).



(a) Phugoid (b) Short period

(c) Mode 1 (d) Mode 2

(e) Mode I (f) Mode II

Figure 6.13: Aerodynamic component of the mode shapes for a very flexible aircraft, $\sigma = 1$, showing the circulation strengths of the vortex rings for the six modes highlighted in Figure 6.10(b).

A suitable reduced-order model should then preserve the relevant information of the unsteady flow to predict the actual dynamic response of the aircraft. This shows that, depending on the frequency content of the excitation, a large number of aerodynamic states in addition to the dominant flight-dynamic and aeroelastic modes may be required to capture the prevalent physics of the problem. The next subsections will explore the dynamics of the full aircraft configuration through the consistent linearisation of, first, the structural DoF and, subsequently, also the aircraft aerodynamics. This insight will finally be used in Subsection 6.2.4 to produce very efficient reduced-order models for the manoeuvring HALE aircraft.

6.2.3 Inertial Coupling Effects on the Aircraft Open-Loop Response

This section will investigate the effect of consistent linearisation of the structural DoF on the dynamic response of the vehicle defined in Figure 6.7 and Table 6.2. The aircraft is subject to various excitations in the form of commanded inputs on ailerons and elevator and the open-loop response is computed using the linearised and mean axes solutions, as well as the full nonlinear solver. To isolate the effect of linearisation of the structural DoF only, the aerodynamics are first computed using the geometrically-nonlinear time-marching description of the UVLM, as derived in Section 3.1, for all results presented in this subsection. The linearised state-space form of the UVLM will however be exercised in the next subsection. The stiffness parameter σ is also used in this study to explore the effect of flexibility on the nonlinear flight dynamic response.

All further investigations in this section will be limited to the HALE configuration with dihedral member ratio $\lambda = 1/4$, which was shown to be stable for the whole range of stiffness values with lightly-damped spiral and phugoid modes (see Figures 6.10-6.12). For the dynamic analysis, the control surface inputs of ailerons and elevator (denoted by subscripts a and e, respectively) are prescribed such that $\delta_a = \pm\delta_a^*$ and $\delta_e = \delta_e^{trim} + \delta_e^*$ with the time histories of $\delta_{a,e}^*$ shown in Figure 6.14. The elevator inputs are prescribed around the trim inputs, δ_e^{trim}, while the ailerons, as defined in Figure 6.7, are not used for trimming the aircraft but are deployed anti-symmetrically with $\pm\delta_a^*$. The open-loop response of the aircraft is computed for 50 s using a time step of 0.02 s.

Figure 6.15(a) shows the angular velocity components of the rigid vehicle expressed in the body-fixed frame A, which is orientated as shown in Figure 6.7, such that rotations around the x, y and z axes respectively correspond to roll, pitch and yaw of the aircraft. The time history of the angular velocity norm, $|\omega_A|$, indicates that the aircraft response remains only lightly damped even long after the command ($t \geq 20$ s). This finding is in agreement with the above stability analysis in Figure 6.10, which suggests that the rigid aircraft is only marginally stable. It was also shown, however, that the spiral mode becomes more stable with increasing flexibility due to wing dihedral. To demonstrate this

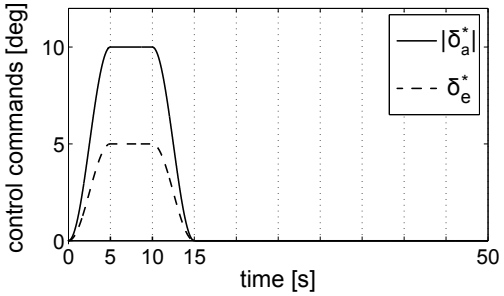
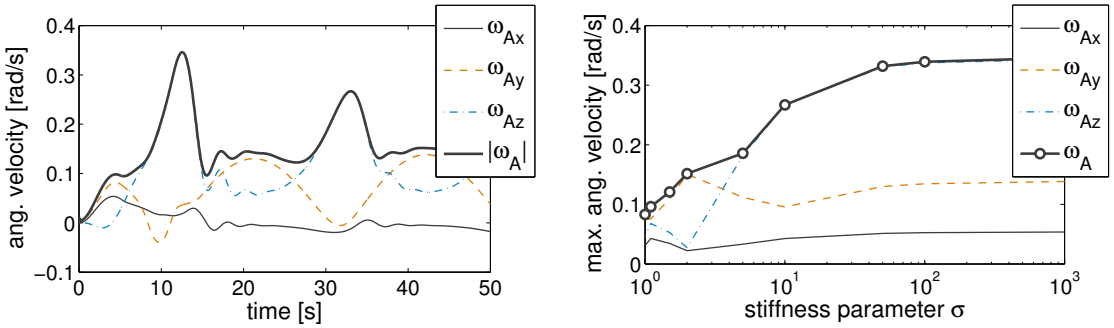


Figure 6.14: Control inputs for ailerons (δ_a^*) and elevator (δ_e^*). Transients are sine functions.

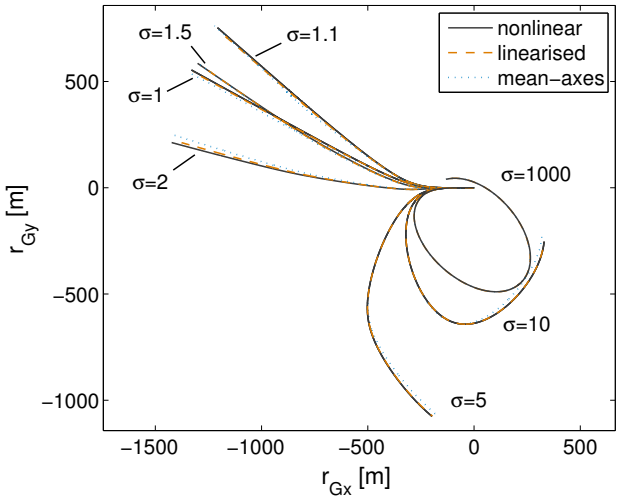


(a) (b)

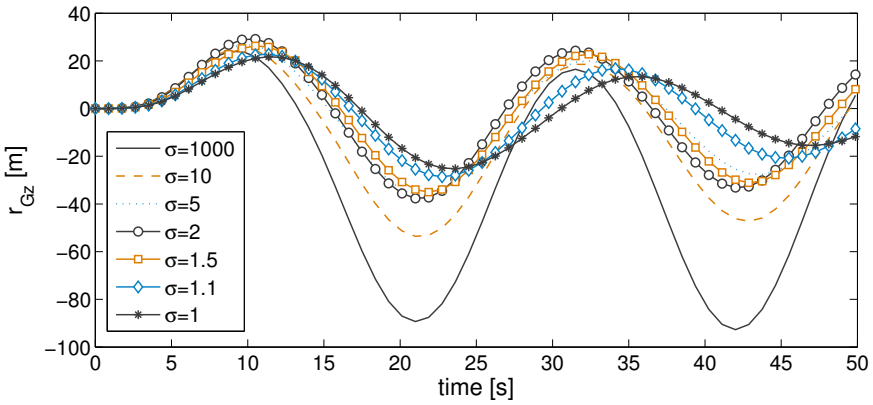
Figure 6.15: Rigid-body angular velocity components of the HALE aircraft in response to Figure 6.14: (a) time history of the rigid vehicle and (b) maximum norm of ω_A and its individual components for varying stiffness computed using the geometrically nonlinear model.

behaviour Figure 6.15(b) compares the maximum norm of the angular velocity ω_A and its components for different values of the flexibility parameter, σ. The yaw rate, ω_{Az}, is damped much faster for flexible platforms ($\sigma < 5$) and the response is dominated by the less stable phugoid mode in this flexibility range.

In addition to the stability characteristics, flexibility impacts the controllability of the aircraft. Figure 6.16(a) shows its trajectory in the x-y plane (top view) for different stiffness values σ and demonstrates control reversal with increasing flexibility of the main wing. For the flexible configuration with $\sigma = 2$, wing twisting results in minimal control authority of the ailerons. Controllability can be further explored on the linear system by evaluating the controllability Gramians, W_c, as defined in Section 4.2, but this will not be investigated further in this work. Figure 6.16(b) shows the effect of flexibility on the altitude response of the HALE aircraft. The frequency of the resulting oscillatory motion matches closely the phugoid mode presented for this configuration in Figure 6.10. The reduction in frequency with increasing flexibility is also captured in this response.



(a) x-y plane using different models



(b) Time history of altitude, z, using the geometrically nonlinear model

Figure 6.16: Trajectory of the HALE aircraft in response to Figure 6.14 for $\lambda = 1/4$ with stiffness of the main wing, σ, as parameter.

To compare the effect of linearisation of the elastic DoF, Figure 6.16(a) also presents the dynamic behaviour obtained using the consistently linearised flexible-body dynamics formulation, Eq. (2.37), which suggests that geometrically nonlinear deformations have a negligible effect on the aircraft motion in the x-y plane. The effect of geometric nonlinearity is very different in the altitude response of the aircraft. This is demonstrated in Figure 6.17, which shows the maximum error of the linearised formulation to compute the vertical position for varying flexibility of the main wing. The maximum norm of the HALE aircraft altitude was used to normalise the error for each σ. The linearised solution accurately captures the rigid-body response for mildly-flexible vehicles ($\sigma \geq 5$ corresponding to 7% wing tip deflections), but the geometrically nonlinear deformations dominate for more flexible configurations.

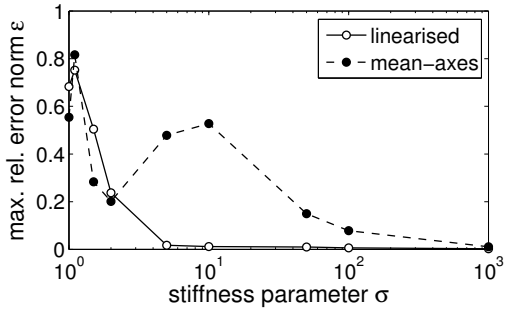
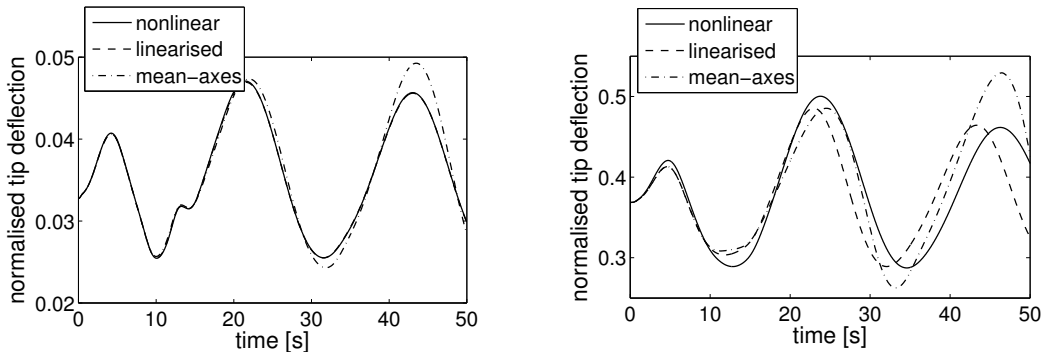


Figure 6.17: Maximum relative error norm of aircraft altitude using linearised and mean axes approximations compared to the nonlinear solution for $\lambda = 1/4$ and varying stiffness σ.

The open-loop response of the HALE aircraft has also been computed using the mean axes approximation, as introduced in Subsection 5.2.2 for the flexible multi-beam configuration. In the problem studied now, aerodynamics are also included but they are computed on the actual instantaneous geometry. For small deformations this converges to the classical mean axes approximation, as it is commonly found in flight dynamic simulations [162], and allows to isolate the effect of inertial decoupling of the flexible-body dynamics equations. The mean axes solution to the rigid-body response of the HALE aircraft is included in Figures 6.16 and 6.17 and compared with the fully-coupled, nonlinear reference solution. The error norm in Figure 6.17 gives an insight into the effect of neglecting the gyroscopic forces due to elastic deformations. One would expect the error to increase with flexibility, as is the case for $\sigma < 2$, but a local maximum occurs at $\sigma = 10$ which represents a rather stiff configuration with 5% maximum wing deformations. We saw from Figure 6.15(b) that the angular velocity of the aircraft, and hence the contribution of the gyroscopic forces, reduces with increasing flexibility. This competition between the opposing effects of gyroscopic forces and flexibility results in the peak at around $\sigma = 10$.



(a) $\sigma = 10$ (b) $\sigma = 1.1$

Figure 6.18: Vertical tip deflection of the right main wing normalised with the semi-span of $B = 16$ m for dihedral ratio of $\lambda = 1/4$.

The right wing tip deflection is presented in Figure 6.18 for a stiff ($\sigma = 10$) and a very flexible ($\sigma = 1.1$) aircraft. Whereas the flexible case exhibits static equilibrium deformations of 37% of the semi-span, the maximum amplitude in the transient around this equilibrium is below 10% of the semi-span. As a result, the linearised formulation is able to capture the amplitudes of the large deformations well even for the very flexible problem, which is presented in Figure 6.18(b). However, as the mass matrix is assumed constant in the linearised approach, the change in geometry due to the deformations and the resulting change in stability behaviour of the aircraft cannot be captured which results in a frequency shift. Figure 6.19 shows the maximum error norm of the vertical wing tip displacement which were normalised with the maximum wing deformations for each σ. The linearised approach predicts the displacements well even for very flexible aircraft with $\sigma = 2$ and wing deformations of up to 26% of the semi-span. For more flexible configurations the resulting phase shift due to geometric nonlinearity effects dominate.

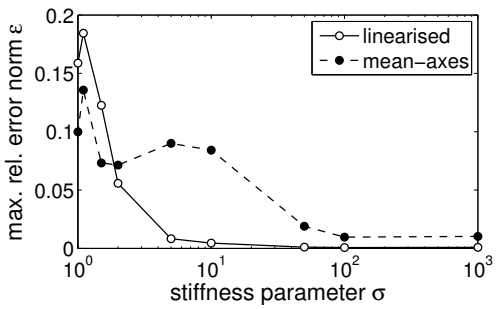


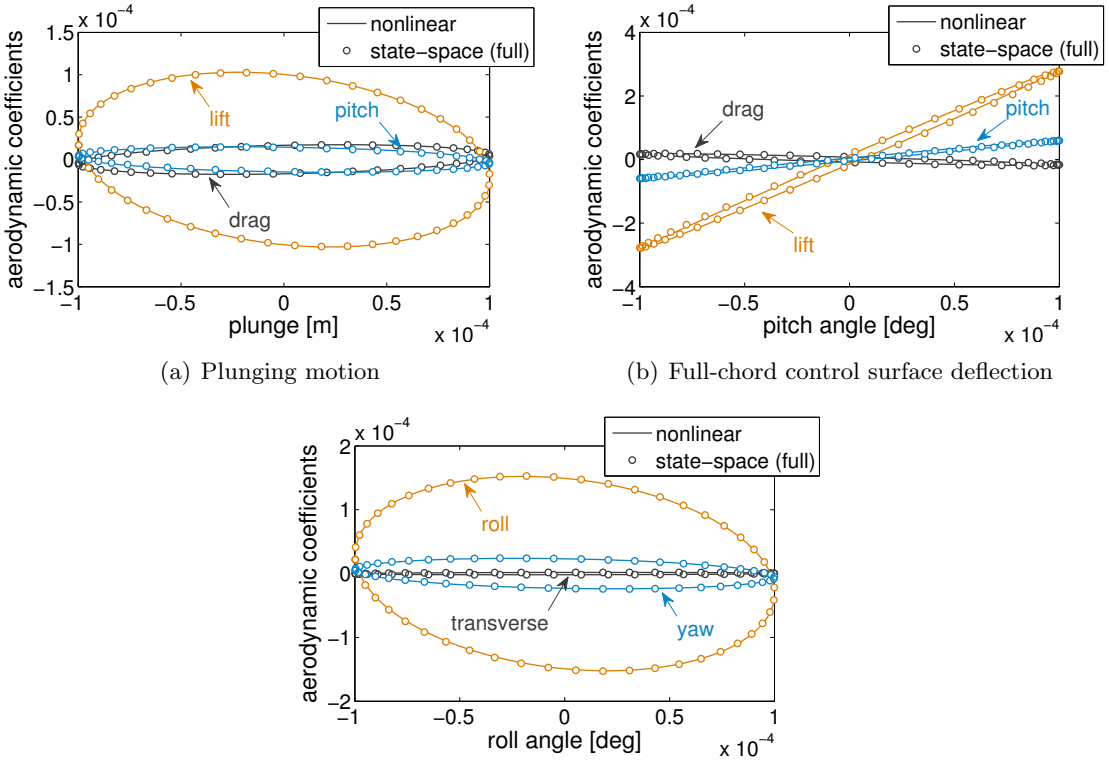
Figure 6.19: Maximum relative error norm of vertical wing tip deflections for $\lambda = 1/4$ and varying σ.

At last, it is shown that the mean axes approximation tends to overpredict the elastic deformations in the open-loop dynamics. Figure 6.18(a) indicates that even for relatively stiff problems ($\sigma = 10$), corresponding to maximum deflections below 5% of the semi-span, the mean axes approximations results in errors around 9% compared to the nonlinear reference solution. Similar to the FMB problem, Figure 6.19 shows that even for near-rigid vehicles ($\sigma \geq 100$) the relative error remains constant around 1% for the commanded manoeuvre.

Whereas it was shown in Figure 6.17 that the mean axes approximation can give a good estimate of the open-loop flight dynamic response for very stiff structures, we see that it results in unreliable predictions of the elastic deformations even for very stiff aircraft. This makes it less suitable for the prediction of dynamic manoeuvre and gust loads. Instead, the proposed consistent linearisation of the structural DoF includes all gyroscopic couplings and accounts for large wing deformations at the trim equilibrium. The linearised flexible-body dynamics equations can also be projected on a few vibration modes of the unconstrained vehicle which will be demonstrated next as a starting point for further model reduction of the aeroelastic framework.

6.2.4 Reduced-Order Modelling of the Manoeuvring Flexible Aircraft

This section will demonstrate the application of balancing methods, as outlined in Subsection 4.3.2, to obtain the unsteady aerodynamic loads of the flexible HALE aircraft subject to commanded antisymmetric aileron inputs. The open-loop response of the manoeuvring vehicle will be modelled using the coupled aeroelastic framework presented in Subsection 3.2.3 which is based on the consistent linearisation of the vehicle aeroelastic DoF. Hence, under the assumption of small displacements and slow manoeuvres, the generalised unsteady aerodynamic loads are computed in time domain using the linearised UVLM. The inputs to the linear aerodynamic system are defined in Eq. (3.18) as the generalised coordinates, u_Φ, and the aerodynamic inputs, u_F, to account for control surface deflections and atmospheric disturbances.



(a) Plunging motion

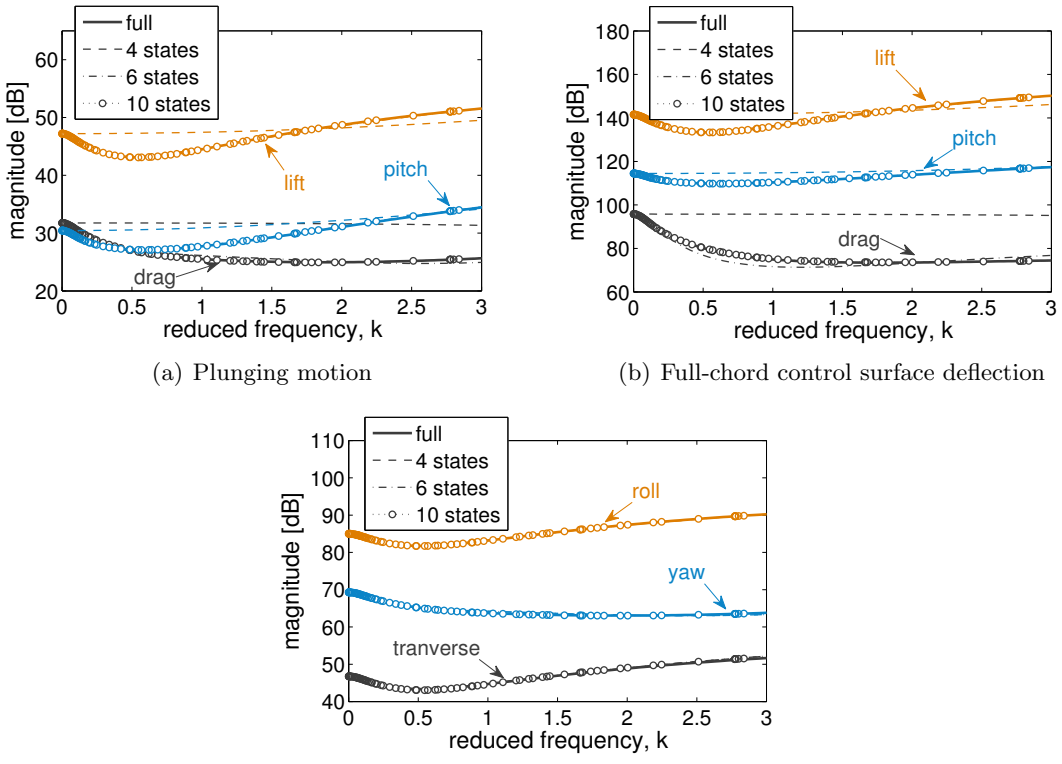
(b) Full-chord control surface deflection

(c) Rolling motion

Figure 6.20: Aerodynamic coefficients for the flexible HALE wing ($\sigma = 5$, no dihedral, and 5 deg AoA) subject to forced harmonic rigid-body motions of the A frame with $\omega = 2\pi$ rad/s: comparison between the geometrically-nonlinear time-marching and the linearised full-order state-space solutions.

Before the reduced-order modelling approach will be applied to flexible aircraft problems, the linearisation of the UVLM is verified for a subproblem of the HALE configuration. The flexible main wing with $\sigma = 5$ and zero-degree dihedral angle of the winglets is subjected to prescribed harmonic motions of the origin of the A frame (fixed to the wing root). Sinusoidal plunge, pitch, and roll perturbations with an excitation frequency

of $\omega = 2\pi$ rad/s (reduced frequency of $k \approx 0.1$) are prescribed with respect to the inertial frame around a geometrically-nonlinear equilibrium condition at 5 deg angle of attack and $V_\infty = 30$ m/s. This problem allows the verification of the aerodynamic load calculation of the aeroelastic framework in Eq. (3.18), where plunging and rolling motions of the flexible wing are prescribed manoeuvres through the input u_Φ and the pitching motion is inputted through u_A to verify a full-chord, full-span control surface deflection. Comparison of the dominant aerodynamic coefficients with the geometrically nonlinear time-marching solution in Figure 6.20, demonstrates the validity of the linearised full-order state-space approach to predict the 3D unsteady aerodynamic loads. Note that, following the familiar definition of the lift and pitching moment coefficients, the aerodynamic forces and moments have been normalised with the dynamic pressure, $(0.5\rho V_\infty)$, and the total wing area of 32 m^2. The resultant moments have been further normalised with the wing chord to obtain aerodynamic moment coefficients.



(a) Plunging motion

(b) Full-chord control surface deflection

(c) Rolling motion

Figure 6.21: Comparison of reduced-order models in terms of frequency response of flexible HALE wing ($\sigma = 5$) with aerodynamic loads due to the harmonic plunging, pitching and rolling motions for different reduced frequencies, $k = \omega c/(2V_\infty)$.

It is now convenient to first demonstrate the proposed reduced-order modelling approach for manoeuvring aircraft, introduced in Subsection 4.3.2, on the simplified HALE wing subject to prescribed harmonic motions. For the converged solution, the size of the

full-order aerodynamic system reaches 4864 states due to the fine discretisation of the wake for a time step of 0.02 s (and the same wing and wake discretisation as in Section 6.2.2). However, wake panels that have converged far downstream may have only a small contribution on the unsteady aerodynamic loads which provides the motivation for model reduction. Figure 6.21 demonstrates the potential of balanced truncation on the large multi-input/multi-output aerodynamic system, which maps the 774 structural and rigid-body inputs to 390 aerodynamic load outputs. Note that the system inputs have been converted to a state-space representation which corresponds to $2 \times 6 \times 64$ nodal displacements and velocities and 6 rigid-body velocities. Figure 6.21 shows the frequency response of different reduced-order aerodynamic systems for the above harmonic plunging, pitching and rolling motions and the corresponding dominant unsteady aerodynamic loads as outputs over a range of reduced frequencies, $k = \omega c/(2V_\infty)$. The number of retained balanced states were chosen according to the HSV of the balanced system (not shown here). The results in Figure 6.21 suggest that as little as 6 aerodynamic states (from the original 4864 states) are sufficient to compute the unsteady loads of the flexible wing subject to rigid-body motions and control surface deflections even at high reduced frequencies.

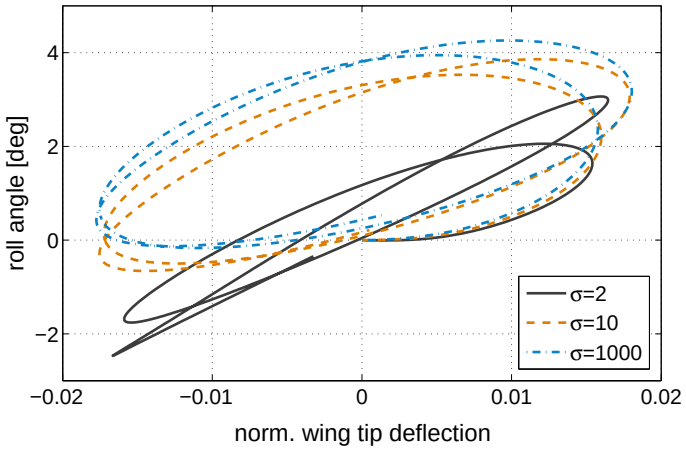
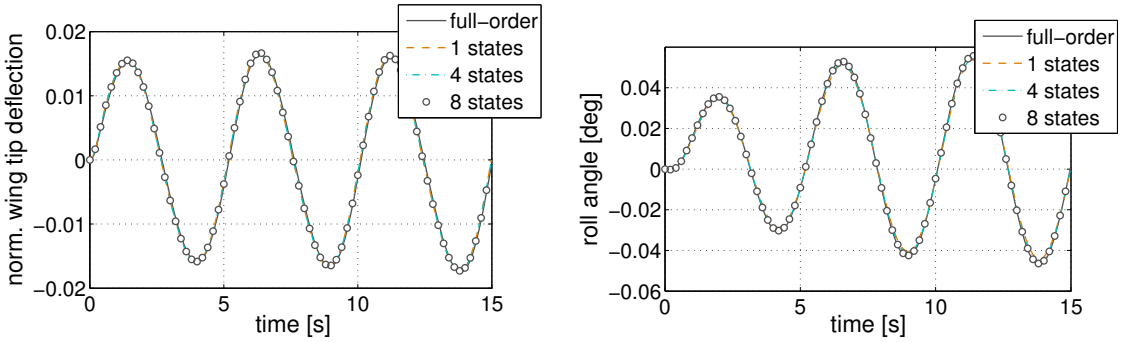


Figure 6.22: Open-loop response of HALE aircraft subject to antisymmetric aileron inputs for the full-order state-space system for varying stiffness, σ. Tip deflections are normalised with $B \cdot \sigma^{-1}$.

At last, modal reduction of the nonlinear flexible-body dynamics EoM, as outlined in Section 2.3, will be demonstrated on the open-loop response of the full HALE configuration subject to antisymmetric, sinusoidal aileron inputs. With a frequency of 1.29 rad/s and amplitude of 5 deg, the aileron excitation is comparable to the Dutch roll mode of the flexible configuration with $\sigma = 5$, as shown in the previous stability analysis in Subsection 6.2.2. The resulting full-order open-loop response is presented in Figure 6.22 in terms of the correlation between the rigid-body response (roll angle of the aircraft) and the structural dynamics behaviour (deflection of the right wing tip normalised with the

semi-span B and the stiffness parameter, σ). The transient response is shown for three cases of σ, where $\sigma = 1000$ corresponds to the near-rigid configuration. Even though the aileron excitation results in small structural deformations below 1%, in addition to the (large) trim deformations, the effect on the rigid-body response is significant. While the near-rigid configuration always returns to its initial roll attitude, the flexible aircraft configurations overshoot instead and thus amplify the gyroscopic coupling between the (stable) structural and flight dynamics.



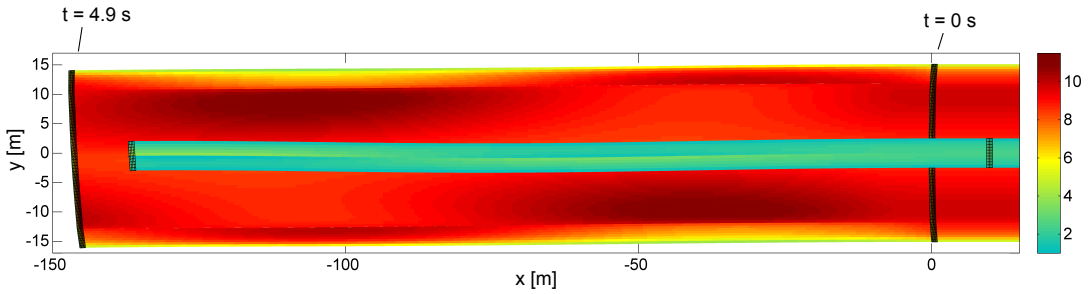
(a) Vertical tip deflection normalised with $B \cdot \sigma^{-1}$

(b) Aircraft roll response

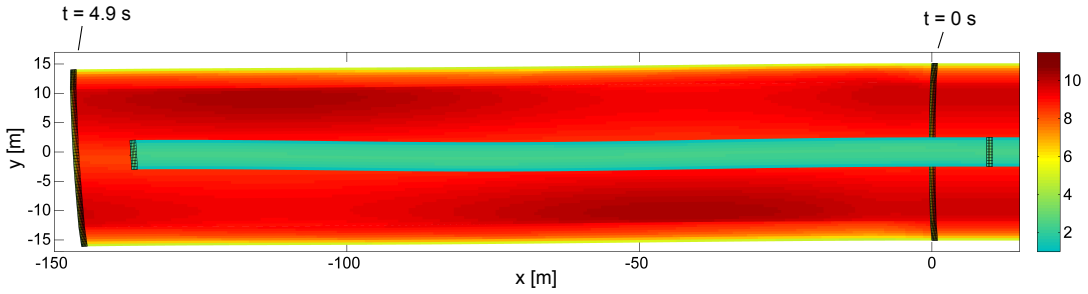
Figure 6.23: Effect of model order of aerodynamic system on open-loop response of HALE for $\sigma = 2$ and all flexible-body dynamics modes.

The reduced-order modelling approach for the time-marching solution of manoeuvring flexible aircraft, as presented in Figure 4.5, enables a twofold reduction of the aerodynamic subsystem and the modal form of the flexible-body dynamics module through separate balanced and modal truncations, respectively. Balanced truncation of the large aerodynamic system will be explored first. Comparison of the aircraft roll response and the resulting elastic deformations for different reduced-order models in Figure 6.23 illustrates that only one (balanced) aerodynamic state is sufficient to represent the main flow features of the full-order aerodynamic model which originally had over 3000 states. More states would be required to resolve the unsteady effects of the control surface deployment.

This is also reflected in Figure 6.24, which shows the time history of the wake of the manoeuvring aircraft for the first period of the antisymmetric aileron input, $0 \leq t \leq 4.9$ s. Note that in the actual simulation the wake is truncated at 15 chord-lengths and Figure 6.24 instead presents the evolution of circulation strength of the trailing edge vortex panels as they are shed into the wake at each time step. The results of the reduced-order system have been retrieved through reverse transformation of the truncated balanced state vector. Comparison with the full-order model shows that variations in the flow due to the aircraft motion are captured accurately despite the tremendous reduction of the aerodynamic model.

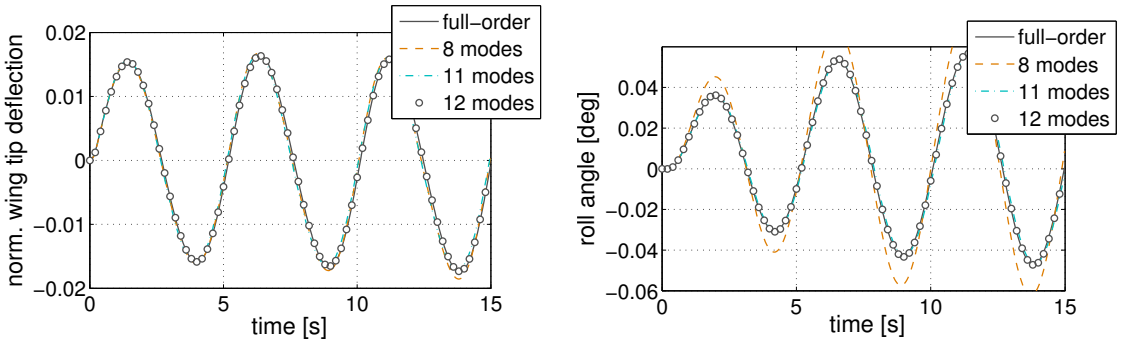


(a) Full-order aerodynamic model with 3120 states



(b) Reduced-order balanced system with four aerodynamic states

Figure 6.24: History of the wake for the manoeuvring flexible aircraft with $\sigma = 2$ subject to aileron inputs, showing circulation strengths of the wake vortex rings, Γ_w.



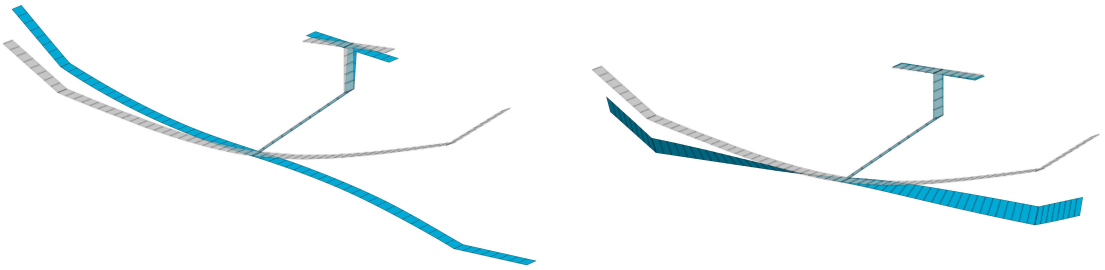
(a) Vertical tip deflection normalised with $B \cdot \sigma^{-1}$

(b) Aircraft roll response

Figure 6.25: Effect of number of flexible-body dynamics modes (ascending order of frequency) on open-loop response of HALE for $\sigma = 2$ and full-order aerodynamic system.

These results have been obtained using the full finite-element model and further model reduction also of the flexible-body dynamics model can be achieved through modal truncation of the structural states, as shown in Figure 6.25. This also reduces the large number of inputs and outputs of the (reduced-order) aerodynamic system. Note that the modal truncation includes all modes in ascending order of the vibration frequency, even though it is clear from the antisymmetric nature of the excitation that antisymmetric bending/torsion modes predominantly contribute to the elastic response of the aircraft. The first anti-

symmetric bending mode (mode 8), in addition to the six rigid-body modes, is sufficient to capture the bending response of the aircraft, as shown in Figure 6.25(a). The vehicle roll response in Figure 6.25(b), however, is strongly affected by the twisting of the main wing due to the aileron excitation. Hence, the first antisymmetric torsion mode (mode 11) is also required to fully capture the dominant lateral dynamics of the HALE aircraft. Both structural modes of the unconstrained aircraft have been depicted in Figure 6.26 for illustration.

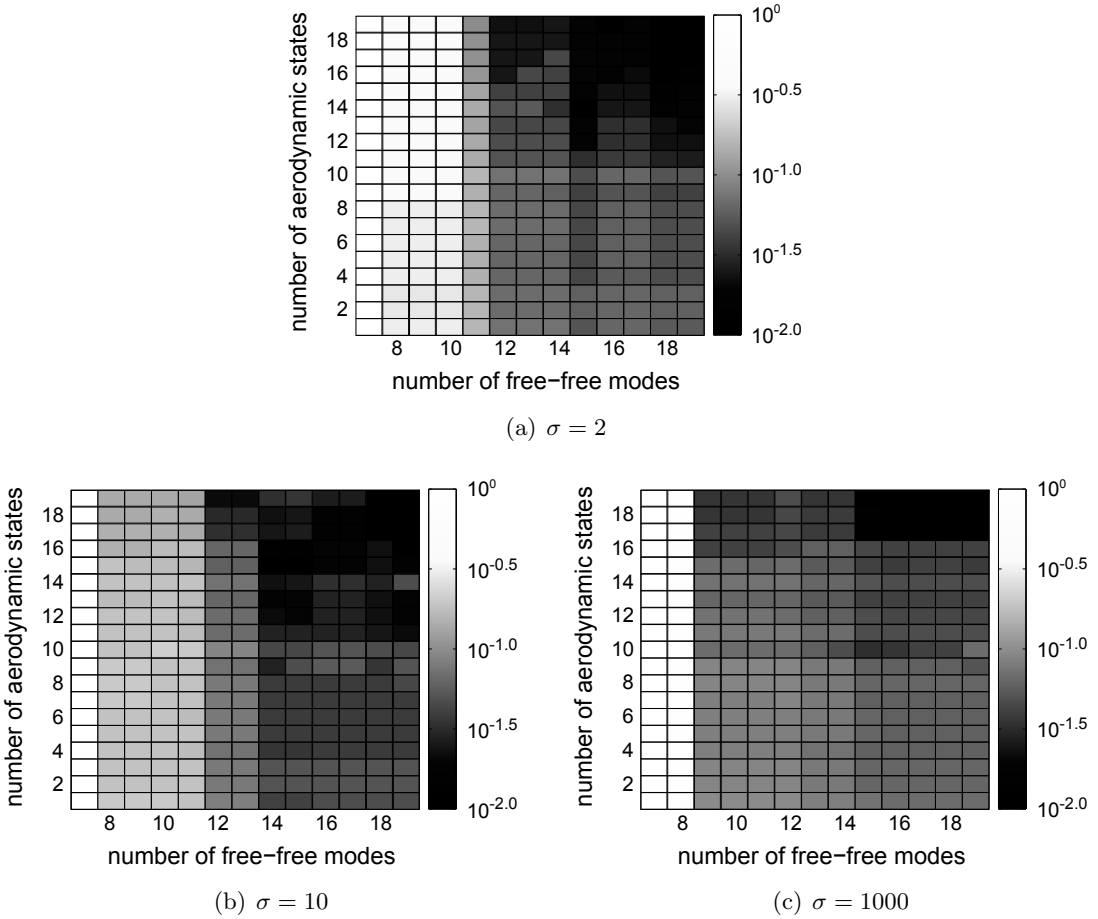


(a) 12.97 rad/s (b) 24.78 rad/s

Figure 6.26: First antisymmetric (a) bending and (b) torsion structural modes of the flexible HALE configuration ($\sigma = 2$) around trimmed flight condition (trim geometry superimposed in gray).

As a result of the model reduction, only eight flexible-body modes (two structural and six rigid-body modes) and a single aerodynamic state are required to model the lateral dynamics of the manoeuvring aircraft with maximum relative errors below 10%, but naturally the elastic response is captured more accurately if additional higher-frequency modes are included in the projection of the flexible-body dynamics EoM. This can be seen from Figure 6.27, which shows the L_∞ error of the elastic (tip deflection) and rigid-body (roll angle) response for the three HALE configurations presented in Figure 6.22, where the maximum of both error norms is shown. The relative error, which is normalised with the maximum wing deflection and roll angle for each σ, respectively, shows the contribution of the elastic modes and balanced aerodynamic states on the accuracy of the reduced-order system response. For the most flexible configuration in Figure 6.27(a), the antisymmetric bending and torsion modes (8,11,12,15,18) clearly dominate the response but, as expected, the number of required elastic modes reduces significantly for the stiffer aircraft in Figures 6.27(b)-(c).

Increasing the number of free-free modes in the projection of the flexible-body dynamics EoM may increase accuracy of the higher frequency response, but it can also deteriorate the effectiveness of balanced truncation of the aerodynamic system. This is evident in Figure 6.27(a), where the inclusion of unnecessary symmetric elastic modes, e.g. modes 13-14 and 16-17, harms the accuracy of the reduced-order models for a given number of aerodynamic states. The symmetric modes contribute little to the system response,



(a) $\sigma = 2$

(b) $\sigma = 10$

(c) $\sigma = 1000$

Figure 6.27: Relative L_∞ error of the HALE aircraft reduced-order open-loop response for varying number of aerodynamic states and free-free modes (including the six rigid-body modes) and three values of the stiffness parameter, σ.

but increase the number of inputs and outputs of the aerodynamic system and more aerodynamic states are required to restore accuracy. This is an important aspect, if the proposed aeroelastic reduced-order modelling approach were to be used for control synthesis and/or optimisation.

In summary, the model reduction approach produces very low-order aeroelastic models which can still accurately predict the dynamic response of flexible manoeuvring aircraft. This is done for very flexible configurations with geometrically nonlinear wing deformations at trimmed flight. The results in Figure 6.27 show that the full-order aerodynamic system can be reduced dramatically (by three orders of magnitude) and still captures the inherent 3D features of the unsteady flow which are tightly coupled with the flexible-body dynamic response of the aircraft. Modal projection of the flexible-body dynamics formulation furthermore allows to control the number of inputs and outputs of the aerodynamic system, which results in closed-form expressions of the EoM that accurately capture the gyroscopic couplings between the rigid-body and the structural dynamics.

Chapter 7

Conclusions

This chapter will highlight the main outcomes of the multidisciplinary effort addressed in this work. The first section will focus on the most important numerical challenges that had to be solved in the integration of very diverse theories. The key contributions of the resulting modelling approach will be presented in Section 7.2. Any accomplishments of this work should nourish the ground for new questions. Section 7.3 will therefore finish this dissertation by identifying pending issues and interesting applications that the presented work can encourage.

7.1 Overall Conclusions

A reduced-order coupled aeroelastic and flight dynamics modelling approach for flexible aircraft with a consistent linearisation of the structural dynamics around a nonlinear static trim equilibrium was presented. This tightly coupled framework efficiently captures the complex interactions between the elastic and flight dynamics response of manoeuvring flexible aircraft.

This work is relevant for the development of next-generation aircraft with very high-aspect-ratio wing configurations. This increases efficiency of long-endurance vehicles, but it can also result in large wing excursions that current design methodologies fail to incorporate. Hence, the design of such aircraft should account for aeroelastic effects such as gust and manoeuvre loads, flutter and control reversal. However, numerical efficiency of the simulation environment is also a requirement for a fast turnaround in the design process and the development of autonomous navigation systems for HALE UAVs.

7.1.1 Theoretical Development

The dynamics of manoeuvring flexible aircraft has commonly been computed using the mean axes approximation to separate the vehicle flight dynamics from the structural response. This crucial assumption enables the use of frequency-based unsteady aerodynam-

ics, such as the doublet-lattice method over a range of reduced frequencies [5]. In this work, we have shown that the resulting aeroelastic predictions are limited to relatively stiff vehicles and may no longer be valid in high-load situations or for very flexible configurations. Although geometrically-nonlinear approaches have recently provided great insight into the effect of large wing deformations on the flight dynamics of flexible aircraft [142, 169, 187, 197], they are computationally too expensive to be effective in aircraft design.

Hence, a major motivation for this work was to develop an efficient low-order representation of the coupled dynamics of very flexible aircraft. To achieve this, we firstly focused on the flexible-body dynamics formulation, which was obtained by extending a geometrically-nonlinear displacement-based beam formulation to account for large rigid-body motions. We have shown that a numerically-efficient implementation can be built using linear elements by parameterising the large rotations of the subcomponent cross-sections using the Cartesian rotation vector. This parameterisation of the local rotations also provides expressions for the linearisation of the rotational degrees of freedom, which was used in the consistent linearisation in only the elastic degrees of freedom using perturbation methods. Hence, under the assumption that the structural subcomponents are subject to small transient deformations, this linearised formulation results in flexible-body dynamics equations written in matrix form, with coefficients that vary only with the vehicle rigid-body velocities. In a time-marching solution, this implies that the damping and stiffness coefficients have to be computed as the body-velocity changes, but the equations are still linear in the structural degrees of freedom. A very large reduction in problem size can then be obtained if the FEM discretisation is approximated by a small number of low frequency vibration modes of the unconstrained structure. Unlike to the mean axes approximation, the linearisation of the structural degrees of freedom in this work is consistent and captures all couplings between the nonlinear rigid-body dynamics and the linearised structural dynamics due to gyroscopic effects. This provides a higher-fidelity approach compared to the mean axes approximation, which naturally neglects these coupling terms, but at a similar computational cost.

The unsteady aerodynamic flow around the instantaneous aircraft geometry was captured in this work using a 3-D geometrically-nonlinear implementation of the unsteady vortex lattice method. The resulting aerodynamic loads of the manoeuvring aircraft are obtained directly in time domain which greatly simplified the integration of the unsteady aerodynamics with the flexible-body dynamics response of the aircraft. The perturbed form of the flexible-body dynamics equations for small transient wing deformations has also been coupled directly with the linearised version of the UVLM, which is computed around a nonlinear aeroelastic trim equilibrium – including a deformed aerodynamic lattice and force-free wakes in the steady state. The size of the resulting aeroelastic and flight-dynamics system is thus comparable to that in the mean axes approximation, but it includes the inertial coupling between the possibly large vehicle flight-dynamics and the

small aeroelastic response. Moreover, it is also not necessary to pre-compute frequency-domain aerodynamics, as it is done in solutions based on the doublet lattice method.

The last part of this thesis demonstrated model reduction of the linearised aeroelastic subsystem in the transient analysis of manoeuvring flexible aircraft. The linearised state-space form of the UVLM is suited for the application of balancing methods which provide optimal model reduction of the aerodynamic subsystem. Completed with the modal form of the (nonlinear) flexible-body dynamics module, which reduces the number of generalised structural coordinates and aerodynamic loads, the proposed reduced-order modelling approach results in a very compact but accurate time-domain description of the flexible-aircraft dynamics. This provides a top-down solution methodology for robust control synthesis, dynamic load calculations, optimisation and real-time simulations based on a higher-fidelity but low-order aeroelastic model. Some of these applications have been demonstrated in this work, as outlined next.

7.1.2 Numerical Simulations

The multi-fidelity descriptions of the flexible-body and aerodynamic modules have been integrated in the framework for Simulation of High-Aspect-Ratio Planes (SHARP) which enables the complete study of very flexible aircraft configurations. The numerical results presented in this dissertation contribute further verification studies of the different modules in SHARP and, secondly, demonstrate the proposed reduced-order methodology on a number of unconstrained problems without and with aerodynamics.

First, the flexible-body dynamics module was exercised on free-flying flexible multi-beam configurations subject to complex time-variant load cases to verify the implementation of the geometrically nonlinear formulation. As opposed to other geometrically nonlinear approaches, i.e. the intrinsic or strain-based formulations, the implemented displacement-based method provides direct physical insight into the coupled problem, which was used to ensure the correct coupling between the structural and rigid-body dynamics response of the flexible body. The nonlinear formulation then provided the reference solution to investigate the effect of geometric nonlinearity on the transient response of the unconstrained structure (without aerodynamics). Further studies finally exercised the modal approach of the flexible-body dynamics module written in tensor form which identified important gyroscopic coupling terms between different elastic modes and the rigid-body motion.

The flexible-body dynamics results in Section 5.2 also served to assess the mean axes approximation. Whereas the rigid-body response always converged to the rigid case for very stiff problems, the mean axes approximation failed to predict the elastic deformations accurately for problems of rotational nature. This result was shown, both analytically and numerically, to be independent of the level of deformation. More importantly, it was shown that the error in the mean axes approximation correlates directly to the angular velocity

of the flexible body. Neglecting the gyroscopic couplings may therefore have an important effect in the aircraft dynamic manoeuvre loads.

To test that, the proposed linearised framework was also exercised in Chapter 6 on a T-tailed aircraft representative of a HALE UAV. Starting from the geometrically-nonlinear trim equilibrium, an eigenvalue analysis of the monolithic aeroelastic and flight-dynamic system revealed the stability characteristics of the flexible aircraft. In particular, it was shown that large wing dihedral, due to either large wing deformations at trim or designed features such as winglets, had a dramatic effect on the (flexible) flight-dynamic modes; the lateral modes were stabilised with detrimental effects on longitudinal modes increasing the likelihood of unstable phugoid modes. Stability analyses also demonstrated the frequency overlap between the aerodynamic, aeroelastic and flight-dynamic modes for very flexible HALE configurations. It further provided an insight into the effect of flow unsteadiness on the aircraft response, thus questioning the validity of quasi-steady models to capture the aerodynamics of manoeuvring aircraft even for relatively stiff vehicles.

The open-loop transient response of flexible configurations subject to commanded lateral control inputs confirmed the dramatic effect of geometrically-nonlinear trim deformations on the (nonlinear) vehicle dynamics and illustrated the coupling between the aircraft structural and flight-dynamics response. Both were shown to be adequately captured even for rather flexible configurations using the linearised formulation which assumes small wing deformations but allows the vehicle flight dynamics to be arbitrarily large due to, for example, aircraft manoeuvres or gusts.

The linearised formulation was then applied to assess the mean axes approximation. It was shown that inertial decoupling of the flexible-aircraft dynamics leads to wrong predictions of the elastic response even for stiff vehicles. The flight dynamics response on the contrary, was found to be adequately predicted using the mean axes approximation which enables the application of decoupled approaches for trajectory control of novel aircraft designs. However, for dynamic load calculations and certification of novel aircraft concepts, the proposed consistent linearisation of the aeroelastic degrees of freedom provides a higher-fidelity alternative to frequency-based aeroelastic tools.

To achieve comparable model order to frequency-based approaches, balanced truncation of the linear aerodynamic system was demonstrated on the open-loop response of the vehicle. This highlighted the potential of balancing methods for optimal model reduction which suggested that as little as one aerodynamic state was enough to capture the unsteady 3-D flow features of manoeuvring flexible aircraft. Similar to the studies without aerodynamics, projection of the flexible-body degrees of freedom onto a few vibration modes provided further model reduction of the nonlinear flexible-body dynamics equations. It also reduced the number of generalised structural coordinates and aerodynamic loads – the inputs and outputs of the aerodynamic system – which has been shown to improve the effectiveness of balanced model reduction of the linear aerodynamic subsystem.

Hence, the proposed balanced model reduction approach of the aeroelastic framework provides a powerful tool for the simulation of highly-efficient flexible aircraft at a similar computational cost compared to linear frequency approaches based on the doublet lattice method. The proposed method however removes kinematic restrictions and obtains the aerodynamic loads directly in time domain, which makes it also ideal for control synthesis and optimization. The former has been demonstrated for the synthesis of a robust flutter suppression system using $\mathcal{H}_\infty$ control, which was exercised on the Goland wing problem at 7% above the flutter velocity. A controller based on a reduced-order model with only two balanced states performed best to stabilise the aeroelastic response. Other applications of the proposed reduced-order modelling approach will be suggested for future work in Section 7.3.

7.2 Key Contributions of this Thesis

This thesis has contributed significantly to the development of a reduced-order modelling approach for the coupled flight dynamics and aeroelastic response of manoeuvring flexible aircraft with large (geometrically-nonlinear) static trim deformations. To arrive at this novel methodology, several key developments were needed:

- A geometrically-nonlinear, displacement-based composite beam formulation was extended to account for the rigid-body motions of flexible aircraft. Coupled with a 3-D unsteady vortex-lattice method the resulting unified framework was applied to a HALE configuration to demonstrate the effect of wing flexibility on the flight dynamics of high-aspect-ratio vehicles.

- A consistent linearisation in the aeroelastic variables and subsequent modal projection around the nonlinear static trim equilibrium of very flexible aircraft has been derived and was used to demonstrate the effect of geometric nonlinearity on the flight dynamic response of flexible aircraft.

- The proposed linearisation preserves all gyroscopic coupling terms which was shown to be critical for the accurate prediction of manoeuvre loads. Comparison to the mean axes approximation analytically and numerically demonstrated that standard frequency approaches based on the doublet-lattice method fail to accurately predict the aeroelastic response for lateral aircraft manoeuvres.

- Model reduction of the unsteady aerodynamics using balancing methods resulted in a low-order description of the integrated flexible-aircraft dynamics around geometrically-nonlinear trim equilibria which was demonstrated for manoeuvring HALE aircraft and the synthesis of a robust $\mathcal{H}_\infty$ controller for flutter suppression.

- Synthesis of a robust $\mathcal{H}_\infty$ controller for flutter suppression demonstrated the top-down approach for unstable systems.

7.3 Recommendations for Future Work

The implementation of the framework for Simulation of High-Aspect-Ratio Planes (SHARP) in collaboration with Dr Joseba Murua has produced a very comprehensive simulation tool to model the static and dynamic characteristics of very flexible configurations. This dissertation has presented a number of testcases to demonstrate many of the capabilities of the code, but the proposed low-order description of the vehicle dynamics certainly leaves more scope for application in aircraft aeroelastic design. To conclude, we present a critical overview on how the modelling approach can be improved further to cater for these futures applications.

7.3.1 Application of the Simulation Framework

The numerical studies in Chapter 6 demonstrated the stability and open-loop characteristics of a representative HALE configuration for different geometries (varying the size of winglets) and flexibility (decreasing weight). Further studies can be done to leverage the benefits of the time-domain representation of the aeroelastic system in MATLAB®, as will be outlined next.

Optimisation of composite wing structures and aeroelastic tailoring can be explored to take advantage of the directionality property of anisotropic materials, which has been demonstrated for weight reduction [75], passive flutter suppression [111] and gust alleviation [147]. The derivation of the beam equations in Chapter 2 accounts for fully-populated cross-sectional mass and stiffness matrices which can capture the bending coupling in anisotropic materials. However, incorporation of a suitable homogenisation procedure in SHARP is required to obtain the (composite) material properties in the 1-D beam representation [50]. Interfacing the stability tool in SHARP with the MATLAB® Optimisation Toolbox would then provide an ideal starting point to explore aeroelastic tailoring on a full aircraft configuration including 3-D unsteady aerodynamics and large trim deformations.

Robust control for gust load alleviation should be explored to demonstrate the proposed reduced-order modelling approach for a range of excitation frequencies. Application of balancing methods to manoeuvring flexible aircraft demonstrated significant model reduction by several orders of magnitude. It is necessary to investigate if this reduction potential also holds over a range of frequencies for very flexible aircraft subject to continuous turbulence. Further discrete gust responses of the HALE configuration could also serve to identify the limits of the consistent linearisation of the aeroelastic degrees of freedom which assumes small transient wing deformations (around geometrically-nonlinear trim equilibria). Critical gust lengths may result in large wing excursions which may not be captured adequately with the linearised approach and hence exceed the robustness properties of a $\mathcal{H}_\infty$ controller synthesised from the reduced-order linearised model [39].

Autonomous navigation and active flutter suppression of full HALE configurations should be explored further to demonstrate the application of the proposed top-down aeroelastic modelling approach. Active flutter suppression systems in addition to aeroelastic tailoring have a huge potential for substantial weight reduction [144]. The $\mathcal{H}_\infty$ control synthesis presented in Chapter 6 could be easily extended to a free-flying aircraft configuration to minimise flutter vibrations. The second aspect is concerned with autonomous guidance and navigation of highly-efficient UAVs. This challenge has been addressed in the robotics community using model predictive control (MPC) for motion planning and navigation of autonomous unmanned vehicles around a predefined map. This has been demonstrated, for example in Refs. [26, 61], only for rigid platforms. For autonomous navigation of high-aspect-ratio HALE vehicles, the controller would need to know some information about the flexibility effects which can significantly alter the vehicle response, as shown in Chapter 6. This could be addressed by exploring MPC methods using the (nonlinear) reduced-order modelling framework in SHARP that captures the dynamics of manoeuvring flexible aircraft.

Real-time flight simulations of very flexible aircraft can provide useful information about the robustness of the designed gust alleviation and flutter suppression controllers due to pilot inputs and atmospheric turbulence. The dramatic model reductions achieved in this work could enable real-time simulations of modern flexible aircraft configurations based on the medium-fidelity aeroelastic framework in SHARP for manoeuvring vehicles.

Experimental demonstration of the aeroservoelastic modelling approach on a small-scale UAV with high-aspect-ratio wings should be considered. Each module in the developed framework has been validated individually against experimental results, but validation of the coupled geometrically-nonlinear response requires real flight data of very flexible configurations. As an alternative to the development of the very flexible X-HALE [38], modification of an off-the-shelf model sailplane, as proposed by Iscold *et al.* [93], could provide a low cost platform for validation of the geometrically-nonlinear aeroelastic and flight-dynamics framework in SHARP. Application of the controllers would also demonstrate robustness of the autonomous navigation, gust alleviation and flutter suppression systems and highlight the benefits of using higher-fidelity aeroelastic tools in the control synthesis.

7.3.2 Improvements to the Current Methodology

Some of the applications proposed for future work may challenge and/or exceed the applicability of the analysis methods behind SHARP. This subsection will therefore propose some modifications to either improve efficiency of the current implementation or extend the theory.

Numerical efficiency of the aeroelastic framework can be improved significantly by implementing the aerodynamic and flexible-body dynamic modules in compiled program-

ming languages, such as C or Fortran. Application of the reduced-order framework for control synthesis heavily relies on built-in MATLAB®, but alternative approaches exist. As shown by Simpson *et al.* [181], the low-level routines in SHARP can be efficiently coded in compiled languages and interfaced using the Python environment, which also provides libraries incorporating all standard methods in system and control theory. The authors also demonstrated the numerical benefits of the parallelisation of the time-domain solution to the UVLM to significantly reduce the simulation run-time.

The issue of objectivity in the FE discretisation of the geometrically-exact beam formulation in Chapter 2 remains an open problem in this work which has been tackled in the numerical studies using a very fine mesh with linear interpolation. Computational efficiency could be improved, however, by either using 3-noded elements in the discretisation of the beam equations or implementing an objective interpolation of the rotational degrees of freedom [44]. The former has also been shown by Simpson *et al.* [181] to provide sufficient convergence.

The interfacing between the aerodynamic and flexible-body dynamic subproblems can also be improved using the (quadratic) shape functions in the interpolation of the beam variables. The mapping procedure proposed by Brown [24] enables the interpolation of the aerodynamic loads and structural motion at non-matching discrete interfaces. This would *overcome the limitation of coincident meshes* of the aerodynamic and structural subdomains, as assumed in Chapter 3, and therefore enable individual mesh refinement to improve mesh convergence and computational efficiency of each module in the aeroelastic framework.

Balanced truncation of nonlinear systems [102, 161] can extend the proposed reduced-order aeroelastic framework to geometrically nonlinear problems to overcome the limitation of small wing deformations in the transient. This is relevant for nonlinear trajectory control and load alleviation of UAVs subject to long gusts which can lead to large wing excursions; a situation that is likely to occur in the autonomous navigation of high-aspect-ratio aircraft operating at high altitudes. A nonlinear reduced-order aeroelastic model that accounts for geometrically-nonlinear wing deformations would therefore provide an ideal starting point to investigate the application of nonlinear control methods to very flexible aircraft problems.

The modular integration of the aircraft aerodynamics and flexible-body dynamics in a unified framework, as presented in Chapter 3, enables *higher-fidelity aerodynamic solution methods* to be used in the framework to obtain the unsteady aerodynamic loads. In fact, a *hybrid CFD/UVLM solution* that can capture viscous effect, stall, thickness of wings and the aerodynamics of non-lifting surfaces or propellers for manoeuvring flexible aircraft, may provide the ideal balance between model fidelity and computational cost. Balancing methods combined with other model reduction methods for large-scale systems, such as

POD, can be applied to the resulting aerodynamic system to further reduce the model order [8, 200].

Bibliography

[1] *European Aeronautics: A Vision for 2020.* Office for Official Publications of the European Communities, Luxembourg, 2001. ISBN 9289405597.

[2] *Flightpath 2050: Europe's Vision for Aviation.* Office for Official Publications of the European Communities, Luxembourg, 2011. ISBN 9789279197246.

[3] O. P. Agrawal and A. A. Shabana. Dynamic analysis of multibody systems using component modes. *Computers & Structures*, 21(6):1303–1312, 1985. doi: 10.1016/0045-7949(85)90184-1.

[4] O. P. Agrawal and A. A. Shabana. Application of deformable-body mean axis to flexible multibody system dynamics. *Computer Methods in Applied Mechanics and Engineering*, 56(2):217–245, 1986. doi: 10.1016/0045-7825(86)90120-9.

[5] E. Albano and W. P. Rodden. A Doublet-Lattice Method for Calculating Lift Distributions on Oscillating Surfaces in Subsonic Flow. *AIAA Journal*, 7(2):279–285, 1969. doi: 10.2514/3.5086.

[6] D. Amsallem and C. Farhat. An Online Method for Interpolating Linear Parametric Reduced-Order Models. *SIAM Journal on Scientific Computing*, 33(5):2169–2198, 2011. doi: 10.1137/100813051.

[7] G. L. Anderson. On the extensional and flexural vibrations of rotating bars. *International Journal of Non-Linear Mechanics*, 10(5):223–236, 1975. doi: 10.1016/0020-7462(75)90014-1.

[8] A. C. Antoulas. *Approximation of Large-scale Dynamical Systems.* Society for Industrial and Applied Mathematics, Philadelphia, USA, 2005. ISBN 9780898715293.

[9] J. Argyris. An excursion into large rotations. *Computer Methods in Applied Mechanics and Engineering*, 32(1-3):85–155, 1982. doi: 10.1016/0045-7825(82)90069-X.

[10] M. L. Baker, D. L. Mingori, and P. J. Goggin. Approximate subspace iteration for constructing internally balanced reduced order models of unsteady aerodynamic systems. In *37th AIAA Structures, Structural Dynamics and Materials Conference*, AIAA 1996-1441, Salt Lake City, UT, USA, 1996. doi: 10.2514/6.1996-1441.

[11] G. Balas, R. Chiang, A. Packard, and M. Safonov. *Robust Control Toolbox Users Guide.* The MathWorks, Inc., Natick, MA, USA, 2006.

[12] M. C. C. Bampton and R. R. Craig. Coupling of substructures for dynamic analyses. *AIAA Journal*, 6(7):1313–1319, 1968. doi: 10.2514/3.4741.

[13] K. J. Bathe and G. Noh. Insight into an implicit time integration scheme for structural dynamics. *Computers & Structures*, 98–99:1–6, 2012. doi: 10.1016/j.compstruc.2012.01.009.

[14] K. J. Bathe and E. L. Wilson. *Numerical Methods in Finite Element Analysis*. Prentice Hall, 1976.

[15] O. A. Bauchau. *Flexible Multibody Dynamics*. Springer, London, UK, 2010. ISBN 9400703341.

[16] O. A. Bauchau and N. J. Theron. Energy decaying scheme for non-linear beam models. *Computer Methods in Applied Mechanics and Engineering*, 134(1-2):37–56, 1996. doi: 10.1016/0045-7825(96)01030-4.

[17] O. A. Bauchau, A. Epple, and S. Heo. Interpolation of finite rotations in flexible multi-body dynamics simulations. *Proceedings of the Institution of Mechanical Engineers, Part K: Journal of Multi-body Dynamics*, 222(4):353–366, 2008. doi: 10.1243/14644193JMBD155.

[18] P. Benner and E. S. Quintana-Ortí. Model Reduction Based on Spectral Projection Methods. In *Dimension Reduction of Large-Scale Systems*, volume 45 of *Lecture Notes in Computational Science and Engineering*, pages 5–48. Springer Berlin Heidelberg, 2005. ISBN 978-3-540-27909-9.

[19] G. Berkooz, P. Holmes, and J. L. Lumley. The Proper Orthogonal Decomposition in the Analysis of Turbulent Flows. *Annual Review of Fluid Mechanics*, 25(1):539–575, 1993. doi: 10.1146/annurev.fl.25.010193.002543.

[20] R. L. Bisplinghoff and H. Ashley. *Principles of Aeroelasticity*. John Wiley & Sons, Inc., New York, USA, 1962. ISBN 0486495000.

[21] M. Blair, R. A. Canfield, and R. W. Roberts. Joined-wing aeroelastic design with geometric nonlinearity. *Journal of Aircraft*, 42(4):832–848, 2005. doi: 10.2514/1.2199.

[22] V. L. Bond, R. A. Canfield, J. E. Cooper, and M. Blair. Experimental nonlinear static deflections of a subscale joined wing. *Journal of Aircraft*, 49(1):329–333, 2012. doi: 10.2514/1.C031423.

[23] E. L. Brown. *Integrated Strain Actuaction in Aircraft with Highly Flexible Composite Wings*. PhD thesis, Mechanical Engineering, Massachusetts Institute of Technology, Cambridge, MA, USA, 2003.

[24] S. A. Brown. Displacement Extrapolation for CFD+CSM Aeroelastic Analysis. In *38th AIAA Structures, Structural Dynamics, and Materials Conference*, AIAA 1997-1090, Kissimmee, FL, USA, 1997. doi: 10.2514/6.1997-1090.

[25] S. Bruner, S. Baber, C. Harris, N. Caldwell, P. Keding, K. Rahrig, L. Pho, and R. Wlezian. NASA n+3 subsonic fixed wing silent efficient low-emissions commercial transport (SELECT) vehicle study. Technical Report NASA CR-2010-216798 REVA, NASA, 2010.

[26] A. Bry and N. Roy. Rapidly-exploring random belief trees for motion planning under uncertainty. In *2011 IEEE International Conference on Robotics and Automation (ICRA)*, 2011. doi: 10.1109/ICRA.2011.5980508.

[27] C. S. Buttrill, T. A. Zeiler, and P. Arbuckle. Nonlinear simulation of a flexible aircraft in maneuvering flight. In *AIAA Flight Simulation Technologies Conference*, AIAA 87-2501, Monterey, CA, USA, 1987. doi: 10.2514/6.1987-2501.

[28] J. R. Canavin and P. W. Likins. Floating Reference Frames for Flexible Spacecraft. *Journal of Spacecraft and Rockets*, 14(12):724–732, 1977. doi: 10.2514/3.57256.

[29] A. Cardona. Superelements Modelling in Flexible Multibody Dynamics. *Multibody System Dynamics*, 4(2-3):245–266, 2000. doi: 10.1023/A:1009875930232.

[30] A. Cardona and M. Géradin. A beam finite element non-linear theory with finite rotations. *International Journal for Numerical Methods in Engineering*, 26(11): 2403–2438, 1988. doi: 10.1002/nme.1620261105.

[31] A. Cardona and M. Géradin. Time integration of the equations of motion in mechanism analysis. *Computers & Structures*, 33(3):801–820, 1989. doi: 10.1016/0045-7949(89)90255-1.

[32] A. Cardona and M. Géradin. Modelling of superelements in mechanism analysis. *International Journal for Numerical Methods in Engineering*, 32(8):15651593, 1991. doi: 10.1002/nme.1620320805.

[33] R. K. Cavin and A. R. Dusto. Hamilton's principle - Finite-element methods and flexible body dynamics. *AIAA Journal*, 15(12):1684–1690, 1977. doi: 10.2514/3.7473.

[34] R. K. Cavin, J. W. Howze, and C. Thisayakorn. Eigenvalue properties of structural mean-axis systems. *Journal of Aircraft*, 13(5):382–384, 1976. doi: 10.2514/3.44532.

[35] C. E. S. Cesnik and E. L. Brown. Modeling of High Aspect Ratio Active Flexible Wings for Roll Control. In *43rd AIAA Structures, Structural Dynamics, and Materials Conference*, AIAA 2002-1719, Denver, CO, USA, 2002. doi: 10.2514/6.2002-1719.

[36] C. E. S. Cesnik and E. L. Brown. Active warping control of a joined-wing airplane configuration. In *44th AIAA Structures, Structural Dynamics and Materials Conference*, Norfolk, VA, 2003. AIAA. doi: 10.2514/6.2003-1715.

[37] C. E. S. Cesnik and D. H. Hodges. VABS: A New Concept for Composite Rotor Blade Cross-Sectional Modeling. *Journal of the American Helicopter Society*, 42(1): 27–38, 1997. doi: 10.4050/JAHS.42.27.

[38] C. E. S. Cesnik, P. J. Senatore, W. Su, E. M. Atkins, and C. M. Shearer. X-HALE: a very flexible unmanned aerial vehicle for nonlinear aeroelastic tests. *AIAA Journal*, 50(12):2820–2833, 2012. doi: 10.2514/1.J051392.

[39] R. G. Cook, R. Palacios, and P. Goulart. Robust Gust Alleviation and Stabilization of Very Flexible Aircraft. *AIAA Journal*, 51(2):330–340, 2013. doi: 10.2514/1.J051697.

[40] E. Cosserat and F. Cosserat. Thorie des corps dformables. *Bulletin of the American Mathematical Society*, 19, 1913. doi: 10.1090/S0002-9904-1913-02334-6.

[41] R. R. Craig. Rotating beam with tip mass analyzed by a variational method. *The Journal of the Acoustical Society of America*, 35(7):990–993, 1963. doi: 10.1121/1.1918644.

[42] R. R. Craig. *Structural dynamics: An Introduction to Computer Methods*. John Wiley & Sons, Inc., New York, USA, 1981. ISBN 0-471-04499-7.

[43] R. C. Cribbs, P. P. Friedmann, and T. Chiu. Coupled helicopter Rotor/Flexible fuselage aeroelastic model for control of structural response. *AIAA Journal*, 38(10): 1777–1788, 2000. doi: 10.2514/2.838.

[44] M. A. Crisfield and G. Jelenić. Objectivity of Strain Measures in the Geometrically Exact Three-Dimensional Beam Theory and its Finite-Element Implementation. *Proceedings of the Royal Society of London. Series A: Mathematical, Physical and Engineering Sciences*, 455(1983):1125–1147, 1999. doi: 10.1098/rspa.1999.0352.

[45] A. Da Ronch, K. Badcock, Y. Wang, A. Wynn, and R. Palacios. Nonlinear model reduction for flexible aircraft control design. In *AIAA Atmospheric Flight Mechanics Conference*, AIAA 2012-4404, Minneapolis, MN, USA, 2012. doi: 10.2514/6.2012-4404.

[46] D. A. Danielson and D. H. Hodges. Nonlinear Beam Kinematics by Decomposition of the Rotation Tensor. *Journal of Applied Mechanics*, 54(2):258–262, 1987. doi: 10.1115/1.3173004.

[47] B. F. De Veubeke. The dynamics of flexible bodies. *International Journal of Engineering Science*, 14(10):895–913, 1976. doi: 10.1016/0020-7225(76)90102-6.

[48] M. Dillsaver, C. Cesnik, and I. Kolmanovsky. Gust load alleviation control for very flexible aircraft. In *AIAA Atmospheric Flight Mechanics Conference*, AIAA 2011-6368, Portland, OR, USA, 2011. doi: 10.2514/6.2011-6368.

[49] M. Dillsaver, C. Cesnik, and I. Kolmanovsky. Gust response sensitivity characteristics of very flexible aircraft. In *AIAA Atmospheric Flight Mechanics Conference*, AIAA 2012-4576, Minneapolis, MN, USA, 2012. doi: 10.2514/6.2012-4576.

[50] J. Dizy, R. Palacios, and S. T. Pinho. Homogenisation of slender periodic composite structures. *International Journal of Solids and Structures*, 50(9):1473–1481, 2013. doi: 10.1016/j.ijsolstr.2013.01.017.

[51] E. H. Dowell and K. C. Hall. Eigenmode Analysis in Unsteady Aerodynamics: Reduced Order Models. *Applied Mechanics Reviews*, 50(6):371–387, 1997. doi: 10.1115/1.3101718.

[52] E. H. Dowell, R. Clark, D. Cox, H. C. Curtis Jr, J. W. Edwards, K. H. Hall, D. A. Peters, R. Scanlan, E. Simiu, F. Sisto, and T. W. Strganac. *A Modern Course in Aeroelasticity*. Number 116 in Solid Mechanics and Its Applications. Springer Netherlands, 4th edition, 2005. ISBN 978-1-4020-2039-1.

[53] M. Drela. Integrated simulation model for preliminary aerodynamic, structural, and control-law design of aircraft. In *40^{th} AIAA Structures, Structural Dynamics and Materials Conference*, AIAA Paper 1999-1394, St. Louis, Missouri, USA, 1999. doi: 10.2514/6.1999-1394.

[54] A. R. Dusto, G. W. Brune, G. M. Dornfield, J.E. Mercer, S. C. Pilet, P. E. Rubbert, R. C. Schwanz, P. Smutny, E. N. Tinoco, and J. A. Weber. A method for predicting the stability characteristics of an elastic airplane. Volume 1: FLEXSTAB theoretical description. Technical report, NASA CR-114712, 1974.

[55] J. R. Dykman and W. P. Rodden. Structural dynamics and quasistatic aeroelastic equations of motion. *Journal of Aircraft*, 37(3):538–542, 2000. doi: 10.2514/2.2634.

[56] J. M. Elzebda, D. T. Mook, and A. H. Nayfeh. Numerical Simulations of Steady and Unsteady Vorticity-Dominated Aerodynamic Interference. *Journal of Aircraft*, 31(5):1031–1036, 1994. doi: 10.2514/3.46606.

[57] D. Enns. *Model reduction for control system design*. PhD thesis, Department of Aeronautics and Aerospace, Stanford University, USA, 1984.

[58] W. Eversman and A. Tewari. Consistent rational-function approximation for unsteady aerodynamics. *Journal of Aircraft*, 28(9):545–552, September 1991. doi: 10.2514/3.46062.

[59] C. Farhat, M. Lesoinne, P. Stern, and S. Lantéri. High performance solution of three-dimensional nonlinear aeroelastic problems via parallel partitioned algorithms: methodology and preliminary results. *Advances in Engineering Software*, 28(1):43–61, 1997. doi: 10.1016/S0965-9978(96)00028-2.

[60] C. Farhat, M. Lesoinne, and P. Le Tallec. Load and motion transfer algorithms for fluid/structure interaction problems with non-matching discrete interfaces: Momentum and energy conservation, optimal discretization and application to aeroelasticity. *Computer Methods in Applied Mechanics and Engineering*, 157(12):95–114, 1998. doi: 10.1016/S0045-7825(97)00216-8.

[61] T. Faulwasser, B. Kern, and R. Findeisen. Model predictive path-following for constrained nonlinear systems. In *48th IEEE Conference on Decision and Control*, pages 8642–8647, 2009. doi: 10.1109/CDC.2009.5399744.

[62] P. P. Friedmann. Renaissance of Aeroelasticity and Its Future. *Journal of Aircraft*, 36(1):105–121, 1999. doi: 10.2514/2.2418.

[63] P. P. Friedmann, J. J. McNamara, B. J. Thuruthimattam, and I. Nydick. Aeroelastic analysis of hypersonic vehicles. *Journal of Fluids and Structures*, 19(5):681–712, 2004. doi: 10.1016/j.jfluidstructs.2004.04.003.

[64] T. C. Fung. Numerical dissipation in time-step integration algorithms for structural dynamic analysis. *Progress in Structural Engineering and Materials*, 5(3):167–180, 2003. doi: 10.1002/pse.149.

[65] Y. C. Fung. *An Introduction to the Theory of Aeroelasticity*. Dover Publications Inc, New York, NY, USA, 2002. ISBN 9780486495057.

[66] M. Gams, M. Saje, S. Srpčič, and I. Planinc. Finite element dynamic analysis of geometrically exact planar beams. *Computers & Structures*, 85(17-18):1409–1419, 2007. doi: 10.1016/j.compstruc.2006.08.081.

[67] J. A. Garcia. Numerical investigation of nonlinear aeroelastic effects on flexible high-aspect-ratio wings. *Journal of Aircraft*, 42(4):1025–1036, 2005. doi: 10.2514/1.6544.

[68] W. Gawronski. *Advanced Structural Dynamics and Active Control of Structures*. Springer, New York, USA, 2004. ISBN 9780387721330.

[69] M. Géradin and A. Cardona. *Flexible Multibody Dynamics: A Finite Element Approach*. John Wiley & Sons Ltd, Chichester, UK, 2001. ISBN 0471489905.

[70] M. Géradin and D. Rixen. *Mechanical Vibrations: Theory and Application to Structural Dynamics*. John Wiley & Sons Ltd, Chichester, UK, 2nd edition edition, 1997. ISBN 047197546X.

[71] M. Ghoreyshi and R. Cummings. Unsteady aerodynamics modeling for aircraft maneuvers: a new approach using time-dependent surrogate modeling. In *30th AIAA Applied Aerodynamics Conference*, AIAA 2012-3327, New Orleans, USA, 2012. doi: 10.2514/6.2012-3327.

[72] K. Glover. All optimal Hankel-norm approximations of linear multivariable systems and their L^∞-error bounds. *International Journal of Control*, 39(6):1115–1193, 1984. doi: 10.1080/00207178408933239.

[73] M. Goland. The flutter of a uniform cantilever wing. *Journal of Applied Mechanics*, 12(4):A197–A198, 1945.

[74] G. H. Golub and C. F. Van Loan. *Matrix Computations*. The John Hopkins University Press, London, UK, 3rd edition, 1996. ISBN 0801854148.

[75] S. Guo. Aeroelastic optimization of an aerobatic aircraft wing structure. *Aerospace Science and Technology*, 11(5):396–404, 2007. doi: 10.1016/j.ast.2007.01.003.

[76] S. Haghighat, J. R. R. A. Martins, and H. H. T. Liu. Aeroservoelastic Design Optimization of a Flexible Wing. *Journal of Aircraft*, 49(2):432–443, 2012. doi: 10.2514/1.C031344.

[77] S. Haghighat, J. R. R. A. Martins, and H. H. T. Liu. Model-Predictive Gust Load Alleviation Controller for a Highly Flexible Aircraft. *Journal of Guidance, Control and Dynamics*, 35(6):1751–1766, 2012. doi: 10.2514/1.57013.

[78] K. C. Hall. Eigenanalysis of Unsteady Flows about Airfoils, Cascades and Wings. *AIAA Journal*, 32(12):2426–2432, 1994. doi: 10.2514/3.12309.

[79] B. Hallissy and C. E. S. Cesnik. High-fidelity aeroelastic analysis of very flexible aircraft. In *52nd AIAA Structures, Structural Dynamics and Materials Conference*, AIAA 2011-1914, Denver, CO, USA, 2011. doi: 10.2514/6.2011-1914.

[80] S. J. Hammarling. Numerical solution of the stable, non-negative definite Lyapunov equation. *IMA Journal of Numerical Analysis*, 2(3):303–323, 1982. doi: 10.1093/imanum/2.3.303.

[81] M. Y. Harmin and J. E. Cooper. Aeroelastic behaviour of a wing including geometric nonlinearities. *The Aeronautical Journal*, 115(1174):767–788, December 2011.

[82] M. Y. Harmin and J. E. Cooper. Dynamic aeroelastic prediction for geometrically nonlinear aircraft. In *International Forum on Aeroelasticity and Structural Dynamics*, IFASD 2011-050, Paris, France, June 2011.

[83] H. M. Hilber, T. J. R. Hughes, and R. L. Taylor. Improved numerical dissipation for time integration algorithms in structural dynamics. *Earthquake Engineering & Structural Dynamics*, 5(3):283–292, 1977. doi: 10.1002/eqe.4290050306.

[84] S. V. Hoa. Vibration of a rotating beam with tip mass. *Journal of Sound and Vibration*, 67(3):369–381, 1979. doi: 10.1016/0022-460X(79)90542-X.

[85] D. H. Hodges. Finite rotation and nonlinear beam kinematics. *Vertica*, 11(1/2): 297–307, 1987.

[86] D. H. Hodges. A mixed variational formulation based on exact intrinsic equations for dynamics of moving beams. *International Journal of Solids and Structures*, 26 (11):1253–1273, 1990. doi: 10.1016/0020-7683(90)90060-9.

[87] D. H. Hodges. Geometrically exact, intrinsic theory for dynamics of curved and twisted anisotropic beams. *AIAA Journal*, 41(6):1131–1137, 2003. doi: 10.2514/2.2054.

[88] D. H. Hodges. *Nonlinear Composite Beam Theory*. Progress in Astronautics & Aeronautics, Vol 213. American Institue of Aeronautics and Astronautics, Reston, Virginia, USA, 2006.

[89] K. M. Hsiao and J. Y. Jang. Dynamic analysis of planar flexible mechanisms by co-rotational formulation. *Computer Methods in Applied Mechanics and Engineering*, 87(1):1–14, 1991. doi: 10.1016/0045-7825(91)90143-T.

[90] K. M. Hsiao, J. Y. Lin, and W. Y. Lin. A consistent co-rotational finite element formulation for geometrically nonlinear dynamic analysis of 3-D beams. *Computer Methods in Applied Mechanics and Engineering*, 169(1–2):1–18, 1999. doi: 10.1016/S0045-7825(98)00152-2.

[91] A. Ibrahimbegović. On finite element implementation of geometrically nonlinear Reissner's beam theory: three-dimensional curved beam elements. *Computer Methods in Applied Mechanics and Engineering*, 122(1-2):11â26, 1995. doi: 10.1016/0045-7825(95)00724-F.

[92] A. Ibrahimbegović and M. A. Mikdad. Finite rotations in dynamics of beams and implicit time-stepping schemes. *International Journal for Numerical Methods in Engineering*, 41(5):781814, 1998. doi: 10.1002/(SICI)1097-0207(19980315)41:5¡781::AID-NME308¿3.0.CO;2-9.

[93] P. Iscold, G. A. S. Pereira, and L. A. B. Torres. Development of a hand-launched small UAV for ground reconnaissance. *IEEE Transactions on Aerospace and Electronic Systems*, 46(1):335–348, 2010. doi: 10.1109/TAES.2010.5417166.

[94] M. Iura and S. N. Atluri. On a consistent theory, and variational formulation of finitely stretched and rotated 3-D space-curved beams. *Computational Mechanics*, 4(2):73–88, 1988. doi: 10.1007/BF00282411.

[95] G. Jelenić and M. A. Crisfield. Geometrically exact 3D beam theory: implementation of a strain-invariant finite element for statics and dynamics. *Computer Methods in Applied Mechanics and Engineering*, 171(12):141–171, 1999. doi: 10.1016/S0045-7825(98)00249-7.

[96] T. R. Kane, A. K. Banerjee, and R. R. Ryan. Dynamics of a cantilever beam attached to a moving base. *Journal of Guidance, Control, and Dynamics*, 10(2): 139–151, 1987. doi: 10.2514/3.20195.

[97] M. Karpel. Design for active flutter suppression and gust alleviation using state-space aeroelastic modeling. *Journal of Aircraft*, 19(3):221–227, 1982. doi: 10.2514/3.57379.

[98] J. Katz and A. Plotkin. *Low-Speed Aerodynamics*. Cambridge Aerospace Series. Cambridge University Press, New York, NY, USA, 2nd edition, 2001. ISBN 0521665523.

[99] G. J. Kennedy and J. R. R. A. Martins. A homogenization-based theory for anisotropic beams with accurate through-section stress and strain prediction. *International Journal of Solids and Structures*, 49(1):54–72, 2012. doi: 10.1016/j.ijsolstr.2011.09.012.

[100] T. Kier, G. Looye, M. Scharpenberg, and M. Reijerkerk. Process, methods and tools for flexible aircraft flight dynamics model integration. In *International Forum on Aeroelasticity and Structural Dynamics (IFASD)*, Stockholm, Sweden, 2007.

[101] P. Konstadinopoulos, D. F. Thrasher, D. T. Mook, A. H. Nayfeh, and L. Watson. A vortex-lattice method for general, unsteady aerodynamics. *Journal of Aircraft*, 22 (1):4349, 1985. doi: 10.2514/3.45078.

[102] S. Lall, J. E. Marsden, and S. Glavaki. A subspace approach to balanced truncation for model reduction of nonlinear control systems. *International Journal of Robust and Nonlinear Control*, 12(6):519535, 2002. doi: 10.1002/rnc.657.

[103] A. Laub, M. Heath, C. Paige, and R. Ward. Computation of system balancing transformations and other applications of simultaneous diagonalization algorithms. *IEEE Transactions on Automatic Control*, 32(2):115–122, 1987. doi: 10.1109/TAC.1987.1104549.

[104] J. G. Leishman. *Principles of Helicopter Aerodynamics*. Cambridge University Press, New York, USA, 2nd edition, 2006. ISBN 0521858607.

[105] E. Livne. Aeroelasticity of joined-wing airplane configurations: Past work and future challenges – A survey. In *19th AIAA Applied Aerodynamics Conference*, Seattle, WA, USA, 2001. doi: 10.2514/6.2001-1370.

[106] E. Livne and T. A. Weisshaar. Aeroelasticity of Nonconventional Airplane Configurations – Past and Future. *Journal of Aircraft*, 40(6):1047–1065, 2003. doi: 10.2514/2.7217.

[107] A. E. H. Love. *A Treatise on the Mathematical Theory of Elasticity*. Dover Publications Inc, New York, NY, USA, 4th edition, 1944. ISBN 1113223650.

[108] M. H. Love, P. S. Zink, P. A. Wieselmann, and H. Youngren. Body freedom flutter of high aspect ratio flying wings. In *46th AIAA Structures, Structural Dynamics, and Materials Conference*, AIAA 2005-1947, Austin, TX, USA, 2005. doi: 10.2514/6.2005-1947.

[109] D. J. Lucia. The SensorCraft configurations: A non-linear AeroServoElastic challenge for aviation. In *46th AIAA Structures, Structural Dynamics and Materials Conference*, AIAA Paper 2005-1943, pages 1768 – 1774, Austin, TX, USA, 2005. doi: 10.2514/6.2005-1943.

[110] D. J. Lucia, P. S. Beran, and W. A. Silva. Reduced-order modeling: new approaches for computational physics. *Progress in Aerospace Sciences*, 40(1–2):51–117, 2004. doi: 10.1016/j.paerosci.2003.12.001.

[111] A. Manan, G. A. Vio, M. Y. Harmin, and J. E. Cooper. Optimization of aeroelastic composite structures using evolutionary algorithms. *Engineering Optimization*, 42 (2):171–184, 2010. doi: 10.1080/03052150903104358.

[112] *Matlab R2013a Documentation*. The Mathworks, Inc. `http://www.mathworks.co.uk/help/techdoc` Last retrieved: 23 April 2012.

[113] T. Mauermann. *Flexible Aircraft Modelling for Flight Loads Analysis of Wake Vortex Encounters*. PhD thesis, Technische Universität Carolo-Wilhelmina zu Braunschweig, Braunschweig, Germany, 2011.

[114] M. I. McEwan, J. R. Wright, J. E. Cooper, and A. Y. T. Leung. A combined modal/finite element analysis technique for the dynamic response of a non-linear beam to harmonic excitation. *Journal of Sound and Vibration*, 243(4):601–624, June 2001. doi: 10.1006/jsvi.2000.3434.

[115] L. Meirovitch. Hybrid state equations of motion for flexible bodies in terms of quasi-coordinates. *Journal of Guidance, Control, and Dynamics*, 14(5):1008–1013, 1991. doi: 10.2514/3.20743.

[116] L. Meirovitch and I. Tuzcu. Integrated approach to the dynamics and control of maneuvering flexible aircraft. Technical Report NASA/CR-2003-211748, NASA, 2003.

[117] L. Meirovitch and I. Tuzcu. Unified Theory for the Dynamics and Control of Maneuvering Flexible Aircraft. *AIAA Journal*, 42(4):714–727, 2004. doi: 10.2514/1.1489.

[118] L. Meirovitch and I. Tuzcu. The Lure of the Mean Axes. *Journal of Applied Mechanics*, 74(3):497–504, 2007. doi: 10.1115/1.2338060.

[119] D. Meyer and G. Franklin. A connection between normalized coprime factorizations and linear quadratic regulator theory. *IEEE Transactions on Automatic Control*, 32 (3):227–228, 1987. doi: 10.1109/TAC.1987.1104569.

[120] D. G. Meyer. A Fractional Approach to Model Reduction. In *American Control Conference*, pages 1041 –1047, 1988.

[121] D. G. Meyer. The construction of special coprime factorizations in discrete time. *IEEE Transactions on Automatic Control*, 35(5):588 –590, 1990. doi: 10.1109/9.53531.

[122] R. D. Milne. Dynamics of the Deformable Plane. Technical Report 3345, Her Majesty's Stationary Office, London, UK, 1962.

[123] R. D. Milne. Some remarks on the dynamics of deformable bodies. *AIAA Journal*, 6(3):556–558, 1968. doi: 10.2514/3.4541.

[124] D. T. Mook and A. H. Nayfeh. Application of the vortex-lattice method to high-angle-of-attack subsonic aerodynamics. SAE Technical Paper 851817, SAE International, Warrendale, PA, USA, 1985.

[125] B. Moore. Principal component analysis in linear systems: Controllability, observability, and model reduction. *IEEE Transactions on Automatic Control*, 26(1):17–32, 1981. doi: 10.1109/TAC.1981.1102568.

[126] J. Murua. *Flexible Aircraft Dynamics with a Geometrically-Nonlinear Description of the Unsteady Aerodynamics*. PhD thesis, Department of Aeronautics, Imperial College London, UK, 2012.

[127] J. Murua, R. Palacios, and J. M. R. Graham. Assessment of Wake-Tail Interference Effects on the Dynamics of Flexible Aircraft. *AIAA Journal*, 50(7):1575–1585, 2012. doi: 10.2514/1.J051543.

[128] J. Murua, R. Palacios, and J. M. R. Graham. Applications of the unsteady vortex-lattice method in aircraft aeroelasticity and flight dynamics. *Progress in Aerospace Sciences*, 55:46–72, 2012. doi: 10.1016/j.paerosci.2012.06.001.

[129] J. Murua, R. Palacios, and J. M. R. Graham. Open-Loop Stability and Closed-Loop Gust Alleviation on Flexible Aircraft Including Wake Modeling. In *53rd AIAA Structures, Structural Dynamics, and Materials Conference*, AIAA 2012-1484, Honolulu, HI, USA, 2012. doi: 10.2514/6.2012-1484.

[130] N. M. Newmark. A method of computation for structural dynamics. *Journal of Engineering Mechanics*, 85:67–94, 1959.

[131] B. F. Ng, R. Palacios, J. M. R. Graham, and E. C. Kerrigan. Robust control synthesis for gust load alleviation from large aeroelastic models with relaxation of spatial discretisation. In *Proceedings of the EWEA 2012*, Copenhagen, Denmark, 2012.

[132] T. E. Noll, S. D. Ishmael, B. Henwood, M. E. Perez-Davis, G. C. Tiffany, M. Gaier, J. M. Brown, and T. Wierzbanowski. Technical findings, lessons learned, and recommendations resulting from the helios prototype vehicle mishap. In *NATO/RTO AVT-145 Workshop on Design Concepts, Processes and Criteria for UAV Structural Integrity*, Florence, Italy, 2007. NASA.

[133] G. Offner, T. Eizenberger, and H. H. Priebsch. Separation of reference motions and elastic deformations in an elastic multi-body system. *Proceedings of the Institution of Mechanical Engineers, Part K: Journal of Multi-body Dynamics*, 220(1):63–75, 2006. doi: 10.1243/146441905X69263.

[134] R. Palacios. Nonlinear normal modes in an intrinsic theory of anisotropic beams. *Journal of Sound and Vibration*, 330(8):1772–1792, 2011. doi: 10.1016/j.jsv.2010.10.023.

[135] R. Palacios and C. E. S. Cesnik. Cross-Sectional Analysis of Non-Homogeneous Anisotropic Active Slender Structures. *AIAA Journal*, 43(12):2624–2638, 2005. doi: 10.2514/1.12451.

[136] R. Palacios and C. E. S. Cesnik. Geometrically Nonlinear Theory of Composite Beams with Deformable Cross Sections. *AIAA Journal*, 46(2):439–450, 2008. doi: 10.2514/1.31620.

[137] R. Palacios, J. Murua, and R. Cook. Structural and Aerodynamic Models in the Nonlinear Flight Dynamics of Very Flexible Aircraft. *AIAA Journal*, 48(11):2648–2559, 2010. doi: 10.2514/1.52446.

[138] M. Patil. Nonlinear aeroelastic analysis of joined-wing aircraft. In *44th AIAA Structures, Structural Dynamics and Materials Conference*, AIAA 2003-1487, Norfolk, VA, USA, 2003. doi: 10.2514/6.2003-1487.

[139] M. J. Patil and D. H. Hodges. On the importance of aerodynamic and structural geometrical nonlinearities in aeroelastic behavior of high-aspect-ratio wings. *Journal of Fluids and Structures*, 19(7):905–915, 2004. doi: 10.1016/j.jfluidstructs.2004.04.012.

[140] M. J. Patil and D. H. Hodges. Flight dynamics of highly flexible flying wings. *Journal of Aircraft*, 43(6):1790–1798, 2006. doi: 10.2514/1.17640.

[141] M. J. Patil, D. H. Hodges, and C. E. S. Cesnik. Nonlinear Aeroelastic Analysis of Complete Aircraft in Subsonic Flow. *Journal of Aircraft*, 37(5):753–760, 2000. doi: 10.2514/2.2685.

[142] M. J. Patil, D. H. Hodges, and C. E. S. Cesnik. Nonlinear aeroelasticity and flight dynamics of high-altitude long-endurance aircraft. *Journal of Aircraft*, 38(1):88–94, 2001. doi: 10.2514/2.2738.

[143] M. J. Patil, D. H. Hodges, and C. E. S. Cesnik. Limit-cycle oscillations of high-aspect-ratio wings. *Journal of Fluids and Structures*, 15(1):107–132, 2001. doi: 10.1006/jfls.2000.0329.

[144] E. W. Pendleton, D. Bessette, P. B. Field, G. D. Miller, and K. E. Griffin. Active aeroelastic wing flight research program: Technical program and model analytical development. *Journal of Aircraft*, 37(4):554–561, 2000. doi: 10.2514/2.2654.

[145] D. A. Peters, S. Karunamoorthy, and W. Cao. Finite state induced flow models. Part I: Two-dimensional thin airfoil. *Journal of Aircraft*, 32(2):313–322, 1995. doi: 10.2514/3.46718.

[146] D. Petot. Modélisation du décrochage dynamique. *La Recherche Aérospatiale*, 5: 60–72, 1995.

[147] C. L. Pettit and R. V. Grandhi. Optimization of a wing structure for gust response and aileron effectiveness. *Journal of Aircraft*, 40(6):1185–1191, 2003. doi: 10.2514/2.7208.

[148] B. Raghavan and M. J. Patil. Flight Dynamics of High Aspect-Ratio Flying Wings: Effect of Large Trim Deformation. *Journal of Aircraft*, 46(5):1808–1812, 2009. doi: 10.2514/1.36847.

[149] B. Raghavan and M. J. Patil. Flight control for flexible, high-aspect-ratio flying wings. *Journal of Guidance, Control, and Dynamics*, (1):64–74, 2010. doi: 10.2514/1.45471.

[150] E. Reissner. On one-dimensional large-displacement finite-strain beam theory. *Studies in Applied Mathematics*, 52:87–95, 1973.

[151] C. Reschke. *Integrated Flight Loads Modelling and Analysis for Flexible Transport Aircraft*. PhD thesis, TU Stuttgart, Germany, 2006.

[152] C. Reschke and G. Looye. Comparison of model integration approaches for flexible aircraft flight dynamics modelling. In *International Forum on Aeroelasticity and Structural Dynamics (IFASD)*, Mnchen, 2005.

[153] W. P. Rodden. *Theoretical and Computational Aeroelasticity*. Crest Publishing, USA, 2011. ISBN 0692012419.

[154] W. P. Rodden and J. R. Love. Equations of Motion of a Quasisteady Flight Vehicle Utilizing Restrained Static Aeroelastic Characteristics. *Journal of Aircraft*, 22(9): 802–809, 1985. doi: 10.2514/3.45205.

[155] M. C. Romanowski. Reduced order unsteady aerodynamic and aeroelastic models using Karhunen-Loève eigenmodes. In *AIAA Symposium on Multidisciplinary Analysis and Optimization*, Bellevue, WA, USA, 1996. doi: 10.2514/6.1996-3981.

[156] M. C. Romanowski and E. H. Dowell. Using eigenmodes to form an efficient euler-based unsteady aerodynamics analysis. In *ASME International Mechanical Engineering Congress and Exposition*, Fairfield, NJ, USA, 1994.

[157] G. J. J. Ruijgrok. *Elements of Airplane Performance*. Delft University Press, Delft, Netherlands, 2nd edition, 2009. ISBN 9789065622327.

[158] J. Rule, R. Clark, and D. Cox. Aerodynamic Model Reduction Through Balanced Realization. *AIAA Journal*, 42(5):1045–1048, 2004. doi: 10.2514/1.9596.

[159] M. Sadeghi and Feng Liu. Coupled fluid-structure simulation for turbomachinery blade rows. In *43rd AIAA Aerospace Sciences Meeting and Exhibit*, AIAA 2005-0018, Reno, NV, USA, January 2005. AIAA. doi: 10.2514/6.2005-18.

[160] M. G. Safonov and R. Y. Chiang. A Schur method for balanced-truncation model reduction. *IEEE Transactions on Automatic Control*, 34(7):729 –733, 1989. doi: 10.1109/9.29399.

[161] J. M. A. Scherpen. Balancing for nonlinear systems. *Systems & Control Letters*, 21 (2):143–153, 1993. doi: 10.1016/0167-6911(93)90117-O.

[162] D. Schmidt. *Modern Flight Dynamics*. McGraw-Hill, New York, USA, 2011. ISBN 007339811X.

[163] D. K. Schmidt and D. L. Raney. Modeling and Simulation of Flexible Flight Vehicles. *Journal of Guidance, Control, and Dynamics*, 24(3):539–546, 2001. doi: 10.2514/2.4744.

[164] M. C. Van Schoor and A. H. Von Flotow. Aeroelastic characteristics of a highly flexible aircraft. *Journal of Aircraft*, 27(10):901–908, 1990. doi: 10.2514/3.45955.

[165] J. Schuler and K. König. Integral control of large flexible aircraft. Technical Report RTO MP-36, NATO Research and Technology Organisation, Ottawa, Canada, 1999.

[166] A. A. Shabana. Substructure synthesis methods for dynamic analysis of multibody systems. *Computers & Structures*, 20(4):737–744, 1985. doi: 10.1016/0045-7949(85)90035-5.

[167] A. A. Shabana. Flexible multibody dynamics: Review of past and recent developments. *Multibody System Dynamics*, 1(2):189–222, 1997. doi: 10.1023/A:1009773505418.

[168] C. M. Shearer and C. E. S. Cesnik. Modified Generalized Alpha Method for Integrating Governing Equations of Very Flexible Aircraft. In *47th AIAA Structures, Structural Dynamics, and Materials Conference*, AIAA Paper 2006-1747, 2006. doi: 10.2514/6.2006-1747.

[169] C. M. Shearer and C. E. S. Cesnik. Nonlinear Flight Dynamics of Very Flexible Aircraft. *Journal of Aircraft*, 44(5):1528–1545, 2007. doi: 10.2514/1.27606.

[170] C. M. Shearer and C. E. S. Cesnik. Trajectory control for very flexible aircraft. *Journal of Guidance, Control, and Dynamics*, 31(2):340–357, 2008. doi: 10.2514/1.29335.

[171] F. J. Silvestre. Aeroservoelastic Investigations of a High-Aspect-Ratio Motor Glider. In *Advances in Aerospace Guidance, Navigation and Control*, pages 639–658. Springer Verlag, Berlin, Germany, 2013. ISBN 978-3-642-38252-9.

[172] F. J. Silvestre and R. Luckner. Integrated Model for the Flight Mechanics of a Flexible Aircraft in the Time Domain. In *International Forum on Aeroelasticity and Structural Dynamics (IFASD)*, Seattle, Washington, USA, 2009.

[173] F. J. Silvestre and P. Paglione. Dynamics and Control of a Flexible Aircraft. In *AIAA Atmospheric Flight Mechanics Conference*, Honolulu, HI, USA, 2008. AIAA Paper 2008–6876. doi: 10.2514/6.2008-6876.

[174] J. C. Simo. A finite strain beam formulation. The three-dimensional dynamic problem. Part I. *Computer Methods in Applied Mechanics and Engineering*, 49(1):55–70, 1985. doi: 10.1016/0045-7825(85)90050-7.

[175] J. C. Simo and N. Tarnow. A new energy and momentum conserving algorithm for the non-linear dynamics of shells. *International Journal for Numerical Methods in Engineering*, 37(15):25272549, 1994. doi: 10.1002/nme.1620371503.

[176] J. C. Simo and L. Vu-Quoc. A three-dimensional finite-strain rod model. Part II: Computational aspects. *Computer Methods in Applied Mechanics and Engineering*, 58(1):79–116, 1986. doi: 0045-7825(86)90079-4.

[177] J. C. Simo and L. Vu-Quoc. On the Dynamics of Flexible Beams Under Large Overall Motions – The Plane Case: Part II. *Journal of Applied Mechanics*, 53(4): 855–863, 1986. doi: 10.1115/1.3171871.

[178] J. C. Simo and L. Vu-Quoc. The role of non-linear theories in transient dynamic analysis of flexible structures. *Journal of Sound and Vibration*, (3):487–508, 1987. doi: 10.1016/0022-460X(87)90410-X.

[179] J. C. Simo and L. Vu-Quoc. On the dynamics in space of rods undergoing large motions – A geometrically exact approach. *Computer Methods in Applied Mechanics and Engineering*, 66(2):125–161, 1988. doi: 10.1016/0045-7825(88)90073-4.

[180] J. C. Simo, N. Tarnow, and M. Doblare. Non-linear dynamics of three-dimensional rods: Exact energy and momentum conserving algorithms. *International Journal for Numerical Methods in Engineering*, 38(9):1431–1473, 1995. doi: 10.1002/nme.1620380903.

[181] R. Simpson and R. Palacios. Numerical aspects of nonlinear flexible aircraft flight dynamics modeling. In *54^{th} AIAA Structures, Structural Dynamics, and Materials Conference*, Boston, MA, USA, 2013. doi: 10.2514/6.2013-1634.

[182] S. Skogestad and I. Postlethwaite. *Multivariable Feedback Control: Analysis and Design*. John Wiley & Sons Ltd, Chichester, UK, 2005. ISBN 9780470011676.

[183] M. J. Smith, M. J. Patil, and D. H. Hodges. Cfd-based analysis of nonlinear aeroelastic behavior of high-aspect ratio wings. In *42nd AIAA Structures, Structural Dynamics, and Materials Conference*, AIAA 2001-1582, Seattle, WA, USA, 2001. doi: 10.2514/6.2001-1582.

[184] M. Spieck. The ultra-green aircraft-some aspects from the aeroelastic point of view. Technical Report JAXA-SP-07-008E, Japan Aerospace Exploration Agency (JAXA), 2008.

[185] B. K. Stanford and P. S. Beran. Analytical Sensitivity Analysis of an Unsteady Vortex Lattice Method for Flapping Wing Optimization. *Journal of Aircraft*, 47(2): 647–662, 2010. doi: 10.2514/1.46259.

[186] B. L. Stevens and F. L. Lewis. *Aircraft Control and Simulation*. John Wiley & Sons, Inc., New York, NY, USA, 1992.

[187] W. Su and C. E. S. Cesnik. Nonlinear Aeroelasticity of a Very Flexible Blended-Wing-Body Aircraft. *Journal of Aircraft*, 47(5):1539–1553, 2010. doi: 10.2514/1.47317.

[188] W. Su and C. E. S. Cesnik. Dynamic response of highly flexible flying wings. *AIAA Journal*, 49(2):324–339, 2011. doi: 10.2514/1.J050496.

[189] W. Su and C. E. S. Cesnik. Strain-Based Analysis for Geometrically Nonlinear Beams: A Modal Approach. In *53rd AIAA Structures, Structural Dynamics, and Materials Conference*, Honolulu, HI, USA, 2012. doi: 10.2514/6.2012-1713.

[190] T. Theodorsen. General theory of aerodynamic instability and the mechanism of flutter. NACA Report No. 496, 1935.

[191] M. Vidyasagar. *Control System Synthesis: A Factorization Approach*. MIT Press, Cambridge, USA, 1987. ISBN 0262720124.

[192] M. Vidyasagar. Normalised coprime factorizations for nonstrictly proper systems. *IEEE Transactions on Automatic Control*, 33(3):300 –301, 1988. doi: 10.1109/9.408.

[193] G. Vinnicombe. The robustness of feedback systems with bounded complexity controllers. *Automatic Control, IEEE Transactions on*, 41(6):795–803, 1996. doi: 10.1109/9.506232.

[194] H. Wagner. Über die Entstehung des dynamischen Auftriebes von Tragflügeln. *Zietschrift für Angewandte Mathematik und Mechanick*, 5(1):17, 1925.

[195] Y. Wang, R. Palacios, and A. Wynn. Robust aeroelastic control of very flexible wings using intrinsic models. In *54th AIAA Structures, Structural Dynamics, and Materials Conference*, AIAA 2013-1485, Boston, MA, USA, 2013. AIAA. doi: 10.2514/6.2013-1485.

[196] Z. Wang, P. C. Chen, D. D. Liu, D. T. Mook, and M. J. Patil. Time Domain Nonlinear Aeroelastic Analysis for HALE Wings. In *47th AIAA Structures, Structural Dynamics, and Materials Conference*, AIAA Paper 2006-1640, Newport, RI, USA, 2006. doi: 10.2514/6.2006-1640.

[197] Z. Wang, P. C. Chen, D. D. Liu, and D. T. Mook. Nonlinear-Aerodynamics/Nonlinear-Structure Interaction Methodology for a High-Altitude Long-Endurance Wing. *Journal of Aircraft*, 47(2):556–566, 2010. doi: 10.2514/1.45694.

[198] T. M. Wasfy and A. K. Noor. Computational strategies for flexible multibody systems. *Applied Mechanics Reviews*, 56(6):553–613, 2003. doi: 10.1115/1.1590354.

[199] M. R. Waszak and D. K. Schmidt. Flight dynamics of aeroelastic vehicles. *Journal of Aircraft*, 25(6):563–571, 1988. doi: 10.2514/3.45623.

[200] K. Willcox and J. Peraire. Balanced Model Reduction via the Proper Orthogonal Decomposition. *AIAA Journal*, 40(11):2323–2330, 2002. doi: 10.2514/2.1570.

[201] J. R. Wright and J. E. Cooper. *Introduction to Aircraft Aeroelasticity and Loads*. John Wiley & Sons Ltd, Chichester, UK, 2008. ISBN 0470858400.

[202] S. H. Zerweckh, A. H. Von Flotow, and J. E. Murray. Flight testing a highly flexible aircraft - Case study on the MIT Light Eagle. *Journal of Aircraft*, 27(4):342–349, 1990. doi: 10.2514/3.25278.

[203] K. Zhou, J. C. Doyle, and K. Glover. *Robust and Optimal Control*. Prentice-Hall, Upper Saddle River, NJ, USA, 1996.